UNIVERSITY OF SUSSEX

DOCTORAL THESIS

Towards the trapping of electrons in the Geonium Chip Penning trap

Author:
Ryan WILLETTS

Supervisor:
Dr. José VERDÚ-GALIANA

A thesis submitted in partial fulfilment of the requirements for the degree of Doctor of Philosophy

in the

Geonium Chip Group
School of Mathematical and Physical Sciences

Submitted January 2022

Declaration of Authorship

I hereby declare that this thesis has not been and will not be, submitted in whole or in part to another University for the award of any other degree.

Please note that prior to this doctoral work, the author undertook examined research projects while a member of the same research group and so the author had some prior knowledge of the general research area. These research projects contributed to the degrees of i) *BSc* in *Physics* and ii) *MSc* in *Frontiers of Quantum Technology*, where both degrees were awarded by the *University of Sussex*.

When the author first joined the Geonium Chip research group, the existing trap had been built predominantly by Dr Jonathan Pinder, Dr April Cridland Mathad and Dr John Lacy. Some of the research which is included in this thesis was obtained with the help of others, but these instances have been declared within the main body of the thesis.

All the raw data for the calibration of the magnetic field source (§5.1.2), for the demonstrations of the 300 mT fields (§5.1.3) and for the 500 mT field (§5.1.4) were measured by the author. The analysis of the calibration (§5.1.2) and the analysis of the 300 mT fields (§5.1.3) were conducted predominantly by Dr José Verdú-Galiana but with input from the author. The analysis of the 500 mT field (§5.1.4) was undertaken solely by the author, but with a method which is similar to that which was used to analyse the 300 mT fields (§5.1.3).

Signed:

_____

Date:

_____

UNIVERSITY OF SUSSEX

Abstract

Sussex Centre for Quantum Technologies

School of Mathematical and Physical Sciences

Doctor of Philosophy

Towards the trapping of electrons in the Geonium Chip Penning trap

by Ryan WILLETTS

The Geonium Chip Penning trap is a unique scalable Penning trap technology with applications in quantum technology, with a particular focus on the detection of single microwave photons. The trap has not yet demonstrated the trapping of electrons, but this thesis includes work towards this goal. A comprehensive photoelectric characterisation of the cryogenic trapping chamber has been undertaken, with applications in leak detection and the validation of the electrostatic model of the trap, among others. The calibration of a novel planar magnetic field source has been undertaken, which has been verified by the measurement of homogeneous magnetic fields of up to 500 mT. This scalable magnetic field source has other potential engineering applications. A control program for the magnetic field source has been implemented, which provides active quench protection and controls the magnetic field distribution. A new trap loading procedure has been programmed, which implements an electron impact ionisation technique. An ionisation curve has been obtained which is in good agreement with that of helium, which suggests that secondary electrons are being produced in the trap. Resistive wall destabilisation has been investigated which has resulted in new electronic filters.

Acknowledgements

Thank you to Dr. José Verdú-Galiana, who supervised the author during this research project and without whom the research could not have been undertaken. Also, another significant thank you to Dr Jonathan Pinder, who has provided the author with much help in the laboratory. Thank you to the past-and-present members of the research group who have also provided the author with guidance: Dr April Cridland Mathad, Dr John Lacy, Dr Alberto Jesús Uribe Jiménez and Raquel Álvarez García. Thank you to other various members of the University of Sussex which include the administrative staff, the technical staff and members of other research groups. Thank you to the School of Mathematical and Physical Sciences at the University of Sussex for providing the author with funding, which enabled the author to conduct the research. Finally, thank you to the author's family and friends who supported the author during the difficulties encountered during this research.

Contents

List of Figures

List of Tables

List of Abbreviations

AC	**A**lternating **C**urrent
CAD	**C**omputer **A**ided **D**esign
CSGE	**C**ontinuous **S**tern-**G**erlach **E**ffect
CPT	**C**harge-**P**arity-**T**ime
CPU	**C**entral **P**rocessing **U**nit
DC	**D**irect **C**urrent
DUT	**D**evice-**U**nder-**T**est
EUT	**E**lectrode-**U**nder-**T**est
FFT	**F**ast **F**ourier **T**ransform
GCPT	**G**eonium **C**hip **P**enning **t**rap
PCB	**P**rinted **C**ircuit **B**oard
SOLT	**S**hort-**O**pen-**L**oad-**T**hru
QED	**Q**uantum **E**lectro**d**ynamics
UV	**U**ltra**v**iolet
VNA	**V**ector **N**etwork **A**nalyser

Chapter 1

Introduction

1.1 The motivation for the Geonium Chip Penning trap

1.1.1 A selected history of the Penning trap

The Penning trap was initially developed by multiple groups [1] and named by Hans Dehmelt [2, 3], who designed the trap with influence from the work of Frans Penning [1] ([4]). Dehmelt developed a now-widely-employed general electronic detection technique; the *bolometric technique* [5] and Dehmelt also developed a method to continuously (and non-destructively) determine the electron spin state; the *Continuous Stern-Gerlach Effect* [6]. Dehmelt was the first to trap a single electron [7] and Dehmelt later denoted a single trapped electron within a Penning trap as *geonium* [8]. Dehmelt was awarded a share of the 1989 Nobel prize [9] for their work, alongside Wolfgang Paul and Norman Ramsey.

1.1.2 Comparing the Geonium Chip Penning trap to alternative planar Penning trap technologies

In 2005, the first planar Penning trap was proposed [10] at Mainz with circular electrode geometry, which later successfully trapped (100 - 1000 [11]) electrons [11, 12], while at room temperature. This trap moved to Ulm and shortly afterwards it was modified and successfully trapped electrons again [13, 14], while at cryogenic temperature using a dilution refrigerator [13]. This trap [13] managed to trap a small cloud of electrons ("such

peaks can be associated with few electrons excitation or even perhaps with excitation of a single electron" [13]) and it was considered for integration in quantum systems [15]. It was suggested that "the strong anharmonicity of the axial potential in the planar trap prevented us from observing a single electron" [13].

Planar Penning traps with circular electrode geometry were further optimised at Harvard with the intent to trap a single electron [16–18], eventually trapping a small cloud of two electrons after apparatus improvements [19], while at cryogenic temperature using a dilution refrigerator [16, 19]. Before the improvements [16, 18] it was suggested that "the trap stability and detection sensitivity remain to be improved" [18] and after the improvements it was suggested that "all efforts to measure a smaller linewidth were not successful and were limited by axial frequency instabilities" [19]. This optimisation proposed a much smaller (several orders of magnitude) degree of axial frequency broadening at 5 K than was observed in Mainz and Ulm [16]. Despite the use of dilution refrigerators, these traps [13, 16] both had axial amplifier temperatures of approximately 5 K without feedback cooling, a temperature which is in principle achievable in the Geonium Chip Penning trap experiment without a dilution refrigerator. This optimisation [16] determined that in order to minimise the undesired axial frequency shifts (thermal broadening) (§2.1.2), the amplitude coefficients a_k (most significantly a_2) had to be minimised, by optimising the expansion coefficients C_{ki} of the axial potential (§2.1.1). It was determined that [16] the Mainz [11] and Ulm [13, 14] traps were not sufficiently optimised, but one harmonic optimisation achieved $C_1 = C_3 = C_4 = C_6 = 0$; $C_2 = 1$ and $a_2 = a_3 = a_4 = a_5 = 0$ [16, Eqn. 50 and Table 1] by optimising the electrode voltages and the electrode geometry. It was also discussed that [16] naturally for cylindrical traps with reflection symmetry along $\hat{u}_z$, that odd-k the coefficients C_k and low-order a_k vanish, but this isn't true [16] for the planar Penning traps with circular electrode geometry [10–19]. However [16], a *mirror-image* [16] trap may be formed from electrodes mirrored in two parallel opposing (separated in z) planes $\hat{u}_x = \hat{u}_y$, which creates a symmetric axial potential along $\hat{u}_z$. Also, the *mirror-image* trap can be orthogonalized (where the axial frequency is independent of the tuning of the electrode voltages [16, 20]).

One fundamental benefit of the Geonium Chip Penning trap [21] is that the axial potential (§3.2) is symmetric along $\hat{u}_z$ (and $\hat{u}_x$) and so there should naturally be vanishing odd-order anharmonicities along $\hat{u}_z$ (and $\hat{u}_x$) [21]. The Geonium Chip Penning trap was conceptualised [21] by projecting the conventional cylindrical trap [20] onto a chip, as depicted in Figure 1.1. However, the Geonium Chip Penning trap [21] differs from the other planar Penning traps [10–19] in that the electrodes are in the $\hat{u}_x - \hat{u}_z$ plane (rather than in the $\hat{u}_x - \hat{u}_y$ plane) and so symmetry along $\hat{u}_z$ is maintained. This also means that the magnetic field axis $\hat{u}_z$ is parallel to the surface of the Geonium Chip Penning trap (§3.3), whereas $\hat{u}_z$ runs perpendicular from the surface of the chip in the other traps [10–19]. The Geonium Chip Penning trap is still a planar trap and so there is a fundamental asymmetry, but the asymmetry is along $\hat{u}_y$ where the most troublesome anharmonicity is C_{012} [21] (§3.2), rather than along $\hat{u}_z$ [10–19]. However [21], rather than try to eliminate anharmonicities [16, Eqn. 50] as described above, the electrode voltages in the Geonium Chip Penning trap are optimised by finding an optimal tuning ratio $T_c^{\text{opt}}(y)$ which cancels the frequency shift - but the anharmonicites themselves may be non-zero (§2.1.2). Furthermore, the ultra elliptical regime [22] (§3.2) may be used to limit the vertical motion along $\hat{u}_y$ and so the trapped particle would sample less of the asymmetric potential along $\hat{u}_y$.

The traps with circular electrode geometry [10–19] are compared to the Geonium Chip Penning trap in Figure 1.2. The electrodes of a trap with circular electrode geometry [13] are depicted in Figure 1.2a, assuming that the 100 μm gaps are centred around the ideal electrode boundaries of 1 mm, 3 mm and 5 mm. It can be seen in Figure 1.2a that there are three concentric electrodes with voltages V_1, V_2 and V_3 [10], which are bounded by gaps with radii $\rho_1 \leq \rho \leq \rho_2$, $\rho_3 \leq \rho \leq \rho_4$ and $\rho_5 \leq \rho \leq \rho_6$ [13]. The electrodes of the Geonium Chip Penning trap are depicted in Figure 1.2b. Also depicted are some example axial potentials produced by both types of trap. The axial potential $\Phi(z)$ (Figure 1.2c) of the trap (depicted in Figure 1.2a) was calculated using the model [10, eq. 8] (equivalent to [16, eq. 11]) for the trap in [13], with electrode voltages $V_1 = 0.0$ V, $V_2 = -5.2$ V and $V_3 = -14.0$ V [13]. The axial potential $\Phi(z)$ (Figure 1.2d) of the Geonium Chip Penning trap

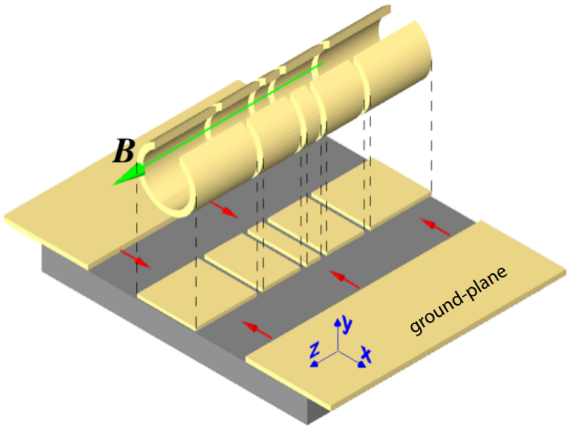

(A) Conception of the Geonium Chip Penning trap, where the electrodes of a conventional cylindrical Penning trap are projected onto the $\hat{u}_x - \hat{u}_z$ plane [21]. Reproduced from [21].

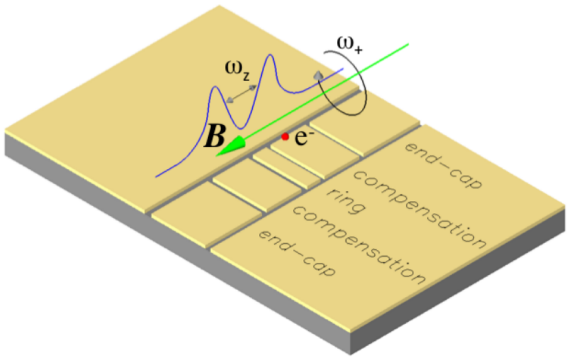

(B) A sketch of the electrodes of the Geonium Chip Penning trap, where a trapped particle is represented with a red circle in the equilibrium trapping position $\vec{r}_0 = (0, y_0, 0)$ [21] (§2.1.1), above the centre of the ring electrode [21]. Reproduced from [21].

FIGURE 1.1: The conception of the Geonium Chip Penning trap [21].

(depicted in Figure 1.2b) was calculated using *Mathematica* functions provided by Dr José Verdú-Galiana, to compute (3.1) using formulae in [22, App. A], with electrode voltages $V_R = -3.5875$ V, $V_C = -5.0255$ V and $V_E = -20.4488$ V. The voltages chosen to make $\Phi(z)$ in Figure 1.2d were those which make the same axial frequency ($\omega_z = 2\pi \cdot 67.97$ MHz for trapped electrons) as the potential $\Phi(z)$ (Figure 1.2c) for the Penning trap with circular electrode geometry.

There also exist other similar traps with alternative designs and/or aims. For example, two-dimensional arrays of planar Penning traps have also been developed, with the *Pixel trap* "for ions or electrons" having been fabricated [23] (Ulm) and another scalable 2D array for ions having been proposed [24] (Zürich). Another alternative planar Penning trap using wires was proposed at Imperial College (London) [25], which later successfully trapped Ca^+ ions [26]. Another alternative Penning trap (similar to the *mirror-image* trap [16, 17] at Harvard) was proposed and tested with Ca^+ ions by Imperial College (London) [27]. Furthermore, a Paul trap at room temperature which was fabricated using printed circuit boards has successfully trapped electrons [28]. Also, a portable Penning trap was used to transport electrons more than 5000 km [29].

Although it has been speculated that planar Penning traps may have successfully trapped just a single electron, it has not been conclusive [13, 19]. The Geonium Chip Penning trap aims to be the first planar Penning trap to conclusively trap a single electron.

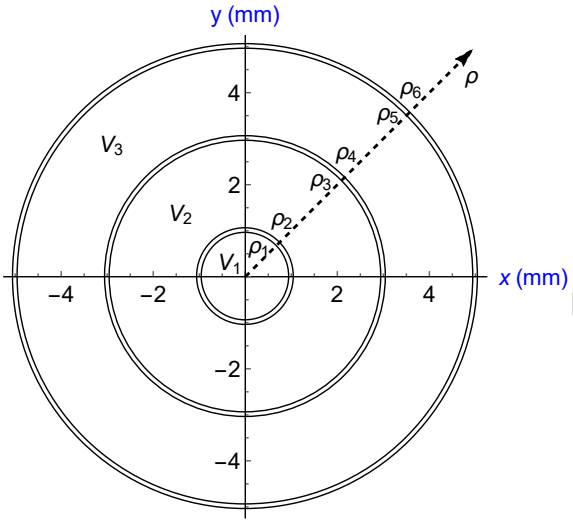

(A) A sketch of a planar Penning trap with circular electrode geometry, using the trap dimensions from [13]. The magnetic field axis z is perpendicular to both the x and y axes [10] and the particles are trapped at $(x, y, z) = (0, 0, z_0 \neq 0)$ [10].

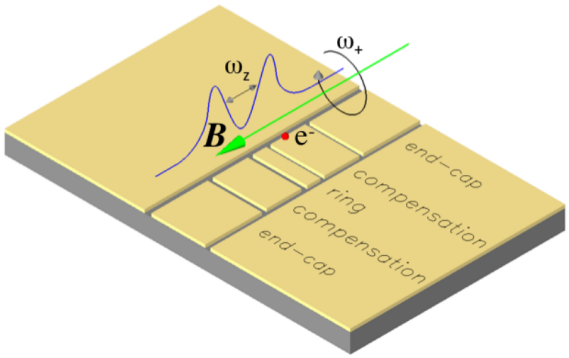

(B) A sketch of the Geonium Chip Penning trap, where a trapped electron is represented as a red circle (at $\vec{r}_0 = (0, y_0, 0)$ [21] (§2.1.1)). Reproduced from [21].

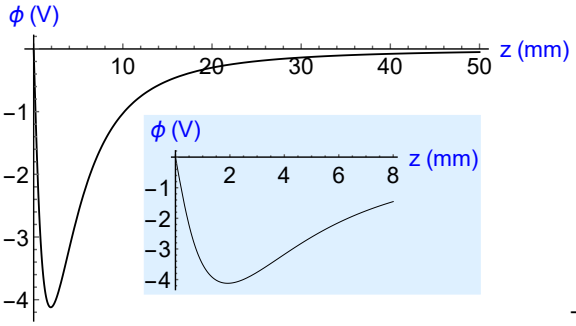

(C) An example plot of an axial potential $\Phi(z)$ produced by the trap depicted in Figure 1.2a, using voltages which were discussed in [13]. Inset: only a small range of z.

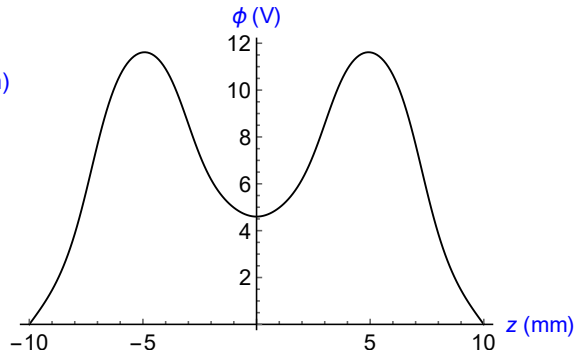

(D) An example plot of an axial potential $\Phi(z)$ produced by the Geonium Chip Penning trap depicted in Figure 1.2b.

FIGURE 1.2: A comparison between the existing planar Penning traps (with circular electrode geometry) and the Geonium Chip (planar) Penning trap. The traps are depicted in Figures 1.2a and 1.2b (respectively) and some example potentials $\Phi(z)$ (with opposite sign) are depicted in Figures 1.2c and 1.2d (respectively). It can be seen that $\Phi(z)$ is less symmetric in Figure 1.2c than in Figure 1.2d, which results from the topology of the traps. It is important to consider that the trap/potential in Figure 1.2a/1.2c is not for an optimised geometry nor optimised set of voltages like the traps discussed in [16, Eqn. 50 and Table 1].

1.1.3 The prospective impact of the Geonium Chip Penning trap

The Geonium Chip Penning trap can in principle trap any charged particle (including ions and electrons), provided that the electric field, magnetic field and detection circuit are optimised for the particle to be trapped (while taking into account trap stability (§7.2.3)). The polarity of the electric field means that only charged particles of one charge-polarity may be trapped indefinitely at any one time in a Penning trap. However, there are variations of the Penning trap which contain both charge-polarities simultaneously: i) an electron-beam ion source [30] and an electron-beam ion trap [31]. At present it is aimed to only trap electrons in the Geonium Chip Penning trap.

With a name derived from Dehmelt's *geonium atom* [8, 22], the Geonium Chip Penning trap was primarily conceptualised as a scalable Penning trap technology, with the aim to implement an electric field source (electrodes) and a magnetic field source within a **scalable** chip (the *Geonium Chip* [22]) [22]. Eventually, the axial detection circuit and the (differential) preamplifier will also be incorporated into the Geonium Chip itself [32, 33]. The Geonium Chip is scalable [22] because of its modular nature (eventually containing the electric field source, the magnetic field source and the detection circuitry). Also, the magnetic field axis $\hat{u}_z$ of the Geonium Chip Penning trap is in the same plane as the electrodes ($\hat{u}_x - \hat{u}_z$) and so trapped particles can be shuttled between different sites (as routinely achieved in cylindrical traps e.g. [34]), which is a requirement for scalability.

Furthermore, the Geonium Chip Penning trap is made more **deployable** than conventional Penning traps by the use of a closed-system cryocooler rather than the use of liquid cryogens (e.g. [35]). This means that the Geonium Chip Penning trap could be implemented into commercial devices, for example in the sector of mass spectrometry where the Geonium Chip Penning trap offers a cheaper technology for a similar degree of precision as existing mass spectrometers [36], where the magnetic field source of the Geonium Chip Penning trap should be cheaper than typical solenoids. The Geonium Chip Penning trap is currently being developed primarily as a technology for single microwave photon detection [37] (§2.4). At present (§3), the Geonium Chip just contains the electric field source (electrodes), while the magnetic field source is separate but bolted to

the Geonium Chip and the detection circuit uses an axial resonator which is also separate from the Geonium Chip.

However, the Geonium Chip Penning trap also provides an opportunity to try to **improve fundamental physics measurements** [36], which are discussed in (§1.2). Firstly, the electric and magnetic field sources are bolted together (Figure 3.6b) (or incorporated into the Geonium Chip in the future) and so they have very little relative motion and so the trap is fundamentally relatively impervious to vibration [36], unlike some cylindrical traps (e.g. [35]). Vibration would mean that the trapped particle would sample a wider volume of magnetic field (which might have a higher degree of inhomogeneity), or experience a time-varying magnetic field, which might broaden the motional frequencies (§2.1.2)). Similarly, the closed-system cryocooler has good temperature stability, which should also reduce the broadening of motional frequencies (§2.1.2). Furthermore, the trapped particle can be trapped at different heights y_0 (§2.1.1) above the chip and so systematic effects relating to electrostatic and magnetic fields may be investigated and subsequently corrected for during high-precision measurements, for example when measuring a g-factor (§1.2.1). Also, the Geonium Chip Penning trap is an elliptical Penning trap (§2.1.1) and the ellipticity may be advantageous, however the ellipticity can also be eradicated by choosing suitable electrode voltages. For example, the ultra elliptical regime (§3.2) could be advantageous when forming crystals (§1.2.4) by reducing the amplitude of the magnetron motion [38], or a "quasi two-dimensional electron gas in free space" [22]. Also, when a particle is put into the ultra elliptical regime [22], the electron should sample less of the magnetic field in one direction and more of the magnetic field in another, so motional frequencies might have less broadening (§2.1.2).

1.2 Applications of Penning traps

1.2.1 Tests of fundamental physics: the g-factor; quantum electrodynamics and charge-parity-time invariance

"The g factor of a charged particle is defined as the proportionality constant between its angular momentum $\vec{J}$ and the corresponding induced magnetic moment $\vec{\mu}$" [39]. High precision measurements of the g-factors of trapped free and bound electrons in Penning traps allow QED to be verified to a high extent and also allow for the determination of the electron mass and the fine structure constant α [40]. One advantage to determining the g-factor with a Penning trap is the ability to use the *Continuous Stern-Gerlach Effect* [6].

The g-factor of a single trapped electron "is the most precisely determined property of an elementary particle" [41], which is in reference to the determination of $g/2$ for the so-called "one-electron quantum cyclotron" in a Penning trap (determined to 0.28 ppt) [35, 42]. The g-factor can be written as a series expansion of the fine structure constant α with the expansion coefficients being calculable from QED [35] and therefore, this [35, 42] determination of the g-factor gave rise to at least two significant outcomes [35]. Firstly, by using theoretical (calculated) expansion coefficients, this [35, 42] determination of the g-factor lead to an improvement of the determination of the (fundamental) fine structure constant α [42], which was determined "12 times more accurately than the next-most-precise method" [35]. Secondly, by using an independent (of g) determination of α, this [35, 42] determination of the g-factor has to a good extent verified models of quantum electrodynamics (by verifying the aforementioned expansion coefficients) [35]. As mentioned in [35], [43, 44] contain information about how the g-factor is related to α.

As reviewed in [40], the g-factors of bound electrons in hydrogen-like ions have been determined for $^{12}C^{5+}$ [34], $^{16}O^{7+}$ [39] and $^{28}Si^{13+}$ [45]. These three determinations of the g-factors of bound electrons have allowed verification of bound-state quantum electrodynamics [34, 39, 45]. Similarly to a free electron as described above, the g-factor for a bound electron may also be expressed as a series expansion, however for a bound electron the expansion is an expansion of both α and the atomic number Z [40]. The most

recent of these determinations [45] is an improvement to the uncertainty of the bound-state g-factor from its predecessor [46]. The determination from the predecessor [46] was "the most precise value of the g factor of a bound electron" [46] where "the excellent agreement between experimental and theoretical value represents to date the most accurate test of bound-state QED calculations in strong fields" [46]. One benefit of verifying QED using a bound electron is that the extreme conditions might be better at showing a limit to existing QED theory [47].

Penning traps have also been used to verify CPT invariance by determining and comparing the g-factors of singly-trapped matter particles and their antimatter counterparts, for example i) the electron and positron [48] and ii) the proton and antiproton [49, 50].

1.2.2 Tests of fundamental physics: antimatter and the weak equivalence principle

Antihydrogen has been made using antimatter plasmas which have been stored in Penning-Malberg traps [51]. Some examples located at CERN [52, 53] aim to measure the gravitation of antihydrogen: ALPHA-2 [54] and ALPHA-g [55], GBAR [56, 57] and AEgIS [58]. Measurements of the gravitation of antihydrogen can be used to test the weak equivalence principle, of high importance to the theory of General relativity [58]. Another Penning-Ioffe trap experiment (ATRAP) for trapping antihydrogen is also underway [59].

1.2.3 Mass spectrometry and nuclear and particle physics

Penning traps have also been used as precise mass spectrometers [60]. For example, the most precise determinations of i) the atomic mass of the proton and also ii) the proton to electron mass ratio have been determined [61] using a ratio of motional frequencies and the Invariance Theorem [62]. Also, the atomic mass of the electron has been determined most precisely [63] using the Continuous Stern-Gerlach Effect [6]. Furthermore, the antiproton-to-proton charge-to-mass ratio has been precisely determined which also helps to verify the weak equivalence principle [64].

Penning trap mass spectrometry also has uses in nuclear and particle physics, for example in neutrino physics as described in the review article [65]. One such application is in the KATRIN Collaboration which uses two Penning trap mass spectrometers [66] with the intent to reduce the upper limit for the neutrino mass [67]. Also, the determination [46] of the g-factor described above also allowed for an estimation of the nuclear charge radius of ^{28}Si [46]. Penning traps can also have applications in the measurements of nuclear magnetic moments [68]. The high charge-to-mass ratio of electrons allows trapped single electrons to be used as highly sensitive impulse sensors to detect charged particles [69].

1.2.4 Quantum computing

The DiVincenzo criteria [70] are a set of requirements for quantum computing. A single trapped electron in a Penning Trap has been proposed for use in quantum computing [71] and for example may perform the Deutsch algorithm [71, 72]. Up to three qubits may be encoded into a single trapped electron [71]. There exists "a universal set of quantum gates on every single electron" [73] which can also be formed between all single trapped electrons in a Penning Trap array [73, 74]. The experimental implementation of "quantum information processing with trapped electrons" [75] has also been discussed.

There has also been an alternative similar proposal for a two-dimensional array of Penning traps (but not for electrons), with applications in quantum computation and quantum simulation [24]. Quantum simulation has been theorised with a Coulomb ion crystal in a Penning trap [76–79] and there has begun experimental progress [80, 81]. Penning traps can facilitate electron-electron entanglement which can make a universal quantum gate or have uses in quantum metrology [82]. A Penning trap based quantum metrology experiment is being undertaken with applications in quantum logic and spectroscopy [83] and quantum enhanced sensing has been demonstrated in a Paul trap with potential applications in measuring g-factors in Penning traps [84]. Furthermore, hybrid quantum systems might be better with a single trapped electron rather than with a single trapped ion [85].

A room temperature Paul trap has trapped electrons with potential applications for trapped electron qubits [28]. To help realise qubit operations in a cryogenic planar Paul trap, a modified Stern-Gerlach effect may be used [86] which fulfils the DiVincenzo criteria [70, 86], similar to the use of the Continuous Stern-Gerlach Effect [6] in a Penning trap.

Chapter 2

Theory of the Geonium Chip Penning trap

2.1 The motion of a trapped particle in an elliptical Penning trap

2.1.1 The ideal motion

The electrostatic quadrupole potential

An ideal Penning trap is comprised of an electrostatic quadrupole potential and an homogeneous magnetic field [87]. The dynamics of a trapped particle in an ideal hyperbolic Penning trap (with circular/cylindrical [88], non-elliptical symmetry in the x-y plane) have been determined analytically [87, 89, 90]. These equations of motion are also valid for cylindrical Penning traps [20], which also exhibit this circular symmetry. However, if the quadrupole field gains an additional term proportional to $(x^2 - y^2)$ and thus no longer exhibits circular symmetry, the trap becomes an *elliptical trap* [88].

The ideal elliptical quadrupole potential ϕ_{quad} as a function of the three cartesian spatial coordinates x, y and z may be defined using [21]

$$\phi_{\text{quad}}(x,y,z) = \underbrace{C_{002} \cdot \left(z^2 - \frac{x^2 + (y-y_0)^2}{2}\right)}_{\phi_{\text{conventional}}} + \underbrace{\frac{1}{2} C_{002}\epsilon \cdot (x^2 - (y-y_0)^2)}_{\phi_{\text{elliptical}}}. \tag{2.1}$$

The (dimensionless) ellipticity ϵ is a function of the curvatures of the ideal elliptical quadrupole potential in each of the three spatial dimensions [21]

$$\epsilon = \frac{C_{200} - C_{020}}{C_{002}}, \tag{2.2}$$

where the curvatures may be defined using [21]

$$C_{002} = \frac{1}{2} \cdot \frac{\partial^2 \phi_{\text{quad}}}{\partial z^2}|_{\vec{r}_0} \tag{2.3}$$

$$C_{020} = \frac{1}{2} \cdot \frac{\partial^2 \phi_{\text{quad}}}{\partial y^2}|_{\vec{r}_0} \tag{2.4}$$

$$C_{200} = \frac{1}{2} \cdot \frac{\partial^2 \phi_{\text{quad}}}{\partial x^2}|_{\vec{r}_0}. \tag{2.5}$$

All three curvatures are evaluated at the equilibrium trapping position $\vec{r}_0 = (0, y_0, 0)$, around which the particle is trapped [21], where the quadrupole field exhibits no force on the trapped particle [91]. The equilibrium position y_0 may be defined using the relation [21]

$$\frac{\partial \phi_{\text{quad}}(0, y_0, 0)}{\partial y}|_{y=y_0} = 0. \tag{2.6}$$

The ideal elliptical quadrupole potential ϕ_{quad} (2.1) has two terms $\phi_{\text{conventional}}$ and $\phi_{\text{elliptical}}$. The first term $\phi_{\text{conventional}}$ is the ideal quadrupole field for a conventional Penning trap with circular symmetry (e.g. of similar form to the potential defined in [89]) and $\phi_{\text{elliptical}}$ is an additional electrostatic field which introduces an ellipticity.

Two electrostatic quadrupole potentials, both defined by $\phi_{\text{quad}}(x, y, z)$ (2.1), are plotted in Figures 2.1a and 2.1b. Both potentials are identical except for the ellipticity ϵ, where in Figure 2.1a the ellipticity ϵ is non-zero at positive five (which would form an elliptical Penning trap), whereas in Figure 2.1b the ellipticity is zero (which would form a conventional trap with circular symmetry). In Figure 2.1a the ellipticity is set arbitrarily high to $\epsilon = 5$ to exaggerate the ellipticity of an elliptical potential, but note that for $|\epsilon| \geq 1$, particles would not be trapped [88]. The curvature C_{002} (2.3) in both Figures 2.1a and 2.1b is that implied in [21] for a trapped electron with an axial frequency of $2\pi \cdot 28$ MHz (thus $C_{002} \approx 88\ \text{kV/m}^2$).

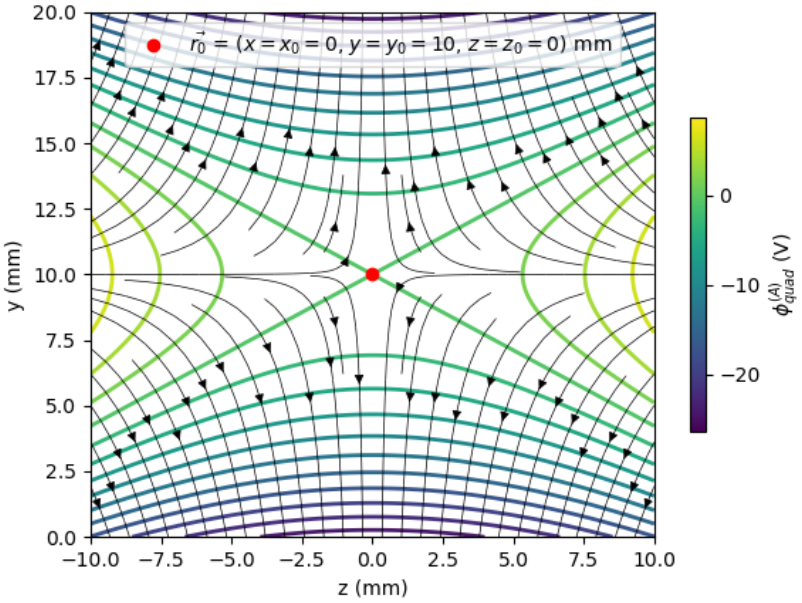

(A) Plotting an elliptical electrostatic potential $\phi^{(A)}_{\text{quad}}(x, y, z, y_0 = 10\text{ mm}, \epsilon = +5)$.

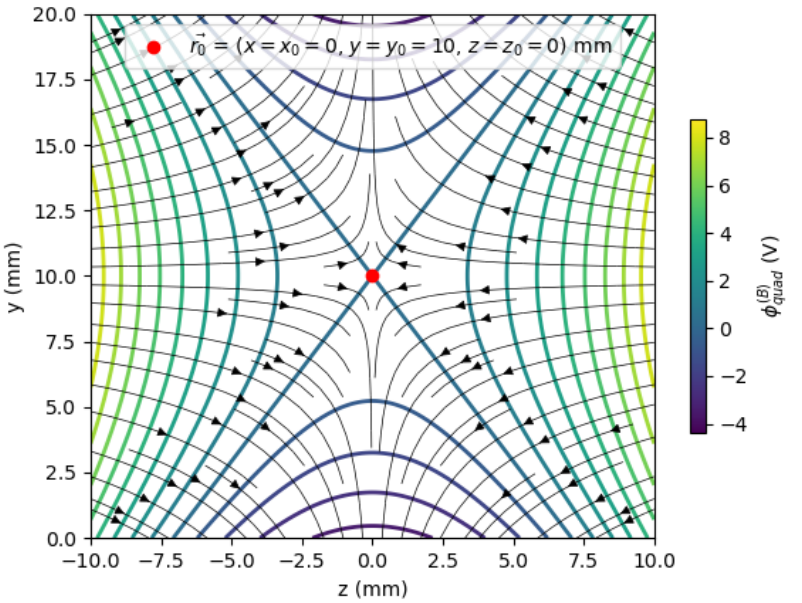

(B) Plotting a non-elliptical electrostatic potential $\phi^{(B)}_{\text{quad}}(x, y, z, y_0 = 10\text{ mm}, \epsilon = 0)$.

FIGURE 2.1: Plots of two different electrostatic potentials $\phi_{\text{quad}}(x, y, z)$ (2.1) in the plane $x = 0$, both with equilibrium height $y_0 = 10$ mm. Figure 2.1a shows an elliptical Penning trap with $\epsilon = +5$ (dimensionless) and Figure 2.1b shows a non-elliptical Penning trap with $\epsilon = 0$ (dimensionless). The thicker, multi-coloured lines represent equipotential lines in the electrostatic potentials while the thinner, black arrows represent the electrostatic field lines, which always run perpendicular to the equipotential lines. The equilibrium positions $\vec{r_0}$ are marked with filled red circles.

The dynamics of a trapped particle

The classical dynamics of a trapped particle in an ideal elliptical Penning trap have been determined [88] and verified [92]. A particle in an ideal elliptical Penning trap undergoes two decoupled motions: a (simple harmonic) *axial* motion in $\hat{u}_z$ and an elliptical epicyclical radial motion in $\hat{u}_x$ and $\hat{u}_y$ composed of a *modified cyclotron motion* and a *magnetron drift* [87, 88]. The *modified* cyclotron motion is sometimes denoted the *reduced* cyclotron motion [21]. A particle with a mass m and an electric charge q in an ideal elliptical Penning trap (a superposition of an homogeneous magnetic field $\vec{B} = B_0\hat{u}_z$ with an elliptical electrostatic quadrupole potential $\phi_{\text{quad}}(x, y, z)$) is acted upon by the Lorentz force [93]

$$\vec{F} = -q\vec{\nabla}\phi_{\text{quad}} + q(\dot{\vec{r}} \times \vec{B}). \tag{2.7}$$

After applying the Lorentz force to Newton's Second Law, for the case of an elliptical electrostatic potential (2.1), the equations of motion may be written

$$\frac{\partial^2}{\partial t^2}\begin{pmatrix} x \\ y - y_0 \end{pmatrix} = \frac{qB_0}{m}\overbrace{\begin{pmatrix} 0 & 1 \\ -1 & 0 \end{pmatrix}}^{\mathbf{M}_1}\frac{\partial}{\partial t}\begin{pmatrix} x \\ y - y_0 \end{pmatrix} + \frac{qC_{002}}{m}\overbrace{\begin{pmatrix} (1-\epsilon) & 0 \\ 0 & (1+\epsilon) \end{pmatrix}}^{\mathbf{M}_2}\begin{pmatrix} x \\ y - y_0 \end{pmatrix} \tag{2.8a}$$

$$m\frac{\partial^2 z}{\partial t^2} = -2qC_{002}z, \tag{2.8b}$$

where it can be seen that the $\hat{u}_x$ and $\hat{u}_y$ (*radial*) motion (2.8a) is decoupled from the $\hat{z}$ (*axial*) motion (2.8b). The axial motion (2.8b) is an ideal simple harmonic motion with the solution [22]

$$z(t) = A_z\cos(\omega_z t) \tag{2.9a}$$

$$A_z = \sqrt{\frac{2E_z}{m\omega_z^2}} \tag{2.9b}$$

$$\omega_z = \sqrt{2C_{002}\frac{q}{m}}, \tag{2.9c}$$

where E_z is the energy of the axial motion [22]. The equation of motion for the radial motion (2.8a) is not as simple to solve, because the equations of motion for x and y are coupled, because the matrix $\mathbf{M}_1$ which results from the magnetic field $\vec{B}$ has off-diagonal terms.

Kretzschmar solved for the dynamics of the radial motion [88]. Kretzschmar shows how alternative equations of motion may be obtained by performing a canonical transformation to the Hamiltonian, which may be solved as an eigenvalue problem to give the motional frequencies [88]

$$\omega_p = \sqrt{\frac{1}{2}(\omega_c^2 - \omega_z^2) + \frac{1}{2}\sqrt{\omega_c^2\omega_1^2 + \epsilon^2\omega_z^4}} \tag{2.10a}$$

$$\omega_m = \sqrt{\frac{1}{2}(\omega_c^2 - \omega_z^2) - \frac{1}{2}\sqrt{\omega_c^2\omega_1^2 + \epsilon^2\omega_z^4}}, \tag{2.10b}$$

with

$$\omega_c = \frac{qB_0}{m} \tag{2.11a}$$

$$\omega_1 = \sqrt{\omega_c^2 - 2\omega_z^2}. \tag{2.11b}$$

The frequencies ω_p and ω_m may be denoted the *modified cyclotron* frequency and the *magnetron* frequency respectively [88]. The *modified* cyclotron frequency is sometimes denoted the *reduced* cyclotron frequency [21]. The frequencies ω_p and ω_m are functions of the *true cyclotron* frequency ω_c and the frequency ω_1 [88]. The frequency ω_1 is without a colloquial name because it has no obvious physical interpretation, however it gives rise to the stability condition $2\omega_z^2 < \omega_c^2$ [23]. These frequencies may also be written [88]

$$\omega_p = \frac{1}{2}(\omega_c + \omega_1) \tag{2.12}$$

$$\omega_m = \frac{1}{2}(\omega_c - \omega_1) \tag{2.13}$$

and thus (which is also true for an ideal Penning trap with circular symmetry [87])

$$\omega_c = \omega_p + \omega_m. \tag{2.14}$$

These frequencies form parts of the motional solutions which were first identified by Kretzchmar [88] and are written here with the notation of Verdú [21]

$$x(t) = A_p\xi_p \cos(\omega_p t) + A_m\xi_m \cos(\omega_m t) \tag{2.15a}$$

$$y(t) - y_0 = A_p\eta_p \sin(\omega_p t) + A_m\eta_m \sin(\omega_m t). \tag{2.15b}$$

The amplitudes $A_p\xi_p$ and $A_p\eta_p$ are the semi-axes of the elliptical modifed cyclotron motion and the amplitudes $A_m\xi_m$ and $A_m\eta_m$ are the semi-axes of the elliptical magnetron drift motion [88]. The scaling factors A_p and A_m have dimensions of length [22] whereas the dimensionless scaling factors ξ_p, ξ_m, η_p and η_m represent semi-axes of unit ellipses [88]. The radial amplitudes may be defined using [22]

$$A_p = \frac{1}{\omega_p}\sqrt{\frac{2E_p}{\gamma_p m}} \tag{2.16a}$$

$$\gamma_p = 1 - \frac{\omega_z^2}{2\omega_p^2} \simeq 1 \tag{2.16b}$$

$$A_m = \sqrt{\frac{2E_m}{(\omega_m^2 - \frac{\omega_z^2}{2})m}}, \tag{2.16c}$$

where E_p and E_m are the energies of the modified cyclotron and magnetron motions [22]. The equations (2.16) for the amplitudes may be derived by considering the potential and kinetic energies of the trapped particle (e.g. as stated in [94]). The dimensionless semi-axes were also derived by Kretzschmar [88] and in the notation of Verdú may be written [22]

$$\xi_{p,m} = \sqrt{\frac{\omega_c^2 + \epsilon\omega_z^2 \pm \sqrt{\omega_c^2\omega_1^2 + \epsilon^2\omega_z^4}}{(2\omega_p/\omega_1)\cdot\sqrt{\omega_c^2\omega_1^2 + \epsilon^2\omega_z^4}}} \tag{2.17a}$$

$$\eta_{p,m} = \sqrt{\frac{\omega_c^2 - \epsilon\omega_z^2 \pm \sqrt{\omega_c^2\omega_1^2 + \epsilon^2\omega_z^4}}{(2\omega_p/\omega_1)\cdot\sqrt{\omega_c^2\omega_1^2 + \epsilon^2\omega_z^4}}}, \tag{2.17b}$$

where the modified cyclotron (denoted p) / magnetron (denoted m) motions correspond to addition/subtraction respectively within the numerators in (2.17a) and (2.17b).

Figure 2.2 below shows a saddle potential (Figure 2.2a) and the ideal motion of a trapped particle (Figure 2.2b). Both plots have a curvature C_{002} (2.3) of ≈ 88 kV/m^2, however the ellipticity was arbitrarily chosen to be $\epsilon = +5$ in Figure 2.2a and $\epsilon = +0.95$ in Figure 2.2b. Also, while both plots share the same equilibrium positions $x_0 = 0$ and $z_0 = 0$, the equilibrium heights were arbitrarily chosen to be $y_0 = 10$ mm in Figure 2.2a and $y_0 = 0$ mm in Figure 2.2b. The saddle potential (Figure 2.2a) is the electrostatic potential $\phi_{\text{quad}}(x, y, z)$ from Figure 2.1a, but with ϕ_{quad} also plotted on the vertical axis - this is **not** a plot with three spatial dimensions. This saddle potential gives rise to a phenomenological explanation of the magnetron motion which orbits a potential hill, when also considering the equivalent saddle potential when plotting as a function of x instead of as a function of y.

Finally, the dynamics of a trapped particle may be summarised visually, using a plot of an example particle motion. A trapped electron in a Penning trap with an ellipticity $\epsilon = 0.95$ (2.2), a curvature $C_{002} \approx 88$ kV/m^2 (2.3) and a magnetic field strength $B_0 = 0.5$ T has a reduced/modified cyclotron frequency $\omega_p = 2\pi \cdot 14$ GHz, an axial frequency $\omega_z = 2\pi \cdot 28$ MHz and a magnetron frequency $\omega_m = 2\pi \cdot 9$ kHz. When the real motion of such a particle is plotted, the three eigenmotions are not clearly distinguishable and so for Figure 2.2b, the frequencies have been arbitrarily set such that all three eigenmotions are distinguishable; the frequencies are $(\omega_p, \omega_m, \omega_z) = 2\pi \cdot (4000, 10, 100)$ Hz. In principle, the particle motion (Figure 2.2b) could be representative of a trapped particle in a Penning trap, however no solution has been numerically determined yet for the ellipticity ϵ nor the magnetic field strength B_0 for a trapped electron with these frequencies. In the $\hat{u}_x$-$\hat{u}_y$ plane, the one single complete elliptical orbit with a high amplitude is the magnetron drift motion, while the higher frequency elliptical motion with a much smaller amplitude is the modified/reduced cyclotron motion. The oscillation along $\hat{u}_z$ is the axial motion.

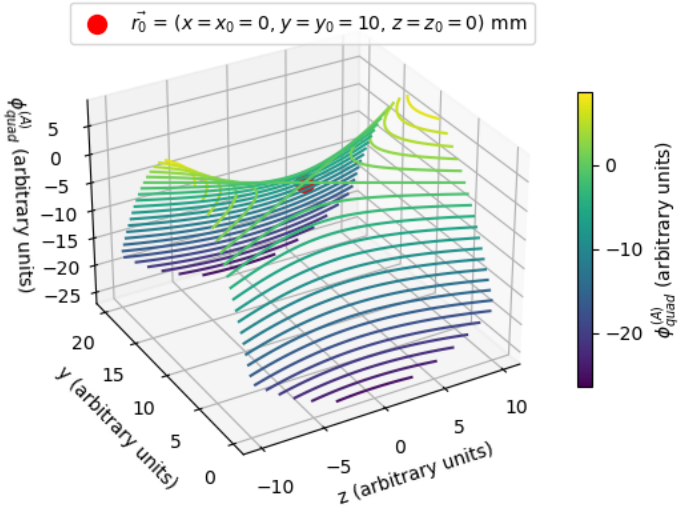

(A) A plot of the same electrostatic potential that was plotted $\phi^{(A)}_{\text{quad}}(x, y, z, y_0 = 10 \text{ mm}, \epsilon = +5)$ (2.1) in Figure 2.1a, again in the plane $x = 0$. To help the interpretation of the plot, the numerical coordinate of the vertical axis ϕ_{quad} is also used to colour the plot as shown in the colour-bar.

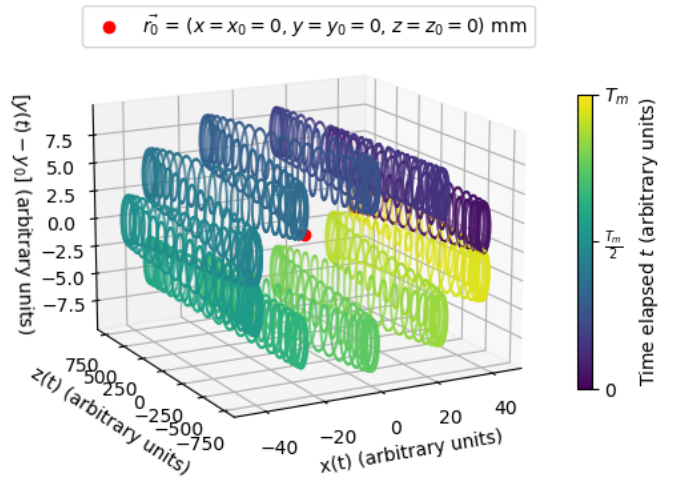

(B) Plotting the motion of a trapped particle in an ideal elliptical Penning trap with potential $\phi^{(C)}_{\text{quad}}(x, y, z, y_0 = 0 \text{ mm}, \epsilon = +0.95)$ (2.1). The time t ranges from $t = 0$ to the time period $t = T_m$ of the magnetron motion and as can be seen in the associated colour-bar, the colour smoothly changes as a function of the time t.

FIGURE 2.2: A plot of the saddle potential and an ideal motion of a trapped particle. Note that the electrostatic potentials are different in Figures 2.2a and 2.2b, so as to make each plot as clear as possible to interpret.

2.1.2 The effects of imperfections in a real trap

A real Penning trap deviates from the ideal case discussed in §2.1.1. Electric anharmonicities [21] and magnetic inhomogeneities [22] (imperfections [95]) are deviations from the ideal case and introduce energy/temperature dependent shifts to the motional eigenfrequencies [21, 22]. In a real (imperfect) trap, the energies E_p, E_z and E_m of the modified cyclotron motion, axial motion and magnetron drift motions respectively are to a good extent independent from one another and each energy fluctuates, which may be described by Boltzmann distributions [95]. Therefore, fluctuating energies cause fluctuating frequencies, which when time-averaged reduce the *visibility* of trapped particles [21].

Electric anharmonicities

The curvatures defined in (2.3), (2.4) and (2.5) form part of a set of expansion coefficients C_{ijk} which may be used to define any potential $\phi_{\text{quad}}(x,y,z)$ as an infinite polynomial expansion in space [21]

$$\phi_{\text{quad}}(x,y,z) = \sum_{i,j,k=0}^{i,j,k=\infty} \underbrace{\frac{1}{i!j!k!} \cdot \frac{\partial^{i+j+k}\phi_{\text{quad}}(x,y,z)}{\partial x^i \partial y^j \partial z^k}\Big|_{(0,y_0,0)}}_{C_{ijk}} x^i y^j z^k. \tag{2.18}$$

The ideal quadrupole potential is only a function of the above-mentioned curvatures C_{002}, C_{020} and C_{002}, with all other terms (excluding C_{000}) denoted anharmonicities which act as perturbations to the ideal potential [21]. Considering terms up to and including the fourth order in (2.18), there are linear relationships between the frequency shifts and energies and so the frequency shifts may be defined using an (electric) *frequency-shifts matrix* $\mathbf{M}^{(\phi)}$ defined by [21]

$$\begin{pmatrix} \Delta\nu_p \\ \Delta\nu_z \\ \Delta\nu_m \end{pmatrix} = \underbrace{\begin{pmatrix} M^{(\phi)}_{1,1} & M^{(\phi)}_{1,2} & M^{(\phi)}_{1,3} \\ M^{(\phi)}_{2,1} & M^{(\phi)}_{2,2} & M^{(\phi)}_{2,3} \\ M^{(\phi)}_{3,1} & M^{(\phi)}_{3,2} & M^{(\phi)}_{3,3} \end{pmatrix}}_{\mathbf{M}^{(\phi)}} \begin{pmatrix} \Delta E_p \\ \Delta E_z \\ \Delta E_m \end{pmatrix}, \tag{2.19}$$

where the resulting frequency shifts for the modified cyclotron, axial and magnetron motions are defined as $\Delta\nu_p = \Delta\omega_p/2\pi$, $\Delta\nu_z = \omega_z/2\pi$ and $\Delta\nu_m = \omega_m/2\pi$ respectively. The matrix $\mathbf{M}^{(\phi)}$ is the sum of nine other 3×3 matrices $\mathbf{M}^{(ijk)}$, where the matrix $\mathbf{M}^{(ijk)}$ results from a perturbation Hamiltonian due to the term C_{ijk} (2.18) [21]. For example, while in a selected electrostatic potential and also while in a magnetic field $B_0 = 0.5$ T, a trapped single electron may exhibit frequency shifts defined by [22]

$$\mathbf{M}^{(\phi)} = \begin{pmatrix} 1.7 \times 10^{-16} & 6.3 \times 10^{-16} & -1.7 \times 10^{-10} \\ 6.3 \times 10^{-16} & -8.1 \times 10^{-12} & 1.1 \times 10^{-5} \\ -1.7 \times 10^{-10} & 1.1 \times 10^{-5} & 1.2 \times 10^{-4} \end{pmatrix} \cdot \begin{pmatrix} \nu_p \\ \nu_z \\ \nu_m \end{pmatrix} (\mathrm{k_B\,K})^{-1}, \tag{2.20}$$

which is written such that the numerical 3×3 matrix represents the fractional shifts $\Delta\nu_i/\nu_i$ [22]. The Boltzmann constant is denoted k_B.

It is most important to eliminate the element $M_{2,2}^{(\phi)} = \frac{\Delta\nu_z}{\Delta E_z}|_{\Delta E_p = \Delta E_m = 0}$, because all three motional eigenfrequencies may be measured through ω_z [21]. Of the nine elements $M_{2,2}^{(ijk)}$ which sum to make $M_{2,2}^{(\phi)}$, all are equal to zero other than $M_{2,2}^{(004)}$ and $M_{2,2}^{(012)}$ [21]. An electronic compensation, the *optimal tuning ratio* $T_C^{(\mathrm{opt})}$, may be applied to fulfil the condition $M_{2,2}^{(004)} = -M_{2,2}^{(012)}$ and thus eliminate any dependence of the axial frequency ω_z on the axial energy ΔE_z [21]. Note that the anharmonicities C_{004} and C_{012} may not be zero - it is just the matrix element which is compensated [21]. As described in [21], the compensation of electrical anharmonicities has also been discussed for hyperbolic [96] and cylindrical [20] Penning traps.

Magnetic inhomogeneities

Analogously to the electric frequency shifts matrix $\mathbf{M}^{(\phi)}$ resulting from the electric anharmonicities, there are *magnetic frequency shifts matrices* which result from magnetic inhomogeneities [22]. Analogous to the series expansion of the quadrupole potential (2.18), the $\hat{u}_z$ component of the magnetic field B_z may also be expressed as an infinite polynomial

expansion in space [97]

$$B_z(x,y,z) = \sum_{i,j,k=0}^{i,j,k=\infty} \underbrace{\frac{1}{i!j!k!} \cdot \frac{\partial^{i+j+k} B_z(x,y,z)}{\partial x^i \partial y^j \partial z^k}\bigg|_{(0,y_0,0)}}_{B_{z,ijk}} x^i (y-y_0)^j z^k; \quad i,j,k \in \mathbb{N}, \tag{2.21}$$

where all terms other than $B_{z,000} = B_0$ are denoted *magnetic inhomogeneities*.

Penning traps commonly require homogeneous magnetic fields (where only the homogeneous term $B_{z,000} = B_0$ is non-zero) or *magnetic bottle* fields ($B_{z,000} = B_0 \neq 0$, $B_{z,020} \neq 0$) [97] and so the most important magnetic inhomogeneities occur within B_z rather than within B_x nor B_y. Furthermore, with concern to the topology of the Geonium Chip Penning trap, the most significant inhomogeneities $B_{z,ijk}$ are those with $j \neq 0$ (i.e. those along $\hat{u}_y$) and in particular (of lowest order) the gradient $B_{z,010}$ and curvature $B_{z,020}$ [22]. The inhomogeneities $B_{z,010}$ and $B_{z,020}$ cause linear shifts to the motional eigenfrequencies which are dependant on the particle's energies [22], with the inhomogeneities introducing magnetic frequency shift matrices $\mathbf{M}^{(B_{010})}$ and $\mathbf{M}^{(B_{020})}$ respectively [22]. Similarly to the net electric frequency shift matrix (2.19), these magnetic frequency shift matrices may be defined by [22]

$$\begin{pmatrix} \Delta\nu_p \\ \Delta\nu_z \\ \Delta\nu_m \end{pmatrix} = \underbrace{\begin{pmatrix} M_{1,1}^{(B_{0n0})} & M_{1,2}^{(B_{0n0})} & M_{1,3}^{(B_{0n0})} \\ M_{2,1}^{(B_{0n0})} & M_{2,2}^{(B_{0n0})} & M_{2,3}^{(B_{0n0})} \\ M_{3,1}^{(B_{0n0})} & M_{3,2}^{(B_{0n0})} & M_{3,3}^{(B_{0n0})} \end{pmatrix}}_{\mathbf{M}^{(B_{0n0})}} \begin{pmatrix} \Delta E_p \\ \Delta E_z \\ \Delta E_m \end{pmatrix}. \tag{2.22}$$

The matrices $\mathbf{M}^{(B_{010})}$ and $\mathbf{M}^{(B_{020})}$ may be calculated using perturbative Hamiltonians [22], where for example a magnetic field with $B_0 = B_{z,000} = 0.5$ T at $y_0 = 1.45$ mm produced by a single current flowing along $\hat{u}_x$ at $z = 0$ and immediately below the surface

of the chip, has matrices [22]

$$\mathbf{M}^{(B_{010})} = \begin{pmatrix} 5.6\times10^{-9} & 2.3\times10^{-7} & 6.9\times10^{-9} \\ 2.3\times10^{-7} & -6.5\times10^{-2} & 5.6\times10^{-10} \\ 6.9\times10^{-9} & 5.6\times10^{-10} & -9.5\times10^{-6} \end{pmatrix} \cdot \begin{pmatrix} \nu_p \\ \nu_z \\ \nu_m \end{pmatrix} (\mathrm{k_B\,K})^{-1} \tag{2.23a}$$

$$\mathbf{M}^{(B_{020})} = \begin{pmatrix} -1.9\times10^{-11} & 7.1\times10^{-6} & 8.6\times10^{-8} \\ 7.1\times10^{-6} & 0 & -7.7\times10^{-8} \\ 8.6\times10^{-8} & -7.7\times10^{-8} & -9.3\times10^{-10} \end{pmatrix} \cdot \begin{pmatrix} \nu_p \\ \nu_z \\ \nu_m \end{pmatrix} (\mathrm{k_B\,K})^{-1}. \tag{2.23b}$$

The largest element in both magnetic frequency shifts matrices (2.23a) and (2.23b) is the central element $\mathbf{M}^{(010)}_{2,2}$, which affects ω_z and if uncompensated could make a trapped particle undetectable [22].

Similar investigations of electric and magnetic frequency shifts have been undertaken for cylindrical Penning traps [93].

2.1.3 The Gabrielse-Brown invariance theorem

The Gabrielse-Brown invariance theorem [62, 87] states that the free cyclotron frequency ω_c (2.11a) may be calculated only from the three measurable motional eigenfrequencies ω_p (2.10a), ω_z (2.9c) and ω_m (2.10b)

$$\omega_c^2 = \omega_p^2 + \omega_z^2 + \omega_m^2. \tag{2.24}$$

To derive [62, 87] this relation, Brown and Gabrielse solved the equations of motion for an imperfect trap, while using the assumptions that i) the magnetic field axis has a misalignment with the trap $\hat{u}_z$ axis and that ii) the electrostatic field has ellipticity and that iii) the electrodes (electric field source) are not geometrically ideal [62, 87]. The invariance theorem (2.24) requires the assumption that high order anharmonicities are either negligible or compensated for [62]. This theorem is extremely significant, because even in an imperfect (and elliptical) Penning trap, ω_c may be obtained (which does not exist for a trapped particle in a Penning trap because of the electrodes) [62, 87]. This theorem

has an important application in mass spectrometry, which compares the free cyclotron frequencies for different particles [98].

2.2 The electronic detection technique

As stated in (§2.1), a trapped electron in an elliptical Penning trap with a magnetic field $B_{z,000} = B_0 = 0.5$ T can have the following measurable motional eigenfrequencies: a reduced cyclotron frequency $\omega_p = 2\pi \cdot 14$ GHz, an axial frequency $\omega_z = 2\pi \cdot 28$ MHz and a magnetron frequency $\omega_m = 2\pi \cdot 9$ kHz. The axial and magnetron frequencies are typically in the radiofrequency domain, the reduced cyclotron frequency is typically in the microwave domain and there are no internal transitions nor other transitions in the optical domain. Therefore, there are no optical transitions in the system of a trapped electron in a Penning trap. Assuming that $\omega_c \approx \omega_p$ (by considering (2.12) with $\omega_1 \approx 0$ (2.11b)), in order to reach an optical ω_p with wavelength 750 nm, a magnetic field strength of approximately 14.3 kT would be required, which is not currently achievable experimentally.

However, a radiofrequency electronic detection technique, the *bolometric technique* first employed by Dehmelt [5] and later modelled [91, 99, 100], may be applied to measure the axial frequency [37]. This bolometric technique [5] is non-destructive (the trapped particle is not lost) [37]. The detection method involves connecting a tank (parallel RLC) circuit to an electrode and measuring the impedance as a function of frequency [5, 91, 99, 100]. The tank circuit may consist of a real inductor with an inductance L_c, a resonance resistance R_c and a parasitic capacitance C_p [99]. The trapped electron induces oscillating image charges on the trap electrodes, which flow in the tank circuit and modify the impedance [99]. The trapped electrons may be modelled as a series LC circuit which is in parallel to the components of the tank circuit [91], as shown in Figure 2.3. If there are N electrons trapped, the equivalent inductance of the electrons is $L_i = L_i^{(1)}/N_e$ and the equivalent capacitance is $C_i = N_e \cdot C_i^{(1)}$, where $L_i^{(1)}$ and $C_i^{(1)}$ are the equivalent inductance and capacitance for one trapped electron [99].

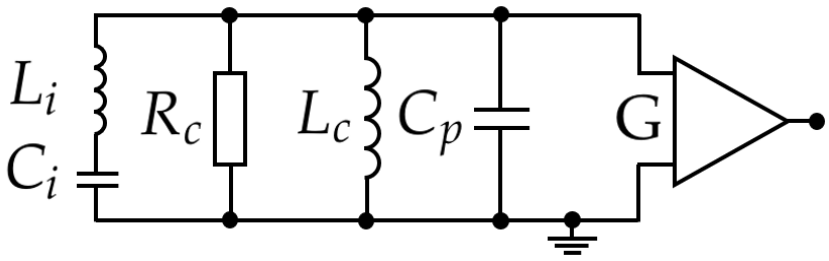

FIGURE 2.3: Equivalent electrical circuit schematics for a single trapped electron interacting with a detection coil (*parallel tank circuit* [91]), based upon a figure available in [91]. The voltage across the coil is amplified with a gain G and then measured using a spectrum analyser [91].

The impedance $Z(\omega)$ of the equivalent circuit shown in Figure 2.3 for one trapped electron may be defined by ([100] while neglecting the electron equivalent resistance r_n)

$$Z(\omega) = \left(\frac{1}{i\omega L_i + \frac{1}{i\omega C_i}} + \frac{1}{R_p} + \frac{1}{i\omega L_c} + i\omega C_p \right)^{-1}. \tag{2.25}$$

A formula for the modulus $|Z(\omega)|$ of $Z(\omega)$ defined in (2.25) was determined using Python in-build symbolic maths functions from the module *SymPy* and some simulated measurable resonances $|Z(\omega)|$ are shown below in Figure 2.4. The analytic solution for $|Z(\omega)|$ (with $r_n \neq 0$) is written in [100]. When no electrons are trapped the lineshape (2.25) is a Lorentzian function [99].

The simulated measurable resonances were based upon measurements (conducted by other members of the research group) of a loaded axial frequency detection coil which formed a real tank circuit in the Geonium Chip Penning trap laboratory. These measurements determined a coil resonance resistance $R_c = 58$ kΩ, an inductance $L_c = 1.1$ μH and a resonant frequency $\omega_{\mathrm{LC}} = 2\pi \cdot 24.816$ MHz, giving a parasitic capacitance $C_p = 1/(L_c \cdot {\omega_{\mathrm{LC}}}^2) \approx 37.4$ pF. A theoretical calculation (conducted by Dr José Verdú) of the effective coupling distance (2.28) through a correction electrode gave $D_{\mathrm{eff}}^{(z)} = 2.83$ mm and thus the electron's equivalent inductance was $L_i \approx 284$ H, which meant that at resonance ($\omega_z = \omega_{\mathrm{coil}}$) the equivalent capacitance was $C_i \approx 1.45 \times 10^{-19}$ F.

The simulated measurable resonances $|Z(\omega)|$ in Figure 2.4 show the effects on the axial resonance of different numbers N_e of electrons (Figures 2.4a and 2.4b) and different

electron axial frequencies $\nu_{z,n} = \omega_{z,n}/2\pi$ (Figure 2.4b), with n being a counter to distinguish the particular value of $\omega_{z,n}$. Both figures (Figures 2.4a and 2.4b) are in agreement with [99, Fig. 4]. Figure 2.4a shows that when the trapped electrons are in resonance with the detection circuit ($\omega_z = \omega_{\text{coil}}$), the width $\Delta\omega_z$ of the axial dip is larger for larger numbers of electrons N_e, which is in agreement with the theory [99, 100] and experimental investigation [18, 19]. Figure 2.4b shows that when the trapped electrons are off-resonant with the axial detection circuit ($\omega_z \neq \omega_{\text{coil}}$), the dip is replaced with an asymptotic function (by comparison of the plot for $\nu_{z,2}$ to the plots for $\nu_{z,1}$ and $\nu_{z,3}$), which again is wider for larger numbers N_e of trapped electrons (by comparison of the plots for $\nu_{z,1}$ and $\nu_{z,3}$). In the Geonium Chip Penning trap experiment, rather than measure $|Z(\omega)|$ explicitly, a *Rohde and Schwarz FSV30* spectrum analyser is used to display the amplified voltage (Johnson noise [101]) spectrum $V(\omega)$, as discussed in (§3.5).

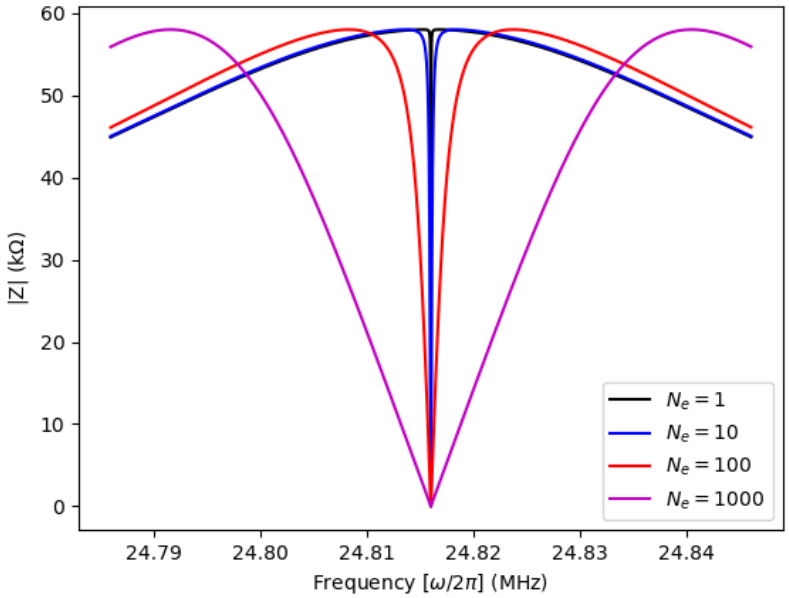

(A) Four simulated resonances of trapped electrons, with different numbers N_e of trapped electrons and the same axial frequency $\nu_z = \omega_{z,n}/2\pi = 24.816$ MHz.

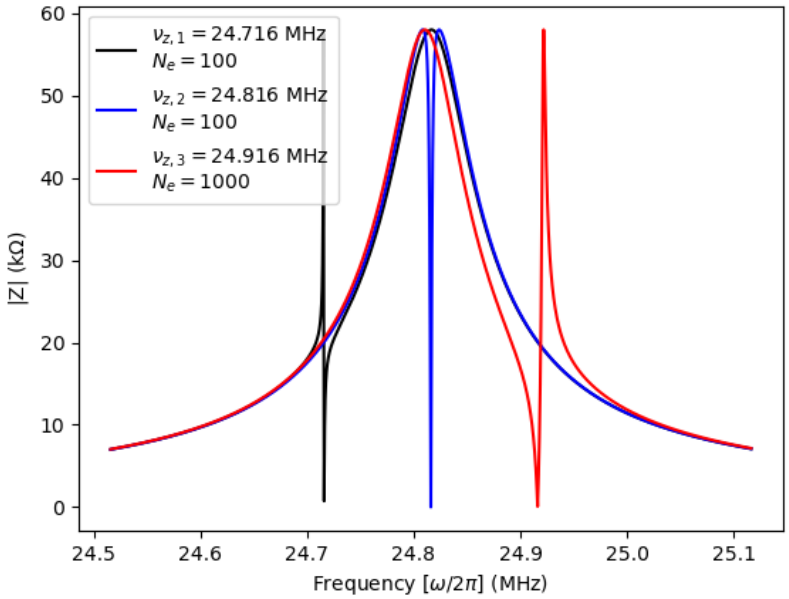

(B) Three simulated resonances of trapped electrons with different numbers N_e of trapped electrons and also with different axial frequencies $\nu_{z,n} = \omega_{z,n}/2\pi$.

FIGURE 2.4: Plotting simulated resonances of the axial detection circuit while electrons are trapped.

2.3 Temperature and cooling

2.3.1 An introduction to temperature and cooling

Although typically a quantity used to characterise an ensemble [95], temperature may be defined for a single trapped particle because the motional energy is governed by a Boltzmann distribution with a fixed temperature [95]. In the case of an ideal Penning trap (§2.1.1), each of the three eigenmotions of a trapped particle have a temperature which is independent from the other two [95]. In the case of a real (imperfect (§2.1.2)) trap [95], the motions may be coupled to some extent [95], however these couplings might not overcome external excitations [95] and so each motion may still reach a different thermal equilibrium [95]. Temperature is also discussed in [102].

A trapped particle may be cooled (have its velocity slowed [103]) using a variety of techniques [103], but the two most relevant for the trapping of electrons in the Geonium Chip Penning trap (in the near future) are *resistive cooling* [91, 103] (§2.3.2) and *rf* [radiofrequency/RF] *side-band cooling* [103] (developed [104] as mentioned in [103]). An example of resistive cooling is the cooling of the axial motion (§2.2) and an example of RF sideband cooling is magnetron cooling (§6.1.2). For example, thermal equilibrium while undergoing resistive cooling would be achieved once the trapped particle has dissipated enough energy into the coupled electronic circuit (§2.3.2) such that the temperature of the trapped particle has reached the temperature of the coupled electronic circuit [103].

2.3.2 Resistive cooling

The oscillating charge $q_{\text{ind}}\left(\vec{r}(t)\right)$ induced by the trapped particle on an electrode forms a current $I_{\text{ind}}(t)$, which flows through the external tank circuit and which may be written [91]

$$q_{\text{ind}}\left(\vec{r}(t)\right) = -q\Lambda_{\Sigma}(\vec{r}) \tag{2.26a}$$

$$I_{\text{ind}}(t) = \nabla q_{\text{ind}}(\vec{r}) \cdot \dot{\vec{r}}(t), \tag{2.26b}$$

where $\Lambda_\Sigma(\vec{r})$ is a dimensionless quantity which depends on the topology of that electrode [91]. This induced current $I_{\text{ind}}(t)$ makes an induced voltage $V_{\text{ind}}(t)$ over the impedance $Z(\omega)$ of the external tank circuit, which makes a *self-induced potential* [91] ϕ_{ind} [91]. This potential ϕ_{ind} corresponds to an electric field which produces a force $\vec{F}_{\text{ind}}$ which acts back on the trapped particle [91]. The combination of Ohm's Law with (2.26a) and (2.26b) may give ϕ_{ind} [91], which maybe propagated to $\vec{F}_{\text{ind}}$ [91]

$$\phi_{\text{ind}} = -V_{\text{ind}} \cdot \Lambda_\Sigma(\vec{r}) = qZ(\omega)\Lambda_\Sigma(\vec{r})\nabla\Lambda_\Sigma(\vec{r}) \cdot \dot{\vec{r}} \tag{2.27a}$$

$$\vec{F}_{\text{ind}} = -q \cdot \nabla\phi_{\text{ind}} = -q^2 Z(\omega)\big(\nabla\Lambda_\Sigma(\nabla\Lambda_\Sigma \cdot \dot{\vec{r}}) + \Lambda_\Sigma(\dot{\vec{r}} \cdot \nabla)\nabla\Lambda_\Sigma\big). \tag{2.27b}$$

This force $\vec{F}_{\text{ind}}$ is proportional to $\dot{\vec{r}}$ and so the force is dissipative and causes resistive cooling [91], where the energy of the particle motion is dissipated through ohmic heating of the impedance $Z(\omega)$ [91].

To simplify the expression (2.27b) for this force, the *effective coupling displacement* [91] $\vec{D}_{\text{eff}}^{-1}$ may be defined [91]

$$\vec{D}_{\text{eff}}^{-1}(y_0;\Sigma) = \lim_{\vec{r}(t)\to(0,y_0,0)} \nabla\Lambda_\Sigma\big(\vec{r}(t)\big) = \left(\frac{1}{D_{\text{eff}}^{(x)}}, \frac{1}{D_{\text{eff}}^{(y)}}, \frac{1}{D_{\text{eff}}^{(z)}}\right). \tag{2.28}$$

The magnitude of each Cartesian component of $\vec{D}_{\text{eff}}^{-1}$ may be denoted an *effective coupling distance* [91] (dimensions of distance [91]). By normalising ϕ_{ind} (2.27a) by choosing $V_{\text{ind}} = 1$ V and then by considering the definition (2.28) [91], it can be reasoned that $\vec{D}_{\text{eff}}^{-1}$ represents the *normalised electric field* [91] at the equilibrium trapping position $\vec{r}_0 = (0, y_0, 0)$ [91], produced by the induced charge $q_{\text{ind}}\big(\vec{r}(t)\big)$ at that electrode [91]. The expression (2.27b) for the force $\vec{F}_{\text{ind}}$ may be simplified by using the definition $\vec{D}_{\text{eff}}^{-1}$ (2.28) [91] and then by also applying (2.27a) and (2.27b), culminating in the induced voltage V_{ind} [91]

$$\vec{F}_{\text{ind}}(\omega) = -q^2 Z(\omega)\vec{D}_{\text{eff}}^{-1} \cdot \big(\vec{D}_{\text{eff}}^{-1} \cdot \dot{\vec{r}}\big) \tag{2.29a}$$

$$V_{\text{ind}}(\omega) = -qZ(\omega)\vec{D}_{\text{eff}}^{-1} \cdot \dot{\vec{r}}. \tag{2.29b}$$

By applying Newton's Second Law to the force $\vec{F}_{\text{ind}}(\omega)$ (2.29a) and by assuming that each of the ith components of the Cartesian motion are decoupled from the others [91], the resulting differential equation for the ith Cartesian component may be solved for the time constant $\tau^{(i)}$ of the resistive cooling [91]

$$\tau^{(i)}(\omega) = \frac{m}{q^2} \cdot \frac{1}{Z(\omega)} \cdot \left(D_{\text{eff}}^{(i)}\right)^2. \tag{2.30}$$

In the case of the Geonium Chip Penning trap it is possible for the $\hat{u}_x$ and $\hat{u}_y$ motions to be cooled simultaneously and so the *overall* [91] time constant $\tau^{(\text{overall})}$ may be written [91]

$$\frac{1}{\tau^{(\text{overall})}} = \frac{1}{\tau^{(x)}} + \frac{1}{\tau^{(y)}} \tag{2.31}$$

and if $\tau^{(x)} > 0$ and $\tau^{(y)} > 0$, cooling through both $\hat{u}_x$ and $\hat{u}_y$ motions simultaneously is quicker than if cooling was only to occur through one motion.

The effective coupling distances (2.28) $D_{\text{eff}}^{(x)}$, $D_{\text{eff}}^{(y)}$ and $D_{\text{eff}}^{(z)}$ for an electrode depend on the topological constants of the electrode and also the effective coupling distances are functionally dependent on the equilibrium trapping height y_0 [91]. The effective coupling distances $D_{\text{eff}}^{(i)}$ are not the same for every electrode [91]. The optimal tuning ratio $T_C^{(\text{opt})}$ discussed in §2.1.2 only exists for a finite range of y_0 [21, 91], the *useful trapping interval* [91]. In order for a motion to be visible, $D_{\text{eff}}^{(i)}$ must be minimised [91], which may be reasoned by considering (2.29b). For example, this means that for the Geonium Chip Penning trap, within this useful trapping interval, the axial motion (with $\hat{u}_z$ component only) is readily visible through a correction electrode but not through the ring electrode [91], whereas the cyclotron motion (with $\hat{u}_x$ and $\hat{u}_y$ components only) is readily visible through the ring electrode but not through a correction electrode [91].

As mentioned in [91], $\vec{D}_{\text{eff}}^{(-1)}$ have also been determined for hyperbolic traps [105] and cylindrical traps [87]. Resistive cooling of an electron gas has been observed [5] and studied [99], as mentioned in [103]. The resistive cooling of ion ensembles has also been experimentally demonstrated [106]. Resistive cooling has also been demonstrated with

ion clouds [107].

The resistive-wall destabilisation effect

The three measurable eigenmotions with frequencies ω_z, ω_p and ω_m (defined in §2.1.1) may each be modelled as quantum harmonic oscillators [87] with the Hamiltonian operators $\hat{H}_z$, $\hat{H}_p$ and $\hat{H}_m$ respectively. The axial $\hat{H}_z$ and radial $\hat{H}_{\text{rho}}$ Hamiltonians may be written [87] (with a change of notation from "ρ" to "rho")

$$\hat{H}_z = \hbar\omega_z\left(\hat{a}_z^\dagger\hat{a}_z + \frac{1}{2}\right) \tag{2.32a}$$

$$\hat{H}_{\text{rho}} = \underbrace{\hbar\omega_p\left(\hat{a}_p^\dagger\hat{a}_p + \frac{1}{2}\right)}_{\hat{H}_p} + \underbrace{-\hbar\omega_m\left(\hat{a}_m^\dagger\hat{a}_m + \frac{1}{2}\right)}_{\hat{H}_m}, \tag{2.32b}$$

where the $\hat{a}^\dagger$ operators are creation operators and the $\hat{a}$ operators are annihilation operators [87]. These Hamiltonians give rise to the energy eigenvalues [87] (with a change of notions from "k" to "n_z", "n" to "n_p" and "l" to "n_m")

$$E_z = E_k = \hbar\omega_z\left(n_z + \frac{1}{2}\right) \tag{2.33a}$$

$$E_{\text{rho}} = \underbrace{\hbar\omega_p\left(n_p + \frac{1}{2}\right)}_{E_p} + \underbrace{-\hbar\omega_m\left(n_m + \frac{1}{2}\right)}_{E_m} \tag{2.33b}$$

of energy eigenstates defined by [87]

$$\hat{H}_z\left|n_z\right\rangle = E_z\left|n_z\right\rangle \tag{2.34a}$$

$$\hat{H}_{\text{rho}}\left|n_p, n_m\right\rangle = E_{\text{rho}}\left|n_p, n_m\right\rangle = E_{\text{rho}}\left|n_p\right\rangle \otimes \left|n_m\right\rangle \tag{2.34b}$$

with [87] $n_z = 0, 1, 2...$, $n_p = 0, 1, 2...$ and $n_m = 0, 1, 2....$

From the radial eigenvalue equation (2.33b), it can be seen that the magnetron energy E_m is negative in polarity. When kinetic energy is removed from the magnetron

motion its radius increases [87], because the the trapped particle moves down the "repulsive radial potential hill" (electrostatic) [87]. One way in which kinetic energy may be removed from the magnetron motion is by resistive cooling. If the magnetron radius becomes large enough, the trapped particles collide with the trap electrodes and thus are no longer trapped [87]. This effect was investigated experimentally where it was denoted *resistive-wall destabilisation* [108] and this work was later expanded upon [109]. For example [108] (in particular using a crude interpolation of [108, Figure 3]), for an experimental setup with a resistive-wall RC circuit with $R \approx 10^4\ \Omega$ and $C = 194$ pF, the radius of the magnetron motion exponentially grew by $\exp(\delta_{\omega_i} t)$ with a time constant $\delta_{\omega_i} \approx 100\ \mathrm{s}^{-1}$.

These investigations [108, 109] were undertaken in the field of plasma physics, where the magnetron mode in a Penning trap is analogous to the $l = 1$ diocotron mode of a plasma [103]. Electron plasma phenomena should also be considered, including for example the density distribution during electron loading [110], plasma turbulence [111], the interaction with background gas [109] and effects of a magnetic field [112]. Furthermore, of particular relevance to elliptical Penning traps [92] is bifurcation, which may occur where the plasma centre-of-charge is displaced [113]. Such bifurcation has been experimentally verified [113] and there have been theoretical investigations undertaken about their stability [114] and equilibria [115].

Drags exerted on a rotating plasma can also cause radial (magnetron) expansion which may be counteracted by torque produced by *rotating wall electric fields* [116]. The strength of the torque produced with the rotating wall technique may achieve steady-state confinement, plasma compression or plasma expansion [116]. As described in [116], the first implementations of the rotating wall technique for ions (Mg^+) and electrons were [117, 118] (respectively).

A discussion in (§7.2.5) underestimates that when using the typical photocathode bias voltage $V_{\mathrm{cath}} = -70$ V (§6.1.3), 30,000 secondary electrons should be trapped in the $(1\ \mathrm{mm})^3$ trapping volume every second. However, each secondary electron is independently affected by resistive wall destabilisation effect. Numerical simulations of the motion of trapped electrons performed by Dr José Verdú-Galiana showed that unless the

resistive wall effect were to be mitigated, typically the magnetron radius of the trapped electrons would grow such that the electrons would likely be grounded (collide with the trap electrodes) after less than approximately 1 μs. The axial frequencies for the loading (Figure 6.3) and detection (Figure 6.2) potentials should be $\omega_z = 2\pi \cdot 61.4$ MHz and $\omega_z = 2\pi \cdot 25.8$ MHz (respectively). These axial frequencies correspond to axial time periods of 16.3 ns and 38.8 ns (respectively) and so is it possible that an axial motion would have still existed prior to the loss of electrons as a result of resistive-wall loss (i.e. 38.8 ns < 1 μs). Therefore, it is possible that an axial signal (§2.2) would still have been observable if the trap were to be continuously loaded with electrons. However, any trapped electrons would undergo a large-amplitude magnetron motion and so if the trap was not harmonic enough (§2.1.2) for enough time, any trapped electrons might not have been observable. Nonetheless, for stable trapping, the resistive-wall effect needed to be mitigated and some of the attempted mitigations of the resistive-wall effect in the Geonium Chip Penning trap experiment are discussed in (§6.1.2).

2.4 Selected application: single microwave photon detection

2.4.1 The Continuous Stern-Gerlach Effect

A single electron trapped in the the Geonium Chip Penning trap may be used to detect single microwave photons [37]. At high magnetic field strengths (denoted B_0 (2.11a) and $B_{z,000}$ (2.21)), the measurable frequency ω_p is very similar to ω_c (2.11a) [37] - for example see (2.14) where $\omega_m \ll \omega_p$. Therefore, trapped electrons in magnetic fields ranging between 0.1 T and 2.0 T would have a range of ω_p between approximately $2\pi \cdot 2.8$ GHz and $2\pi \cdot 56$ GHz which is in the microwave domain [37]. If the frequency ω_γ of a single microwave photon matches ω_p, the photon may induce an electric dipole transition in the trapped electron, in other words causing a jump in the modified cyclotron quantum harmonic oscillator number n_p (2.33b) [37]. Therefore, a measurement of an increase in n_p would be the detection of a microwave photon.

In order to measure n_p, the *Continuous Stern-Gerlach Effect* [6, 119] (CSGE) may be used. The Continuous Stern-Gerlach Effect requires the use of a *magnetic bottle* [6], which may be defined $\Delta\vec{B}_{\text{circ}}$ for a trap with circular symmetry (i.e. centred around $(x, y, z) = (0, 0, 0)$ mm) [6, 120]

$$\Delta\vec{B}_{\text{circ}} = B_2\left\{\left[z^2 - \frac{x^2+y^2}{2}\right]\hat{u}_z - z(x\hat{u}_x + y\hat{u}_y)\right\}, \tag{2.35}$$

where B_2 is the curvature of the magnetic field with the same dimensions as T/m^2 [6]. This can be modified such that the bottle is centred around $\vec{r}_0$ (§2.1.1) (analogous to $\phi_{\text{conventional}}$ (2.1))

$$\Delta\vec{B} = B_2\left\{\left[z^2 - \frac{x^2+(y-y_0)^2}{2}\right]\hat{u}_z - z[x\hat{u}_x + (y-y_0)\hat{u}_y]\right\} \tag{2.36}$$

and an example of such a bottle field (along with an homogeneous term B_0) is shown in Figure 2.5.

The magnetic moment $\vec{\mu} = |\vec{\mu}|\hat{u}_z$ of the trapped electron aligns with the axial component $B_z\hat{u}_z$ (2.21) of the magnetic field [121] and so the energy $E = \vec{\mu}\cdot\Delta\vec{B}$ [121] only depends on the $\hat{u}_z$ component of the bottle. The trapping volume implies $x = y = 0$ (in a cylindrical trap) [121] (or $x = y - y_0 = 0$ for the Geonium Chip Penning trap) and so the Hamiltonian for the interaction of the trapped electron with the bottle $\Delta\vec{B}$ only has a z component which is harmonic [120, 121]. This perturbs the equation of motion (2.8b) for the axial motion, which perturbs the axial frequency from $\omega_{z,0}$ to $\omega_{z,0} + \Delta\omega_z$ [121], where [121]

$$\Delta\omega_z \simeq \omega_{z,0} + \underbrace{\frac{B_2\mu_B}{m\omega_{z,0}}(2n_p + 1 + gn_s)}_{\Delta\omega_z}, \tag{2.37}$$

which is an approximation using a Taylor expansion [121]. This derivation also wrote the magnetic moment $|\vec{\mu}|$ of the electron as the sum of the magnetic moments for the cyclotron and spin magnetic moments [121], which are functions of the cyclotron and spin quantum numbers n_p and n_s (respectively) and also of the Bohr magneton μ_B [121]. The shift $\Delta\omega_z$ (2.37) is thus dependent on the cyclotron quantum number n_p (2.33b) and so the

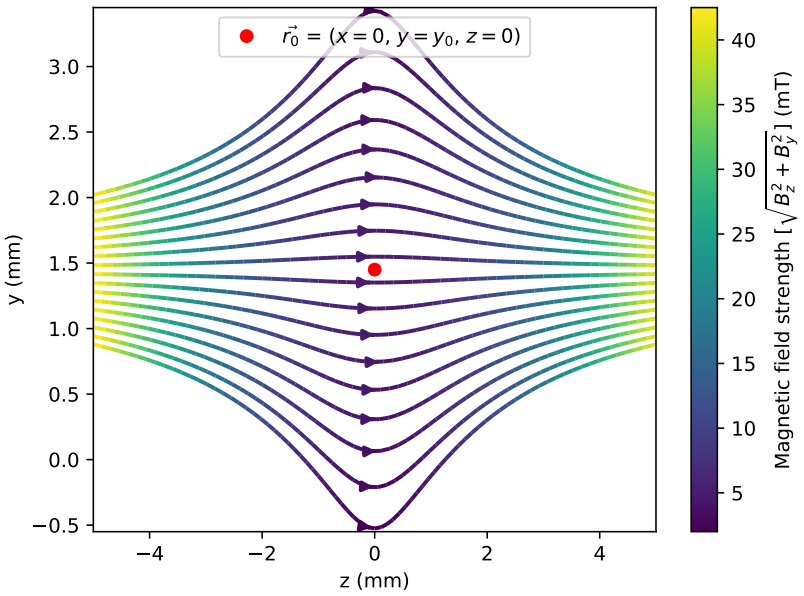

FIGURE 2.5: A plot of a magnetic bottle field $\vec{B}(z,y) = B_0\hat{u}_z + \Delta\vec{B}$ using (2.36), in the plane $x = 0$ and with $y_0 = 1.45$ mm. The field has an homogenous term $B_0 = 5$ mT and a curvature $B_2 = 1.5$ mT/mm^2 [37]. The arrow tails represent the magnetic field lines and their colours represent the magnitude of the magnetic field $\sqrt{B_z^2 + B_y^2}$. The equilibrium trapping position (§2.1.1) is depicted with a red circle.

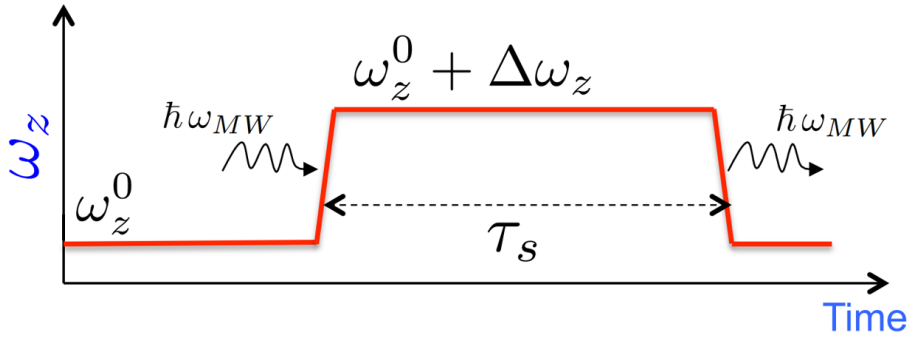

FIGURE 2.6: A graphic [37] to depict the Continuous Stern-Gerlach Effect [37] (2.37). A microwave photon with energy $\hbar\omega_{\mathrm{MW}}$ is absorbed by the trapped electron which causes the axial frequency to shift from ω_z^0 to $(\omega_z^0 + \Delta\omega_z)$ [37]. The frequency ω_z^0 [37] is a different notation for the frequency $\omega_{z,0}$ (2.37). The photon is spontaneously emitted, once the spontaneous radiative decay lifetime τ_s of the cyclotron oscillator (§2.4.2) has elapsed [37]. Adapted from [37].

detection of a single microwave photon may be achieved by measuring a change in ω_z [37], which is shown in Figure 2.6. This concept may be interpreted phenomenologically that a change in the cyclotron quantum number n_p causes a change in the magnetic moment μ which causes a change in the effective electrostatic trapping potential [37]. One important consequence is that [37] the shift $\Delta\omega_z$ (2.37) depends on n_p and so if N_γ photons are absorbed, the total axial frequency shift $\Delta\omega_{z,N_\gamma}$ is a scalar multiple of the shift $\Delta\omega_{z,1}$ produced by the absorption of one photon, i.e. $\Delta\omega_{z,N_\gamma} = N_\gamma \cdot \Delta\omega_{z,1}$. As stated in [37], a trapped electron in a magnetic field with $B_2 = 1.5\ \mathrm{mT/mm^2}$ [120] with an unperturbed axial frequency $\omega_{z,0} = 2\pi \cdot 30$ MHz would experience a shift in the axial frequency of $\Delta\omega_z = 2\pi \cdot 30$ Hz per single jump in the cyclotron oscillator n_p.

In the case of the planar magnetic field source for the Geonium Chip Penning trap (§5), the magnetic bottle may be achieved with a non-zero curvature $B_2 = B_{z,020}$ (2.21) [97]. This curvature would produce a magnetic field component $B_{z,020}(y - y_0)^2\hat{u}_z$ (2.21) which explicitly would not modify the axial motion $\hat{u}_z$ but rather that of $\hat{u}_y$. However, $B_{z,020} \simeq -B_{z,002}$ [97], which would produce a magnetic field component $B_{z,002}z^2\hat{u}_z$ which would modify the axial motion and couple the axial and modified cyclotron motions as required.

2.4.2 Single microwave photon detection using the Geonium Chip Penning trap

Itinerant microwave photons will be detected using the Continuous Stern-Gerlach Effect (§2.4.1). In order to detect an itinerant microwave photon, the photon will be guided into a chamber (the *boxed CPW-trap* [22] (§3.2)), which will act as a microwave cavity [22, 37]. Once inside the cavity, the photon will travel through a transmission line (for example one formed from the trap electrodes - a coplanar-waveguide transmission line [21, 37]) in order to reach the trapped electron [37] at the location $\vec{r}_0 = (0, y_0, 0)$ (§2.1.1). The cavity dimensions will be chosen such that the cavity modes will have different frequencies than the frequency ω_p of the quantum cyclotron oscillator [22, 37]. This means that while in the trapping region the photon only acts as a propagation mode [37] (to encourage the MW

photon to be absorbed into the cyclotron oscillator, rather than to become a cavity mode). This use of the Purcell effect [22, 122] also inhibits spontaneous emission of cyclotron radiation into the cavity [22, 37] before the measurement of $\Delta\omega_z$ can be completed.

Maximising the internal quantum efficiency

In order to evaluate the effectiveness of the principle of single microwave photon detection using a trapped electron in the Geonium Chip Penning trap, it is important to consider the cross section of the microwave photon absorption. The absorption cross section has been discussed in detail [37], in the form of the *internal quantum efficiency* [37]. The discussion [37] considers the probability of a classical electromagnetic wave (with the energy of one microwave photon) being absorbed into the trapped electron's quantum cyclotron oscillator, raising the cyclotron oscillator state from $|n_p\rangle = |0\rangle$ to $|n_p\rangle = |1\rangle$ (2.33b). The absorption probability rate $\Gamma_{|0\rangle\rightarrow|1\rangle}$ is calculated using Fermi's golden rule [37], where the perturbation Hamiltonian for the transition is the interaction between the photon's electric field $\vec{E}$ and the electric dipole moment operator $\vec{p}$ for the electron's quantum cyclotron oscillator [37]

$$\Gamma_{|0\rangle\rightarrow|1\rangle} = \frac{2\pi}{\hbar} |\langle 0| \vec{E} \cdot \vec{p} |1\rangle|^2 g_p(E) \tag{2.38}$$

where the density of the final available energy states of the cyclotron oscillator is denoted $g_p(E)$ [37].

The internal quantum efficiency η_{internal} can be defined as the product of the absorption probability rate $\Gamma_{|0\rangle\rightarrow|1\rangle}$ (2.38) with the rate τ_{MW} at which the microwave photons enter the trap [37]. The two typical quasi-TEM propagation modes in a coplanar-waveguide transmission line are the *even* and *odd* modes [37], where the normalised electric fields (normalised to 1 V - thus equivalent to $\vec{D}_{\text{eff}}^{-1}$ (§2.3.2)) $E_{\text{CPW}}^{\text{even}}$ and $E_{\text{CPW}}^{\text{odd}}$ of the even and odd modes (respectively) are orientated along $\hat{u}_x$ and $\hat{u}_y$ (respectively) [37]. Therefore, the expanded perturbation Hamiltonian of (2.38) has one component for each quasi-TEM

mode [37], but because the trap can be designed to only support one [37], internal quantum efficiencies $\eta_{\text{internal}}^{\text{even}}$ and $\eta_{\text{internal}}^{\text{odd}}$ may be defined for both the even and odd quasi-TEM modes (respectively) [37]

$$\eta_{\text{internal}}^{\text{even,odd}}(y_0) = \frac{Y_p^{\text{even,odd}}(y_0)}{Y_L^{\text{CPW}} + Y_p^{\text{even,odd}}(y_0)}. \tag{2.39}$$

Here, $Y_p^{\text{even}}(y_0)$ and $Y_p^{\text{odd}}(y_0)$ are the characteristic admittances of the cyclotron oscillator for the even and odd modes (respectively) [37] and Y_L^{CPW} is the transformed load admittance of the transmission line at the location $\vec{r}_0 = (0, y_0, 0)$ (§2.1.1) of the trapped electron [37]. The positional dependence (y_0) of the cyclotron characteristic admittance Y_p results from the fact that Y_p is a function of the cyclotron characteristic inductance L_p [37], which depends on the electric coupling of the electron to the trap/transmission line [37], via the effective coupling distance [37, 91] $D_{\text{eff}}^{(i)}$ (§2.3.2) which is dependent on the height y_0 [91].

By considering (2.39), it can be seen that in order for the internal quantum efficiency $\eta_{\text{internal}}^{\text{even,odd}}(y_0)$ to tend towards one [37], $Y_p(y_0)$ must be much greater than Y_L^{CPW} [37] (i.e. $Y_p(y_0)$ must be maximised [37] and Y_L^{CPW} must be minimised [37]), because the internal quantum efficiency (2.39) takes the form of a *beam-splitter* [37]. Some values for the cyclotron characteristic admittances $Y_p^{\text{even}}(y_0)$ and $Y_p^{\text{odd}}(y_0)$ are plotted as functions of the trapping height y_0 in [37], where it can be seen that $Y_p^{\text{even}}(y_0)$ and $Y_p^{\text{odd}}(y_0)$ are typically higher for a smaller electrode width. The largest plotted cyclotron characteristic admittance $Y_p(y_0)$ is approximately 40 pS [37] (which is still very low [37]) and so it is necessary to minimise the transformed load Y_L^{CPW} [37] by making the untransformed load Y_L an ideal open-circuit [37] or by minimising dielectric substrate losses [37]. The transmission line admittance was estimated using a model to be $Y_L^{\text{CPW}} \simeq 900$ pS [37] which gives rise to internal quantum efficiencies $\eta_{\text{internal}}^{\text{even}}$ and $\eta_{\text{internal}}^{\text{odd}}$ (2.39) of approximately 1%-2% [37] (for 9 pS $\lessapprox Y_p(y_0) \lessapprox$ 18 pS).

The effective internal quantum efficiency $\eta_{\text{internal}}^{\text{even,odd}}(y_0)$ may be increased by increasing the effective cyclotron characteristic admittance Y_p [37]. One method would be to use multiple trapped electrons rather than just the one [37], where N_e trapped electrons

would increase the collective characteristic admittance to $N_e \cdot Y_p$ [37]. However, the spontaneous radiative decay lifetime τ_s of the cyclotron oscillator (into the transmission line) would reduce by a factor of N_e [37] and the photon detection is only be possible when the measurement time τ_m is shorter than τ_s, so this would only be useful for $N_e \leq 1000$ [37]. Alternatively, the cyclotron characteristic admittance Y_p is higher when the magnitude of the electric field $|E_{CPW}(y_0)|$ of the coplanar waveguide transmission line at the position $\vec{r}_0 = (0, y_0, 0)$ (§2.1.1) of the trapped electron is stronger [37, 123], which will be reasoned here-on. The characteristic admittance of the cyclotron oscillator $Y_p^{\text{even,odd}}$ may be defined as a function of the equivalent inductance $L_p^{\text{even,odd}}$ of the cyclotron oscillator [37], which may then be defined as a function of the electric field strength of the microwave photon [37]

$$Y_p^{\text{even,odd}} = \frac{1}{\omega_p L_p^{\text{even,odd}}} \tag{2.40a}$$

$$L_p^{\text{even,odd}} = \frac{m}{q^2 |E_{\text{CPW}}^{\text{even,odd}}|^2}. \tag{2.40b}$$

Therefore, by considering (2.40b) it can be seen that an increase in the electric field strength $|E_{\text{CPW}}^{\text{even,odd}}|$ reduces the equivalent inductance $L_p^{\text{even,odd}}$, which (by considering (2.40a)) causes an increase in the characteristic admittance Y_p.

It was demonstrated [123] that a previous (micro-fabricated) version of the Geonium Chip attenuated $|E_{CPW}(y_0)|$ by an acceptable $\approx$ 30 %, however it is intended for the quantum cyclotron oscillator (that is the trapped electron) to interact with the coplanar waveguide transmission line via an antenna which will be mounted to the ring electrode [32], for example like one used in a near field scanning microwave microscope [124]. The antenna should provide a stronger coupling to the quantum cyclotron oscillator than the coplanar-waveguide transmission line [32] (by increasing the electric field of the microwave photon at $\vec{r}_0$), however the introduction of the antenna would perturb/distort the electrostatic potential $\phi(x, y, z)$ [32] and make it anharmonic [32] (§2.1.2). Therefore, Dr Alberto Jesús Uribe Jiménez simulated the effect of the introduction of an antenna

on the electrostatic trapping potential $\phi(x,y,z)$ [32], in order to investigate the expansion coefficients C_{ijk} (2.18) (in particular C_{002}, C_{004}, C_{006} and C_{012} [32]). It was concluded [32] from the simulations that both i) the perturbation is not significant and that ii) the trapping height y_0 is acceptable.

Maximising the overall quantum efficiency

Finally, the microwave photon would only be detected if the measurement time duration τ_m to measure n_p is less than the radiative lifetime τ_s [37]. Therefore, the *overall quantum efficiency* [37] for the even and odd modes may be written [37]

$$\eta_{\text{overall}}^{\text{even,odd}} = \eta_{\text{internal}}^{\text{even,odd}} \theta(\tau_s - \tau_m), \tag{2.41}$$

where the Heaviside theta function $\theta(\tau_s - \tau_m)$ [37] has the value 1 for $\tau_m < \tau_s$ (i.e. when the photon can be measured prior to its spontaneous emission) or the value 0 for $\tau_s \geq \tau_m$ (i.e. when the photon is spontaneously emitted prior to its measurement). The Purcell effect (discussed above) implies that cyclotron spontaneous emission into the cavity may be neglected [37] and so only cyclotron spontaneous emission into the coplanar waveguide transmission line is of concern [37]. The time τ_s has been estimated to be on the orders of 1 s to 100 s for trapping heights $y_0 > 1$ mm [37].

The measurement of n_p is actually a measurement of the axial frequency via the Continuous Stern-Gerlach Effect [37] (§2.4.1) and so τ_m is actually the time required to determine the shift in the axial frequency $\Delta\omega_z$ [37]. A direct measurement of ω_z is slow [37] and so only the shift $\Delta\omega_z$ will be measured [37], by instead measuring the phase evolution of ω_z [37] (by using the typical bolometric axial detection circuitry to instead measure the phase of the axial motion [37] (§2.2)), as first published in [125]. The measurement time τ_m may be calculated via [37, 125]

$$\tau_m = \frac{\sigma(\Delta\phi)}{\Delta\omega_z}, \tag{2.42}$$

where $\sigma(\Delta\phi)$ is the smallest phase difference of the axial motion which allows the cyclotron state (2.33b) $n_p = 1$ to be distinguished from $n_p = 0$ [37]. The "worst case" [125] is the Fourier limit which occurs when $\sigma(\Delta\phi) = 360°$ [125].

It was demonstrated that [125] for $\sigma(\Delta\phi) = 45°$, a shift $\Delta\omega_z/2\pi = 180$ mHz required a measurement time $\tau_m = 800$ ms. The measurement time τ_m is inversely proportional to the shift $\Delta\omega_z$ (2.42) and $\Delta\omega_z$ is proportional to the curvature of the magnetic bottle B_2 (2.37) and so a stronger B_2 corresponds to a reduced τ_m [37]. It is possible that due to the electron being trapped so close to the magnetic field source in the Geonium Chip Penning trap [37], a shift in $\Delta\omega_z$ of at least 1 kHz might be possible [37] (that a high B_2 might be possible). Therefore, by scaling [37] the demonstration [125] while assuming still that $\sigma(\Delta\phi) = 45°$, this would give rise to a measurement time $\tau_m = (0.8s \times 180\,\text{mHz})/1\,\text{kHz} \approx 150\,\mu\text{s}$, which would be shorter than τ_s - which as stated above is on the orders of 1 s to 100 s [37].

Consideration 1: the limit to the number of stored photons

In practice, the number n_p (2.33b) of energy quanta which can be stored in the cyclotron quantum harmonic oscillator with state $|n_p\rangle$ and frequency ω_p is limited. For example, one such limitation is that the equations of motion (§2.1.1) predict that as the number n_p of quanta increases, the motional displacements (2.15b) of the electron (along both $\hat{u}_x$ and $\hat{u}_y$) will increase and eventually the trapped electron would become grounded on the electrodes at $\Delta y = |y(t) - y_0|$). By considering the worst case of the equation of motion along $\hat{u}_y$ (2.15b) where the electron is at its lowest y (where $\sin(\omega_p t) = \sin(\omega_m t) = 1$) and also by considering that the cyclotron amplitude A_p is dependent on the cyclotron energy E_p (2.16a), these can be used to estimate the maximum number $n_{p,\max}$ of cyclotron quanta before the electron would be lost from the trap. By setting the cyclotron quantum harmonic oscillator energy equal to $E_p = \hbar\omega_p(n_{p,\max} + 1/2)$ and rearranging, it can be written that

$$n_{p,\max} = \frac{(\Delta y - A_m\eta_m)^2\omega_p\gamma_p m}{2\hbar\eta_p^2} - \frac{1}{2}. \tag{2.43}$$

This (2.43) has been numerically evaluated while assuming i) an ellipticity (2.2) $\epsilon = 0.41$ [21], ii) a curvature C_{002} (2.3) of $\approx 88\,\mathrm{kV/m^2}$ [21], iii) a trapping height $y_0 = 1.45$ mm and thus $\Delta y = 1.45$ mm and finally iv) motional energies (2.33b) of $E_p = E_z = k_B \cdot 4.2$ K and $E_m = -k_B \cdot 4.2$ K (thermalised to a temperature (§2.3.1) of 4.2 K). The values of A_m, η_m, ω_p, γ_p and η_p were calculated using the equations in (§2.1.1). The maximum number $n_{p,max}$ of cyclotron quanta varies quite-linearly (see Figure 2.7) with the magnetic field strength $B_{z,000}$ (2.21), from 1.6×10^8 at 0.1 T to 3.2×10^9 at 2 T. The maximum cyclotron quanta $n_{p,max}$ is explicitly linearly dependent on the reduced cyclotron frequency ω_p (2.43), however some other variables are also implicitly functions of ω_p.

This would suggest that the trapped electron in an ideal trap (§2.1.1) should absorb an impressively high number photons, however in a real (imperfect) trap (§2.1.2), perhaps the cyclotron frequency would become undefined before the electron could absorb enough photons to be lost from the trap, however many single microwave photons would absorbed before this loss. Furthermore, an electron with a large number of cyclotron quanta n_p might have a very large total axial frequency shift (2.37). For example, a multi-photon absorption from $|n_p = 0\rangle$ to $|n_p = 10^8\rangle$ might cause the axial frequency to become off-resonant with the detection circuit (rendering the electron undetectable) (§2.2) and so the electrostatic trapping potential (2.18) might have to be varied (§6.1.3) in order to bring ω_z (2.9c) back into resonance.

However, to conclude, the calculations in this section suggest that a trapped electron should be able to detect a significant number of single microwave photons.

Consideration 2: false positives and the maximum trap temperature

Firstly, it is true that a change in the spin state n_s would also cause a similar shift $\Delta\omega_z$ (2.37) to that caused by a change in the cyclotron oscillator state n_p, so a change in the spin state n_s might be falsely identified as the detection of a single microwave photon, i.e. a false positive for the detector. However, the g-factor is not exactly 2 [35], which distinguishes the axial frequency shift due to a change in the spin state n_s from a change

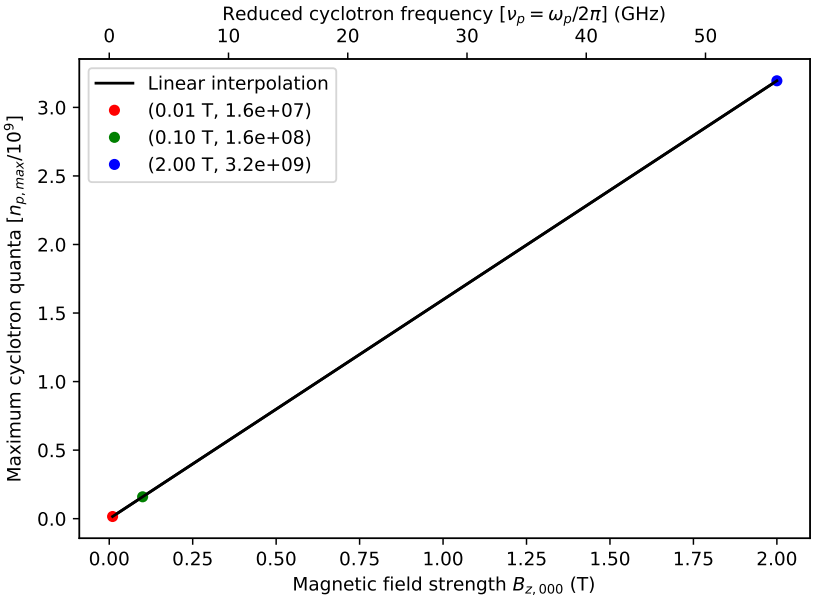

FIGURE 2.7: Plotting the numerical evaluation of (2.43). The maximum cyclotron quanta $n_{p,\max}$ prior to electron loss is plotted as functions of the magnetic field strength $B_{z,000}$ and the reduced cyclotron frequency ν_p (calculated using (2.10a)). The black line is a linear interpolation of (2.43) evaluated at 1001 values of $B_{z,000}$.

in the cyclotron oscillator state n_p (2.33b). Furthermore, the spin-photon and cyclotron-photon interactions are electric dipole and magnetic dipole transitions respectively [37] and the magnetic dipole transition is much weaker than the electric dipole transition [37], so a change in the axial frequency most likely results from a change in n_p.

Secondly, a trapped electron in the Geonium Chip Penning trap would only be useful as a single microwave photon detector if the signal-to-noise ratio were to exceed unity, otherwise itinerant thermal (noise) photons would be measured as false positives of itinerant signal microwave photons. In other words, the number of itinerant signal photons during the measurement/interaction time needs to exceed the number of thermal (noise) photons from the trap, i.e. the trap needs to be cold enough with temperature T. The number of noise photons at a frequency ω_p absorbed during the measurement time may be estimated by normalising the power of the Johnson-Nyquist voltage noise [101] V_J to the energy of each photon, where in this context the bandwidth Δf of the Johnson-Nyquist noise is equal to the inverse of the measurement time τ_m (§2.4.2). Therefore, the

numbers of signal N_{signal} and noise N_{noise} photons may be written into the equality

$$\underbrace{1}_{N_{\text{signal}}} \geq \underbrace{\frac{\overbrace{\left(\sqrt{4k_bT\Delta fR}\right)^2}^{V_J^2}/R}{\hbar\omega_p} \cdot \tau_m}_{N_{\text{noise}}} \tag{2.44}$$

and then eventually

$$T \leq \frac{\hbar\omega}{4k_B}, \tag{2.45}$$

which in magnetic fields between 0.1 T and 2.0 T ($\omega_p = 2\pi \cdot 2.8$ GHz and $\omega_p = 2\pi \cdot 56$ GHz respectively) [37] gives $T \leq\approx 34$ mK and $T \leq\approx 672$ mK respectively. Equation (2.45) would predict a minimum temperature of 1.8 K at 150 GHz, which is in good agreement with the previous demonstration of single microwave photon detection using a trapped electron in a Penning trap [120], where a dilution refrigerator was required in order to investigate thermal photons of 150 GHz between temperatures of 4.2 K and 80 mK in run times of ≈ 55 minutes, with just one photon visible at 1.6 K and no photons visible at 80 mK. This discussion has been formulated using principal ideas from Dr José Verdú-Galiana.

2.4.3 Alternative single microwave photon detectors

Single microwave photon detectors are also being developed using alternative technologies to the Geonium Chip Penning trap. The efficient single photon detection of photons in the microwave domain is more difficult than for photons in the optical domain [126], because the energies of microwave photons are many orders (4-5) of magnitude lower than the energies of optical photons [127, 128]. Microwave detectors of high microwave field powers may be evaluated by comparing their efficiencies with units of $\text{pF}/\sqrt{\text{Hz}}$. However, the reduced cyclotron quantum harmonic oscillator mode of a trapped electron in the Geonium Chip Penning trap (assuming a unity internal quantum efficiency for photon absorption (2.39)) should absorb all itinerant single microwave photons (§2.4.2) and so the single microwave photon detector technologies should be compared using

alternative attributes. Several alternative single microwave photon detection technologies exist including those based on Josephson Junctions, transmons, quantum dots and masers.

Many single microwave photon detectors use Λ (lambda) three-level systems [37] which are unable to measure multiple simultaneous single microwave photons and may destroy the detected photon [124]. However, a trapped electron in the Geonium Chip Penning trap acts as a "linear and reversible quantum microwave transducer" [124] which can detect multiple single microwave photos simultaneously [37, 124] and also non-destructively [37, 124], as demonstrated in a cylindrical Penning trap [120]. Many single microwave photon detectors using Λ systems are based on Josephson-Junctions, for example [126, 129–133]. However, theoretical work [134] for a Josephson-junction scheme [126] (which demonstrated a detection efficiency for single photons of (0.66 ± 0.06) [126] and a reset time of $\sim$ 400 ns [126]) proposes that two simultaneously itinerant photons might be detected. One disadvantage of Josephson-junction based schemes is that a dilution refrigerator may be required [126, 135] ($\sim$10 mK) or [136] (30 mK), which can be expensive. Furthermore, it was initially assumed that for another Josephson-junction experiment, that i) for one single photon absorber (or for "the cluster [of absorbers] size being smaller than a wavelength" [129]) "the maximal achievable detection efficiency is 50%" [129] and that ii) for multiple well-separated absorbers this could be improved to detection efficiencies of 80% and 90% for two and three qubits [129]. Another improvement was proposed [130] to reach "100% efficiency with only one absorber" [130] by "embedding the three-level system in a semi-infinite line" [130]. Additionally, the implementation of multiple Josephson junctions as constituents of a *quantum metamaterial* [131] has also been proposed as a non-destructive detector [131] for single microwave photons [131], with predicted "detection fidelities approaching unity" [131] and "large detection bandwidths" [131]. This metamaterial [131] is denoted the "*Josephson traveling-wave photodetector*" [131] and was "inspired by the Josephson traveling-wave parametric amplifier [136] [citation consistent with this thesis]", with an experimentally-determined 75% quantum efficiency [136]. A ratio which represents one Josephson-junction detector's ability

to both i) wait for an itinerant photon and also ii) have a short down-time after detection [133] (which represents the sensitivity), is calculated to be up to $\sim 10^7$ [133] assuming junction leads and resonator temperatures of <90 mK and <30 mK respectively [133] and it is proposed that the ratio might reach $\sim 10^9$ [133]. One motivation for another Josephson junction scheme is to "reveal the existence of weak signals in a thermal noise background" [132], where the sensitivity is considered via the Kumar-Caroll index [132], "which is a good indicator of the signal-to-noise ratio" [132].

Another alternative single microwave photon detection technology uses the transmon qubit, which as referenced in [37] has previously been reviewed (modelled as a Λ system) in [137]. One benefit with transmon schemes is that they can be used to make quantum non-demolition measurements [137], with measurements of one such transmon scheme [138] (involving the coupling of a transmon to two cavities) showing that the detection was 90% quantum non-demolition [138]. This scheme may also be used to detect multiple single photons [138]. Another quantum non-demolition scheme [139] using a transmon qubit in a 3D superconducting cavity was experimentally determined to have a photon survival probability of (0.87 ± 0.03) and a single photon detection quantum efficiency of (0.84 ± 0.02). This scheme may also be used to detect multiple single photons by measuring parity [139] and after cascading multiple detectors it may be possible to make a "number-resolved photon counter" [139]. Another scheme [140] used a transmon coupled to a resonator with a readout fidelity of $\sim$ 80% [140], however this scheme used a dilution refrigerator [140]. This technology also allowed for the measurement of the average photon occupancy number in the resonator for multiple (up to five) single microwave photons [140]. One final alternative quantum non-demolition scheme [127] uses a transmon which incoherently interacts with a resonator [127], with both the transmon and resonator also interacting with a cold bath [127]. The scheme has experimentally demonstrated a 58% detection efficiency [127]. One application of [127] is [141] which detects the single microwave photon fluorescence of donor spins in silicon [141], which exhibited a detection efficiency of (0.53 ± 0.1) in a 5 μs detection window [141].

Another alternative technology which mimics a photodiode device implements a

double quantum dot in a nanowire which is itself in a microwave resonator [128] and allows for the continuous measurement of multiple single microwave photons with a measured quantum efficiency of 6% [128]. The experiment uses a dilution refrigerator which helps to achieve an electronic temperature of 40 mK [128]. Also proposed for single microwave photon detection is a cascade amplifier based on the one-atom maser [142] with a quantum efficiency of up to 93% [142].

Single microwave photon detection has applications in quantum communication, quantum information, microwave spectroscopy [37] and also in quantum networks [124].

2.4.4 A summary and comparison of the benefits of using the Geonium Chip Penning trap as a single microwave photon detector

The detection of single microwave photons with a trapped electron in the Geonium Chip Penning trap has some advantages.

- Firstly, the measurement of the cyclotron quantum number n_p through the axial frequency ω_z (§2.4.1) is a quantum non-demolition measurement [120] (and [143] cited within). This is because the Hamiltonian $\hat{H}_p$ (2.32b) for the cyclotron oscillator interaction commutes with the interaction $\hat{H}_{\text{CSGE}} = -\vec{\mu} \cdot \Delta\vec{B}$ of the magnetic moment with the magnetic bottle [120], i.e. $[\hat{H}_{\text{CSGE}}, \hat{H}_p] = 0$ [120]. This implies that the state n_p of the quantum cyclotron oscillator is not affected by the measurement of n_p [120] (2.32b). One benefit of this is that the axial frequency can be continuously measured without disturbing the absorption/measurement and so it is not a prerequisite to know the arrival time of the photon, unlike for example [134]. Another benefit [37] which results is that the axial frequency ω_z (2.9c) (through which the photon is detected) is independent of the cyclotron oscillator frequency ω_p (the mode which absorbs the photon) and so the same electronic detection circuit (§2.2) for ω_z can be used to detect itinerant microwave photons of different frequencies. Some other technologies (e.g. some Λ systems (§2.4.3)) are not quantum non-demolition and so their incorporation into quantum technologies might be limited, unlike the Geonium Chip Penning trap.

- As discussed in [37], a second advantage is that many microwave photons may be stored as phonons in the cyclotron oscillator (§2.4.2) and so the system may be used to simultaneously detect multiple itinerant single microwave photons, whereas other technologies (e.g. some Λ systems (§2.4.3)) may only be able to detect one single photon before the system requires reinitialising. Furthermore, the Geonium Chip Penning trap might be able to (§2.4.2) absorb orders of magnitude more single microwave photons than those technologies [134, 140] which might be able to detect multiple single photons.

- A third advantage is the tune-ability of the system [37]. Firstly, the frequency ω_p of the detectable microwave photons may be chosen by selecting an appropriate magnetic field strength B_0 ($\omega_p \simeq \omega_c(B_0)$) [37] (§2.4.1)). Secondly, the curvature B_2 finitely broadens the cyclotron resonance to allow a wider bandwidth of frequencies to be absorbed [37], however the Q-factor is still high at $\Delta\omega_p/\omega_p \simeq 10^{-7}$ [144] as referenced in [37]. The magnetic field strength B_0 (§2.1.1) and the curvature B_2 (2.36) of the bottle field can be arbitrarily set and changed (in-situ) to vary the photon absorption bandwidth and centre frequency.

- Although single microwave photon detection is yet to be demonstrated using a trapped electron in the Geonium Chip Penning trap (§2.4.2), this scheme has already been demonstrated experimentally using a cylindrical Penning trap [120, 121] as discussed above (§2.4.2). The Geonium Chip Penning trap should act as a deployable (§1.1.3) single microwave photon detector. Although a dilution refrigerator will be required for this technology, the apparatus will consist of a closed-system (§3.1) which will be robust to external environmental changes.

Chapter 3

The realisation of the Geonium Chip Penning trap experiment

The Geonium Chip Penning trap experiment has previously been discussed in several papers [21, 22, 33, 37, 91, 97, 124, 145], in several doctoral theses [32, 36, 102, 123, 146] and also in two patents [147, 148]. The Geonium Chip Penning trap experiment underwent many changes during the time permitted for the research discussed in this thesis. However, the general principles and their implementation remained consistent and so this chapter introduces these concepts.

3.1 Overview

The particle trapping region is inside a small, electrically grounded, hermetically sealed cryogenic trapping chamber, which is in thermal contact with the second cooling stage of a *Sumitomo Heavy Industries SRP-062B* two-stage cold-head, at a temperature of $\approx$ 4 K. The first stage cold-head reaches $\approx$ 60 K. Surrounding this cryogenic chamber are two concentric cylindrical radiation shields (one for each cooling stage), which are in a much larger vacuum vessel at room temperature. This setup collectively helps to form a cryostat and the inside of which (excluding the radiation shields) is depicted in Figure 3.1.

The Geonium Chip (a printed circuit board) containing a planar set of electrodes (in the $\hat{u}_x$-$\hat{u}_z$ plane) forms a wall of the cryogenic trapping chamber and this board is also

mounted to a planar set of current-carrying wires (also in the $\hat{u}_x$-$\hat{u}_z$ plane). Both the Geonium Chip and the magnetic field source are also in good thermal contact with the second stage coldhead and so they are also at a temperature of ≈ 4 K. A superconducting helical resonator is in electrical connection with the right correction electrode in order to measure the axial frequency (§2.2). This resonator is also denoted the *axial resonator*. The voltage spectrum of the axial resonator is amplified by a ≈ 4 K cryogenic preamplifier and then again outside the cryostat with a commercial amplifier, before being displayed on a spectrum analyser. In order to load electrons, an optical fibre introduces UV light through a vacuum flange into the cryostat, which is collimated and shone through a window in the cryogenic trapping chamber, towards a target on one of the walls of the cryogenic trapping chamber. The UV source is a *Hamamatsu L10290* deuterium source which outputs wavelengths as low as 200 nm.

Outside the cryostat exist the power supplies for the electric field source, the magnetic field source and the preamplifier, among other control devices including function generators and two custom-build control computers.

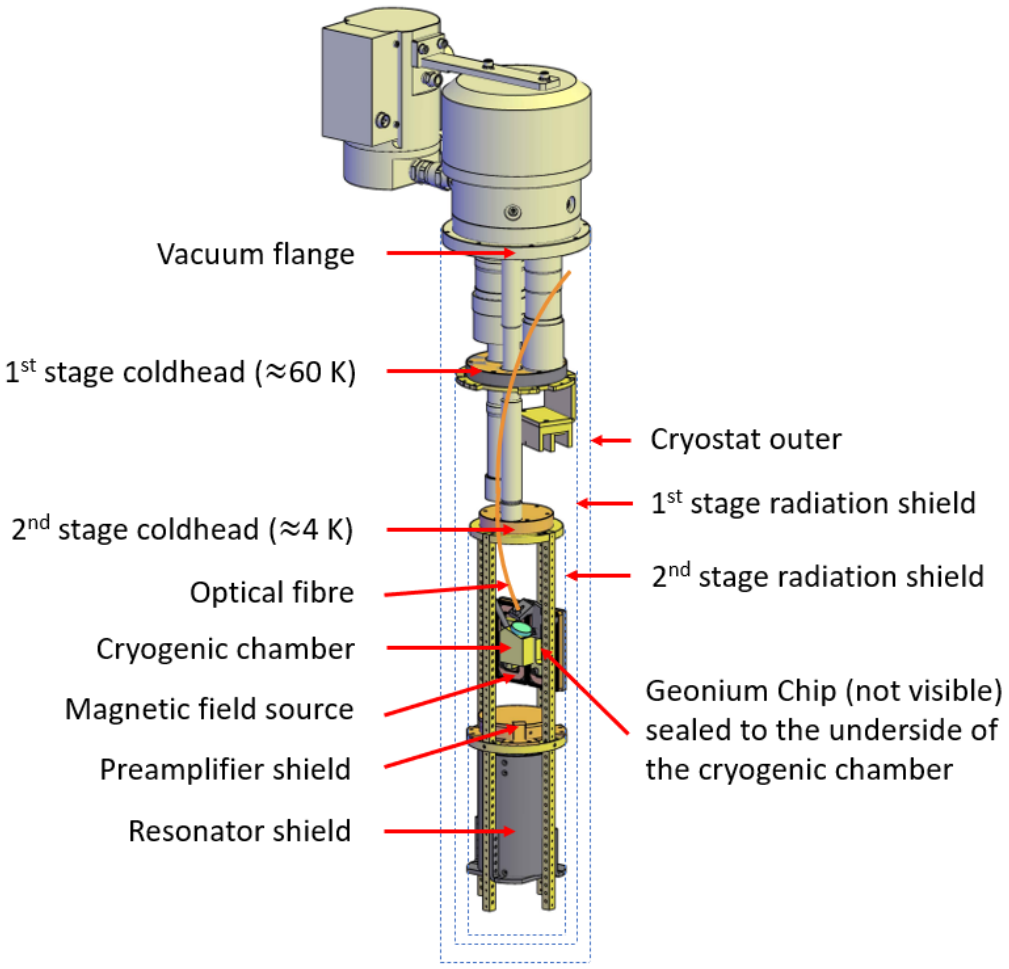

FIGURE 3.1: The inside of the large vacuum vessel which helps to form a cryostat. The vacuum flange in the top of the picture forms one of the hermetic seals. Adapted from a CAD model (Dr Jonathan Pinder).

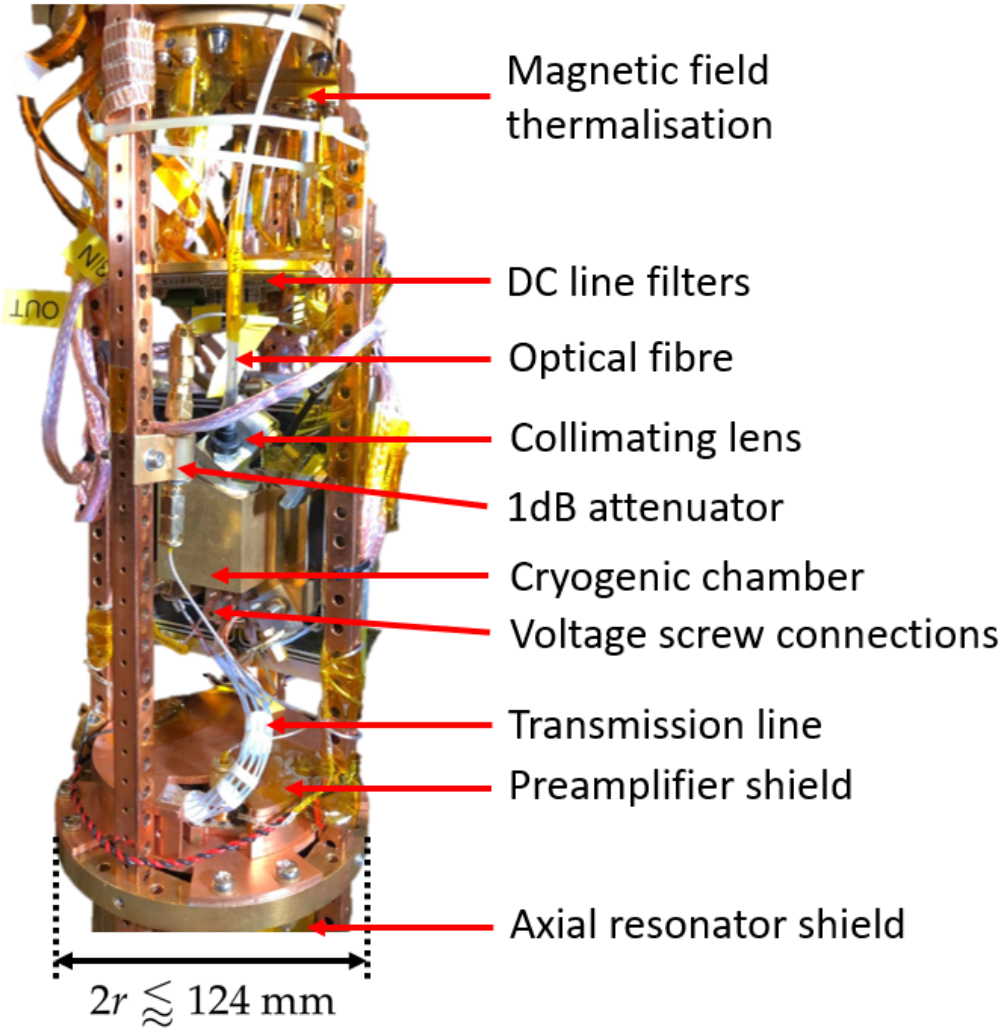

FIGURE 3.2: A photograph of the second-stage (≈ 4 K) region, bounded by the second-stage radiation shield (Figure 3.1). The diameter of the experiment is slightly shorter ($\pm \approx 5$ mm) than the inner diameter of the inner radiation shield at 124 mm [36]. The transmission line is superconducting and is also shown in the schematics in Figure 3.8. The voltage screw connections on the chip are shown in the photographs in Figure 3.3.

3.2 The electric field source

The Geonium Chip's electrostatic field source is a planar electrode structure which is an evolution from conventional cylindrical [20] electrode structures [21]. The chip contains five flat rectangular electrodes in the $\hat{u}_x - \hat{u}_z$ plane, with each symmetrically centred around $x = 0$ and together sandwiched between two ground-planes [21]. The chip may eventually form a coplanar waveguide in the $\hat{u}_x - \hat{u}_z$ plane [21, 149]. The five electrodes are also arranged symmetrically centred around $z = 0$, with a *ring* electrode centred on $z = 0$, which is sandwiched within two *correction* electrodes and finally bounded by two outer *endcap* electrodes [21]. There are electrically-insulating gaps which surround each of the five central electrodes [21]. These topological symmetries along both $\hat{u}_x$ and $\hat{u}_z$ give rise to symmetries in the electrostatic potential which imply that odd anharmonicities (C_{ijk} where i and/or k are odd (2.18)) are eradicated [21]. Throughout this thesis, the origin of the Cartesian co-ordinate system $(x = 0, z = 0)$ is at any y above the centre of the ring electrode and in this section the co-ordinate $y = 0$ is defined as the surface of the Geonium Chip.

The general electrostatic potential $\phi_{\text{quad}}(x, y, z)$ (2.18) can be defined as an infinite polynomial expansion in space (§2.1.2). To obtain the electrostatic potential produced by the trap electrodes, a Green's Function method to solve The Laplace Equation using Dirichlet boundary conditions may be used [150]. Using this method, the electrostatic potential produced by the Geonium Chip may also be written as a sum of the contributions from each of the electrodes [21]

$$\phi(x, y, z) = V_R \cdot f_R(x, y, z) + V_C \cdot f_C(x, y, z) + V_E \cdot f_E(x, y, z) + f_{\text{gaps}}(x, y, z | V_R, V_C, V_E), \tag{3.1}$$

where V_R, V_C and V_E are the DC voltages applied to the ring electrode, correction electrodes and the endcap electrodes respectively [21]. The functions $f_C(x, y, z)$ and $f_E(x, y, z)$ each depend on the pairs of their respective electrodes [21]. The functions $f_R(x, y, z)$, $f_C(x, y, z)$ and $f_E(x, y, z)$ depend on the trap topology but not on the applied voltages [21] (the voltage is the same at all x and z for a given electrode), whereas the function

f_{gaps} does also depend on the electrode voltages (for example an approximation may be applied where the voltages across any gap changes linearly with z) [21]. The functions $f(x, y, z)$ are analogous to $\Lambda_\Sigma(\vec{r})$ when expressing the *self-induced potential* [91] ϕ_{ind} [91] (2.27a). It is sometimes convenient to refer to the (dimensionless) tuning ratios T_C and T_E for the correction electrode and the endcap electrode respectively (for example when determining y_0 [21]) defined by [21]

$$T_C = \frac{V_C}{V_R} \tag{3.2}$$

$$T_E = \frac{V_E}{V_R}. \tag{3.3}$$

The most recent realisation of the Geonium Chip is of a double-sided printed circuit board design. The substrate of the board is alumina (Al_2O_3), which although electrically insulating does not accumulate charge on its surface [151]. This is beneficial because the inter-electrode gaps are visible to any trapped ions and any accumulated charge would perturb the trapping potential (3.1) and would thus introduce electrical anharmonicities (§2.1.2). The trap electrodes were milled [152] into the top-side copper-pour (and subsequently polished and then gold-plated by the research group) and the electrode voltage bias lines were milled [152] from the bottom-side copper-pour. To provide electrical insulation and structural reinforcement, a second layer of alumina was subsequently fixed to the bottom-side copper-pour by Dr Jonathan Pinder, using epoxy as an adhesive. The top and bottom sides of the chip (prior to bottom-side reinforcement and top-side polishing) are shown below in Figure 3.3. The Geonium Chip's high frequency properties have been characterised [32].

In the experimental setup, the Geonium Chip acts as the sixth (bottom) wall in an electrically grounded cube, denoted the *boxed CPW-trap* [22], as depicted below in Figure 3.5 (but note that the side electrodes do not exist in the most recent iteration of the Geonium Chip). The introduction of the five extra grounded surfaces modifies the functions $f(x, y, z)$ in (3.1) [22]. An example electrostatic potential produced by the boxed CPW-trap is shown below in Figure 3.4, using the voltages $V_R = -0.5$ V, $V_C = -0.700422$ V and $V_E = -2.85$ V (with the dimensionless tuning ratios $T_C = 1.400844$ and $T_E = 5.7$). This potential invokes an axial frequency of approximately $\omega_z = 2\pi \cdot 25.3756$ MHz and also a

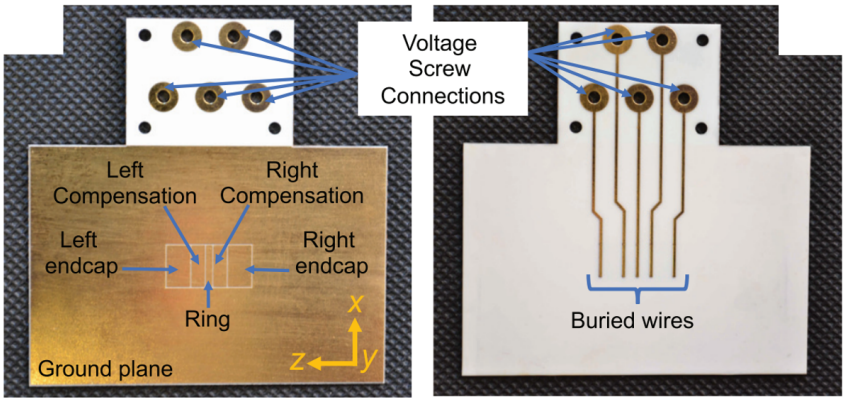

FIGURE 3.3: Photographs of the Geonium Chip. The top-side of the chip (left) is shown prior to polishing and additional gold-plating. The bottom-side of the chip (right) is shown prior to reinforcement. The chips used at present also feature curved corners, to reduce the risk of the chip cracking. Voltages are applied to the electrodes through the buried wires (buried once reinforced). Adapted from [124].

trapping height $y_0 = 1.45$ mm. This potential was used during some trapping attempts. This potential was calculated using *Mathematica* functions which were provided by Dr José Verdú-Galiana, to compute (3.1) using formula in [22, App. A].

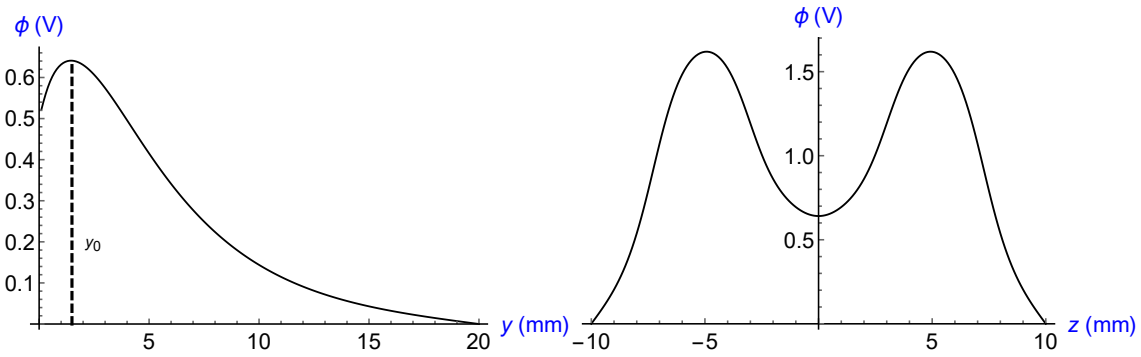

(A) The smooth black line shows a plot of $\phi(y)$ at the equilibrium trapping position where $x = 0$ and $z = 0$. The equilibrium trapping height is shown with a dashed black line at $y_0 = 1.45$ mm.

(B) A plot of $\phi(z)$, at the equilibrium trapping position where $x = 0$ and $y = y_0 = 1.45$ mm. The depth of the trap was calculated numerically to be approximately 0.98 eV. As expected from the topological symmetry, the potential is symmetric around $z = 0$.

FIGURE 3.4: Plotting an electrostatic potential (3.1) produced by the Geonium Chip electrodes in a boxed CPW-trap, showing $\Phi(y)$ (Figure 3.4a) and $\Phi(z)$ (Figure 3.4b). Initially, y_0 was determined by plotting $\Phi(y)$ and then $\Phi(z)$ was plotted at this determination of y_0. A plot of $\Phi(x)$ is less useful because the boxed CPW-trap is symmetrical along $\hat{u}_x$ and so the equilibrium occurs at $x = 0$. Both potentials (Figures 3.4a and 3.4b) have been multiplied by (-1) for ease of interpretation.

Two additional *side electrodes* [22] may be introduced to the Geonium Chip, both spanning the length of the five trap electrodes along z and positioned either side of the five trap electrodes [22], as depicted in Figure 3.5. The voltage V_G on the side electrodes may be varied to change the trap ellipticity ϵ (2.2) [22] and increase the trapping height y_0 [22] (§2.1.1). Some choices of V_G may even put the trapped particles into the *ultra elliptical regime* [22] where ϵ approaches +1 [22]. In this case ($\epsilon \to 1$), ω_m approaches zero and the trapped ions become trapped in a $\hat{u}_x$-$\hat{u}_z$ plane with $y = y_0$ [22], potentially allowing the formation of a *quasi two-dimensional electron gas in free space* [22]. There also exist voltages V_G which set the ellipticity ϵ to zero, i.e. where the circular symmetry (§2.1.1) of conventional traps is achieved, where $\phi_{\text{elliptical}} = 0$ (2.1). As can be seen in Figure 3.3, the most recent Geonium Chips do not at present make use of side electrodes, because they are not necessary to trap electrons (see (§6.1.3) for the electrostatic potentials which are in current use). However, it is intended that the ultra elliptical regime will be investigated in the future, which would require the use of side electrodes.

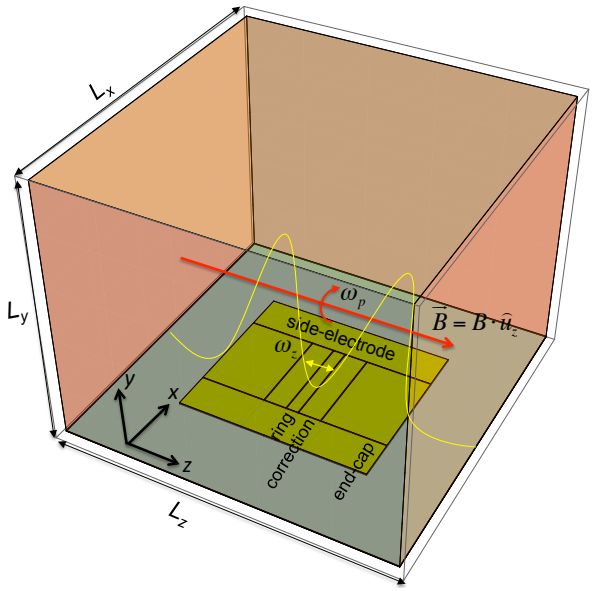

FIGURE 3.5: A model showing (reproduced from [22]) the Geonium Chip with side electrodes, depicted as a component of the *boxed CPW-trap* [22]. The two endcap electrodes, the two correction electrodes and the ring electrode (also depicted in Figure 3.3) are visible sandwiched in the $\hat{u}_z$-$\hat{u}_x$ plane between the two side electrodes which run the length of the chip along $\hat{u}_z$ [22]. The centre of the 3D Cartesian position system is in the centre of the ring electrode [22]. The axial and modified cyclotron motions (§2.1.1) are depicted with frequencies ω_z and ω_p respectively.

The high frequency properties of the Geonium Chip are discussed in [32, 33].

3.3 The magnetic field source

The details of the operation of the magnetic field source will be discussed in more detail in Chapter (§5). As described in [97], superconducting solenoids which produce homogeneous magnetostatic fields with strengths on the order of 1 T have many applications, for example in magnetic resonance imaging [153], nuclear magnetic resonance [154], mass spectrometry [155] and in precision measurements [156]. Also as described in [97], superconducting solenoids can achieve excellent temporal stabilities, for example $\sim$ 20 ppt/h [157] which for example employed passive self-shielding coils [158, 159], active helium cryogen pressure regulation and an actively controlled pair of Helmholtz coils.

Superconducting solenoids can produce magnetic fields $\vec{B} = B_0\hat{u}_z$ which are homogeneous to less than a few ppm in a volume of the order of cubic centimetres [97], for example [160]. However, a trapped electron cooled to a temperature of 4 K in an homogeneous 1 T field would only occupy a much smaller volume of approximately $2 \times 2 \times 70$ μm^3 [97]. The temperature and cooling of a trapped particle has been discussed in (§2.3.1) - in order to cool an electron to 4 K, the axial motion of the electron could be resistively cooled (§2.3.1) to the 4 K temperature of the axial resonator (§3.5), the magnetron motion could be cooled via RF sideband cooling (§2.3.1) (coupling to the 4 K axial motion) and the cyclotron motion could be cooled by emitting synchrotron radiation [103]. Furthermore, heavy ions would still occupy a much smaller volume than a cubic centimetre: for example an ion with a mass 200 Da (1 Da = 1 a.m.u.) and charge $\pm e$ would occupy approximately $110 \times 110 \times 70$ μm^3 [97]. Therefore, it is typically unnecessary to need such a large volume (a cubic centimetre) in which the magnetic field is homogeneous [97]. Typical superconducting solenoid magnetic field sources may be spatially large and require liquid helium cryogen [157, 160, 161] and thus are not scalable. A smaller, scalable magnetic field source may be built if: the trapped particle is trapped closer to the magnetic field source; the source only has to produce an homogeneous field in a small volume of

a few mm^3 and if liquid cryogens may be avoided by the use of a *closed-cycle* pulse-tube cryocooler [97]. To a good extent, the Geonium Chip Penning trap's magnetic field source is such a scalable magnetic field source.

The Geonium Chip's planar magnetic field source has previously been discussed [36, 97, 123, 145–148]. The general model of the planar field source consists of two concentric sets of four currents in closed rectangular loops, all coplanar in the x-z plane [97]. There are four currents (I_0, I_1, I_2 and I_3), with one loop in each of the two sets carrying one of the four currents which are independent from one another [97]. The source is symmetrical, with lines of symmetry i) in the $\hat{u}_z$ direction around $z = 0$ and ii) in the $\hat{u}_x$ direction around $x = 0$. The ith current runs with opposite sense in each of the two sets, so that at equilibrium trapping positions $x = z = 0$, for all vertical positions $y = y_0$ above the surface of the source, the magnetic field only has an axial $\hat{u}_z$ component $\vec{B}(0, y_0, 0) = B_z(0, y_0, 0)\hat{u}_z$ [97]. A sketch of the model and a photograph of the source are shown below in Figures 3.6a and 3.6b respectively.

The currents (I_0, I_1, I_2 and I_3) may be denoted the *main*, *shim 1*, *shim 2* and *shim 3* [36] currents. The most recent realisation of the magnetic field source was designed and fabricated by Dr Jonathan Pinder. Although the best temporal stability would occur when driving the currents in persistent mode [36], the currents in the existing source are continuously driven with a *Rohde & Schwarz HMP4040* power supply [36]. Each ideal current loop (denoted a *coil* [36]) is comprised of many loops of superconducting NbTi copper stabilised wire rather than just one loop [36], to increase the current density for a given current [36]. The source currently installed in the experiment was built by Dr Jonathan Pinder to the design detailed in [36], however to further increase the current density [32], the diameter of the NbTi wire was reduced from 400 μm to 100 μm [32] to increase the number of turns to 120, 225, 1995, 1982 in the main, shim 1, shim 2 and shim 3 coils (respectively) [97].

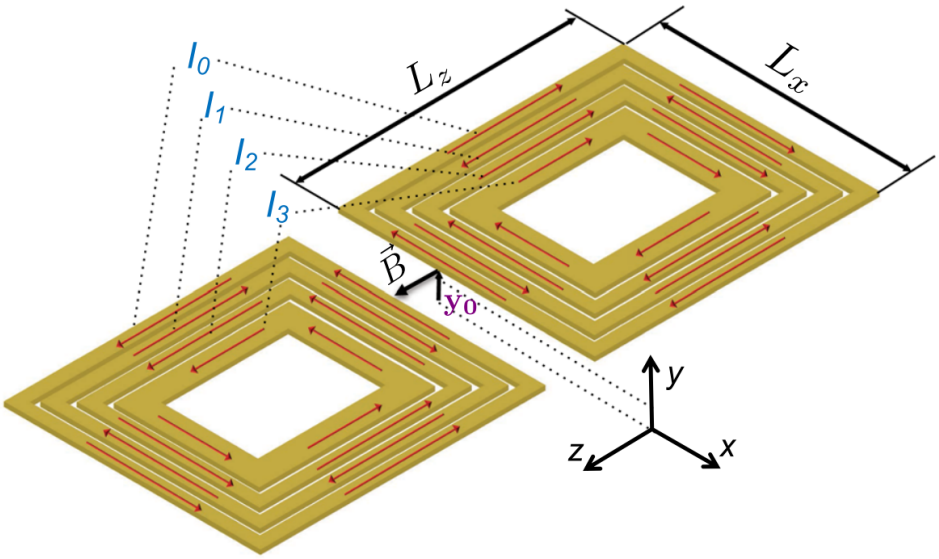

(A) Schematics of the model of the field source [97]. The origin of the Cartesian system is at the centre of the source. Reproduced from [97].

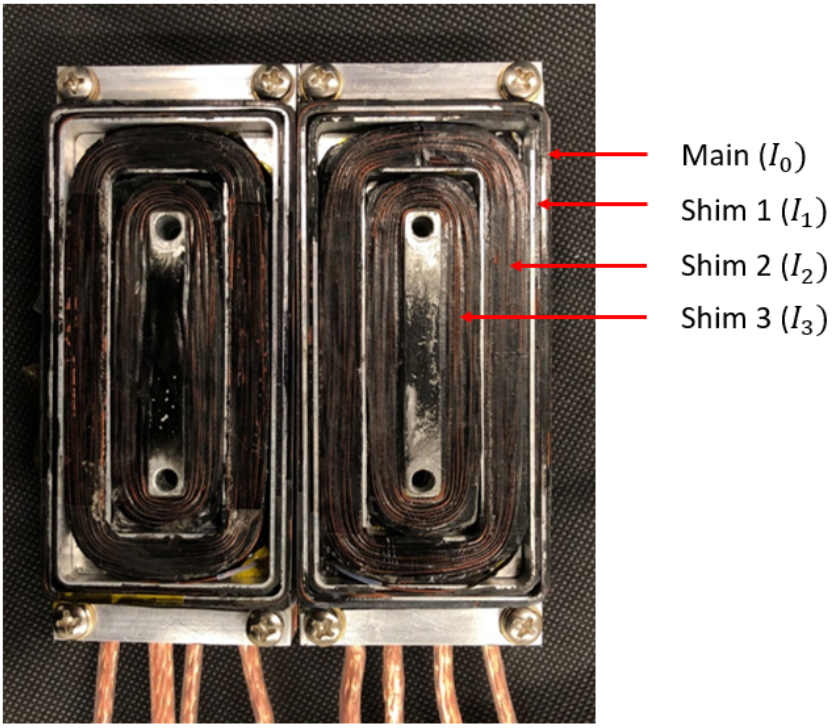

(B) A photograph of the field source. Each set of four loops contains two cylindrical holes, through which the mounting bolts are threaded to secure the chamber and chip to the magnetic field source (e.g. see Figures 3.1 and 3.2).

FIGURE 3.6: Introducing the planar magnetic field source of the Geonium Chip Penning trap.

Although the NbTi coils themselves do not exhibit any ohmic heating while superconducting, the non-superconducting wiring between the coils and the room temperature power supply does exhibit ohmic heating, which is dissipated by the use of air and water cooling systems [32]. On one occasion, prior to the installation of the air and water cooling systems, the room temperature electronic filters [146] of the previous magnetic field source with 400 μm NbTi wire [36] became hot enough to melt some of the solder. One of the biggest thermal concerns is the risk of a superconductor quench (§5.2), which may permanently damage the coils. The *calibration* and the operation of the Geonium Chip Penning Trap's planar magnetic field source is discussed in (§5).

3.3.1 Correcting for imperfect coil winding

In order to initially calibrate the magnetic field source (§5.1), least-square fits are conducted to measured magnetic fields using a fit model which is based on the Biot-Savart law (5.5). This model assumes that for each real coil the current density is i) homogeneous throughout that coil and ii) limited to a precisely known finite volume. It is true that the effective current density and effective cross-section are free fitting parameters (see Table 5.1), however the calibration would be more reliable if the true current density distribution and volume (cross-section distribution) were to be known. Therefore, if a coil is wound imperfectly such that either/both of these conditions are not met, then the calibration would be unreliable. The coils in the magnetic field source were manufactured by Dr Jonathan Pinder from NbTi wire which was held in place by epoxy [36]. Therefore, firstly, the real current density distribution throughout the coils is unknown, but this could be measured using a non-invasive technique [162]. Secondly, the volume of the coils could be made more accurate by accurately measuring the physical spatial dimensions of the coil, however the existing model is already reliable. Thirdly, the calibration only used seven magnetic field strength sensors (Hall probes) (§5.1.1) and so this also limits the reliability of the initial calibration. Therefore, it would be possible to correct for imperfect coil winding by improving the initial calibration in these three ways, but it is unlikely that the calibration would improve significantly.

However, once electrons have been trapped in the Geonium Chip Penning trap, it might be possible to fine-tune the calibration and further correct for imperfect coil winding. The magnetic field can be mapped with improved resolution and improved precision using the trapped electron as a magnetic field sensor [97]. The position $\vec{r}_0 = (x = 0, y = y_0, z)$ (§2.1.1) of the trapped electrons can be varied in small steps, which would give a high spatial resolution. The trapping height y_0 may be varied by varying the endcap tuning ratio T_E (3.3) and the axial position z may be varied by introducing asymmetries (along $\hat{u}_z$) into the trapping potential $\phi(x, y, z)$ (3.1). Note that the x co-ordinate of $\vec{r}_0$ cannot be easily changed because of the symmetric (in $\hat{u}_x$) topologies of the sources of the trapping potential (§3.2) and the magnetic field. The magnetic field strength $B_z(y, z)$ along $\hat{u}_z$ can be determined for each position $\vec{r}_0 = (x = 0, y = y_0, z)$ by determining the three motional eigenfrequencies ω_z, ω_p and ω_m with high precisions (e.g. through the axial resonator (§3.5) using a mode-coupling technique [163, 164]) and then [97] using the invariance theorem (§2.1.3). Using this technique, while varying the magnetic field currents and evaluating the resulting mapped magnetic fields, the magnetic field currents may be optimised empirically (in effect this is a fine-tuning of the initial calibration) to further correct for imperfections in the winding of the coils.

3.4 The cryogenic trapping chamber

As described above in (§3.2), the Geonium Chip acts as the sixth (bottom) wall in an electrically grounded cube, denoted the *boxed CPW-trap* [22]. The other five walls are provided by a cryogenic trapping chamber and a mesh which were designed prior to this work by Dr Jonathan Pinder [36]. The internal volume of the chamber is $(20\text{ mm})^3$ [36]. This trapping chamber has many roles: it acts as a DC-ground for the boxed CPW-trap; it forms a microwave cavity that inhibits spontaneous emission of cyclotron radiation (the Purcell effect) [22, 122] (§2.4.2); it forms a hermetically sealed volume in which the pressure may be reduced to increase the trapping lifetime of trapped ions [36] (e.g. [165] using e.g. cryopumping [166]); it has a relatively large thermal mass which to some extent acts as a heatsink at 4 K and finally it may support a photocathode. In particular, regarding the relationship between the pressure of the rest gas and the lifetime of trapped electrons, pressures of $\sim 10^{-8}$ mBar and $\sim 10^{-11}$ mBar gave rise to measured lifetimes (time constants from exponential fits) of (22 ± 2) seconds [11] and 3.5 hours [13] respectively. Furthermore, a rest gas pressure of less than 5×10^{-17} torr ($\approx 7 \times 10^{-17}$ mBar) allowed one electron to remain trapped for months [35] and other work [167] reported a single electron having remained trapped for at least ten months.

The cryogenic trapping chamber which is currently installed in the experiment is built to the design detailed in [36, Figure 4.8], however it has been machined from oxygen free copper rather than from the less-desirable [36] aluminium. The chamber has been gold plated (described in [32]) so that the chamber should remain chemically inert and won't accrue an oxide layer which would otherwise perturb the electrostatic trapping potential [36]. The Geonium Chip is hermetically sealed to the chamber with the use of an indium wire gasket which is cold pressed [36], as shown in Figure 3.7.

The cryogenic trapping chamber also features a UV-transparent sapphire window (to allow for the loading of electrons via the photoelectric effect) and so in order to maintain a DC-grounded boxed CPW-trap, a wide-gap mesh (85 % open [36]) is used to act as one of the DC-grounded walls of the chamber [36]. Instead of a fused-quartz window [36],

to reduce the attenuation of UV light, a sapphire window is used now instead. As described in [32], the latest method to hermetically seal the window to the chamber involves firstly, soldering independent layers of indium to both the window and the chamber at the points of sealing and then secondly, cold pressing the window to the chamber. In order to evacuate gas from the chamber, a pinch-off tube is also installed which allows for a cold-weld under deformation to produce a hermetic seal [36]. As detailed in [32], the latest method to hermetically seal the pinch-off tube to the chamber uses an indium solder joint rather than an *Alusol 45D* solder joint. The most recent iteration of the chamber also includes a photocathode with a gold-leaf target.

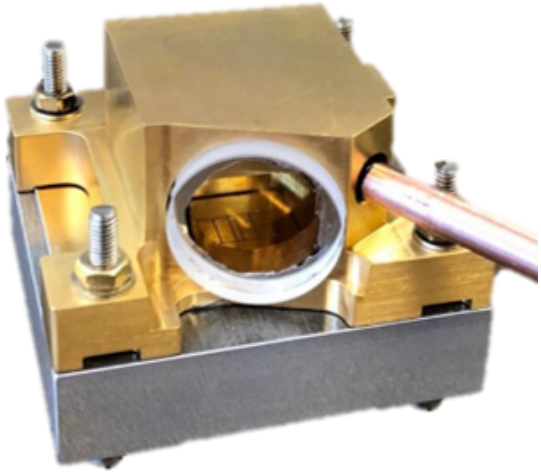

(A) The compression plate [36] is still attached and is visible beneath the chamber.

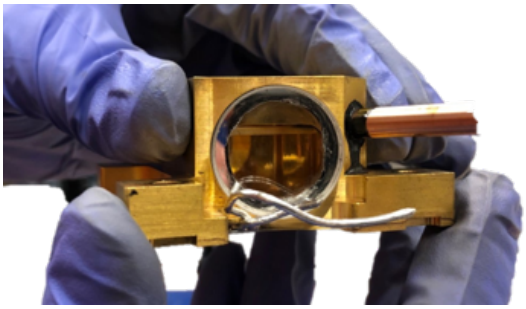

(B) The compression plate has been removed and some excess indium wire gasket is visible.

FIGURE 3.7: Photographs of the Geonium Chip and cryogenic trapping chamber (note, the photographs were taken during different sealing attempts, hence some excess indium is visible in Figure 3.7b but not in Figure 3.7a). In Figure 3.7b the chip electrodes are visible and in Figure 3.7a the mesh frame [36] is visible through the window. By considering the roof of the chamber in Figure 3.7a, it can be seen that the cross section in the $\hat{u}_x - \hat{u}_z$ plane is an irregular trapezium, so the mesh is required to make the internal volume a cuboid to realise the *boxed CPW-trap* [22]. Both photographs show an epoxy seal between the pinch-off tube and the chamber, which as described above has since been discontinued as a sealing method [32].

3.5 The electronic detection system

The physical electronic detection system of the Geonium Chip Penning trap has previously been discussed [32, 36, 146]. The theory of the electronic detection system is discussed in (§2.2) of this thesis, which describes how trapped ions modify the impedance of a real superconducting coil (a tank circuit) connected between an electrode and ground, causing a dip in the frequency response. As discussed in (§2.3.2), either correction electrode may be used to measure the axial motion. Rather than measure all three measurable eigenfrequencies ω_z, ω_p and ω_m directly using independent detection systems, as described in [37], all three measurable eigenfrequencies may be measured through the axial detection system with ω_p and ω_m being measured using a mode-coupling technique [163, 164].

The most significant components of the axial detection circuit are shown in Figure 3.8. The screw connector for the right correction electrode is connected via a superconducting transmission line [146] to the real superconducting coil (axial resonator), which as described in [36, 146], is a helical resonator made from niobium, which has a critical temperature of 9.3 K [36]. The axial resonator has a large volume, with an inner diameter of 47.3 mm and a length of 71 mm [36]. The axial resonator is also connected to the input of a cryogenic preamplifier [36, 146] which is in good thermal contact with the second stage coldhead at $\approx$4 K, to help improve the signal-to-noise ratio while the Johnson voltage noise [101] is low [36].

The preamplifier was designed [146] very similarly to the preamplifier used by Ulmer [168], because the axial frequency ω_z of trapped electrons in the Geonium Chip Penning trap (approximately $2\pi \cdot 28$ MHz (§2.1)) is close to the cyclotron frequency of a trapped proton ($\omega_p = 2\pi \cdot 28.9$ MHz [168]) as measured by Ulmer [168]. At the heart of the preamplifier there are two transistors - there is a dual-gate *NEC NE25139* transistor close to the input of the preamplifier which provides a greater than unity voltage gain. There is also a single-gate *Avago ATF35143* transistor close to the output which provides a greater than unity power gain via impedance matching to the output coaxial cable [146].

In the most recent iteration of the Geonium Chip Penning trap, the DC voltage V_c

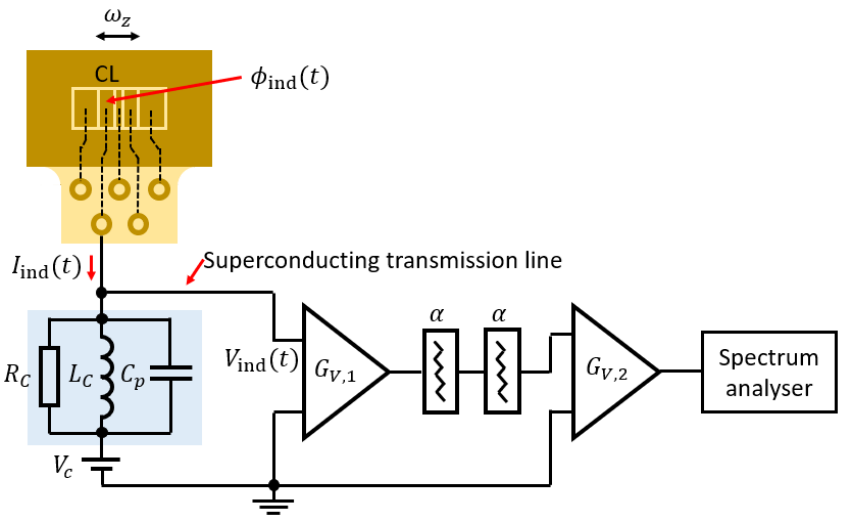

FIGURE 3.8: Schematics of the electronic detection system, which is connected to the voltage screw connection (Figure 3.3) for the left correction electrode. The DC bias V_c for the left correction electrode is applied through the axial resonator (pale blue shading). Two attenuators each with with attenuation $\alpha = 1$ dB are connected in series between the output of the cryogenic preamplifier with a voltage gain $G_{V,1}$ and the room temperature operational-amplifier with a voltage gain $G_{V,2}$. See (§2.2) for further information, including symbol definitions.

for the left correction electrode is supplied through the axial resonator. The cryogenic preamplifier has an input capacitance which is in series with the axial resonator and the first transistor, so the DC voltage V_c is decoupled from the input of the cryogenic preamplifier. The coaxial cables between the output of the preamplifier and the vacuum flange are thermalised with two 1 dB attenuators, where one attenuator is in thermal contact with the second stage coldhead ($\approx$ 4 K) and the other attenuator is in thermal contact with the first stage coldhead ($\approx$ 65 K) [146]. Outside the cryostat, there is an operational amplifier which provides further signal amplification and then the signal is input into a *Rohde and Schwarz FSV30* spectrum analyser which determines and displays the frequency spectrum.

3.5.1 Characterisation of the preamplifier

Microwave analysis theory

The preamplifier was characterised with an *Agilent Fieldfox N9923A* vector network analyser (VNA) at room temperature. Vector network analysis is discussed in [169, Chapter 4] and also in the theses [32, 36, 146]. When measuring a two-port network such as the preamplifier, the VNA first applies a voltage wave (negligible current) with amplitude V_1^- to port 1 and then measures the amplitudes of both the reflected wave V_1^+ at port 1 and the transmitted wave V_2^+ at port 2 [169]. In the setup used for this investigation, the input to the preamplifier was denoted port 1 and the output from the preamplifier was denoted port 2. This is then repeated in a similar way for port 2, where a voltage wave with amplitude V_2^- is applied to port 2 and then the reflected and transmitted wave amplitudes V_2^+ and V_1^+ respectively are measured [169]. The scattering parameters which are the elements of the scattering matrix $\mathbf{S}$ may be defined using [169]

$$\begin{pmatrix} V_1^- \\ V_2^- \end{pmatrix} = \underbrace{\begin{pmatrix} S_{1,1} & S_{1,2} \\ S_{2,1} & S_{2,2} \end{pmatrix}}_{\mathbf{S}} \begin{pmatrix} V_1^+ \\ V_2^+ \end{pmatrix}. \tag{3.4}$$

This method is repeated for many different frequencies ω of the input voltage waves V_1^- and V_2^-, so that a frequency response may be determined [169]. The scattering matrix (3.4) may be transformed into other matrices which are more appropriate for preamplifiers, for example the impedance matrix $\mathbf{Z}$ [169, 170], the hybrid matrix $\mathbf{h}$ [170] and the inverse hybrid matrix $\mathbf{g}$ (denoted $\mathbf{f}$ in [170]). These matrices may be defined by [169, 170]

$$\begin{pmatrix} V_1 \\ V_2 \end{pmatrix} = \underbrace{\begin{pmatrix} Z_{1,1} & Z_{1,2} \\ Z_{2,1} & Z_{2,2} \end{pmatrix}}_{\mathbf{Z}} \begin{pmatrix} I_1 \\ I_2 \end{pmatrix} \tag{3.5a}$$

$$\begin{pmatrix} V_1 \\ I_2 \end{pmatrix} = \underbrace{\begin{pmatrix} h_{1,1} & h_{1,2} \\ h_{2,1} & h_{2,2} \end{pmatrix}}_{\mathbf{h}} \begin{pmatrix} I_1 \\ V_2 \end{pmatrix} \tag{3.5b}$$

$$\begin{pmatrix} I_1 \\ V_2 \end{pmatrix} = \underbrace{\begin{pmatrix} g_{1,1} & g_{1,2} \\ g_{2,1} & g_{2,2} \end{pmatrix}}_{\mathbf{g}} \begin{pmatrix} V_1 \\ I_2 \end{pmatrix}, \tag{3.5c}$$

where the total voltage V_n and the total current I_n may be defined using [169]

$$V_n = V_n^+ + V_n^- \tag{3.6}$$

$$I_n = I_n^+ - I_n^-. \tag{3.7}$$

The scattering parameters in **S** [169] are all complex values and so the elements of **Z**, **g** and **h** are also complex. Of particular relevance to preamplifiers are the input impedance $Z_{1,1}$, the output impedance $Z_{2,2}$, the reverse voltage gain $h_{1,2}$ and the forward voltage gain $g_{2,1}$.

By considering (3.5a) these impedances may be defined using [169]

$$Z_{1,1} = \left.\frac{V_1}{I_1}\right|_{I_2=0} \tag{3.8}$$

$$Z_{2,2} = \left.\frac{V_2}{I_2}\right|_{I_1=0}. \tag{3.9}$$

From (3.8) it can be interpreted that $Z_{1,1}$ is the impedance at port 1, which is the preamplifier's input impedance. The input impedance $Z_{1,1}$ of the preamplifier loads the axial resonator and so $Z_{1,1}$ should be as large as possible to reduce this effect [146]. From (3.8) it can be interpreted that $Z_{2,2}$ is the impedance at port 2, which is the preamplifier's output impedance. One of the important roles of the preamplifier is to provide impedance matching to the coaxial cable which carries the axial signal from the output of the preamplifier to the spectrum analyser. This coaxial cable has a characteristic impedance of $Z_0 = 50\ \Omega$.

Similarly, regarding the hybrid and inverse hybrid parameters, using (3.5b) $h_{1,2}$ may be written [170] and using (3.5c) $g_{2,1}$ may be written

$$h_{1,2} = \left.\frac{V_1}{V_2}\right|_{I_1=0} \quad (3.10) \qquad g_{2,1} = \left.\frac{V_2}{V_1}\right|_{I_2=0}. \quad (3.11)$$

From (3.10) it can be interpreted that $h_{1,2}$ is equal to to the voltage amplification through the preamplifier when a wave is incident at port 2 and transmitted from port 1. Similarly, from (3.11) it can be interpreted that $g_{2,1}$ is equal to to the voltage amplification through the preamplifier when a wave is incident at port 1 and transmitted from port 2. The reverse voltage gain $h_{1,2}$ represents how well the preamplifier electrically insulates the trapped particle from the high-amplitude Johnson noise from the room-temperature electronics (incident at port 2, transmitted from port 1) and therefore the ideal $h_{1,2}$ would be zero. The forward voltage gain $g_{2,1}$ represents the first stage of voltage gain applied to the axial signal while there is small-magnitude Johnson noise ($\approx$ 4 K) and a high signal-to-noise ratio and therefore ideally $g_{2,1}$ would be very large.

Time domain analysis

Ideally, the VNA would be used to measure $g_{2,1}$, $h_{1,2}$, $Z_{1,1}$ and $Z_{2,2}$ while the preamplifier is biased with the voltages used for trapping at $\approx$ 4 K and while the preamplifier is at $\approx$ 4 K. The electrical properties of resistors [146], capacitors [146] and transistors [171] change with temperature (as seen in (§3.5.2)) and so the measurement of the scattering parameters at room temperature is not particularly useful. For example if at $\approx$ 4 K, the $g_{2,1}$ of the preamplifier (at the frequency of a trapped particle) were to determined, the total voltage gain G_V of the axial frequency detection line between the left correction voltage screw connection (Figure 3.3) and the spectrum analyser (depicted in Figure 3.8) could be determined. By knowing this gain G_V and the amplitude of the measured Johnson voltage noise of the tank circuit with the spectrum analyser, the Johnson voltage noise as seen by the trapped electron could be determined, which would allow for an estimation of the axial temperature of the trapped particle.

In order to achieve a reliable measurement with the VNA, a SOLT (mechanical; short, open, load, through) calibration should be applied to correct for the electrical effects of the cabling between the measurement interface (at the input ports of the VNA) and the preamplifier. However, this would require access to the coaxial connectors at the inputs

and outputs of the preamplifier, which would be an engineering challenge in the setup (§3.1) at ≈ 4 K.

A *time domain analysis* [172] technique can be used instead of a mechanical (SOLT) calibration [172] and this was attempted at ≈ 4 K. The *Agilent Fieldfox N9923A* VNA has a time domain analysis capability, where a Fast Fourier Transform is applied to $S_{1,1}(\omega)$ which transforms from $S_{1,1}(\omega)$ in the frequency domain to $c(t)$ in the time domain [172] which mimics *time domain reflectometry* [172]. By observing $c(t)$ in the time domain, reflections corresponding to different artefacts (e.g. impedance mismatches) appear at different times t which correspond to different locations down the line [172]. If it is known which reflections cause which artefacts, a *gating operation* [172] may be applied to remove time domain responses which do not correspond to the device-under-test (e.g. which do not correspond to the preamplifier) [172]. An inverse transform may then be applied to the relevant time domain responses in order to determine $S_{1,1}(\omega)$ (3.4) for the device-under-test only [172].

The voltage biases of the preamplifier affect the input impedance of the preamplifier and so a variation of the voltage biases should change the time domain response $c(t)$ of $S_{1,1}$. The signal-to-noise ratio was not sufficient to distinguish a change in the time domain response $c(t)$ of $S_{1,1}$ and so no reliable gate operation could be applied and so the S-parameters were not determined at ≈ 4 K.

3.5.2 Observing a superconducting transition in the axial resonator

Preamplifier optimally biased for gain at room-temperature

The preamplifier was biased to produce gain while it was at room temperature. The voltage spectrum was measured every five minutes during a cool-down of the Geonium Chip Penning trap experiment from room temperature to ≈ 4 K. The measurement data is shown in Figure 3.9. The Lorentzian curve of the tank circuit is not observable for temperatures lower than approximately 120 K, at which temperature there is a sudden transition to zero gain (most likely as a result of a sudden transition in the gain profile of the preamplifier). The centre frequency ν_0 of the resonance increased from (25.46 ± 0.01)

MHz at room temperature to (25.80 $\pm$ 0.01) MHz at approximately 120 K. This change in ν_0 would probably have been due to the temperature dependencies on the electrical properties of both the axial resonator and of the preamplifier. The plotted temperatures were the mean temperatures of two temperature sensors, where one sensor was close to the second-stage coldhead and one sensor was on the cryogenic trapping chamber (Figure 3.1).

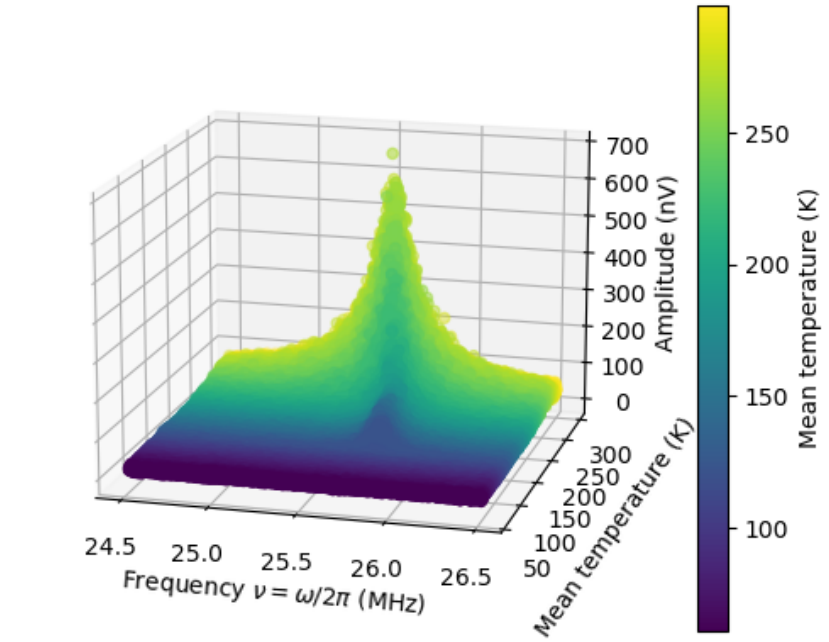

(A)

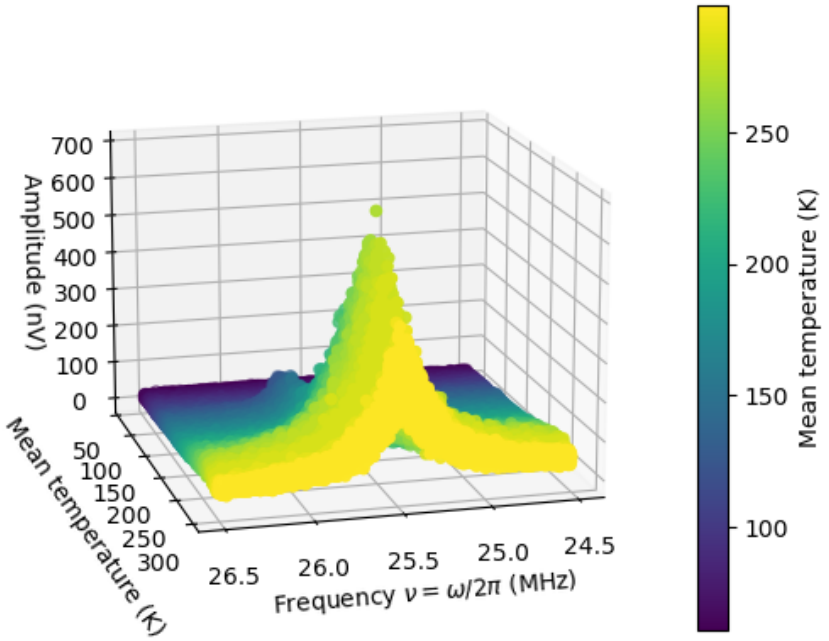

(B)

FIGURE 3.9: Plotting the voltage spectrum of the axial detection circuit as a function of the temperature, while the preamplifier was biased to produce gain while at ≈ 300 K. The data is that measured using the spectrum analyser (with no post-measurement analysis). The difference between Figures 3.9a and 3.9b is the viewing angle - both plots show the same data.

Preamplifier optimally biased for gain at ≈ 4 K

At a later date, the preamplifier was biased to produce gain while it was at ≈ 4 K. The voltage spectrum was measured every five minutes during a cool-down of the Geonium Chip Penning trap experiment from room temperature to ≈ 4 K. The measurement data is shown in Figure 3.10. The tank circuit resonance (§2.2) is only visible for temperatures less than approximately 230 K. Once again, the plotted temperatures were the mean temperatures of two temperature sensors, where one sensor was close to the second-stage coldhead and one sensor was on the cryogenic trapping chamber (Figure 3.1).

A least-squares fit to a Lorentzian function [99] was conducted to each spectrum defined by

$$V(\nu) = V_0 + \frac{A}{\pi} \cdot \frac{\Gamma_{\mathrm{FWHM}}/2}{(\nu - \nu_0)^2 + (\Gamma_{\mathrm{FWHM}}/2)^2}, \tag{3.12}$$

where V_0 is the voltage offset ($\lim_{\nu \to \pm\infty} V(\nu)$) with the same dimensions as V, A is a scalar multiplier with the same dimensions as V Hz, ν_0 is the frequency of the peak of the resonance with the same dimensions as Hz and where Γ_{FWHM} is the full-width-half-maximum with the same dimensions as Hz. Each fit was conducted to 751 data points which were centred around the frequency corresponding to the data point with the highest amplitude. Two example fits are shown in Figure 3.11 for the fitted spectra with the highest and lowest temperatures.

The Q-factor of the axial resonator may be defined using [146, 173]

$$Q = \frac{\nu_0}{\Gamma_{\mathrm{FWHM}}}. \tag{3.13}$$

The four fitting parameters V_0, A, ν_0 and Γ_{FWHM}, along with the Q-factor calculated using (3.13), are shown normalised and on the same axes in Figure 3.12a. The normalisation for quantity x was calculated as $x/x^{(\max)}$, where $x^{(\max)}$ is the maximum value that quantity x achieved. The normalised ν_0 did not clearly change with temperature and so in order to emphasise the temperature dependence of ν_0, the normalised ν_0 was calculated as $(x/x^{(\max)})^{200}$, where the exponent was chosen arbitrarily high.

All the quantities (V_0, A, ν_0, Γ_{FWHM} and the Q-factor) seemed to change rapidly once

a temperature threshold had been reached (see Figure 3.12a) at ≈10 K. The axial resonator is made from pure niobium with a critical temperature $T_{\text{crit}}^{(\text{Nb})} = 9.3$ K [36], which is marked in Figure 3.12a. Therefore, it is likely that the axial resonator started to undergo a superconducting transition at $\approx$ 10 K, assuming that the electrical properties of the cryogenic preamplifier were not also changing simultaneously. During the cool-down and before the system had reached thermal equilibrium at $\approx$ 4 K, there would have been a temperature gradient across the axial resonator and so more of the resonator's volume would have become superconducting as more time elapsed. This plot (Figure 3.12a) shows the normalised parameters as functions of the instantaneous mean temperature at two locations within the cryostat - the experiment had not reached thermal equilibrium at each plotted temperature. Temperature gradients between the coil and the sensors themselves might have contributed to the discrepancy between the theoretical $T_{\text{crit}}^{(\text{Nb})} = 9.3$ K and the observed rapid changes at $\approx$ 10 K.

In order to estimate the Q-factor of the coil once it had become superconducting, a linear least-squares fit and a weighted mean were applied to the data of the Q-factor as a function of time, as shown in Figure 3.12b. Only the blue data points were used for the fit and for the weighted mean. The Q-factor data used in the fit has a non-zero gradient and so in case the axial resonator was still thermalising to $\approx$ 4 K, the Q-factor was evaluated at the final time of 18.92 hours to be (704 $\pm$ 6) (dimensionless). The weighted mean is (683 $\pm$ 36) (dimensionless) where the uncertainty is the standard deviation and the weighted mean is (682.5 $\pm$ 0.7) (dimensionless) where the uncertainty is the standard error. Due to the apparent gradient, it is best to assume that the Q-factor while superconducting is (704 $\pm$ 6) (dimensionless).

It can be seen from Figure 3.12a that for a decreasing mean temperature, the normalised full-width-half-maximum Γ_{FWHM} decreases and the normalised frequency of the resonance peak ν_0 increases, both of which increase the normalised Q-factor (3.13). The changes in these normalised parameters are most significant in the temperature range $T \lessapprox 9.3$ K, which is the temperature range in which the superconducting transition is

expected to occur. The Q-factor may also be defined by [146, 173]

$$Q = \frac{2\pi \cdot \nu_0 \cdot L}{R_{\text{res}}}, \tag{3.14}$$

where R_{res} is the residual surface resistance [146] and L is the effective inductance [173], where it can be seen that $Q \propto 1/R_{\text{res}}$. The resistance R_{res} decreases significantly with decreasing mean temperature as a result of the superconducting transition [146] and so while also considering that $Q \propto 1/R_{\text{res}}$, it would be expected that the normalised Q-factor would increase (significantly) with decreasing mean temperature while $T < 9.3$ K (while superconducting). This is in agreement with both Figures 3.12a and 3.12b. Furthermore, this is in agreement with another observation [168], where a decrease in the temperature corresponded to an increase in the Q-factor of another helical resonator (fabricated from copper rather than Nb) [168], which was also attributed to decreasing resistance (increasing conductivity [168]).

It can also be seen in Figure 3.12a that for a decreasing mean temperature, both the normalised voltage offset V_0 and the normalised scalar multiplier A decrease. In agreement with the changes in the normalised Γ_{FWHM}, ν_0 and Q-factor parameters (discussed above), changes in both the normalised V_0 and normalised A parameters are most significant in the temperature range $T \lessapprox 9.3$ K, which is the temperature range in which the superconducting transition is expected to occur. For a given measurement bandwidth, the Johnson voltage noise across a resistor with resistance R is proportional to the square-root of the resistance R of the resistor [101] and also to the square-root of the temperature T of the resistor [101]. The resistance $R = R_{\text{res}}$ of the coil decreases significantly with decreasing mean temperature as a result of the superconducting transition [146] and so it would be expected that the normalised V_0 and A would decrease (significantly) with decreasing mean temperature for $T < 9.3$ K (while superconducting). This is in agreement with Figure 3.12a.

Some conclusions may be drawn. Firstly, the Q-factor while superconducting is (704

$\pm$ 6) (dimensionless). Secondly, all the normalised Γ_{FWHM}, ν_0, Q-factor, V_0 and A parameters undergo significant changes in the temperature range $T \lessapprox 9.3$ K, which is indicative of a superconducting transition. These changes can be explained using (3.14) and by considering the Johnson noise [101].

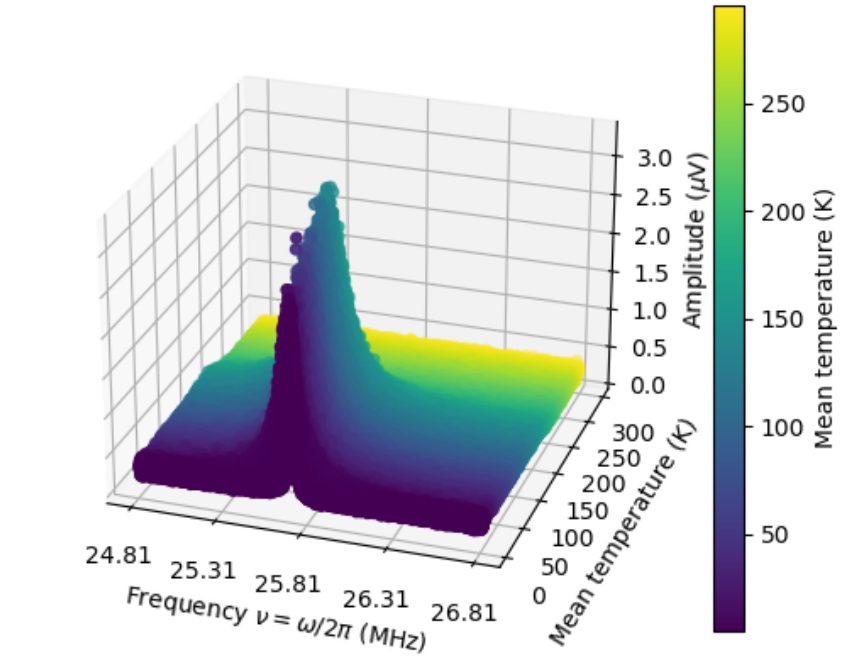

(A)

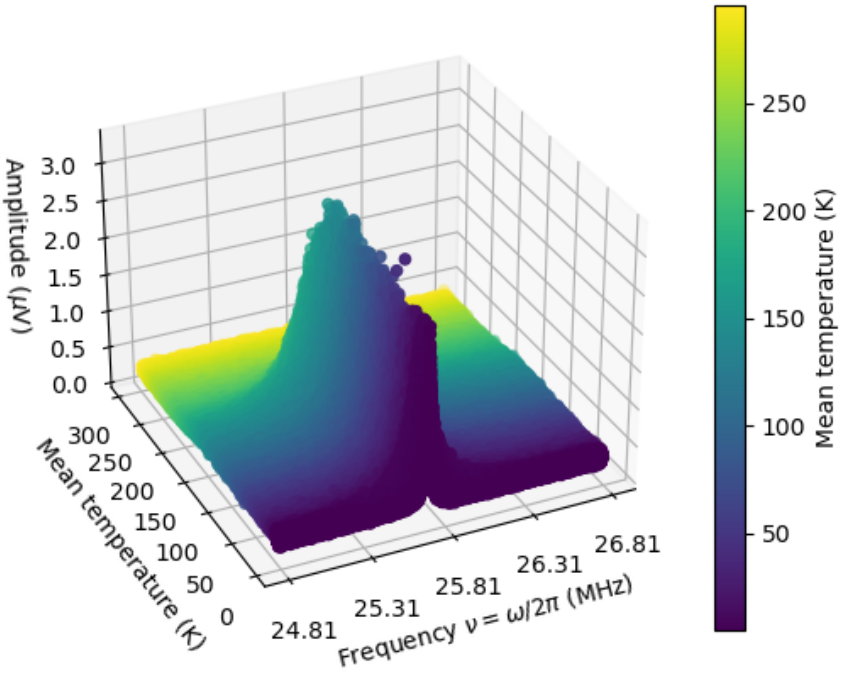

(B)

FIGURE 3.10: Plotting the voltage spectrum of the axial detection circuit as a function of the temperature, while the preamplifier was biased to produce gain while at $\approx$ 4 K. The data is that measured using the spectrum analyser (with no post-measurement analysis). The difference between Figures 3.10a and 3.10b is the viewing angle - both plots show the same data.

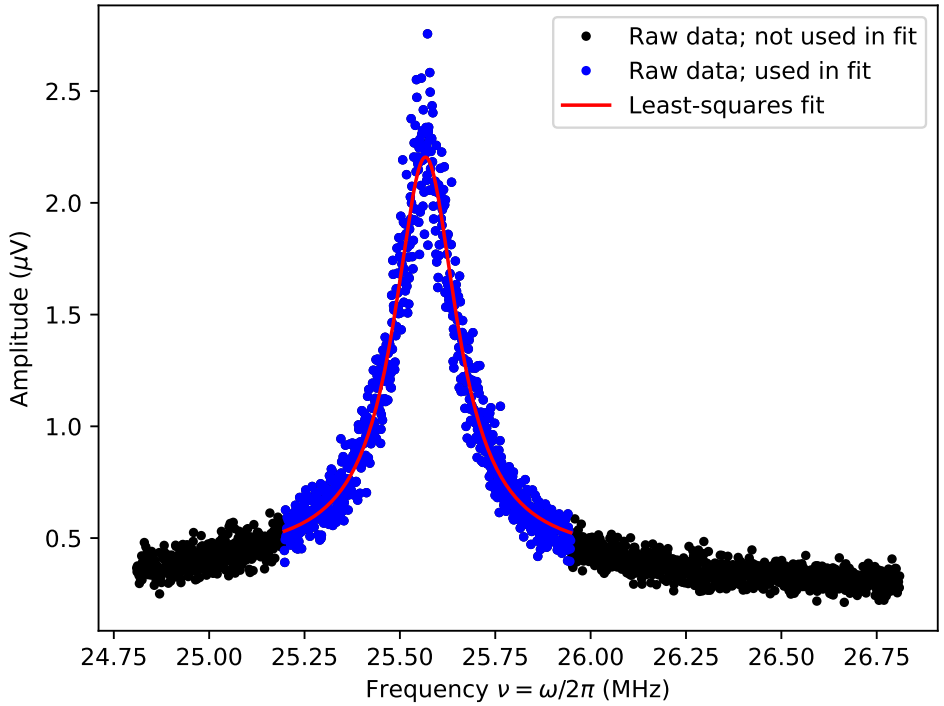

(A) A fit to the spectrum taken at a measured (mean) temperature of 219.10 K. The resonator was not superconducting.

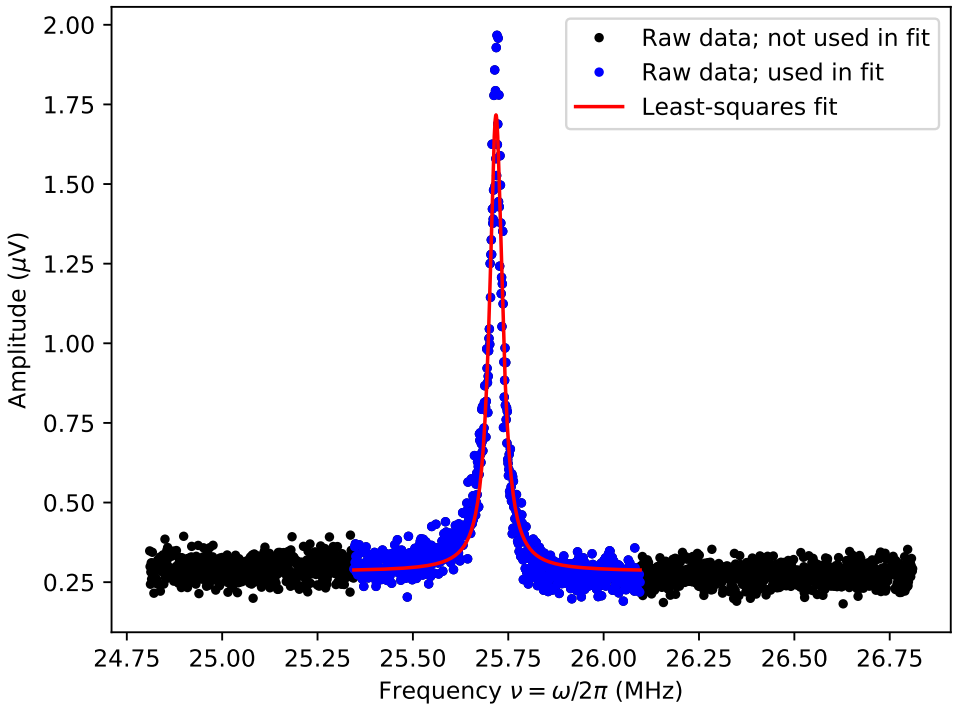

(B) A fit to the spectrum taken at a measured (mean) temperature of 4.94 K. The coil was superconducting.

FIGURE 3.11: Two fits (3.12) to the raw spectra, where Figures 3.11a and 3.11b show the fits conducted at the highest and lowest measured (mean) temperatures respectively.

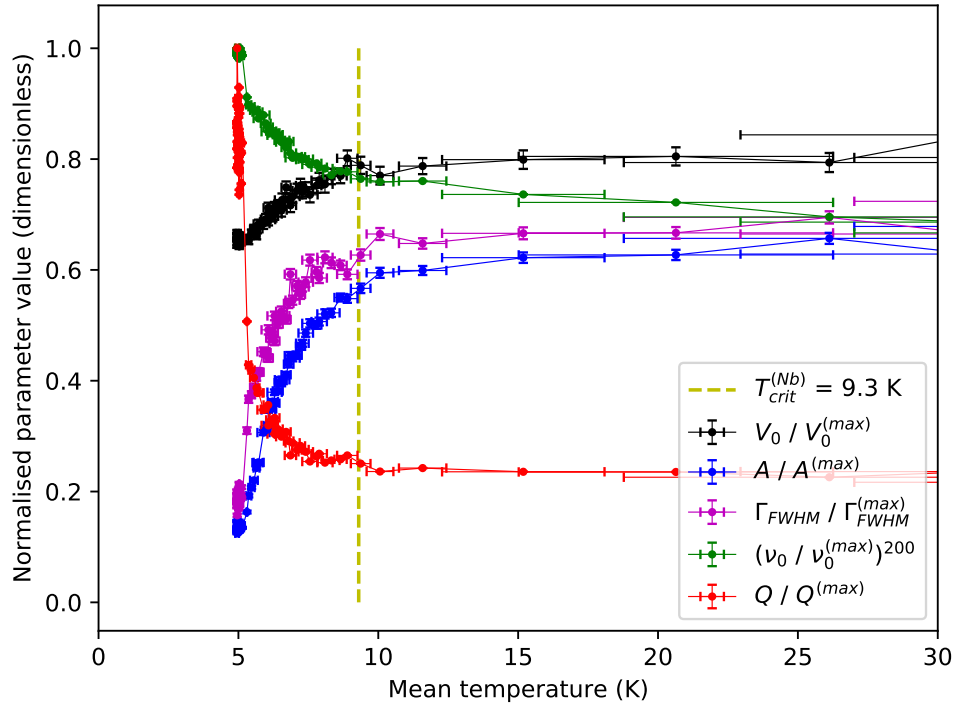

(A) Plots of the normalised parameters, which all start to undergo changes at approximately 10 K. The error bars show the standard deviations.

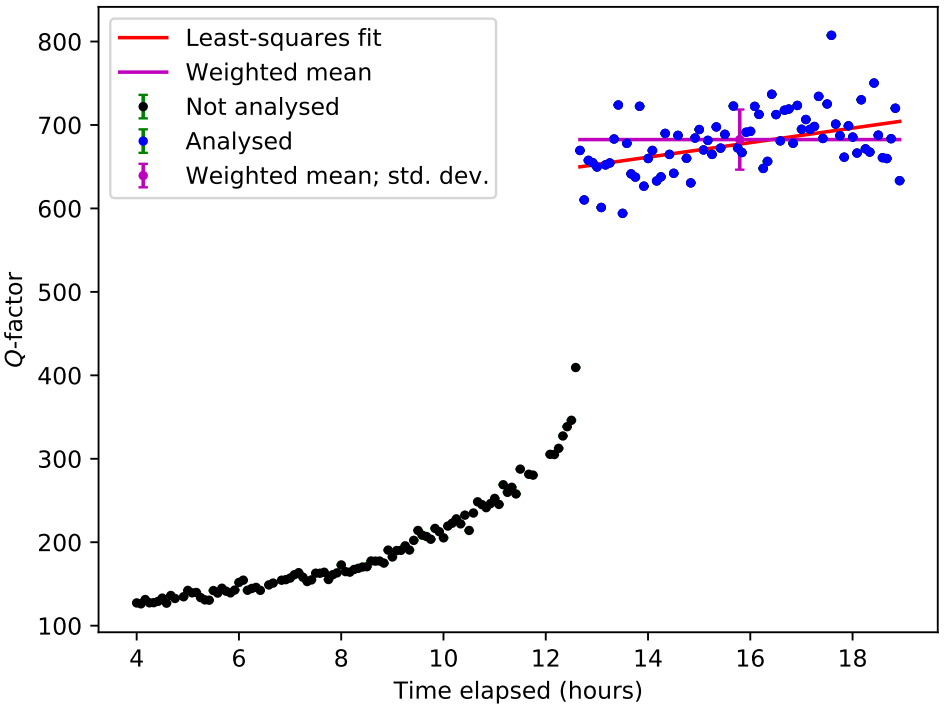

(B) Estimating the Q-factor. The error bars show the standard deviations. The analysis was only conducted to the superconducting region (blue).

FIGURE 3.12: Investigating the superconducting transition.

Chapter 4

A photoelectric characterisation of the cryogenic trapping chamber

The loading of electrons into Penning traps has typically used thermionic emission [174, 175], or field emission points (electron guns) [10, 13, 176]. Loading electrons into the Geonium Chip Penning trap via thermionic emission would be impractical, because of the required high temperatures (e.g. 950 °C to 1200 °C [175]). In particular, this would risk causing a quench of the magnetic field source, due to there only being a low cooling power from the second-stage coldhead ($\approx$ 0.5 W at $\approx$ 4 K [36]). Loading electrons into the Geonium Chip Penning trap with a field emission point would require high voltages (e.g. 1 kV [176]) which would also be impractical due to the heat load of high-voltage cabling and the risk of arcing within the small volume of the experiment. Therefore, a photoelectric [177] loading technique has been developed which has previously been introduced in the theses [32, 36, 146]. This chapter discusses characterisations of the cryogenic trapping chamber (§3.4) with photoelectric measurements, which are useful for modelling the loading technique. This chapter also discusses some applications of photocurrent measurements both while at room temperature and while at $\approx$ 4 K.

The research group has implemented two UV sources. The first was an *Ocean Optics* LED source which outputs 240 nm wavelength light at 24.2 μW, which has since been replaced by a higher power *Hamamatsu L10290* deuterium source which outputs wavelengths as low as 200 nm. No measurements included in this thesis were undertaken

with the *Ocean Optics* LED source. An optical fibre is used to transmit the UV light from the *Hamamatsu* UV source to an *Avantes COL-UV/VIS* collimating lens, which is in contact with the sapphire window of the cryogenic trapping chamber (Figures 3.1 and 3.2). The UV light passes through the window and hits a target on a wall of the chamber. The chamber has a cuboid-shape internal volume of $(20\text{ mm})^3$. The wall with the target is in the plane $z = -10$ mm and ideally, the centre of the target is positioned with a height y_0 (2.6) and also with position $x = 0$. The UV light strikes the target and photoliberates [177] electrons from the surface of the target (subsequently denoted *photoelectrons* and alternatively *primary* electrons (§6.1)), which then follow the magnetic field lines along $\hat{u}_z$ towards the trapping volume (around the equilibrium trapping position $\vec{r}_0 = (0, y_0, 0)$ (§2.1.1)). The most recent iteration of the experiment features a $(3\text{ mm})^2$ square target made with gold leaf, which also acts as a high-voltage (up to 300 V) photocathode to give the primary electrons enough additional kinetic energy to ionise rest gas around $\vec{r}_0$. In all measurements other than in (§4.7.4), the UV target was electrically grounded.

It is very important to note that the photocurrent is very sensitive to minor changes in the apparatus setup, for example it is sensitive to small differences in the alignment of the UV fibre, to changes in the target and also to changes in any electronic filters in the measurement apparatus. Therefore, no photocurrent measurement in any section should be explicitly compared to any other. However, in (§4.4.2), it is demonstrated that normalising one photocurrent measurement to another may be valid in some circumstances.

4.1 An introduction to a typical photocurrent measurement

Photocurrents in the Geonium Chip Penning trap tend to be very small (on the orders of 1-100 picoamps) and so in order to reliably determine the photocurrent, the photocurrent measurements have been automated. The *Hamamatsu L10290* UV source has a moveable shutter which when open/closed, does/does not allow UV to enter the fibre. This shutter and also a *Keithley 6458* picoammeter are also regularly controlled via *LabVIEW*.

Most of the *LabVIEW* programs work in a similar way. The photoelectrons are collected through a collector with voltage bias V_{col} (assuming a grounded target) and V_{col} is set manually and does not change during a photocurrent measurement. The *dark current* $I_{\text{UV off}}$ is defined as the measured electrical current while UV light is absent from the target. Frequently, the dark current is non-zero (electrical noise) and so the photocurrent I_p should be determined as the difference between the currents $I_{\text{UV on}}$ and $I_{\text{UV off}}$, where $I_{\text{UV on}}$ is the measured electrical current when the UV light is present at the target, which may be written

$$I_p = I_{\text{UV on}} - I_{\text{UV off}}. \tag{4.1}$$

Firstly, while the UV shutter is closed (while no UV light is reaching chamber) the picoammeter is queried for N_{bunch} current measurements of $I_{\text{UV off}}$. Then, the UV shutter is opened (allowing UV light to reach the chamber) and the picoammeter is queried for another N_{bunch} current measurements of $I_{\text{UV on}}$. Subsequently, the UV shutter is closed and this is repeated for N_{pairs} pairs (in total) of N_{bunch} measurements of $I_{\text{UV off}}$ and $I_{\text{UV on}}$. Typically, $N_{\text{bunch}} = 50$ and $N_{\text{pairs}} = 5$. Then, linear least-square fits are conducted (within *LabVIEW*) to each of the two sets $I_{\text{UV off}}$ and $I_{\text{UV on}}$ as functions of time and the photocurrent is stated as the difference in the y-intercepts, which is analogous to (4.1) but ignores the effects of drifts (gradients). This is only valid if the gradients of the two fits are similar. In each set of N_{bunch} currents, the first N_{skip} values are not used in the fits, because these data can be noisy or contain artefacts due to running averages. Typically, $N_{\text{skip}} = 15$. Therefore, typically there are $N_{\text{bunch}} \cdot N_{\text{pairs}}$ measurements for both $I_{\text{UV off}}$ and $I_{\text{UV on}}$ with $(N_{\text{bunch}} - N_{\text{skip}}) \cdot N_{\text{pairs}}$ measurements used in each of the two fits.

One example using the typical values of $N_{\text{bunch}} = 50$, $N_{\text{pairs}} = 5$ and $N_{\text{skip}} = 15$ is shown in Figure 4.1. This photocurrent was measured inside the cryostat (§3.1). In this example, the y-intercepts of $I_{\text{UV off}}$ and $I_{\text{UV on}}$ (respectively) are (-747.9 ± 0.6) pA and (-919.7 ± 0.6) pA, which gives a photocurrent of (-171.9 ± 0.8) pA. This method is only valid if the gradients are similar and in the example in Figure 4.1, the gradients of $I_{\text{UV off}}$ and $I_{\text{UV on}}$ (respectively) are (81 ± 5) fA/s and (54 ± 5) fA/s, which are reasonably similar in absolute terms, relative to the y-intercepts. Due to the biasing of the collector

V_{col} and the setup of the ammeter, the measured currents are negative in this example, as is nearly always the case when collecting electrons. Sometimes in this thesis, in order to make data easier to interpret, the polarity of the plotted/stated photocurrent is reversed, but where the polarity has been reversed in this way, this is stated.

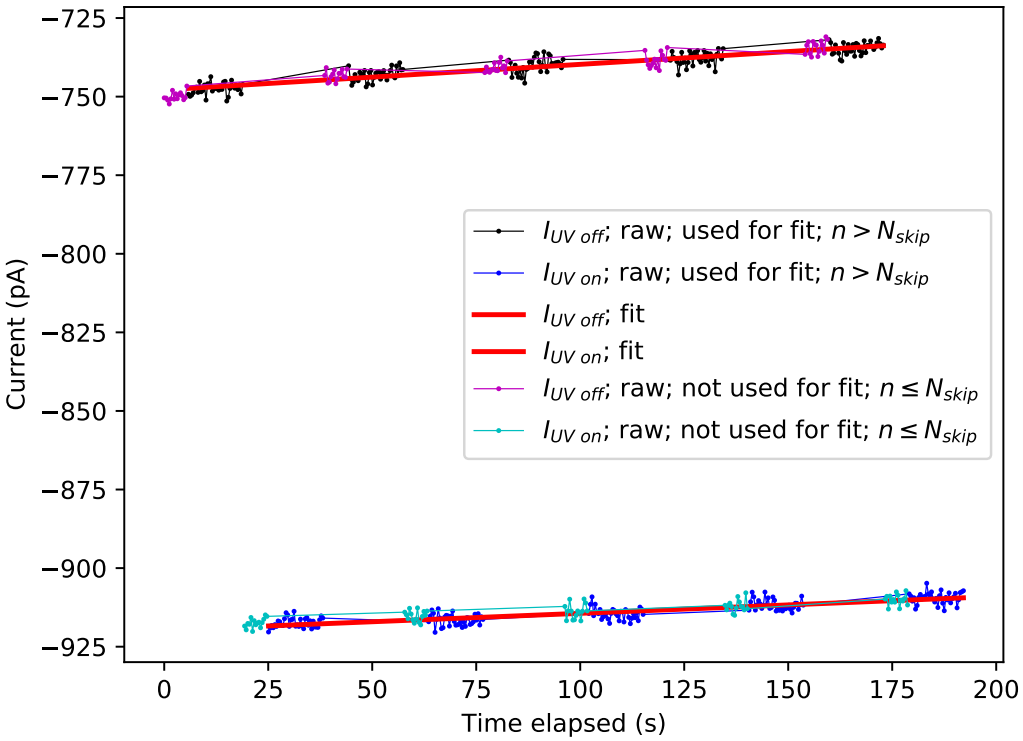

FIGURE 4.1: The analysis of the raw current measurements in a typical measurement. The photocurrent is estimated using the difference in the y-intercepts of $I_{\text{UV off}}$ and $I_{\text{UV on}}$ (black and dark blue respectively). The first $N_{\text{skip}} = 15$ data points (magenta and cyan) in each of the $N_{\text{pairs}} = 5$ pairs of $N_{\text{bunch}} = 50$ are not used in the fit. The fits are shown in red.

4.2 Investigating different UV targets

In order to maximise the number of electrons liberated per unit time (the *photocurrent*), the UV target was optimised. The two most significant factors to optimise are the material (e.g. the chemical element which affects the work function of the target) and the surface

smoothness (although possibly negligible [178]), which affects the reflectivity of the target and the number of interactions before the UV is transmitted away from the target.

A target characterisation setup was built by Dr Jonathan Pinder, which could mount one target at a time. An electrically grounded piece of copper was used as a mounting board for each target-under-test. An electrically conducting (but isolated from the mounting board) stainless steel grating was mounted over the target, to act as a collector for any liberated photoelectrons. This setup was installed inside a vacuum chamber, which was evacuated to approximately 10^{-6} mBar while the measurements were conducted. One optical fibre was used to transmit UV from the *Hamamatsu L10290* UV source to a vacuum flange with an SMA fibre coupler. The other side of the flange was not terminated (no optics were installed) and the UV was aligned with the target-under-test. This setup is depicted in Figure 4.2.

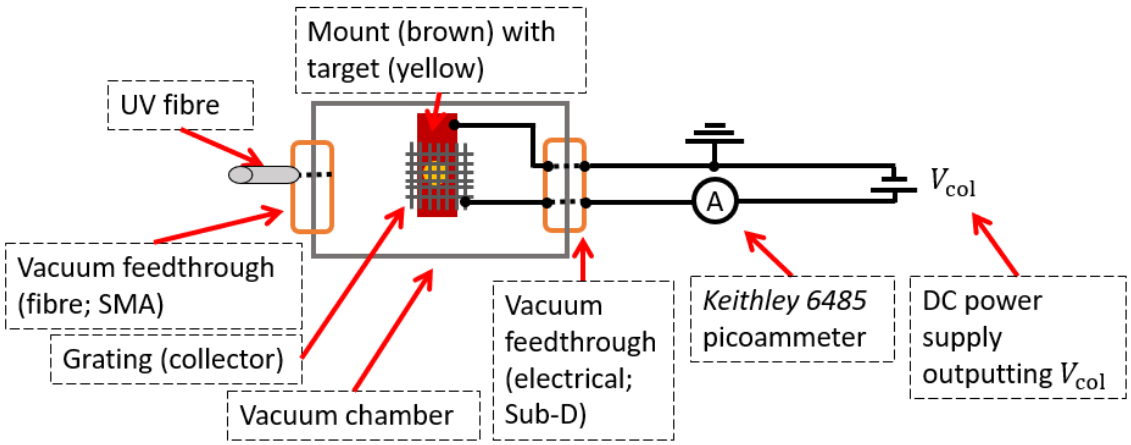

FIGURE 4.2: A general overview of the experimental setup for the determination of the photocurrents produced by a range of targets.

In order to photoliberate electrons from a surface with work function Φ, the incident photons require energies E_γ of at least Φ, which gives a maximum kinetic energy $E_{k,e}$ to the photoelectrons of $E_{k,e} = E_\gamma - \Phi$. A UV photon with the highest energy from the *Hamamatsu L10290* deuterium source with a wavelength of 200 nm has an energy of $E_\gamma = 6.2$ eV and so the highest usable work function would theoretically be $\Phi = 6.2$ eV. However, practically a material with lower Φ should be used in order for the photoelectrons to gain some kinetic energy. Several different targets with possibly low

TABLE 4.1: A table of results for the different target materials. The targets are listed from top to bottom in the chronological order of which their measurements were taken. The stated uncertainties were propagated from the uncertainties in the measured currents while the UV was off/on. The polarities of the photocurrents have been reversed.

Target	Highest photocurrent (pA)
Gold leaf	44 ± 3
Silver paste	3 ± 3
Polished copper, subsequently gold-plated	0.8 ± 0.3
Matt copper, subsequently gold-plated	4 ± 2
Graphite	3 ± 1
Aluminium foil, matt side	0
Aluminium foil, shiny side	0
Gold leaf, repetition	37 ± 3
Microfabricated chip, gold side	8 ± 6
Copper	14 ± 3

enough Φ [179] were investigated: gold leaf, silver paste, two gold plated printed circuit boards (one previously polished and the other left unpolished/matt), a graphite spray, both sides of (grocery-grade) aluminium foil, a prototype microfabricated Geonium Chip with a highly reflective gold surface [36] and some copper.

A *Keithley 6485* picoammeter was used to measure the photocurrent collected at the grating, for a variety of collector bias voltages V_{col} (between the collector and the grounded target). A *LabVIEW* program (§4.1) was used to measure the current through the collector grating with $N_{\text{skip}} = 0$, $N_{\text{bunch}} = 50$ and $N_{\text{pairs}} = 5$, however the photocurrents were instead estimated manually from the current data. This was repeated for different values of the collector bias voltage V_{col} and the highest measured photocurrent is shown in Table 4.1, for each of the targets.

As can be seen from Table 4.1, the gold leaf target produced the highest photocurrent at approximately 40 pA - nearly three times as high as the second-best target (copper). It is interesting to consider the two pieces of gold plated copper, where a matt/rough

surface produced a much higher photocurrent than a smooth (unpolished) surface. The gold leaf has even less effective reflectivity (it has a rough/disordered surface) than the gold-plated matt copper and gives a higher-still photocurrent. These conclusions are most likely due to the effective surface area being higher for a less smooth surface, with an increased likelihood of a reflected UV photon to contact another piece of the target. Also, the quantum efficiency of photoliberation is proportional to $(1 - R(\omega))$ where $R(\omega)$ is the optical reflectivity [180–182] and so an increase in the surface roughness could have resulted in an increase in the measured photocurrent, however experimental results [178] suggest that surface roughness does not significantly effect the photocurrent. It would have been expected for the microfabricated chip with very high surface smoothness [36]) to have the lowest photocurrent, however it did produce a reasonably high photocurrent, possibly due to gold producing a high photocurrent and the microfabricated nature and chemical inertness causing low surface contamination.

This investigation was one of the first photocurrent investigations to be conducted. The experience gained in future photocurrent investigations would recommend that a much higher collector bias V_{col} should have been used and that the stated photocurrents (Table 4.1) should all have been measured with the same V_{col} and calculated using more robust statistical methods. However, the measurements were reliable enough to achieve their purpose of recommending a target and the gold leaf target produced a significantly larger photocurrent than the other targets. One additional benefit is that gold should require less cleaning than alternative cathode materials (§4.7.1). The most recent method developed by Dr Albert Uribe [32] used to adhere gold leaf to the chamber wall is to i) place some distilled water (a solvent) on the chamber wall, then ii) place some gold leaf on the surface of the droplet and then iii) wait until the solvent has evaporated. This causes adhesion via the *London Dispersion Force*, which survives evacuations with a turbopump and also survives thermal cycles between ≈ 4 K and room temperature.

A dimpled/pitted target was manufactured by Dr Alberto Jesús Uribe Jiménez by pitting a thin sheet of copper and then subsequently gold-plating it [32]. This target was investigated and used for example in (§4.3.2). Also investigated was the use of a

transmission photocathode [183]. This is where instead of UV light liberating electrons from a target, UV light passes through a gold-plated window into the cryogenic trapping chamber. If the coating of gold is sufficiently thin (≈ 1 μm for a GaAs-Cs-O transmission photocathode [183]), then electrons may be liberated from the gold coating and travel in the same direction as the incident UV light, towards the trapping volume. It is predicted that the optimal thickness for a gold transmission photocathode is between 15 and 25 nm [184]. In order to investigate this, the window in the cryogenic chamber was replaced with an unprotected gold mirror (*PF10-03-M03* from *ThorLabs*) for trial as a transmission photocathode, however no photocurrent was discernable. If constructed purely from copper, the mesh (§3.4) might eventually also be used as a transmission photocathode [185], however this would not be practical for the creation of secondary electrons (§6.1), because the mesh must remain electrically grounded to form the *boxed CPW-trap* [22].

4.3 Investigating the relation between the photocurrent and the bias voltage of the collector

As the voltage bias V_{col} of the collector increases, electrons of higher energies should be collected and so the measured photocurrent should increase. The relation between the photocurrent and V_{col} thus gives information about the kinetic energy of the photoelectrons. Two measurements of the photocurrent as a function of the collector bias voltage V_{col} were undertaken. The first measurement in (§4.3.1) was undertaken to characterise the photoelectric effect and to verify the electrostatic model of the trap. The second measurement in (§4.3.2) was undertaken to determine at which V_{col} the photocurrent saturates (i.e. stops increasing with increasing V_{col}) in order to determine a sufficient V_{col} for future measurements.

4.3.1 Measurement set 1: verifying electrostatic models

In order to measure the photocurrent, a setup was constructed which is depicted in Figure 4.3. This setup was also used to investigate the effect of the mesh as discussed in (§4.6).

A printed circuit board with one large electrode was fabricated and subsequently gold plated by Dr Jonathan Pinder, which also featured a via through the underside copper pour and through the substrate, so that a DC wire could be soldered to the underside of the electrode. The *Keithley 6458* picoammeter was connected in series between this DC wire and the chamber (electrically grounded). The board was sealed by Dr Jonathan Pinder to the cryogenic trapping chamber using an indium wire gasket (§3.4). The mesh was not installed in the chamber prior to this sealing. The chamber was evacuated to a pressure of approximately 1.6×10^{-6} mBar. The UV was incident through the window, toward a gold leaf target.

The voltage bias V_{col} of the collector was adjusted manually, but the photocurrent measurements were controlled with a *LabVIEW* program (§4.1), with $N_{\text{bunch}} = 40$ and $N_{\text{skip}} = 15$, but the number N_{pairs} was different for different V_{col}.

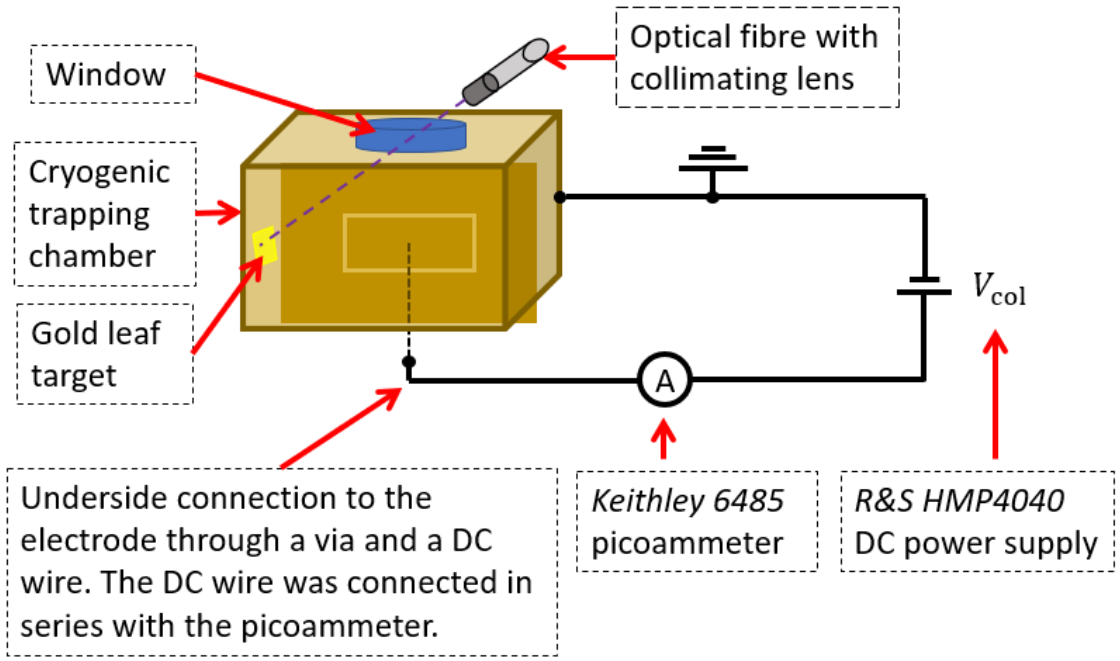

(A) Some simplified circuit schematics.

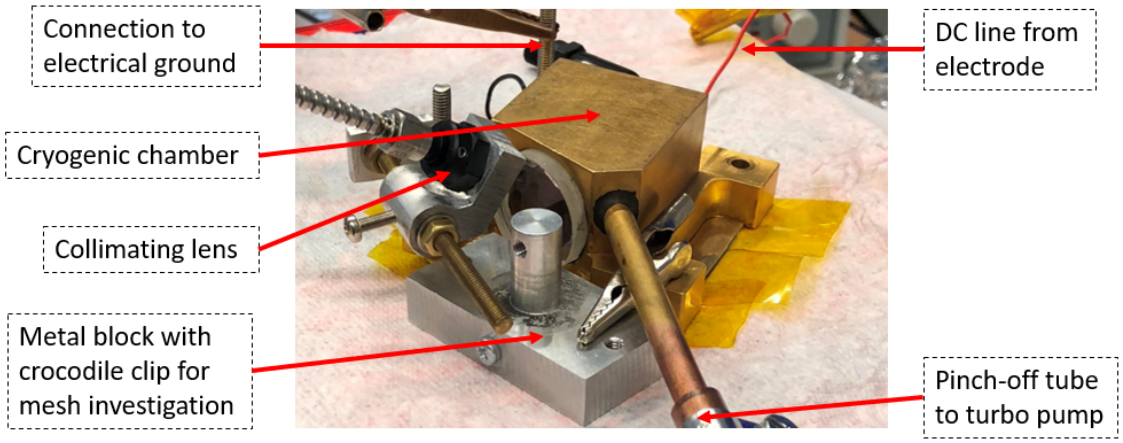

(B) A photograph of the setup.

FIGURE 4.3: Some circuit schematics and a photograph of the setup for determining the photocurrent dependence on the collector bias V_{col}. This setup was also used to determine the photocurrent dependence on the pressure (§4.4).

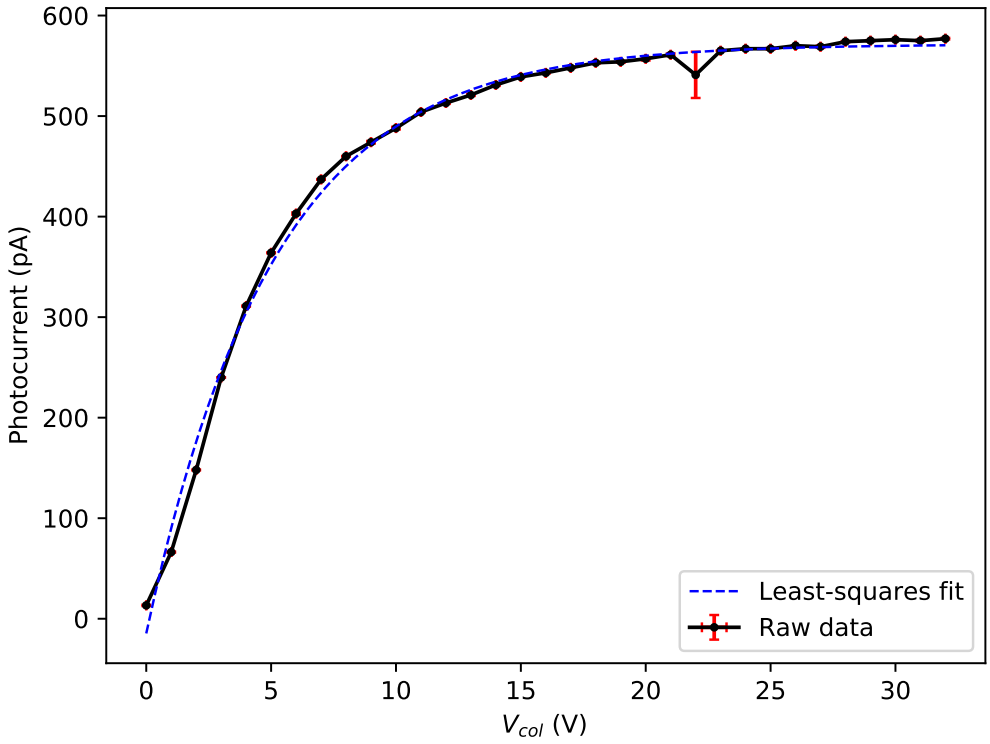

FIGURE 4.4: A plot of the photocurrent as a function of the collector bias voltage V_{col}. A least-squares fit to an exponential decay $(1 - \exp(f(V)))$ is also shown.

The plot of the photocurrent as a function of V_{col} is shown in Figure 4.4. A fit to an exponential function was also conducted and is also shown in the figure.

Dr José Verdú conducted a numerical simulation of the photoelectric effect in the cryogenic chamber, which could be compared to the measurement. The simulation aimed to determine the probability $P_{\text{collected}}$ of a released electron striking the collector for each collector bias voltage V_{col}, under a variety of conditions. This is analogous to the measurement (Figure 4.4) because the photocurrent for a given V_{col} is proportional to the probability $P_{\text{collected}}$ of collection.

For a given photon energy E_γ, the simulation modelled the kinetic energy distribution of the photoelectrons as a *microcanonical ensemble*, i.e. the sum of the three energy components (in Cartesian space) was equal to the difference between E_γ and the work function

Φ; $E_k^{(x)} + E_k^{(y)} + E_k^{(z)} = E_\gamma - \Phi$. For a given photon energy E_γ, the simulation took into account all values of $E_k^{(x)}$ and $E_k^{(y)}$, with $E_k^{(z)}$ being fixed by the microcanonical ensemble constraint. The UV beam has finite radius and so this whole simulation (to determine the relation between $P_{\text{collected}}$ as a function of V_{col} for all $(E_k^{(x)}, E_k^{(y)})$) was undertaken for several liberation heights y_{lib} (the y position at which the electron was liberated from the target). The whole simulation so far was repeated for several energies E_γ based upon the spectral distribution in the manufacturer's data-sheet for the UV source. The entire numerical simulation for each of the energies E_γ was equally weighted to produce a mean theoretical plot of $P_{\text{collected}}$ as a function of V_{col}. The simulation was limited in that it was always assumed that the photoelectrons were liberated from $x_{\text{lib}} = 0$ and also in that the UV beam intensity was homogeneous rather than Gaussian.

The following ideas in the remainder of this section (§4.3.1) are based on those of Dr José Verdú. This simulation has very good agreement with the measured data in Figure 4.4, as can be seen in Figure 4.5. This agreement is significant, because the assumptions used in the simulation have to some extent been verified.

1. For example, the electron trajectories were simulated using electrostatic potentials which were modelled using the Green's function method (§3.2). This Green's function method is also used in other simulations, for example to simulate trapped electrons and to simulate the loading of electrons. Therefore, the results from these other simulations should be reliable. Although the measurement (Figure 4.4) did not include a mesh (which would have been required for the *boxed CPW-trap* [22]), the simulation by Dr José Verdú only assumed an open trap (infinite plane) which did not require an electrically grounded cube either. It is the model of the *boxed CPW-trap* which is used to simulate trapped electrons and the loading of electrons, but the computation time would have been much longer than for the open trap.

2. Also verified is the model of the photoelectrons acting as a microcanonical ensemble, which suggests that the energy is randomly distributed in $E_k^{(x)}$, $E_k^{(y)}$ and $E_k^{(z)}$.

This energy distribution has implications for the loading of the trap, where the electrode voltages need to take into account energy-dependant frequency shifts due to trap anaharmonicities and inhomogeneities (§2.1.2).

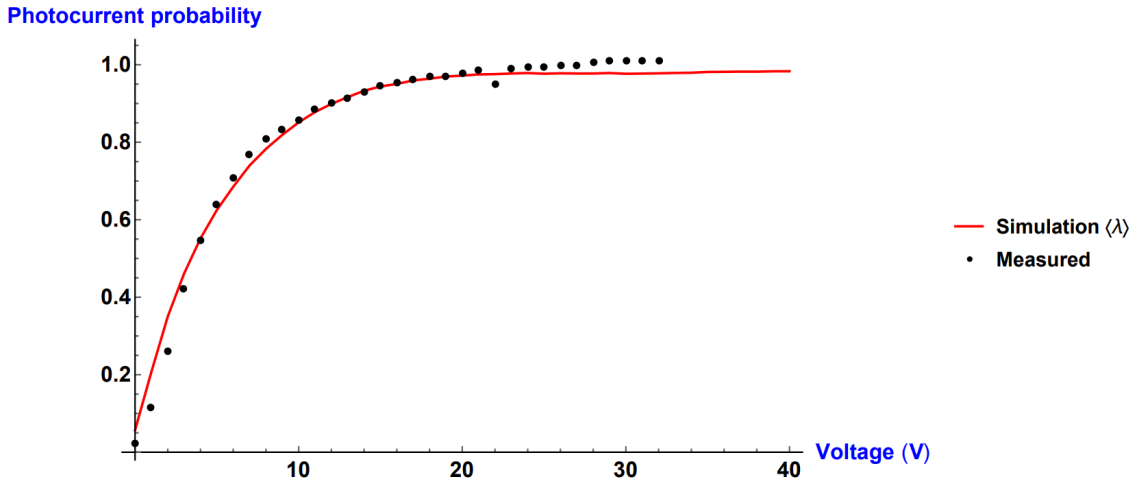

FIGURE 4.5: The result of the numerical simulation (red; continuous) is shown along with a normalisation of the measured data (black; scatter). The plot is from the simulation of Dr José Verdú.

4.3.2 Measurement set 2: investigating the saturation of the photocurrent

The dependence of the photocurrent on the voltage bias V_{col} applied to the collector was investigated once again, in order to determine an appropriate V_{col} for future measurements. This was done by identifying at which V_{col} the majority of the liberated photoelectrons had been collected.

A setup was constructed where the cyrogenic vacuum chamber (§3.4) was suspended above a table in a clamp and where the pinch-off tube was connected to an *Agilent TPS-Flexy* turbopump. The cryogenic chamber had been evacuating for approximately eight weeks (no bake-out had been applied) and the pressure was $(5.7 \pm 0.1) \times 10^{-8}$ mBar. The pressure was measured using a *Varian FRG-700* combined-Pirani-inverted-magnetron pressure gauge which was connected between the turbopump and the pinch-off tube of the cryogenic trapping chamber. The voltage bias V_{col} was monitored with a *Keithley 2110* digital multimeter. Rather than using a gold leaf target, dimples/pits were introduced

to a thin copper sheet which was subsequently gold plated by Dr Alberto Jesús Uribe Jiménez [32]. The photoelectrons were collected through all five electrodes of the Geonium Chip, which were shorted together with copper tape (with an electrically conducting adhesive) at the voltage screw connections (§3.2) of the chip. Some circuit schematics and a photo of the setup are shown in Figure 4.6.

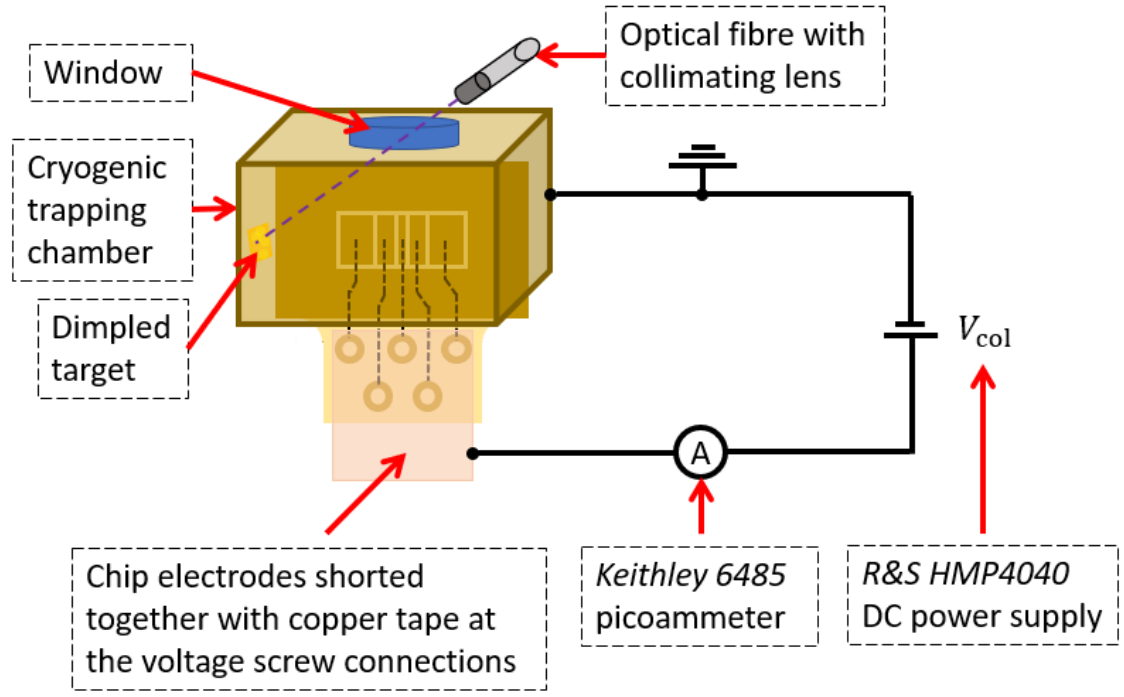

(A) Some simplified circuit schematics.

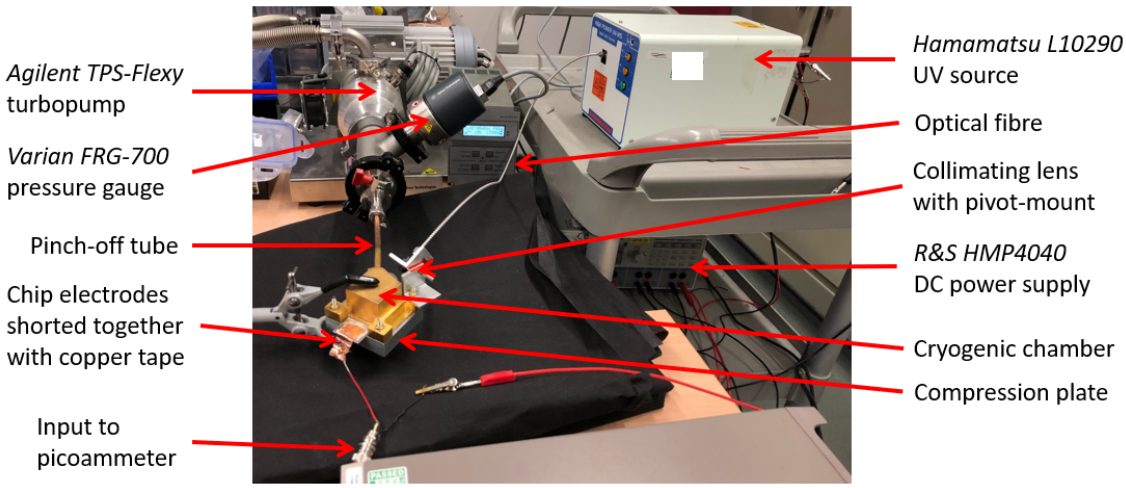

(B) A photograph of the setup.

FIGURE 4.6: Some circuit schematics and a photograph of the setup for determining the photocurrent dependence on the collector bias V_{col}. This setup was also used to determine the photocurrent dependence on the pressure (§4.4).

The photocurrent measurements were controlled with a *LabVIEW* control program. Firstly, the voltage bias V_{col} was measured, then six current values $I_{\text{UV off}}$ were measured, then the UV shutter was opened, then another six current values $I_{\text{UV on}}$ were measured, then V_{col} was measured a second time. The first three current values in each $I_{\text{UV off}}$ and $I_{\text{UV on}}$ were neglected and independent linear least square fits were conducted to each of the remaining two datasets of three values, where the difference in the y-intercepts were saved as the photocurrent value for that V_{col}. This is similar to the *LabVIEW* program discussed in (§4.1), which would be described with $N_{\text{bunch}} = 6$, $N_{\text{pairs}} = 1$ and $N_{\text{skip}} = 3$. Following this, the UV shutter was closed and after a user-defined delay this was repeated, to generate a plot of the photocurrent as a function of the measured voltage bias V_{col}.

The measurement data are shown in Figure 4.7. In the laboratory, the DC power supplies with the highest precision and temporal stability are the *Rohde and Schwarz HMP4040* power supplies, which can output up to 32.05 V (nominal) from each of the four channels. It can be seen from Figure 4.7 that for collector bias voltages V_{col} of greater than 32.05 V, there is only a marginal increase in the measured photocurrent for an increase in V_{col}. Therefore, for measurements which only require a fixed V_{col}, a 32.05 V bias of the collector is sufficient, which can be provided by the *HMP4040*. A fit to an exponential function is also included to demonstrate reproducibility with the first measurement of the photocurrent as a function of V_{col} in (§4.3.2), but the optimal fit parameters have not been included because they are of no further use.

4.4 Investigating the relation between the photocurrent and the pressure

In (§4.4.1), the relation between the photocurrent and the pressure is shown measured twice and the plots may be used as calibration curves to transform a photocurrent value into one of pressure. In (§4.4.2), an application of this transformation is used, whereby it is shown that in a pinched-off cryogenic trapping chamber (§3.4) at room temperature

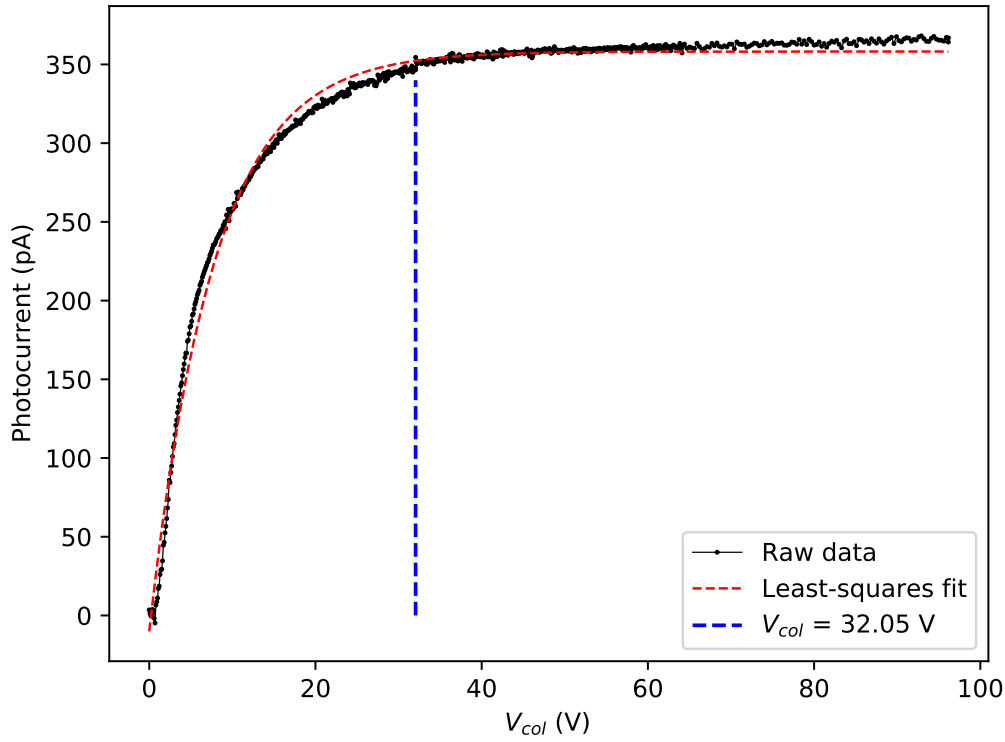

FIGURE 4.7: A plot of the photocurrent (with reversed polarity) as a function of the collector bias voltage V_{col}. A least-squares fit to an exponential decay $(1 - \exp(f(V)))$ is also shown, along with a fiducial marker line at 32.05 V.

and without prior baking-out, the outgassing of water occurs to significantly increase the pressure.

4.4.1 Determining the relation between the photocurrent and the pressure

As discussed in (§3.4), the pressure is inversely linked to the lifetime of trapped electrons. Therefore, electrons in a photocurrent should also be affected by pressure in a similar way, for example due to collisions with rest gas. Therefore, an investigation was conducted to measure the photocurrent dependence on the pressure.

After having measured the photocurrent dependence on the bias voltage (§4.3.2), the setup was amended so that the *Keithley 2110* digital multimeter could be used to measure

the pressure, rather than the collector bias voltage V_{col}. A *Varian FRG-700* combined-Pirani-inverted-magnetron pressure gauge (with useful range between atmosphere and 5×10^{-9} mBar) was connected between the turbopump and the pinch-off tube of the cryogenic trapping chamber. The pressure gauge output a voltage which was monitored with the *Keithley 2110* digital multimeter, which was transformed into a pressure value using a formula provided by the manufacturer. Rather than using a gold leaf target, the dimpled target [32] (§4.3.2) was used. The photoelectrons were collected through all five electrodes of the Geonium Chip, which were shorted together with a copper tape (with an electrically conducting adhesive) at the voltage screw connections (§3.3) on the chip. Some circuit schematics and a photo of the setup are shown in Figure 4.6, where the same setup was also used in (§4.3.2) to measure the photocurrent as a function of V_{col}. The electrodes were biased with +32.05 V (nominal) and the chamber (including the target) were grounded. Some circuit schematics and a photo of the setup are shown in Figure 4.6, in (§4.3.2).

The *LabVIEW* program was also amended (from the program mentioned in (§4.3.2)), so that the measured voltage from the pressure gauge was converted into a pressure value, but the photocurrent measurement method was not amended. Firstly, the program determined the pressure, then measured six current values $I_{\text{UV off}}$, then opened the UV shutter, then measured another six current values $I_{\text{UV on}}$, before finally measuring the pressure a second time. The first three current values in each $I_{\text{UV off}}$ and $I_{\text{UV on}}$ were neglected and independent linear least square fits were conducted to each of the remaining two datasets of three values, where the difference in the y-intercepts was saved as the photocurrent value for the mean of the two pressures. This is similar to the *LabVIEW* program discussed in (§4.1), which would be described with $N_{\text{bunch}} = 6$, $N_{\text{pairs}} = 1$ and $N_{\text{skip}} = 3$. Following this, the UV shutter was closed and after a user-defined delay this was repeated, to generate a plot of the photocurrent as a function of the measured pressure.

Two sets of measurements were undertaken. The first dataset was taken after the cryogenic chamber had been evacuated for approximately eight weeks (no bake-out had

been applied beforehand). Immediately prior to this measurement, the photocurrent was estimated to be (345 ± 2) pA and the pressure was measured to be $(4 \pm 2) \times 10^{-8}$ mBar, where the *LabVIEW* program was used to determine the photocurrent and pressure thirty independent times as described above and the stated values are the (mean $\pm$ standard deviation). The photocurrent as a function of pressure was determined in three stages: i) after the turbo pump had been turned off and while the turbo was spooling down, ii) after the roughing/backing pump had been turned off and iii) after a vent had been opened to equalise the vacuum to one atmosphere. The data is shown in Figure 4.8a. It can be seen that the photocurrent did not start to decrease significantly until the pressure had decreased to $\sim 10^{-4}$ mBar. However, as can be seen in the photograph of the setup (Figure 4.6b), the pressure gauge is far from the vacuum chamber and so the plotted pressures are likely to be slightly lower than the true pressures in the chamber, due to a time-lag in the pressure equalisation.

The second dataset was taken two days later, using the same setup. However, in order to obtain better plot resolution at lower pressures, the photocurrent was measured as a function of pressure while the cryogenic trapping chamber was being evacuated from one atmosphere to $(9 \pm 1) \times 10^{-7}$ mBar. The cryogenic trapping chamber has a small volume ($\gtrapprox (20 \text{ mm})^3$) and is close to the turbopump and so this took approximately 83 minutes. Then, the pressure in the cryogenic chamber was brought to one atmosphere again, repeating the three stages that were used in the first measurement set. The data is shown in Figure 4.8b. It can be seen that there is some hysteresis, which is most likely due to the pressure differential between the cryogenic trapping chamber and the pressure gauge. It can also be seen that the photocurrent only reached approximately 150 pA after the 83 minutes of evacuation, compared to the 350 pA measured after the previous eight-week evacuation. This suggests that without a bake-out, the chamber would need evacuating for a long time to reach a sufficiently low pressure inside the cryogenic trapping chamber.

By considering both measurements in Figures 4.8a and 4.8b, it can be seen that there is a clear trend between the photocurrent and the pressure. There is no pressure gauge

on the cryogenic chamber and so therefore a measurement of the photocurrent could be useful as an indication of the pressure while at room temperature. However, there are many variables to control, including the fibre alignment (which is difficult to control) and the attenuation of the optical fibre. Furthermore, a calibration curve (like those shown in Figure 4.8) should be obtained during a much slower evacuation in order to keep the pressure differential between the chamber and gauge minimal.

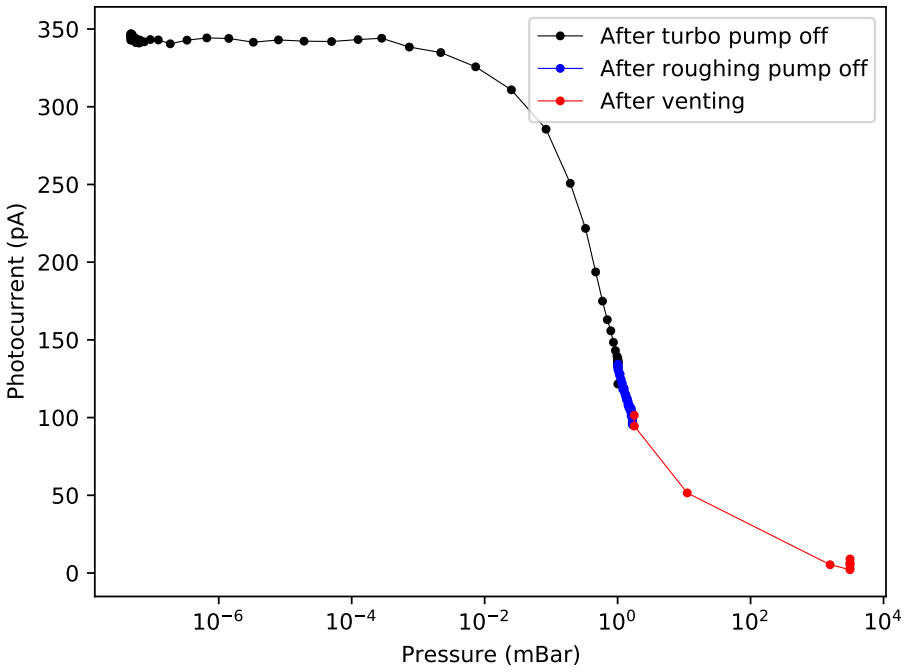

(A) The data obtained in the first set of measurements, with the photocurrents shown with reversed polarity. No uncertainties were recorded.

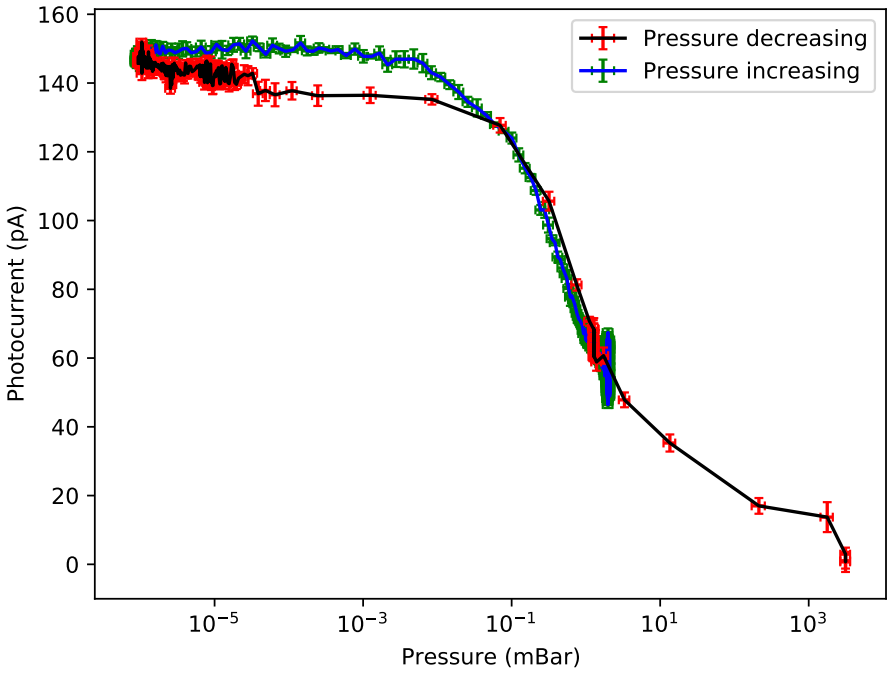

(B) The data obtained in the second set of measurements, with the photocurrents shown with reversed polarity. The black/blue linear interpolations show the data obtained during the evacuation/venting respectively.

FIGURE 4.8: The results from the two independent measurements of the photocurrent as a function of the pressure.

4.4.2 Observing outgassing in a pinched-off chamber

On one occasion, a cryogenic trapping chamber (which had been sealed to a Geonium Chip (§3.4)) was pinched-off (§3.4) after approximately eight days of evacuation. Although a plot of the pressure as a function of time during and immediately after the pinch-off showed no sudden leak, during the next two days the photocurrent gradually decreased, as shown in Figure 4.9. The setup was similar to the setup shown in Figure 4.6. After the chip had been hermetically sealed to the chamber (§3.4) and before the chamber was pinched-off, a bake-out was not performed and the chamber remained at room temperature.

A fit to one single exponential decay did not fit well, however a fit to the sum of two exponential decays $I_1(t)$ and $I_2(t)$ of the form

$$I(t) = I_0 + \underbrace{A_1 \cdot \exp\left(\frac{-(t-t_0)}{\tau_1}\right)}_{I_1(t)} + \underbrace{A_2 \cdot \exp\left(\frac{-(t-t_0)}{\tau_2}\right)}_{I_2(t)} \tag{4.2}$$

was reasonably appropriate (see the plot in Figure 4.9 and the optimal fitting parameters in Table 4.2). The fit to this function (4.2) suggests that there were **two significant sources** which were decreasing the photocurrent (and thus increasing the pressure (§4.4.1)), including perhaps virtual leaks [186] (e.g. outgassing [186]) or real leaks [186]. The fit parameters in Table 4.2 for the fit in Figure 4.9 show that the source of $I_2(t)$ was initially more dominant than the source of $I_1(t)$, but shortly afterwards, the source of $I_1(t)$ was more dominant than the source of $I_2(t)$. This is because the amplitude A_1 was approximately eight times that of A_2 and so initially $I_2(t)$ contributed more to the measured current, but the time constant of its decay τ_1 was approximately 28 times that of τ_2 and so the tail of the fit was dominated by $I_1(t)$. As will be discussed in the remainder of this section (§4.4.2), it is likely that the most dominant source of the photocurrent decay at long times elapsed ($I_1(t)$) was caused by a virtual leak - for example some outgassing. It is unclear what the source of the initial decay $I_2(t)$ was - possibly it was another virtual leak caused by the pinching-off, because this source ended shortly after pinching-off.

TABLE 4.2: Table of results for the fit to the decay of the photocurrent, where the photocurrent had reversed polarity. The stated uncertainties are the standard errors, which were calculated using the diagonal elements of the covariance matrices.

Fit parameter	Optimal value (fit)
I_0	(8.8705 ± 0.0002) pA
t_0	$(1.12 \pm [2 \times 10^8])$ hours
A_1	$(17.5 \pm [6 \times 10^8])$ pA
τ_1	(10.040 ± 0.001) hours
A_2	$(2.22 \pm [8 \times 10^9])$ pA
τ_2	$(0.362 \pm [5 \times 10^{-7}])$ hours

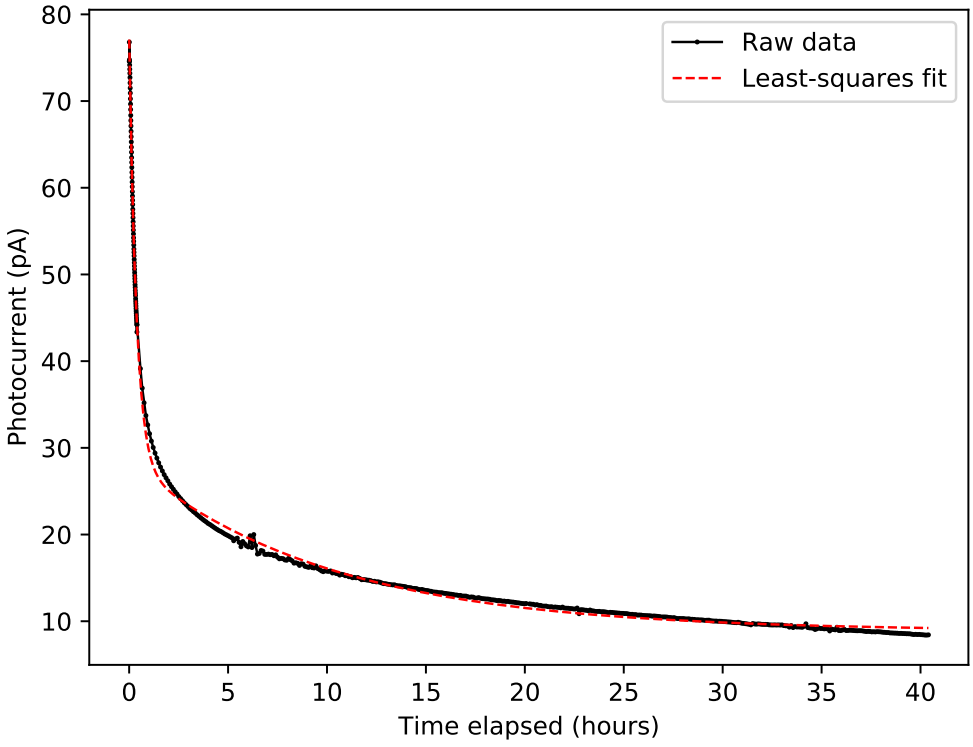

FIGURE 4.9: A plot of the photocurrent (with reversed polarity) as a function of time, measured after a pinch-off. A least-squares fit to (4.2) is also shown using the optimal fit parameters stated in Table 4.2. This fit suggests that there were two significant sources $I_1(t)$ and $I_2(t)$ which contributed to the decay of the photocurrent in this figure, despite it looking like there is only one source.

The optimal fit value for the current ($I^{(\text{pin})}(t=\infty) = I_0$) at infinite time was (8.8705 ± 0.0002) pA, where *pin* refers to the data in the fit after the pinch-off. Regrettably, no measurement of the photocurrent as a function of pressure had recently been undertaken for the setup, so reading the corresponding pressures from Figure 4.8 would have been unreliable. However, immediately prior to pinching-off, the photocurrent measured approximately (73.9 ± 0.1) pA. The experiment had been evacuating for approximately eight days, at which point the pressure at the *FRG-700* gauge read approximately 10^{-7} mBar. Therefore, it may be assumed that this photocurrent of 73.9 pA was the saturation photocurrent $I_{\text{sat}}^{(\text{pin})}$ for the pinch-off dataset, which occurs at low pressures where the photocurrent stops increasing with decreasing pressure. In order to estimate the final (asymptotic) pressure $P^{(\text{pin})}(t=\infty)$ for the pinched-off chamber, the data in Figure 4.9 can be normalised to the *calibration* plot of the photocurrent as a function of pressure (Figure 4.8a). The calibration data (Figure 4.8a) has a saturation photocurrent $I_{\text{sat}}^{(\text{cal})}$ of (344 ± 1) pA.

If it is assumed that minor changes in the setup just stretch the *calibration* plot (where the functional form is maintained but the photocurrent at every pressure is multiplied by the same scaling constant), then the normalised photocurrent at infinite time may be approximated with

$$I^{(\text{cal})}(t=\infty) \approx I^{(\text{pin})}(t=\infty) \cdot \frac{I_{\text{sat}}^{(\text{cal})}}{I_{\text{sat}}^{(\text{pin})}}. \tag{4.3}$$

This may be evaluated as $I^{(\text{cal})}(t=\infty) \approx 8.8705\,\text{pA} \times (344\,\text{pA}/73.9\,\text{pA}) = (41.3 \pm 0.1)$ pA, which corresponds to a pressure of approximately $P^{(\text{cal})}\left(I^{(\text{cal})} = 41.3\,\text{pA}\right) = (33.3 \pm 0.1)$ mBar when reading off the linear interpolation in Figure 4.8a. The bounding data points are quite far from the interpolation location and so this reading has a lot of uncertainty which has not been accounted for. The *saturation vapor pressure* [186] of a single component substance is the equilibrium (steady-state) pressure which is reached when the rate of evaporation/sublimation equals that of condensation [186]. For water, at a temperature of 20°C, the saturation vapor pressure has been determined experimentally to be 23.38 mBar [186], which is similar to the calibrated data of $P^{(\text{cal})}\left(I^{(\text{cal})} = 41.3\,\text{pA}\right) =$

(33.3 ± 0.1) mBar. When taking into account all the uncertainties, it is plausible that there was no real leak and that the dominant source of photocurrent decay at long times elapsed ($I_1(t)$) was caused by a virtual leak - for example some outgassing. This agreement between the determined pressure of (33.3 ± 0.1) mBar and the saturation vapor pressure of 23.38 mBar [186] helps to validate the concept of the calibration curve (Figure 4.8a).

4.5 Baking-out the cryogenic trapping chamber

The measurement of the photocurrent as a function of time after a pinch-off had occurred (§4.4.2) suggests that if the cryogenic trapping chamber were not to be heated during an evacuation, that after pinching-off (§3.4), adsorbed and absorbed water would fill the chamber and eventually bring the chamber to the saturation vapor pressure of water at 23.38 mBar [186]. Although cryocooling/cryopumping [186] should reduce this pressure yet again, condensed particles could affect the electrostatic trapping potential or attenuate the UV light if frozen to the interior face of the window (§4.7.1). Therefore, the cryogenic trapping chamber (§3.4) was baked-out to temporarily increase the rates of i) outgassing [186] and ii) surface desorption [186], while under evacuation to reduce readsorption [186], with the aim to eventually achieve cryovacuum (e.g. [187]). The effects of the bake-out are discussed in (§4.5.1), the control system is discussed in (§4.5.2) and a leak is shown in (§4.5.3).

The first bake-out of the cryogenic trapping chamber was introduced by Dr Alberto Jesús Uribe Jiménez [32]. Dr Alberto Jesús Uribe Jiménez attached two independent k-type thermocouples to the cyrogenic trapping chamber using copper tape, one close to the chip and one close to the window, to monitor the temperatures closest to the indium seals which were most likely to fail. Dr Alberto Jesús Uribe Jiménez surrounded the cyrogenic trapping chamber with a layer of aluminium foil, then wrapped the foil with an *Omega DHT052020LD* heating tape and then applied a further layer of aluminium foil. The heating tape provided the heating and the aluminium foil was used to more evenly

distribute this heat [32], which would otherwise cause an uneven temperature distribution across the chamber. The chamber (§3.4) is constructed from gold-plated copper, the chip (§3.2) has an alumina substrate and finally the chip-chamber, window-chamber and pinch-off-tube-chamber seals (§3.4) were made using indium. The materials have different thermal expansion coefficients and so if the temperature of the chamber is raised too rapidly and/or too unevenly, the indium seals may not have enough time to expand/contract and they may fail. Furthermore, in order to protect the indium seals [188], the maximum bake-out temperature should be limited to 110°C [188], which is lower than the melting temperature of indium while at a pressure of 1 atmosphere ($\approx$ 157°C [189, 190]) and so the maximum set temperature was 107°C. A photograph of a bake-out setup is shown in Figure 4.10, which had the same electrical setup as the one shown in Figure 4.6, but with a gold-leaf target [32] instead.

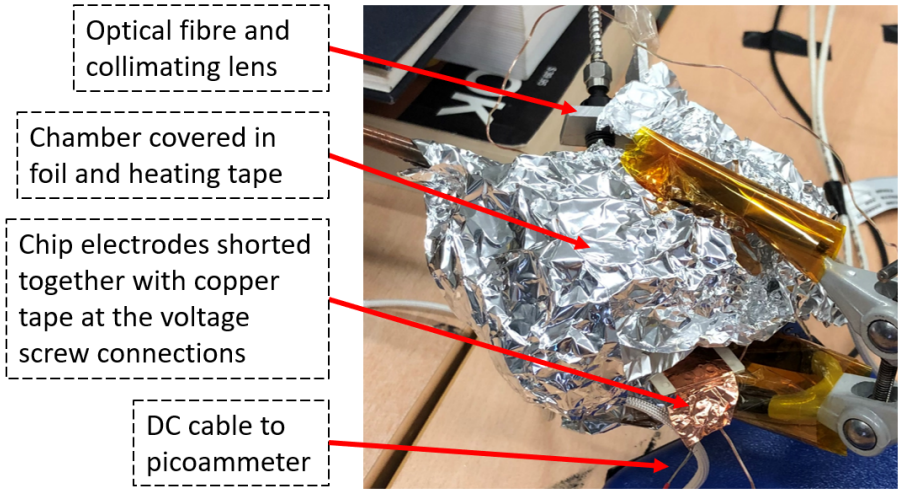

FIGURE 4.10: A photograph of the cryogenic trapping chamber during the bake-out. This setup was used to obtain the measurements in (§4.5.1). The window was left unobscured so that photocurrent measurements could be undertaken.

4.5.1 The effects of baking-out

The discussion included in this section (§4.5.1) will only regard the first bake-out to be attempted. The heating rate during the ramping of the temperature from room-temperature to $\approx$ 100° C was controlled manually by changing the voltage of a variable

autotransformer. The temperatures of both temperature sensors were nearly-continuously monitored and plotted with a *LabVIEW* program, with intermittent breaks in the temperature measurements (approximately daily) to determine the photocurrent and to measure the pressure by reading the *Varian FRG-700* pressure gauge using the pump's in-built readout.

A *LabVIEW* control program measured the currents $I_{\text{UV off}}$ and $I_{\text{UV on}}$ in five pairs of (typically 50 but one time 35) measurements. The gradients on the currents $I_{\text{UV off}}$ and $I_{\text{UV on}}$ with time were negligible and so the photocurrents were determined as the difference in the means of the two sets of currents. The temperatures of both temperature sensors were determined using a *Keithley 2110* digital multimeter. One thermocouple was connected to the *2110*'s thermocouple input for a direct determination of the temperature and the DC voltage was measured across the other thermocouple with the *2110* which was converted into a temperature value within a *LabVIEW* program via the use of a NIST polynomial series calibration.

Plots of the pressure and photocurrent are shown below in Figure 4.11. For temperatures once the bake-out had begun (after two days had elapsed), fits were conducted to the pressure and photocurrent as functions of the time t elapsed

$$x(t) = x_0 + A \cdot \exp\left(\frac{-(t - t_0)}{\tau}\right), \tag{4.4}$$

where x may be the photocurrent I or the pressure P and where x_0, A, t_0 and τ are optimisable parameters (constants). Although there is no obvious explicit physical law to model with such an exponential decrease, the fits predict the saturation values ($x(t = \infty)$). The pressure at infinite time is predicted to be 7.3×10^{-8} mbar (with low uncertainty), which seems reasonable because the pump and vacuum seals are not ultra-high-vacuum rated. The photocurrent at infinite time is predicted to be (463 ± 3) pA (with reversed polarity), which is also reasonable, given that the photocurrent was already close to saturation after just three days had elapsed.

Figure 4.11 shows how the pressure and photocurrent were affected by the bake-out.

The bake-out (the rising of the temperature) began shortly after the second data point had been taken and the temperature of sensor 1 rose from 25.4°C to 109.4°C over 303.4 minutes with an average heating rate of +0.277°C/minute. Once the final temperature had been reached, the power of the heating tape was reduced slightly to maintain a temperature of approximately 107°C and then the heating tape power was left unchanged for the rest of the plotted measurements. As can be seen in Figure 4.11a, after one day of baking, the pressure had more than doubled, possibly due to a combination of i) an increase in the outgassing rate and ii) the ideal gas law which predicts an increase in pressure purely from an increase in the temperature. This is then followed by an exponential decrease over the remaining days, while the pump evacuated the outgassed particles. As can be seen in Figure 4.11b, the photocurrent also initially rose rapidly as a result of baking and nearly saturated after just two days of baking. The mean photocurrent in the first two measurements (prior to the bake-out) was (84.3 ± 0.7) pA (with reversed polarity) and the saturation photocurrent value was (463 ± 3) pA (with reversed polarity), which gives an improvement to the photocurrent of $(463\,\text{pA}/84.3\,\text{pA}) = (5.49 \pm 0.06)$ (dimensionless).

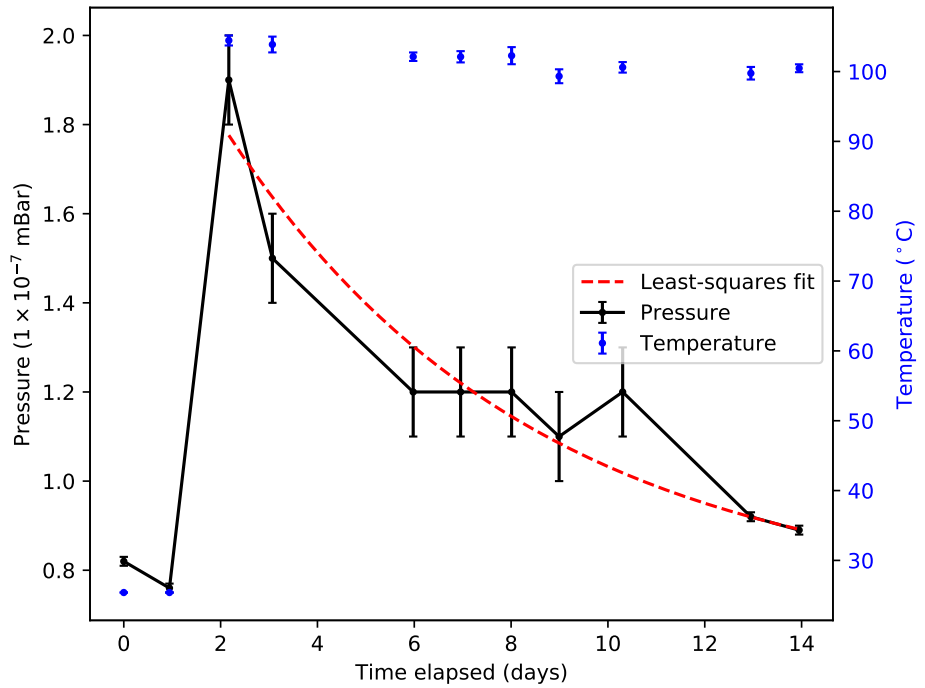

(A) Showing the effect of the bake-out on the pressure. The fit to the pressure excluded the first two data points.

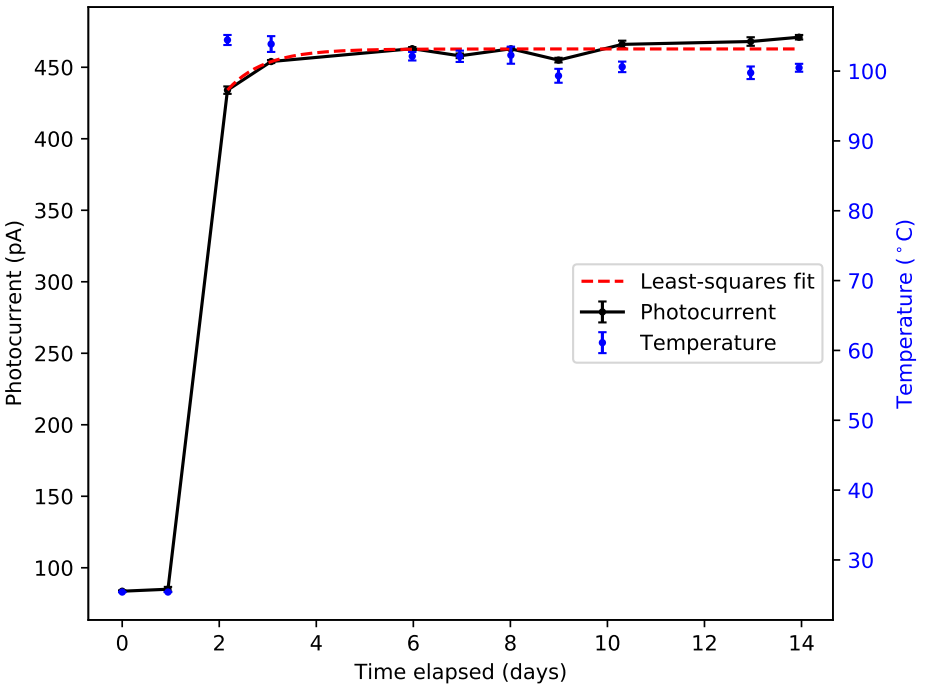

(B) Showing the effect of the bake-out on the photocurrent. The fit to the photocurrent excluded the first two data points.

FIGURE 4.11: Plots of the effects of the bake-out on the pressure and the photocurrent. The bake-out began shortly after the second data point and took approximately five hours to reach 109.4°C. The temperatures which are plotted are those measured using sensor 1 at the same time as the pressure and the photocurrent. No temperature measurement for the first data point was recorded and so it has been assumed that it was the same temperature as measured for the second data point. The polarities of the photocurrents have been reversed.

It was noticed that there was a correlation between the measured dark current $I_{\text{UV off}}$ and the pressure. This is shown in Figure 4.12. The photocurrents were determined as the difference between the mean $I_{\text{UV on}}$ and mean $I_{\text{UV off}}$ and because the dark current is present within both $I_{\text{UV on}}$ and $I_{\text{UV off}}$, the changing dark current with time should not have affected the photocurrent values. It is not clear why this correlation occurred, because the pressure should not have affected the current in the picoammeter cabling. Also, electrical noise ($I_{\text{UV off}}$) should not have affected the pressure gauge reading.

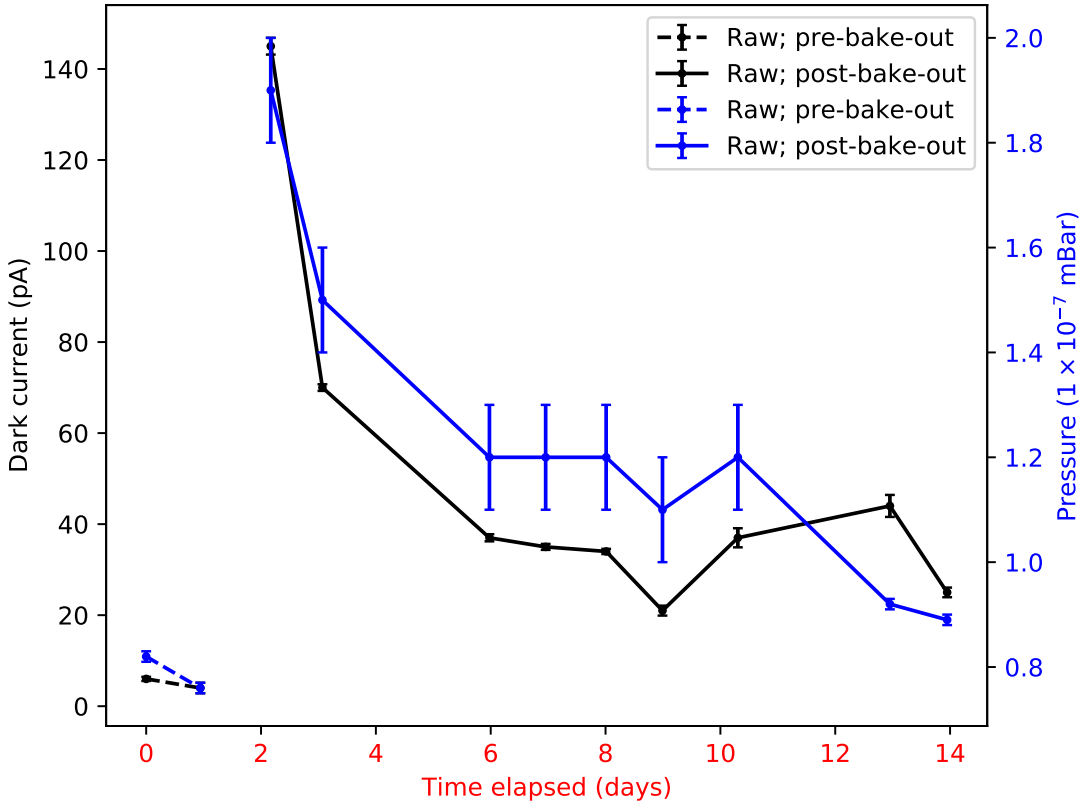

FIGURE 4.12: A plot showing the correlation between the dark current $I_{\text{UV off}}$ and the pressure as read by-eye from the pressure gauge readout.

4.5.2 Controlling the bake-out

A *LabVIEW* program was written to control the heating of the chamber. The program had two main aims: firstly to warm/cool the chamber until a target temperature had been reached and secondly to control the chamber heating/cooling rate. The heating tape was

powered by two *Rohde and Schwarz HMP4040* programmable DC power supplies, where the (combined) eight channels of the devices were connected in series. The heat tape can provide up to 156 W of thermal power at a voltage V_{heat} of 240 V, however in order to sustain a bake-out at $\approx 100°$C, only (V_{heat} = 8 x 6.10 W $\approx$ 50 W) was required.

The most recent iteration of the *LabVIEW* program used a *Keithley 2110* digital multimeter to determine the temperatures of both thermocouples, which had one direct thermocouple input (*temperature sensor 1*) and one DC voltage measurement input (*temperature sensor 2*) which was converted to a temperature value using a NIST polynomial series calibration within the control program. The program used the temperature measurement of temperature sensor 1 to monitor the heating rate (by calculating the gradient of the most recent three data points) and then decided whether or not to adjust V_{heat}. Some pseudo-code to describe the algorithm is included in Figure 4.13. One set of control values (defined in Figure 4.13) were as follows: $|\Delta T_L| = 5$ °C; $|\Delta T_H| = 5$ °C; $T_0 = 104$ °C; $|\Delta V_T| = 0.05$ V; $m_0 = 0.05$ °C/minute; $|\Delta V_L| = 0.3$ V; $m_L = 0.05$ °C/minute; $|\Delta V_H| = 0.3$ V and $m_H = 0.05$ °C/minute.

An example use of the program is shown in Figure 4.14 (but not using the example set of control values above). Figure 4.14a shows the temperature ramping stage (raising the temperature from room temperature to the desired final bake-out temperature), where the raw data for the temperature and heating rate are those calculated in the *LabVIEW* control program. Despite the mean heating rate appearing to be centred around 0°C/minute, the mean of all the raw *LabVIEW* calculated heating rates (Figure 4.14a lower plot) was actually 0.0252°C/minute with a standard deviation of 0.0558°C/minute. This is non-zero (so as to raise the temperature), but small (so as to reduce thermal contraction/extension stresses on the indium seals (§3.4) - note see (§4.5.3) for an example of rapid cooling). Post measurement, in order to verify the *LabVIEW* calculated heating rates, the mean heating rate was checked by determining the gradient of a linear least-squares fit to all the raw data (upper plot), where the gradient was 0.0253°C/minute (with uncertainty $O(10^{-12}$°C/minute)). These values (0.0252 and 0.0253) °C/minute are in reasonable agreement and so the *LabVIEW* estimation of the heating rate (which is

While True:
On the *i*th iteration, query the temperature of sensor 1 which is then denoted T_i.
If the *i*th temperature T_i is in the acceptable range T_{i-1}– $|\Delta T_L|$ <= T_i <= T_{i-1} + $|\Delta T_H|$ (this check is to verify that the temperature reading is valid and not noise/corruption etc):

If the measured temperature T_i is greater than the maximum permitted temperature T_0:
decrease the voltage V_i across the heating tape by $|\Delta V_T|$.

Else if the measured temperature T_i is less than or equal to the maximum temperature T_0:

If the measured heating rate m_i is less than the desired heating rate m_0:
If $|m_0 - m_i| >= |m_L|$:
increase V_i by $|\Delta V_L|$.
Else if $|m_0 - m_i| < |m_L|$:
do not change V_i.

Else if the measured heating rate m_i is greater than the desired heating rate m_0:
If $|m_0 - m_i| >= |m_H|$:
decrease V_i by $|\Delta V_H|$.
Else if $|m_0 - m_i| < |m_H|$:
do not change V_i.

i = *i* +1

FIGURE 4.13: Some pseudo-code to describe the algorithm for controlling the bake-out.

used to set V_{heat}) is reasonable.

Figure 4.14b shows a thermostatic stage (where it was desired that the temperature of the chamber would remain constant with time). The mean of all the raw *LabVIEW* calculated heating rates (Figure 4.14b lower plot) was 0.0001 °C/minute with a standard deviation of 0.1196°C/minute, which is consistent with zero, as was desired. This standard deviation is in agreement with the standard deviation of the temperature data of temperature sensor 1 (Figure 4.14b upper plot) of 0.2°C, which was around a mean of 100.9°C.

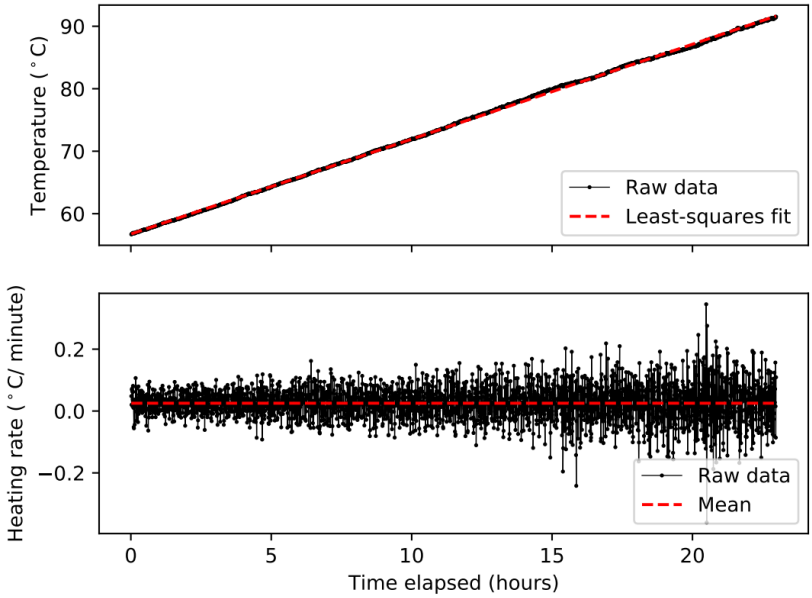

(A) Upper plot: the temperature of sensor 1. Lower plot: the heating rate of sensor 1 as calculated within the control program which was used to determine V_{heat}, with a (mean $\pm$ standard deviation) of $(0.0252 \pm 0.0558)^{\circ}\text{C}/\text{minute}$. The data were obtained during a **temperature ramping stage**.

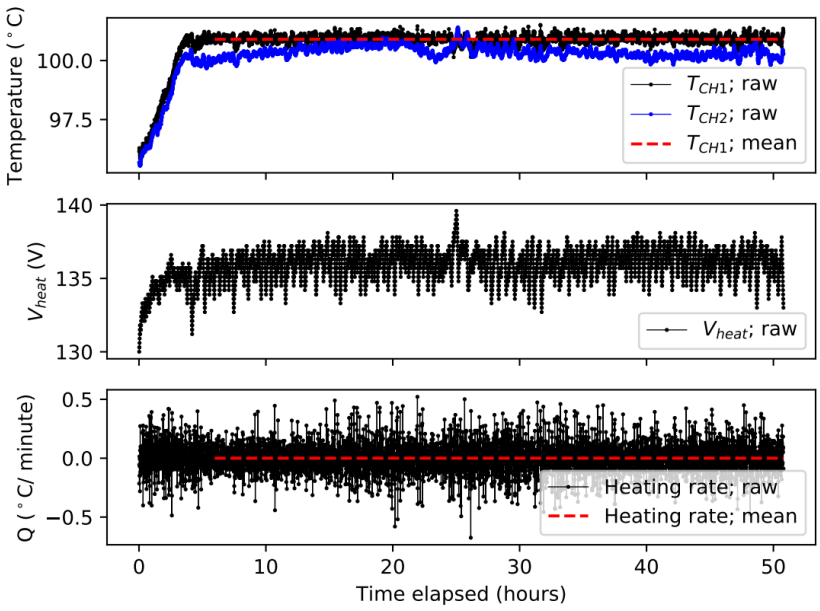

(B) Upper plot: the temperatures T_{CH1} and T_{CH2} of sensors 1 and 2 (respectively). Middle plot: a plot of the heating tape voltage V_{heat}. Lower plot: the heating rate Q of sensor 1 as calculated within the control program which was used to determine V_{heat}. The data were obtained during a **thermostatic stage**.

FIGURE 4.14: Plots from a bake-out during the **temperature ramping stage** (Figure 4.14a) and the **thermostatic stage** (Figure 4.14b). All raw data was determined in the *LabVIEW* control program.

4.5.3 Cooling down too quickly

At the end of another bake-out, a leak occurred during the cooling-down stage. It is likely that the leak occurred as a result of the chamber having cooled too quickly - which likely caused excessive thermal contraction/extension stress on the indium seals (§3.4). Some of the parameters during this cool-down are plotted in Figure 4.15. A linear least-square fit to the temperature (top plot) estimates the mean cooling rate (gradient) at -0.178°C per minute (with uncertainty $O(10^{-8\circ}\text{C/minute})$). At a time elapsed of 78.6 minutes, a rapid pressure rise is visible at the *Varian FRG-700* pressure gauge outside the chamber (central plot), which is consistent with the start of a steady decline in the photocurrent (bottom plot). A *Keithley 2110* digital multimeter was used to convert the voltage output by the pressure gauge into a pressure value using a calibration formula that was provided by the manufacturer of the pressure gauge.

4.6 The effect of the mesh on the UV intensity

As described in (§3.4), the mesh is 85 % open [36]. The mesh strands should reflect some of the incident UV light and thus reduce the intensity of the UV light at the target, so the mesh should reduce the number of liberated electrons and thus reduce the measured photocurrent. This was investigated by firstly measuring the photocurrent without any mesh present and then measuring with the mesh outside the chamber but between the collimating lens and the window.

The same setup as introduced in (§4.3.1) to measure the photocurrent as a function of the collector bias voltage V_{col} was used for these measurements, including the printed circuit board with one large electrode setup which was fabricated by Dr Jonathan Pinder. The chamber was evacuated to a pressure of approximately 1.7×10^{-6} mBar. The collector was biased with a +32 V (nominal) potential relative to the chamber which was grounded. The UV was incident through the window, towards a gold leaf target. A photograph of the measurement is shown in Figure 4.16.

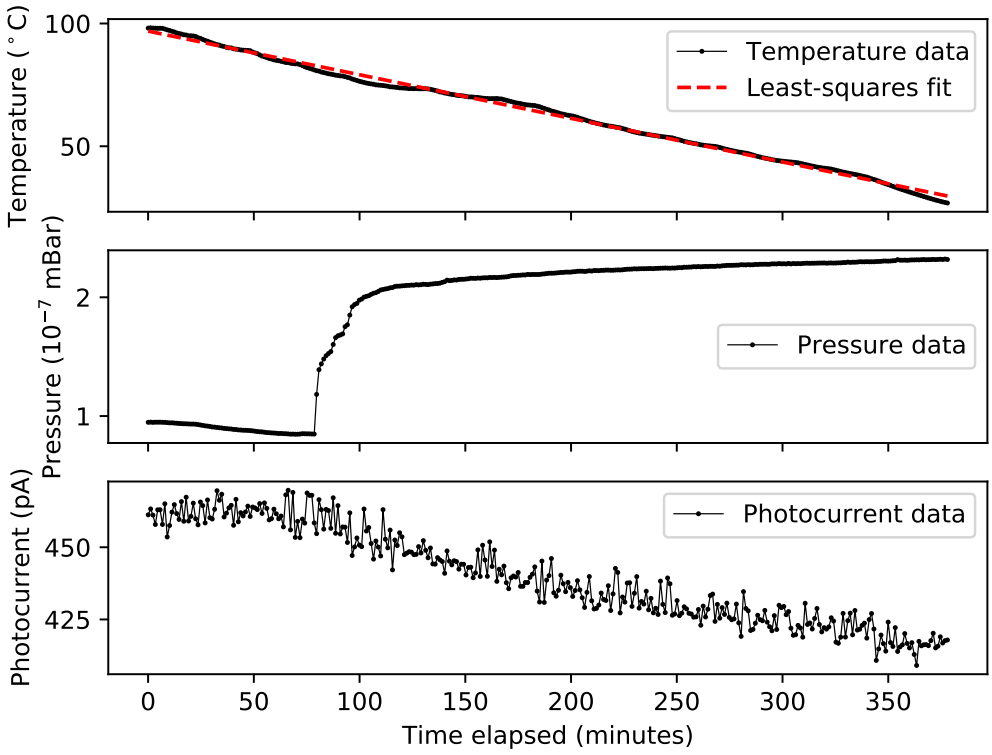

FIGURE 4.15: A failed cooling-down of the chamber at the end of a bake-out. At a time of 78.6 minutes, the pressure rises sharply and the photocurrent starts to decrease, both of which suggest that the vacuum sealing had failed.

The photocurrent measurements were controlled with a *LabVIEW* program (§4.1), which would be described with $N_{\text{bunch}} = 50$, $N_{\text{pairs}} = 5$ and $N_{\text{skip}} = 15$. Firstly, the photocurrent was determined while there was no mesh present, then it took three minutes to set up the mesh and then it took another three minutes to measure the photocurrent while the mesh was present. The photocurrent was determined to be (511.8 ± 0.3) pA without the mesh and (444.7 ± 0.3) pA with the mesh (both photocurrent polarities have been reversed). Therefore, the mesh gave a percentage reduction of (13.09 ± 0.08) %. The mesh is 85 % open [36], and so classically this would predict a 15 % reduction in the photocurrent due to the mesh, which is in reasonable agreement with the measurement.

One limitation of this measurement is that the mesh was outside the chamber, rather than inside the chamber like it would be during trapping attempts. In order to insert

the mesh into the chamber, the setup would have to have been taken apart (so that the chip could be unsealed, the mesh inserted and then the chip resealed (§3.4)) and then the setup would have to have been put back together. Minor changes in the alignment of the fibre can change the measured photocurrent greatly and so if the mesh were to have been put inside the chamber in this way, the photocurrent values might not comparable for the measurements with/without the mesh.

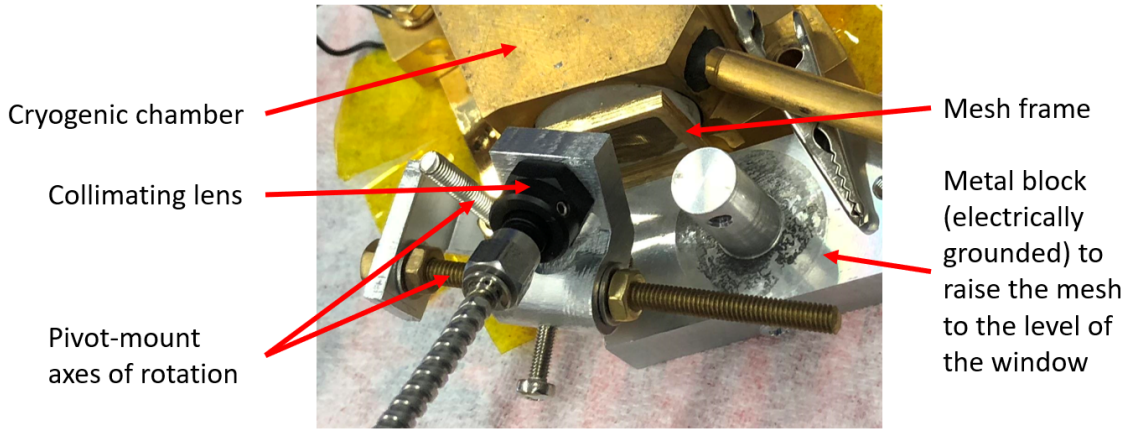

FIGURE 4.16: A photograph of the centre of the setup. The mesh (which is soldered to the mesh frame [36]) is electrically grounded through the metal block and the crocodile clip bridge to the electrically grounded chamber. The fibre mount may pivot about two axes (fabricated by Dr Jonathan Pinder), allowing for the alignment of the fibre towards the target.

4.7 Photocurrent measurements in the Geonium Chip Penning trap

In order to measure photocurrents using the Geonium Chip Penning trap (§3), a similar setup to those used for table-top measurements (Figure 4.6) was used. However, rather than accessing the voltage screw connections (§3.2) on the Geonium Chip, instead DC connections to the electrodes were made through the (filtered) DC voltage bias lines between the voltage screw connections (Figure 3.3) and the vacuum flange feedthrough connections, which are independent for each trapping electrode. Some advantages of using the Geonium Chip Penning trap for photocurrent measurements are i) an increase

in the photocurrent due to a custom-built fibre (§4.7.1), ii) the use of the experiment's magnetic field source (§3.3) as investigated in (§4.7.2) and iii) the use of a low pressure due to cryocooling (§4.5). Also, photoelectric measurements may be used to verify that the trap is working as expected, for example to verify the optical fibre alignment (§4.7.3), or to verify the DC voltage bias connections (the voltage screw connections (§3.2)) to the Geonium Chip (§4.7.4).

4.7.1 A custom-built optical fibre

The most recent iteration of the Geonium Chip Penning trap features a custom-built optical fibre setup with an integrated vacuum flange (designed and fabricated by Dr Jonathan Pinder) to maximise the UV transmission between the *Hamamatsu L10290* UV source and the cryogenic trapping chamber. The FDP-type core of the optical fibre has a wide diameter of 940 μm to improve the coupling of light into the fibre and the core is terminated at each end by an SMA connector. One SMA connector screws into the SMA output of the *Hamamatsu L10290* UV source and the other screws into the *Avantes COL-UV/VIS* collimating lens inside the second stage cooling ($\approx$ 4 K) region (§3.1) of the cryostat, close to the window of the cryogenic trapping chamber as can be seen in Figure 3.2. The core of the fibre passes through a vacuum flange, where a hermetic seal was made with epoxy around the fibre, which should have fewer losses when compared to the previous setup which included a fibre-coupling-feedthrough with associated coupling losses. At both sides of the flange, the core is shrouded in protective thermosetting plastic wrapping. Although the collimating lens with a casing is not rated to cryogenic temperatures, one copy survived three thermal cycles (between room temperature and $\approx$ 4 K) before the lens cracked and a replacement has survived approximately ten such cooldowns. Furthermore, a hole was drilled (by Dr Jonathan Pinder) through the lens casing to allow the lens to be evacuated prior to a cryogenic cooldown (§4.7.1).

In order to characterise the new fibre setup, photocurrent measurements were undertaken at room temperature using the Geonium Chip Penning trap experiment (§3). The pinch-off tube (§3.4) was cut-open such that the chamber was no longer hermetically

sealed and the two radiation shields [36] had been removed to speed up the evacuation of the cryogenic trapping chamber. Firstly, several measurements were undertaken with the old fibre setup (two fibres and a flange with a fibre-coupling-feedthrough) while at pressures of $\sim 10^{-6}$ mBar. The mean photocurrent for this setup was $I_{\text{old}} = (7.8 \pm 0.5)$ pA (with reversed polarity). Subsequently, the experiment was opened and a second set of measurements was undertaken, but with the new fibre setup and while at a pressure $\sim 10^{-5}$ mBar. The mean photocurrent for this setup was $I_{\text{new}} = (190 \pm 2)$ pA (with reversed polarity). This gives a **ratio** of improvement of $I_{\text{new}} / I_{\text{old}} = (24 \pm 2)$. Note, that both pressures $\sim 10^{-5}$ mBar and $\sim 10^{-6}$ mBar were sufficiently low that the background gas should not have significantly affected this comparison (§4.4), in fact with there being a lower pressure present during the measurement with the new fibre, the value (24 ± 2) is potentially an underestimate. This was a very significant improvement to the experiment. This high improvement might suggest that there were difference(s) between the setups (for example different fibre alignments), however the photocurrents were particularly low with the old fibre setup (hence the decision to implement an improved fibre) and other cryovacuum (§4.5) measurements have also verified that the new setup can produce a high photocurrent.

The largest measured photocurrent was (549 ± 12) pA (with reversed polarity), which was measured while using the left endcap electrode as the collector with $V_{\text{bias}} = +10$ V, while all four other electrodes were grounded outside the cryostat. This might be improved in the future if the chamber were first to be baked-out (§4.5) and then pinched-off (§3.4). For this measurement, the pressure inside the outer vacuum vessel but outside the radiation shields (§3.1) was 8.6×10^{-8} mBar, but the chamber had been at 4 K for some time and so there was likely a cryovacuum in the cryogenic trapping chamber. Furthermore, a small homogenous 5 mT field was used to help focus the photoelectrons (§4.7.2), however this should not have increased the magnitude of the photocurrent. Furthermore, a photoelectric measurement at room temperature using a cryogenic trapping chamber (with a similar setup to that depicted in Figure 4.6) measured (53 ± 1) pA when

using all five electrodes as the collector and (31.6 ± 0.2) pA when using just the left end-cap electrode as the collector. If it can be assumed that there is a linear relation between the measured photocurrents, then if the (549 ± 12) pA photocurrent were to have been measured through all five electrodes, this would have instead been $(549 \times 53/31.6)$ pA or (921 ± 20) pA.

An in-situ improvement to the photocurrent while cryogenic

An effect was noticed while the experiment was cryogenic (≈ 4 K), whereby a prolonged exposure of the chamber to UV light caused the photocurrent to increase with time, in a steady manner. This was noticed when the cryogenic chamber (§3.4) had not been pinched-off prior to installation in the experiment, so the chamber most likely contained many adsorbed and absorbed particles. If all electronic devices were turned off and if the collector were to be electrically grounded overnight, at the start of the following day the photocurrent would still remain at the value it had reached at the end of the previous day, which would suggest that the effect was not due to the charging/discharging of any filters etc. Also, if the UV shutter were to be closed to stop UV from reaching the target, then the photocurrent did not continue to increase with time by a significant extent. This effect was observed on two independent cool-downs of the experiment.

This effect might have been due to the UV light evaporating/sublimating particles which had frozen to surfaces as a result of cryopumping (§4.5). In particular, perhaps there were layers of frozen particles on both faces of the UV window and possibly on the collimating lens. This is suggested because during a previous thermal cycle of the experiment, a photocurrent had been observable at room temperature, unobservable once cooled to $\approx$ 4 K and observable again once back at room temperature. Therefore, Dr Jonathan Pinder drilled a hole in the collimating lens casing (which was not initially vacuum compatible) and there has not been any repeated loss of photocurrent at ≈ 4 K.

However, this also could be evidence of an irreversible cold cleaning of the gold-leaf photocathode, via outgassing due to the illumination of UV light [191, pg. 54]. This

article [191] references the measurement of gold [192], where [192] suggests that photoelectrons remove gas from the surface of the gold. It is concluded that UV exposure cleans the photocathode (reduces the threshold/work function) [191, 192]. This is similar to cleaning/rejuvenation via laser irradiation which has demonstrated a significant improvement to the quantum efficiency of photoliberation for copper, magnesium, aluminium, and aluminium–lithium photocathodes [182], where the quantum efficiency decreases with increasing work function [180, 181]. This method is very useful because it is a cold cleaning technique which results in an irreversible cleaning of the photocathode, because the rest of the experiment remains cold and so particles are not desorbed from other places which might later be adsorbed to the cathode. For example, at cryogenic temperatures H_2, CH_4, CO_2 and Ar might reduce the quantum efficiency [193] and also a restoration of the quantum efficiency has been demonstrated by the removal of adsorbed water via baking (§4.5) the photocathode [193]. It was also experimentally demonstrated [192] that a reversal of the photocathode bias voltage polarity (to attract photoelectrons back to the photocathode) also cold-cleaned the cathode in this way, via *electron bombardment* [191, pg. 54], which is analogous to *beam-gas-wall desorption* [194]. Furthermore, this electron bombardment could "remove hydrogen from silver and gold which could not be removed by heating" [191, pg. 54]. Although gold has a poor quantum efficiency of $\sim 10^{-4}$ [195], it is used as a thin-film transmission photocathode to load a cryogenic Penning trap because its photoemission is unaffected by exposure to air or modest vacuum [195] and so less cleaning should be required.

This effect is shown in Figure 4.17. Note that the current is plotted (with reversed polarity), rather than the photocurrent. However, it can be seen that when the UV shutter was closed, the measured current $I_{\text{UV off}}$ was approximately zero and so the current measured while the UV shutter was open was also approximately equal to the photocurrent. A running average was also continuously applied (twenty data points), hence the changes in shutter state show finite gradients rather than sudden jumps in the current.

Between zero and approximately seven minutes elapsed, the UV shutter was open. Then, the shutter was left closed for less than one minute, followed by the shutter being

open for less than one minute, then remaining shut for another two minutes until nine minutes had elapsed. At this point, the UV shutter was opened again and the current **returned to the value** which had previously been reached after seven minutes had elapsed - the growth in the photocurrent was correlated with the presence of UV light.

The UV shutter remained open until 20 minutes had elapsed, at which point the UV shutter was closed and the measurement of the current was paused in time until 25 minutes had elapsed, when the shutter was momentarily closed and then reopened. The shutter remained closed and the measurement remained paused for another minute, followed by another momentary opening of the shutter, followed by another pause and closing of the shutter. At this point the photocurrent was **similar to** the current after 20 minutes had elapsed (after the previous long-duration illumination). This was followed by a long period of the shutter being open until 39 minutes had elapsed.

This data demonstrates that the photocurrent only increased while the UV illuminates the chamber. Three linear least-square fits are shown in Figure 4.17, to time regions where the UV light was illuminating the chamber. These fits (left-to-right respectively) have gradients of 3.25 pA/minute, 2.57 pA/minute and 2.05 pA/min, with uncertainties much lower than the gradients. The gradient does decrease with increasing values of photocurrent, which suggests that the photocurrent would eventually saturate. The previously mentioned maximum measurement of (549 ± 12) pA (§4.7.1) had been achieved after having applied this technique. This technique has formed part of the regular routine for preparing to try to trap electrons.

4.7.2 The relation between the photocurrent and the strength of the magnetic field

A measurement of the photocurrent as a function of the magnetic field strength/magnitude $B_{z,000} = B_0$ (2.21) (2.11a) was conducted. All five trap electrodes were used as a collector (shorted together outside the cryostat) with a voltage bias $V_{\text{col}} = +32.050$ V (nominal). Although the free cyclotron motion does not exist in the presence of an electrostatic field

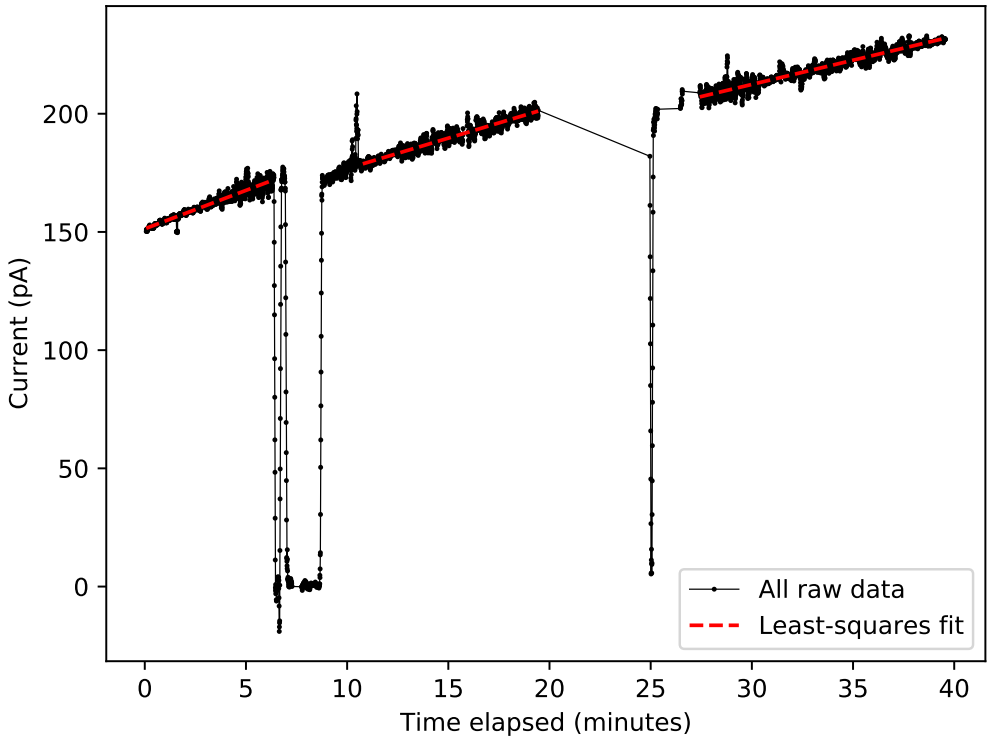

FIGURE 4.17: A plot showing the effect of prolonged exposure of the cryogenic trapping chamber to UV light. Fits are shown to three time regions where the UV light was illuminating the chamber.

(§2.1.3), there was no electrostatic trapping (quadrupole) potential and so the radial dynamics of the photoelectrons may be crudely approximated to be those of a free/true cyclotron motion (§2.1.1). The relation between the circular true cyclotron frequency ω_c and the magnetic field strength B_0 (2.11a) suggests that the radius of the cyclotron motion is inversely proportional to the magnetic field strength. The magnetic field should *focus* the photoelectrons by giving them a cyclotron motion in the $\hat{u}_x = \hat{u}_y$ plane and thus stop them from being collected, so the photocurrent should be inversely proportional to the magnetic field strength.

The pressure inside the outer vacuum vessel but outside the radiation shields (§3.1) was 7.4×10^{-8} mBar, however there was likely a cryovacuum (§4.5) at $\approx$ 4 K and so

the pressure in the chamber was probably lower than this. Two *LabVIEW* control programs were used to control the measurement, one was used to determine the photocurrent and the other was used to control the magnetic field strength. For a given magnetic field strength, the control program used to determine the photocurrent was similar to the *LabVIEW* program which was discussed in (§4.1), which would be described with $N_{\text{bunch}} = 50$, $N_{\text{pairs}} = 5$ and $N_{\text{skip}} = 15$. This procedure was conducted three times for a given magnetic field strength and the mean of the three individual photocurrents have been plotted as a function of the magnetic field strength in Figure 4.18. No photocurrent was discernable at $B_0 = 100$ mT, however the measurement was very noisy and thus inconclusive, so this data point has not been included in the plot.

A fit to $I(B_0) = I_0 + A/B_0$ was attempted to all the data in the plot, however when including the data point with $B_0 = 0$ mT (changed to a small non-zero value to avoid a divide-by-zero error), the fit would not converge. The inverse relation between the photocurrent and magnetic field strength holds for 20 mT $\leq B_0 \leq$ 75 mT. If (as measured) there is no photocurrent for $B_0 = 100$ mT, then this inverse relation is also not valid at very high magnetic field strengths, possibly due to the magnetic field focussing the beam of primary electrons (in the $\hat{u}_x = \hat{u}_y$ plane), thus keeping them from reaching the collector.

Some conclusions may be drawn, even if the relation is not perfectly inverse. Firstly, the photocurrent does decrease with increasing magnetic field strength and so while in the presence of a strong magnetic field, it is likely that the electron beam is focussed and heads towards the equilibrium trapping position $\vec{r}_0$ (§2.1.1). This implies that the magnetic field is still reasonably well aligned along $\hat{u}_z$ for z which are close to the target, despite the magnetic field only being optimised for homogeneity close to $\vec{r}_0$. Secondly, this data is indicative of the energy distribution of the photoelectrons.

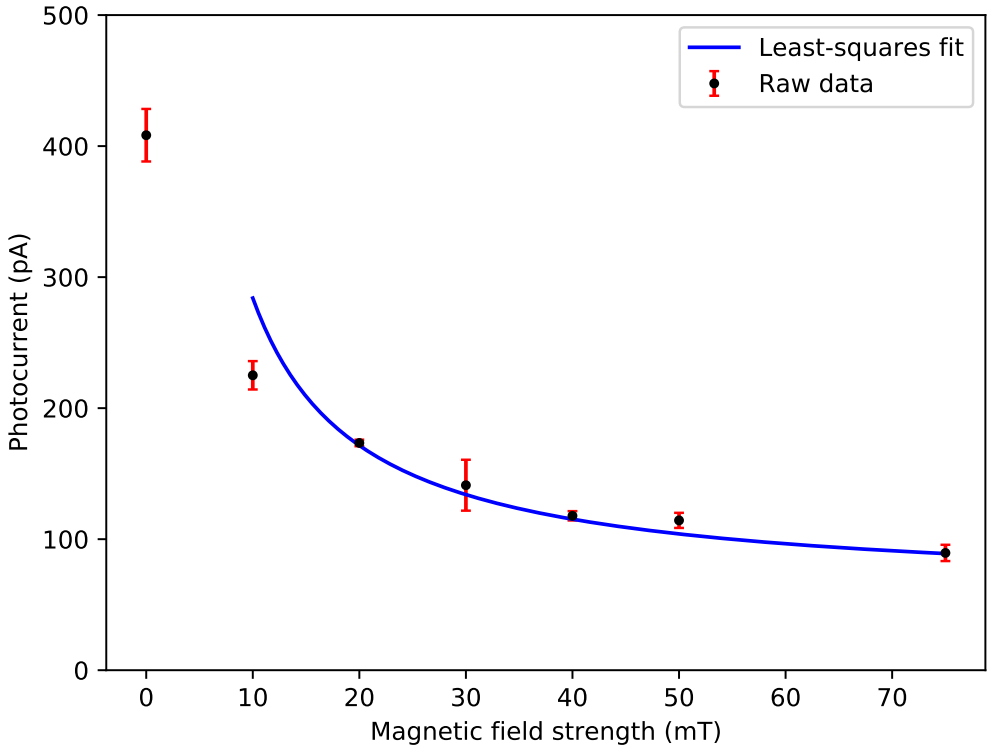

FIGURE 4.18: A plot of the photocurrent (with reversed polarity) as a function of the magnetic field strength. The error bars show the standard deviation.

4.7.3 Application: using the photocurrent to verify the alignment of the optical fibre

There are no explicit sensors to verify that the optical fibre is correctly aligned towards the target, however an electrostatic barrier technique has been developed which can be used for such verification. This section (§4.7.3) discusses the measurements made in one implementation of this technique. Ideally (neglecting plasma effects), all the electrons would be liberated from the target, i.e. no electrons would be liberated from any other interior surface of the chamber. An assumption was made that photoelectrons are liberated from either the target (in an $\hat{u}_x$-$\hat{u}_y$ plane at $z = -10$ mm) or from the opposite wall (an $\hat{u}_x$-$\hat{u}_y$ plane at $z = +10$ mm), i.e. that no electrons are liberated from the top/side walls nor from the chip in the $\hat{u}_z$-$\hat{u}_y$ nor $\hat{u}_z$-$\hat{u}_x$ planes. These planes are depicted in Figure

3.5. Therefore, by reflecting the photoelectrons which are produced at the wall opposite to the target, it is possible to collect only the photoelectrons (I_1) which are produced from the target (this photocurrent I_1 should be high if the fibre is correctly aligned towards the target) - this is the first measurement which will be discussed. Similarly, by reflecting the photoelectrons which are produced at the target, it is possible to collect only the photoelectrons (I_2) produced from the wall which is opposite the target (this photocurrent I_2 should be low if the fibre is correctly aligned towards the target) - this is the second measurement which will be discussed. As a consistency check, photoelectrons (I_3) which were liberated from all the inner surfaces of the chamber were also collected - this is the third measurement which will be discussed. Note that the window and the mesh are not located opposite the target in a $\hat{u}_x - \hat{u}_y$ plane, rather they are located with a slight misalignment from a $\hat{u}_y - \hat{u}_z$ plane (§3.4).

The pressure inside the outer vacuum vessel but outside the two radiation shields (§3.1) was 5.4×10^{-8} mBar, however the experiment was at $\approx$ 4 K and so the cryogenic trapping chamber (§3.4) should have reached a cryovacuum (§4.5) with even lower pressure. The photocurrent measurements were controlled with a *LabVIEW* program (§4.1), which would be described with $N_{\text{bunch}} = 50$, $N_{\text{pairs}} = 5$ and $N_{\text{skip}} = 15$. The following photocurrents I_1 and I_3 were each the mean photocurrent values of six independent measurements of the photocurrent (thus both I_1 and I_3 each took into account $6 \times (50 - 15) \times 10 = 2100$ current measurements). The following photocurrent I_2 was the mean photocurrent value of five independent measurements of the photocurrent (thus I_2 took into account $5 \times (50 - 15) \times 10 = 1750$ current measurements).

In the first measurement, all four Geonium Chip electrodes other than the right endcap electrode were used as the collector (shorted together outside the cryostat) and were biased with $V_{\text{col}} = +32.050$ V (nominal), while the right endcap electrode produced an electrostatic barrier with a voltage bias $V_{\text{bar}} = -10.000$ V (nominal). In this configuration, all photoelectrons released from the target should have been collected, while the barrier should have stopped photoelectrons from the other end of the chamber from being collected. The photocurrent (with reversed polarity) measured $I_1 = (570 \pm 13)$ pA.

For the second measurement, the setup in the first measurement had been reversed (along $\hat{u}_z$) such that all four Geonium Chip electrodes other than the left endcap electrode were used as the collector (shorted together outside the cryostat) and were biased with $V_{\text{col}} = +32.050$ V (nominal), while the left endcap electrode produced an electrostatic barrier with a voltage bias $V_{\text{bar}} = -10.000$ V (nominal). In this configuration, all photoelectrons released from the opposite end of the chamber to the target (z = +10 mm) should have been collected, while the barrier should have stopped photoelectrons from the target being collected. The photocurrent (with reversed polarity) measured $I_2 = (112 \pm 11)$ pA.

In the third measurement, as a consistency check, all five electrodes were used as the collector (shorted together outside the cryostat) and were biased with $V_{\text{col}} = +32.050$ V (nominal), with no electrostatic barrier in place. All photoelectrons, irrespective of their liberation location, should have been collected. The photocurrent (with reversed polarity) measured $I_3 = (597 \pm 20)$ pA.

Some conclusions may be made. Firstly, $I_1 > I_2$ and so it is likely the majority of the photoelectrons were liberated from the target, as required. Therefore, this technique may be used in future to verify the alignment of the optical fibre towards the target. Secondly, due to the conservation of the photocurrent, it should have been true that $I_1 + I_2 = I_3$, however it was measured that $(I_1 + I_2) > I_3$ which violates this conservation. Therefore, it is likely that photoelectrons liberated from both i) the target and ii) not the target were collected in both the first and second measurements for I_1 and I_2. This could be due to the electrodes having a thin span in $\hat{u}_x$ and so photoelectrons liberated from the side walls ($x = \pm 10$ mm) could have been relatively unaffected by the barrier voltages V_{bar} and thus collected.

4.7.4 Application: using the photocurrent to verify the electrode DC bias connections

The pressure inside the outer vacuum vessel but outside the two radiation shields (§3.1) was 5.4×10^{-8} mBar, however the experiment had been at ≈ 4 K for a long time and

so the cryogenic trapping chamber (§3.4) should have reached a cryovacuum (§4.5) with even lower pressure. The Geonium Chip Penning trap only has one electrical connection to each electrode (via the voltage screw connections (§3.2)) and so it is not possible to measure the voltage at the electrodes in order to check the connections (§3.1) while the cryostat is under vacuum. Although the UV light is aimed at the gold leaf target, some of the UV light which hits the target is reflected to other locations in the chamber. A measurement was undertaken to collect low-energy photoelectrons which were not liberated from the target, e.g. to collect those electrons which were liberated from the wall at $z = +10$ mm (the opposite side of the chamber to the target (§3.4)). By using a similar method to that discussed in (§4.7.3), by applying negative voltages V_{bar} to each electrode in turn, electrostatic barriers should have been produced which should have repelled the low-energy photoelectrons and thus reduced the photocurrent.

The gold leaf target had previously been replaced with a photocathode in the same location, where the photocathode consisted of some gold leaf which was placed on an electrode which could be biased with a voltage V_{cath}. The photocathode was biased with a voltage of V_{cath} = -50 V, so that any liberated photoelectrons from the photocathode (undesirable) would be accelerated over the top of the collector (the left endcap electrode) and not collected. A magnetic field which was homogeneous at the equilibrium trapping position $\vec{r}_0$ (§2.1.1) with a magnitude (2.21) (2.11a) $B_{z,000} = B_0 = 35$ mT was applied (§3.3), to induce a cyclotron motion (§2.1.1) and further stop the high-energy photoelectrons from the photocathode from being collected (§4.7.2).

Four measurements of the photocurrent as a function of the barrier voltage V_{bar} were undertaken, where each time a different electrode was selected as the electrode-under-test (EUT) to provide the barrier voltage. The left endcap electrode was used as the collector for all four measurements and was always biased with $V_{\text{col}} = +50$ V. The other three electrodes (excluding the EUT and the left endcap electrode) were set to +0 V (not floating). A *LabVIEW* control program was used to control the measurements. For a given EUT, the program set V_{bar} and then a photocurrent measurement was controlled with a *LabVIEW* program (§4.1), which would be described with $N_{\text{bunch}} = 20$, $N_{\text{pairs}} =$

5 and $N_{\text{skip}} = 5$. Subsequently, the program set the next V_{bar} and then measured the photocurrent and after having repeated this for multiple V_{bar}, a plot was obtained for the photocurrent as a function of V_{bar}.

The plots for the right endcap electrode and the right correction electrode (Figure 4.19a) clearly show that as the magnitude of the barrier voltage V_{bar} increases, the photocurrent decreases. This suggests that the right endcap and right correction electrodes were both biased correctly by the DC voltage supplies. The plots for the ring electrode and the left correction electrode (Figure 4.19b) also show that as the magnitude of the barrier voltage V_{bar} increases the photocurrent decreases, however the trends are less clear and so linear least-squares fits have been included in the plots to help guide the eye. The ring electrode and the left correction electrode are both spatially closer to the collector (which was the left endcap electrode) than both the right endcap electrode and the right correction electrode (§3.2). Therefore, perhaps the electrostatic barriers V_{bar} produced by the ring and left correction electrodes affected the electrostatic potential of the collector electrode more significantly than the barriers of the right endcap and the right correction electrodes. Also, the photocurrent was collected through the left endcap electrode, which verifies the DC connection between the left endcap electrode and the vacuum feedthrough, the latter of which would be connected to a voltage supply during trapping attempts. Therefore, the DC connections between each of the five electrodes and their voltage supplies were successfully verified using this technique.

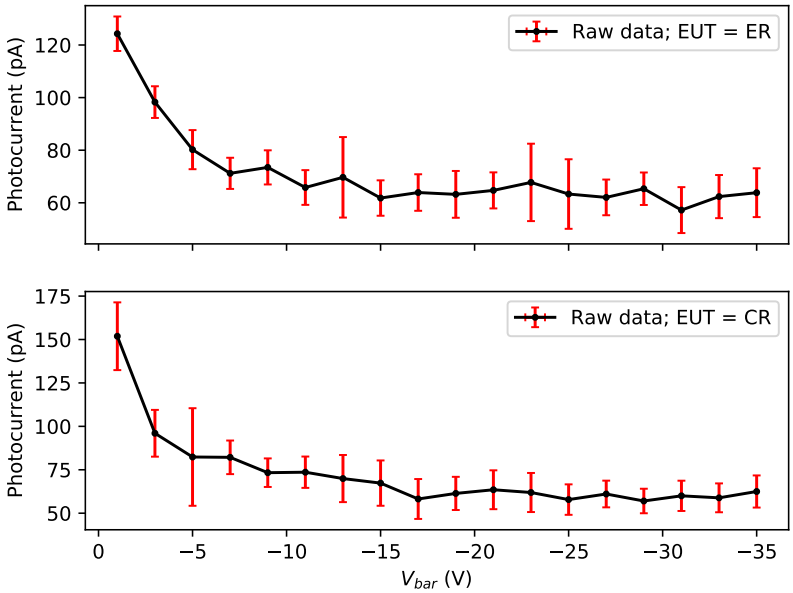

(A) The effects of using the right endcap and right correction electrodes (upper and lower plots respectively) as the EUT to produce the barrier voltage V_{bar}.

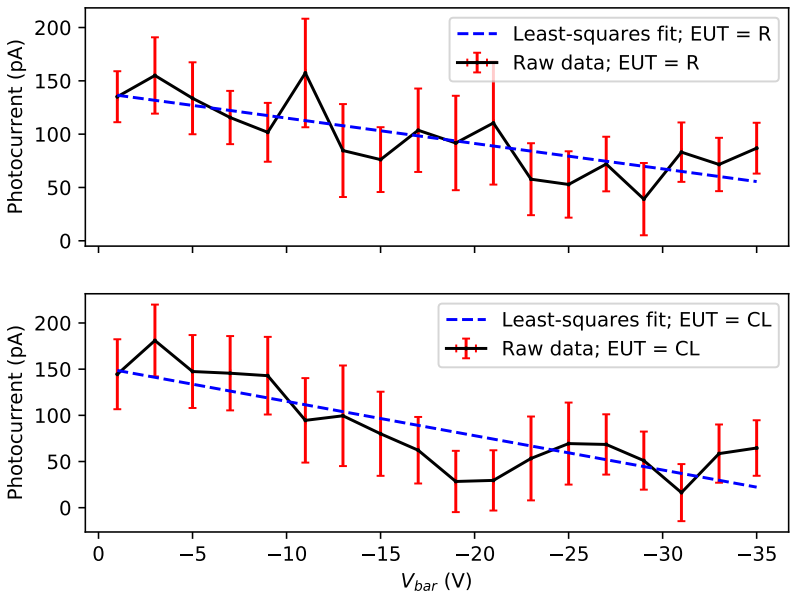

(B) The effects of using the ring and left correction electrodes (upper and lower plots respectively) as the EUT to produce the barrier voltage V_{bar}. The trends are less clear than those shown in Figure 4.19a and so linear least-squares fits are also shown to help guide the eye.

FIGURE 4.19: The relations between the photocurrent (collected through the left endcap) and the barrier voltage V_{bar} of the EUTs.

4.8 A summary of the photoelectric measurements

In (§4.1), the method for a typical photocurrent measurement was introduced. In (§4.2), different UV targets were investigated in order to maximise the photocurrent and it was determined that the best target would be one which would be constructed from gold leaf.

In (§4.3), the relation between the photocurrent and the bias voltage V_{col} of the collector was investigated. The first measurement in (§4.3.1) verified to a good extent other electrostatic models of the trap. The second measurement in (§4.3.1) was undertaken to determine the saturation voltage for use in future measurements. This voltage was approximately $V_{\text{col}} = +32.05$ V, which conveniently is the maximum output voltage for one of the high stability/precision power supplies available in the laboratory.

In (§4.4), the relation between the photocurrent and the pressure was investigated. In (§4.4.1), two measurements of the photocurrent as a function of the pressure were discussed for use as calibration curves. A calibration curve was used in (§4.4.2) to verify that in a pinched-off chamber which has not been baked-out, the outgassing of water causes the pressure to rise to that of the saturation vapor pressure of water at close to 23.38 mBar [186]. This measurement of outgassing lead to a bake-out being undertaken in (§4.5), which increased the photocurrent by a factor of (5.49 ± 0.06) (dimensionless). In (§4.5.3), a leak is shown during a cool-down, which likely resulted from the cool-down having occurred too rapidly.

In (§4.6), the effect of the mesh on the UV transmission into the chamber was investigated, which was reasonably consistent with that expected from the open area of the mesh.

In (§4.7), photocurrent measurements which were undertaken in the Geonium Chip Penning trap (§3) were discussed. A custom-built fibre was introduced in (§4.7.1) and in (§4.7.2) the relation between the photocurrent and the magnetic field strength (§3.3) was investigated. Photoelectric techniques which may be used to verify that the trap is working as expected are also included, for example verifying the optical fibre alignment (§4.7.3) and verifying that the DC voltage bias connections to the Geonium Chip are working as expected (§4.7.4).

Chapter 5

Implementing the magnetic field source

The planar magnetic field source of the Geonium Chip Penning trap has already been introduced in (§3.3). This chapter discusses the calibration and its verification and also discusses the control of the source, with the most significant results already having been published [97].

5.1 Calibration and verification

5.1.1 Introduction to the calibration

As mentioned in (§3.3) for the ideal source, only an axial component $\vec{B} = B_z\hat{u}_z$ exists (there is no component $\vec{B}_x = B_x\hat{u}_x$ nor $\vec{B}_y = B_y\hat{u}_y$) [97]. Furthermore, by considering the magnetic vector potential, in order to obtain a homogenous field $\vec{B} = B_z\hat{u}_z$ it is only required to compensate for the vertical inhomogeneities $B_{z,0j0}$ (2.21) [97] (which summarises the rigorous evaluation in [147]). It is also demonstrated analytically in [147] that when the ideal current loops are modelled as infinitely-long thin wires, the inhomogeneities $B_{z,0j0}$ ($1 \geq j \geq 3$) are each linear functions off all four ideal currents (note, this is the superposition principle [97]). This superposition principle still holds true for the Geonium Chip Penning trap's magnetic field source [97] (where the coils have finite

cross-section) and so a linear system of equations may be defined [97]

$$\overbrace{\begin{pmatrix} B_{z,000} \\ B_{z,010} \\ B_{z,020} \\ B_{z,030} \end{pmatrix}}^{\tilde{B}} = \overbrace{\begin{pmatrix} b^{(0)}_{z,000} & b^{(1)}_{z,000} & b^{(2)}_{z,000} & b^{(3)}_{z,000} \\ b^{(0)}_{z,010} & b^{(1)}_{z,010} & b^{(2)}_{z,010} & b^{(3)}_{z,010} \\ b^{(0)}_{z,020} & b^{(1)}_{z,020} & b^{(2)}_{z,020} & b^{(3)}_{z,020} \\ b^{(0)}_{z,030} & b^{(1)}_{z,030} & b^{(2)}_{z,030} & b^{(3)}_{z,030} \end{pmatrix}}^{\mathbf{\Gamma}(y_0)} \cdot \overbrace{\begin{pmatrix} I_0 \\ I_1 \\ I_2 \\ I_3 \end{pmatrix}}^{\tilde{I}} \tag{5.1a}$$

$$\tilde{I} = \mathbf{\Gamma}^{-1}(y_0) \cdot \tilde{B}, \tag{5.1b}$$

where $\tilde{B}$ is a vector which defines the magnetic field produced by the vector of currents $\tilde{I}$ [97]. In general, the element $b^{(n)}_{z,ijk}$ of the matrix $\mathbf{\Gamma}(y_0)$ corresponds to the inhomogeneity $B_{z,ijk}$ (2.21) in the magnetic field produced solely by the nth pair of loops from a current (normalised to) $I_n = 1$ (with units consistent with those of $\mathbf{\Gamma}(y_0)$) [97]. It is important to note that the elements of the matrix $\mathbf{\Gamma}(y_0)$ are dependent on the trapping height y_0 [97]. The magnetic fields produced by the coils may be calculated from the Biot-Savart Law [97] and so the elements $b^{(n)}_{z,0j0}$ are dependent on both the topology of the source (e.g. the locations of the coils) and also on the current densities (e.g. the number of turns in the coils). Therefore, the determination of the matrix $\mathbf{\Gamma}(y_0)$ may be considered to be a *calibration* [97] of the magnetic field source [97].

Two relevant magnetic field distributions $\tilde{B}$ (5.1a) for Penning traps are the *homogeneous field* [97] $\tilde{B}_h = (B_{z,000} \neq 0, 0, 0, 0)$ and the *magnetic bottle* [97] (non-zero curvature) $\tilde{B}_b = (B_{z,000} \neq 0, 0, B_{z,020} \neq 0, 0)$ [97]. A simulation of an homogeneous field produced by the Geonium Chip Penning trap's magnetic field source is shown in Figure 5.1.

In the ideal model described above (5.1) it is true that $B_{z,020} = -B_{z,002}$ and so the nullification $B_{z,020} = 0$ would also imply that $B_{z,002} = 0$ [97]. However, in the case of the real Geonium Chip Penning trap's magnetic field source, deviations from the model mean that it is only implied that $B_{z,020} \simeq -B_{z,002}$ and so $B_{z,002}$ should also be nullified [97]. The number of magnetic field coefficients which may be controlled is equal to the number of pairs of currents available (four) and so in order to control $B_{z,002}$ without introducing a fifth pair of currents [97], it may be chosen to let $B_{z,030}$ float (remain uncontrolled) [97].

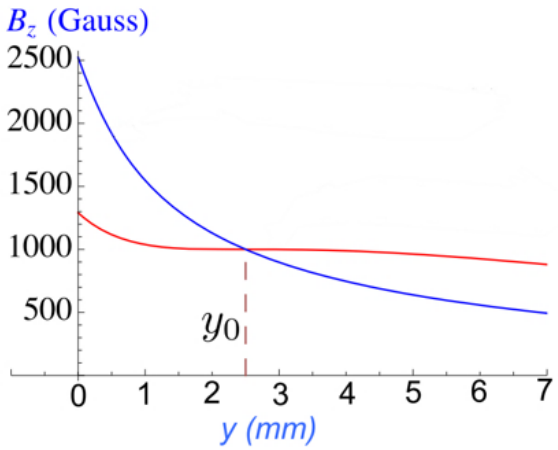

(A) Plotting the axial component $B_z(y)$ (2.21) of the magnetic field, as a function of the height y above the surface of the magnetic field source [97]. Adapted from [97].

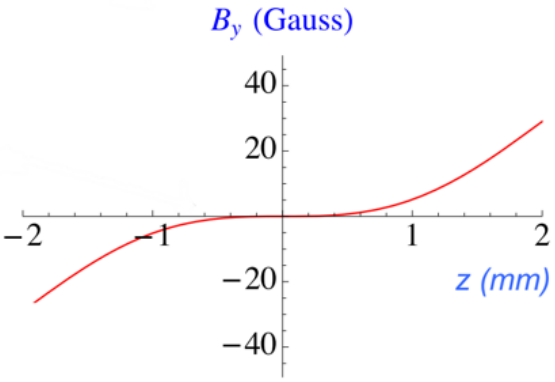

(B) Plotting the vertical component $B_y(z)$ of the magnetic field, as a function of the axial position z [97]. Adapted from [97].

FIGURE 5.1: Plots demonstrating an example target homogenous ($\vec{B} = B_z\hat{u}_z$) magnetic field produced by the field source [97]. The red plots in Figures 5.1a and 5.1b show different components of the compensated field (optimal I_0,I_1, I_2, I_3) [97], whereas the blue plot in 5.1a shows the uncompensated field (I_0 only) [97]. As desired, for locations close to the equilibrium trapping position $\vec{r}_0 = (0, y_0, 0)$ (§2.1.1), the component $B_z(y)$ shows homogeneity and the component $B_y(z)$ is close to zero [97]. Note, 1 mT = 10 G.

Therefore, a new matrix $\mathbf{\Gamma}'(y_0)$, similar to the matrix $\mathbf{\Gamma}(y_0)$ (5.1a), may also be defined [97]

$$\overbrace{\begin{pmatrix} B_{z,000} \\ B_{z,010} \\ B_{z,020} \\ B_{z,002} \end{pmatrix}}^{\tilde{B}'} = \overbrace{\begin{pmatrix} b^{(0)}_{z,000} & b^{(1)}_{z,000} & b^{(2)}_{z,000} & b^{(3)}_{z,000} \\ b^{(0)}_{z,010} & b^{(1)}_{z,010} & b^{(2)}_{z,010} & b^{(3)}_{z,010} \\ b^{(0)}_{z,020} & b^{(1)}_{z,020} & b^{(2)}_{z,020} & b^{(3)}_{z,020} \\ b^{(0)}_{z,002} & b^{(1)}_{z,002} & b^{(2)}_{z,002} & b^{(3)}_{z,002} \end{pmatrix}}^{\mathbf{\Gamma}'(y_0)} \cdot \overbrace{\begin{pmatrix} I_0 \\ I_1 \\ I_2 \\ I_3 \end{pmatrix}}^{\tilde{I}'} \tag{5.2a}$$

$$\tilde{I}' = \mathbf{\Gamma}'^{-1}(y_0) \cdot \tilde{B}'. \tag{5.2b}$$

Prior to the work discussed in this thesis, the first planar Geonium Chip Penning trap magnetic field source prototype was calibrated by Dr April Cridland Mathad [146]

and Dr John Lacy [123]. It was later decided to try to trap with higher magnetic field magnitudes/strengths $B_{z,000} = B_0$ (2.21) (2.11a) and so a second prototype was fabricated by Dr Jonathan Pinder (§3.3), where the coils of the new magnetic field source have much higher effective current densities due to the reduction in diameter of the NbTi wire from 400 μm to 100 μm [32]. Nonetheless, the calibration methods [123, 146] would still be valid for the second prototype, although the matrix $\mathbf{\Gamma}(\mathbf{y_0})$ would contain different numerical values. The first experimental determination of the matrix $\mathbf{\Gamma}(\mathbf{y_0})$ [123, 146] used a single magnetic field sensor (a Hall probe) which was mounted to the arm of a computer-numeric-control machine with a programmable location (x, y and z), to map the magnetic field component $B_z(y)$. As discussed in [123] this method had some limitations, for example i) a long time was required to scan over y which produced large uncertainties and ii) the source could only be calibrated outside the cryostat which risked misalignment when installed in the cryostat.

Therefore [123], a Hall probe array (orientated to measure B_z at different y) (§5.1.1) was used for an improved calibration. Furthermore, the original calibration [123, 146] had been conducted at room-temperature and although a $\approx$ 4 K correction was later applied [146], $\mathbf{\Gamma}(y_0)$ had not been determined specifically at $\approx$ 4 K.

As discussed in (§3.3.1), the calibration presented in this thesis (§5.1.2) (as introduced in this section), could be fine-tuned using a trapped electron as a magnetic sensor [97].

The Hall probe array

Every measurement of $B_z(y)$ was conducted using an *Arepoc s.r.o MULTI-7U* Hall probe array [123]. The array was manufactured with seven permanently fixed Hall probes which shared a bias current and which were arranged in a line with an inter-probe spacing of 0.5 mm [123], as can be seen in Figure 5.2b. After the work in [123], Dr John Lacy mounted the Hall probe array to a block of *Macor* which was mounted centrally on a printed circuit board (the *calibration board*) [97], as can be seen in Figure 5.2c. The calibration board was then mounted to the upper surface of the magnetic field source by Dr John Lacy and Dr Jonathan Pinder, such that the probes were positioned at $x = 0$, $z = 0$

(see Figures 5.2b and 5.2c) [97]. Each Hall probe was orientated to measure B_z at some height y [97]. Generally, the height y is referenced to the surface of the Geonium Chip electric field source (§3.2) (where $y_E = 0$ mm at the surface of the chip), however for convenience, the magnetic field analysis was conducted to a shifted y, where instead $y_B = 0$ mm was defined as the centre of the magnetic field source [97]. By considering (Figure 5.2a) the thicknesses of the magnetic field source, the electric field source (the Geonium Chip) and also the calibration board, y_B may be transformed into y_E using the relation $y_B = y_E + 3.8$ mm. In the coordinate system y_B, the ith probe was positioned at a height $y_{B,i} = [(3.00 + 0.58 + 1.00) + 0.5(i - 1)]$ mm above the centre of the magnetic field source, with $i = 1 \ldots 7$. The electrostatic potential during trapping attempts has typically been optimised for a trapping height $y_{E,0} = 1.45$ mm (2.6) above the surface of the chip, which may be transformed to $y_{B,0} = 5.25$ mm.

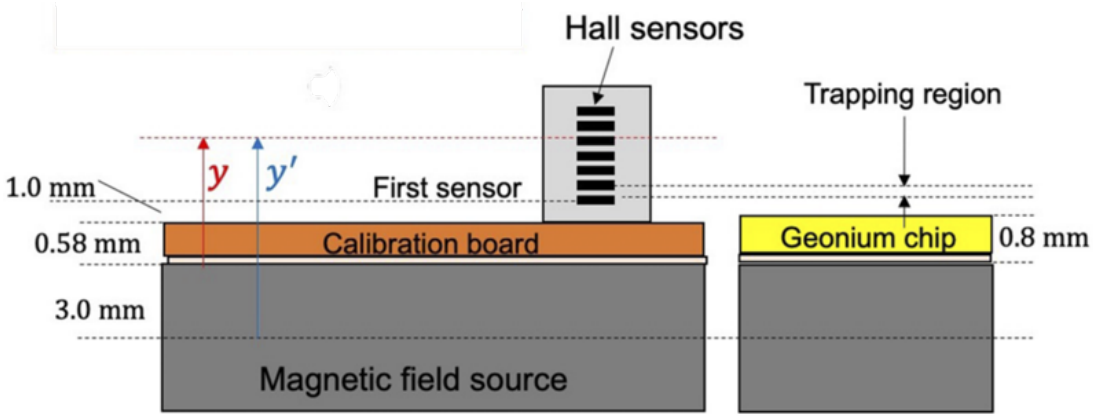

(A) Schematics of the Hall probe array setup. Adapted from [97].

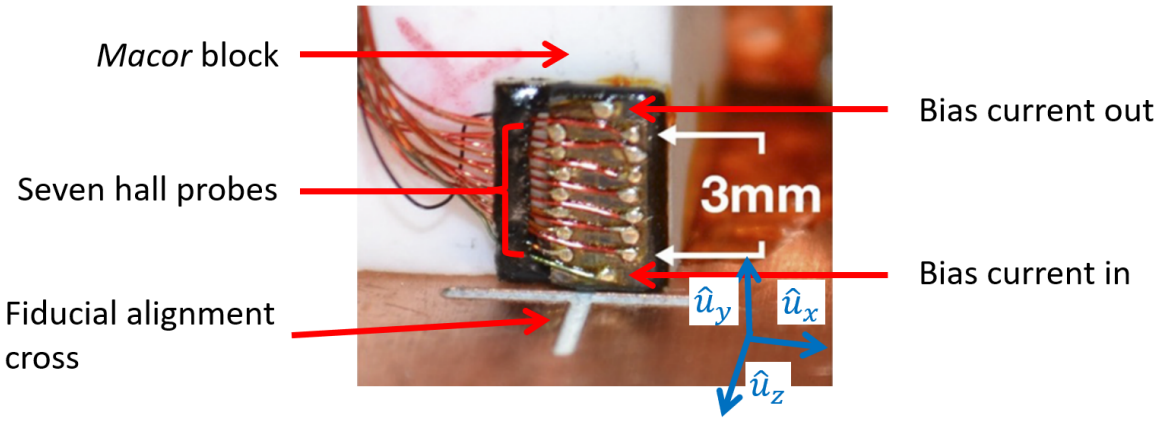

(B) Schematics of the Hall probe array setup. Adapted from [97].

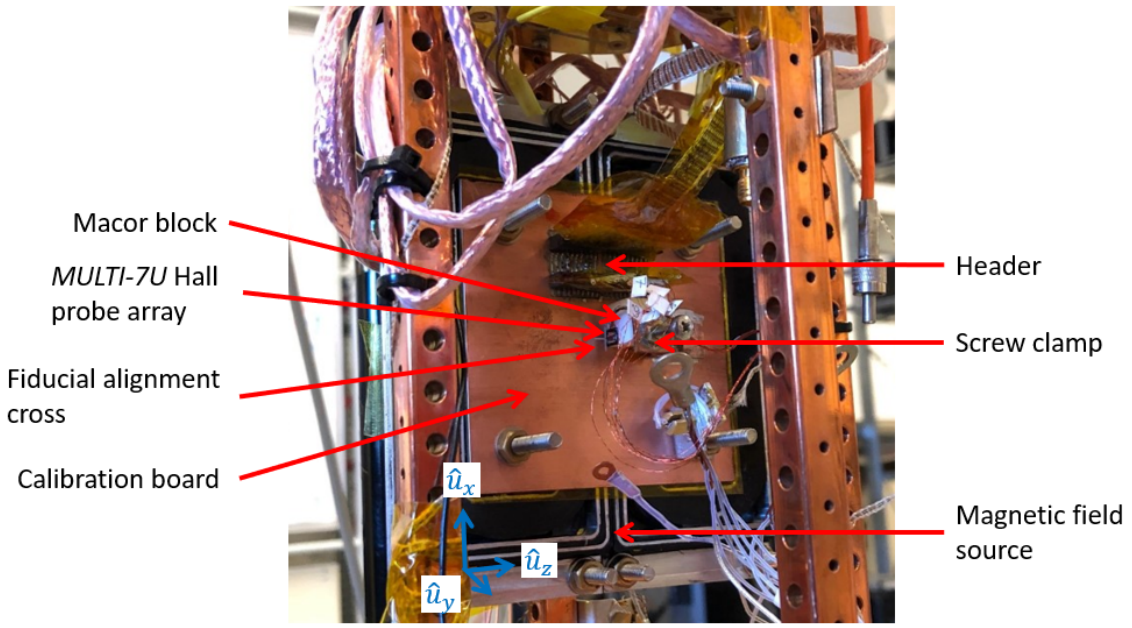

(C) A photograph of the calibration setup inside the cryostat. The setup was fabricated and installed by Dr John Lacy and Dr Jonathan Pinder.

FIGURE 5.2: The setup for the calibration of the magnetic field source. In Figures 5.2b and 5.2c, the unit vectors $\hat{u}$ point in the correct directions but do not originate from the origin of the co-ordinate system - the centre of the fiducial alignment cross is at $(x, y_B, z) = (0, 3.58, 0)$ mm.

5.1.2 Calibration at ≈ 4 K

The work discussed in this section (§5.1.2) has already been published [97] and so only a summary is included in this thesis.

This calibration was conducted in the Geonium Chip Penning trap at ≈ 4 K, so the calibration and resulting magnetic fields should be valid while trying to trap electrons. As described in (§5.1.1), the calibration of the magnetic field source may be achieved by determining the matrices $\mathbf{\Gamma}(y_0)$ and $\mathbf{\Gamma}'(y_0)$, using measurements of the magnetic fields $B_z(y)$ produced by each current separately. As introduced in (§5.1.1), the element $b^{(n)}_{z,ijk}$ of the matrix $\mathbf{\Gamma}(y_0)$ corresponds to the inhomogeneity $B^{(n)}_{z,ijk}$ (2.21) in the magnetic field [97], produced solely by the nth pair of loops from a current (normalised to) $I_n = 1$ (with units consistent with those of the matrix $\mathbf{\Gamma}(y_0)$) [97]. More generally, for example, the elements in the nth column of the matrix $\mathbf{\Gamma}(y_0)$ (5.1) may be determined by setting the currents ($\{I_n \neq 0, I_m = 0, \forall m \neq n\}$ [97]) and then measuring $B_z(y)$, using the Hall probe array (§5.1.1) [97]. Also, the elements $b^{(n)}_{z,002}$ of the fourth row of the matrix $\mathbf{\Gamma}'(y_0)$ (5.2) may be determined in a similar way also from a three-dimensional fit to the $B_z(y)$ data from the Hall probe array (§5.1.1) [97]. For example, the elements $b^{(n)}_{z,0j0}$ of the matrix $\mathbf{\Gamma}(y_0)$ (5.1) and the elements $b^{(n)}_{z,002}$ of the fourth row of the matrix $\mathbf{\Gamma}'(y_0)$ (5.2) may be calculated using

$$b^{(n)}_{z,0j0} = \frac{B^{(n)}_{z,0j0}}{I_n} \tag{5.3a}$$

$$b^{(n)}_{z,002} = \frac{B^{(n)}_{z,002}}{I_n}. \tag{5.3b}$$

In order to simplify the arithmetic (5.3a), each measured $B^{(n)}_z(y)$ with the Hall probe array was determined with a corresponding current $I_n = 1$ A [97].

It is important to note that the coefficients $B^{(n)}_{z,ijk}$ (2.21) change with the height y_0 and so the matrices $\mathbf{\Gamma}(y_0)$ (5.1) and $\mathbf{\Gamma}'(y_0)$ (5.2) will also vary for different heights [97]. Therefore, in order to determine $B^{(n)}_{z,0j0}$ (5.3a) at some height y_0, the measured magnetic field $B^{(n)}_z(y)$

may be expanded around $\vec{r}_0 = (0, y_0, 0)$ (§2.1.1) using a Taylor series expansion [97]. Similarly, in order to determine $B^{(n)}_{z,002}$ (5.3b) another Taylor expansion around $\vec{r}_0 = (0, y_0, 0)$ (§2.1.1) may be applied [97], where both expansions may be written [97]

$$B^{(n)}_z(0, y, 0) = \sum_{j=0}^{j=\infty} B^{(n)}_{z,0j0}(y - y_0)^j \tag{5.4a}$$

$$B^{(n)}_z(0, y_0, z) = \sum_{j=0; j \text{ odd}}^{j=\infty} B^{(n)}_{z,00k} z^k. \tag{5.4b}$$

In practice, the Taylor series coefficients $B^{(n)}_{z,0j0}$ (5.4a) may be determined by conducting a polynomial fit around the equilibrium trapping position y_0, with consideration to the normalisation factor $1/(j!)$ which arises due to the differing coefficient definitions from polynomial and Taylor series [97]. Similarly, the Taylor series coefficients $B^{(n)}_{z,00k}$ (5.4b) may be determined from an equivalent polynomial fit around z while similarly also considering the use of a normalisation factor $(1/k!)$ [97].

The Hall probe array (§5.1.1) could only measure B_z at seven values of y and therefore polynomial fits to the seven raw data points gave unreliable (§5.1.4) high-order coefficients (5.4a) [97]. Therefore, in order to obtain more data points for a smoother plot to obtain more reliable high-order polynomial coefficients, prior to conducting a fit to a polynomial function (5.4a), the raw data $B^{(n)}_z(y)$ was used in a fit to a physical model of the magnetic field produced by the nth pair of coils [97]. The model was created by Dr José Verdú-Galiana and modelled each coil with finite spatial dimensions and with an effective current density J_n as a free fitting parameter [97]. The model performed a three-dimensional numerical integration of the Biot-Savart Law, where the magnetic field is evaluated at $\vec{r}$ due to source currents at $\vec{r}'$ [36]

$$\vec{B}^{(n)}(\vec{r}) = \frac{\mu_0}{4\pi} \oint dV' \frac{\vec{J}_n \times (\vec{r} - \vec{r}')}{|\vec{r} - \vec{r}'|^3}. \tag{5.5}$$

The fit to the nth current pair also included a tilt θ_n of the Hall probe array as a free fitting parameter, where it was assumed that the array had a tilt θ relative to the $\hat{u}_x - \hat{u}_z$ plane

TABLE 5.1: Results from the fits (5.5) to $B_z^{(n)}(y)$, for the nth pair of currents. The optimal fitting parameters θ_n and J_n are shown along with $A_{\text{effective}}^{(n)}$ (5.7) and $N_{\text{effective}}^{(n)}$ (5.6). The counted number of turns $N_{\text{coil}}^{(n)}$ in each real coil of the nth set of currents has been included for comparison to $N_{\text{effective}}^{(n)}$, which are in good agreement [97]. The weighted mean and standard deviation of θ is $(6.6 \pm 1.8)^\circ$ [97].

n	θ_n (°)	J_n (A/mm^2)	$A_{\text{effective}}^{(n)}$ (mm^2)	$N_{\text{effective}}^{(n)}$	$N_{\text{coil}}^{(n)}$
0	(6.2 ± 0.4)	(25.54 ± 0.05)	0.03915	123	120
1	(7.9 ± 1.0)	(31.37 ± 0.06)	0.03188	226	225
2	(1.4 ± 1.9)	(37.73 ± 0.07)	0.02651	1992	1995
3	(9.0 ± 1.2)	(43.93 ± 0.10)	0.02276	1977	1982

[97]. However [97], the tilt angle was most likely due to an asymmetry in the winding of the coils along $\hat{u}_z$, rather than due to a real misalignment of the sensor board, with the idea proposed as a result of the rewinding of one coil changing θ.

In order to help validate the fits, the predicted number of turns $N_{\text{effective}}^{(n)}$ in one coil in the nth pair of currents may be calculated using the effective cross sectional area $A_{\text{effective}}^{(n)}$ of one coil in the nth pair of currents [97]

$$N_{\text{effective}}^{(n)} = \frac{A_{\text{coil}}^{(n)}}{A_{\text{effective}}^{(n)}} \qquad (5.6) \qquad\qquad A_{\text{effective}}^{(n)} = \frac{I_n}{J_n}, \qquad (5.7)$$

where $A_{\text{coil}}^{(n)}$ is the cross sectional area of one fabricated coil in the nth pair of currents. The fits to the measured $B_z^{(n)}(y)$ are shown in Figure 5.3 and the fitting parameters are shown in Table 5.1.

This procedure was applied to determine the matrices $\mathbf{\Gamma}(y_0)$ (5.1) and $\mathbf{\Gamma}'(y_0)$ (5.2). The fits of the raw Hall probe array measurements to the Biot-Savart model (5.5) were used to numerically evaluate $B_z^{(n)}(y)$ for 200 values of y in the range of y which was measurable by the Hall probe array (§5.1.1). A polynomial fit was conducted from order $j = 0$ up to and including order $j = 10$, in order to determine the Taylor series coefficients $B_{z,0j0}^{(n)}$ (5.4a) [97]. Note that changing the highest order in the polynomial fit also changes each of the previous coefficients and so j needs to be chosen arbitrarily high, even if not all of the fit coefficients will be used to calculate the matrices $\mathbf{\Gamma}(y_0)$ (5.1) or $\mathbf{\Gamma}'(y_0)$ (5.2). The elements

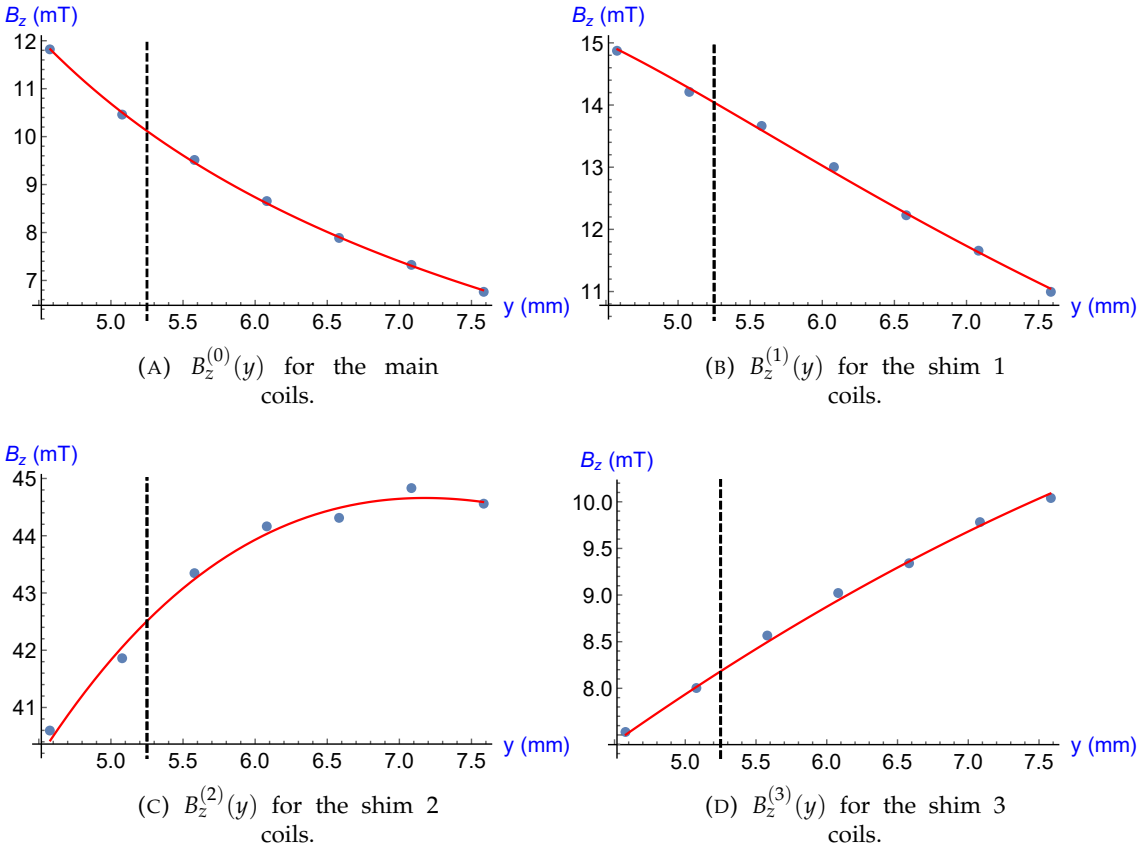

(A) $B_z^{(0)}(y)$ for the main coils.

(B) $B_z^{(1)}(y)$ for the shim 1 coils.

(C) $B_z^{(2)}(y)$ for the shim 2 coils.

(D) $B_z^{(3)}(y)$ for the shim 3 coils.

FIGURE 5.3: Plots of $B_z^{(n)}(y)$. The blue circles show the mean raw data measured with the Hall probe array, the continuous red lines show the fits to the Biot-Savart Law (5.5) and the black vertical dashed lines show the trapping height $y_{B,0} = 5.25$ mm or $y_{E,0} = 1.45$ mm [97].

$b_{z,0j0}^{(n)}$ (5.3a) of the matrix $\mathbf{\Gamma}(y_0)$ have been determined using this method, for a trapping height $y_{E,0} = 1.45$ mm or $y_{B,0} = 5.25$ mm [97]. Similarly, in order to obtain the elements $b_{z,002}^{(n)}$ in the final row (5.3b) of the matrix $\mathbf{\Gamma}'(y_0)$ a similar method was used, whereby the three-dimensional model (5.5) which was generated from the measurements of $B_z^{(n)}(y)$, was used to calculate $B_z^{(n)}(z)$ for 200 values of z [97]. Then, analogously, polynomial fits were conducted to each I_n in order to determine the Taylor series coefficients $B_{z,00k}^{(n)}$ (5.4b) and then the elements $b_{z,002}^{(n)}$ (5.3b) were determined [97].

The matrix $\mathbf{\Gamma}(y_0)$ was calculated to be [97]

$$\overbrace{\begin{pmatrix} (10.117 \pm 0.014) & (14.041 \pm 0.023) & (42.46 \pm 0.05) & (8.183 \pm 0.019) \\ (-2.152 \pm 0.024) & (-1.343 \pm 0.026) & (2.60 \pm 0.10) & (0.971 \pm 0.025) \\ (0.486 \pm 0.010) & (-0.054 \pm 0.005) & (-0.91 \pm 0.05) & (-0.064 \pm 0.003) \\ (-0.118 \pm 0.004) & (0.061 \pm 0.005) & (0.084 \pm 0.006) & (-0.00115 \pm 0.00009) \end{pmatrix}}^{\mathbf{\Gamma}(y_{E,0}=1.45\text{ mm})}, \quad (5.8)$$

where the elements $b^{(n)}_{z,0j0}$ in the jth row ($i = 0, 1, 2, 3$) have units mT/mm^j [97]. The matrix $\mathbf{\Gamma}'(y_0)$ was calculated to be [97]

$$\overbrace{\begin{pmatrix} (10.117 \pm 0.014) & (14.041 \pm 0.023) & (42.46 \pm 0.05) & (8.183 \pm 0.019) \\ (-2.152 \pm 0.024) & (-1.343 \pm 0.026) & (2.60 \pm 0.10) & (0.971 \pm 0.025) \\ (0.486 \pm 0.010) & (-0.054 \pm 0.005) & (-0.91 \pm 0.05) & (-0.064 \pm 0.003) \\ (-0.610 \pm 0.01) & (0.073 \pm 0.005) & (0.92 \pm 0.05) & (0.092 \pm 0.003) \end{pmatrix}}^{\mathbf{\Gamma}'(y_{E,0}=1.45\text{ mm})}, \quad (5.9)$$

where the elements $b^{(n)}_{z,0j0}$ in the jth row ($i = 0, 1, 2$) have units mT/mm^j [97] and the elements $b^{(n)}_{z,002}$ in the final row have units mT/mm^2.

5.1.3 Measurements of 300 mT homogeneous fields

The work discussed in this section (§5.1.2) has already been published [97] and so only a summary is included in this thesis.

In order to verify the calibration procedure (§5.1.2) [97], the matrix $\mathbf{\Gamma}(y_0)$ (5.8) was used (5.1b) to determine currents $\tilde{I}$ for an homogeneous magnetic field distribution [97] and similarly, the matrix $\mathbf{\Gamma}'(y_0)$ (5.9) was also used (5.2b) to determine currents $\tilde{I}'$ for another homogeneous magnetic field distribution [97]. These calculated current sets $\tilde{I}$ and $\tilde{I}'$ should have produced two homogeneous fields, both with $B_{z,000} = 0$ mT, $B_{z,010} = 0$ mT/mm and $B_{z,020} = 0$ mT/mm^2 and with the former ($\tilde{I}$) also setting $B_{z,030} = 0$ mT/mm^3 and the latter ($\tilde{I}'$) also setting $B_{z,002} = 0$ mT/mm^2. However, the required current sets contained high currents, which not only complicate the supply of the currents but also

increases the thermal load - which for each current I_n is proportional to the square of that current [97].

Therefore, the currents were optimised with the aim to reduce the thermal load by reducing the maximum current [97]. This optimisation was achieved graphically for $\tilde{I}$ by plotting I_0, I_1, I_2 and I_3 each as functions of I_3 and by then determining the I_3 with the lowest maximum I_n in $\tilde{I}(I_3)$ [97]. This optimisation was repeated for $\tilde{I}'$ [97]. This method comes at the expense of losing control of one magnetic field inhomogeneity [97], where the fourth inhomogeneity is left *floating* [97]. The resulting *reduced* [97] sets of currents are denoted $\tilde{I}_{\text{reduced}}$ or $\tilde{I}'_{\text{reduced}}$. Furthermore, as part of the optimisations, the currents I_1, I_2 and I_3 were normalised to that of I_0, in order to take into account systematic errors in each of the nominal output currents from the power supply.

These two reduced (optimised) sets of currents $\tilde{I}_{\text{reduced}}$ and $\tilde{I}'_{\text{reduced}}$ were scaled for 300 mT imperfectly-homogeneous magnetic fields which were defined by [97]

$$\underbrace{\begin{pmatrix} B_{z,000} = 300\ \text{mT} \\ B_{z,010} = 0 \\ B_{z,020} = 0 \\ B_{z,030} \neq 0 \end{pmatrix}}_{\tilde{B}_{\text{reduced}}} = \mathbf{\Gamma}(y_{E,0} = 1.45\ \text{mm}) \cdot \underbrace{\begin{pmatrix} 7.886\ \text{A} \\ 0.0991\ \text{A} \\ 3.633\ \text{A} \\ 7.888\ \text{A} \end{pmatrix}}_{\tilde{I}_{\text{reduced}}} \tag{5.10}$$

and

$$\underbrace{\begin{pmatrix} B_{z,000} = 300\ \text{mT} \\ B_{z,010} = 0 \\ B_{z,020} \neq 0 \\ B_{z,002} = 0 \end{pmatrix}}_{\tilde{B}'_{\text{reduced}}} = \mathbf{\Gamma}'(y_{E,0} = 1.45\ \text{mm}) \cdot \underbrace{\begin{pmatrix} 6.768\ \text{A} \\ 0.0013\ \text{A} \\ 3.730\ \text{A} \\ 6.770\ \text{A} \end{pmatrix}}_{\tilde{I}'_{\text{reduced}}}. \tag{5.11}$$

The current sets $\tilde{I}_{\text{reduced}}$ (5.10) and $\tilde{I}'_{\text{reduced}}$ (5.11) were driven through the magnetic field source and the resulting magnetic fields $B_z(y)$ were measured using the Hall probe array (§5.1.1) [97], with the final B_z at each y being the mean of 111 measurements determined over approximately eight minutes and twenty seconds. In order to determine the

magnetic field distributions $\tilde{B}^{(\text{meas})}_{\text{reduced}}$ and $\tilde{B}'^{(\text{meas})}_{\text{reduced}}$ of the measured reduced fields $B_z(y)$, a method was applied which was similar to that used for determining the Taylor series coefficients (5.4) in the determination of the elements of the matrices $\mathbf{\Gamma}(y_0)$ and $\mathbf{\Gamma}'(y_0)$ (§5.1.2) [97]. Firstly [97], in order to increase the number of data points used in the polynomial fit from 7 (one per Hall probe) to 500, a fit to the Biot-Savart Law (5.5) was again conducted, but this time only using the effective current densities J_0, J_2 and J_3 as the fitting parameters. The effective current density J_1 was fixed to the value for J_1 which was determined (estimated from a fit) in the calibration (Table 5.1) [97], in order to improve the fit by reducing the number of fitting parameters [97]. It was chosen [97] to fix J_1 rather than any other J_n, because in both current sets $\tilde{I}_{\text{reduced}}$ (5.10) and $\tilde{I}'_{\text{reduced}}$ (5.11), I_1 was the smallest current and $I_1 \leq 0.1$ A, so I_1 did not contribute significantly to the magnetic fields.

It also appeared that two of the seven Hall probes had some offset and so the magnetic field distributions $\tilde{B}^{(\text{meas})}_{\text{reduced}}$ and $\tilde{B}'^{(\text{meas})}_{\text{reduced}}$ of the measured fields were each defined as the mean of two distributions [97], where one distribution was fit to the measurements from all seven probes and the other distribution was just fit to the measurements from the five less unreliable probes [97]. This is discussed in more detail in the paper [97]. The results of the measured fields are shown in Tables 5.2 and 5.3; the fields are reasonably homogeneous [97]. Plots of the measured magnetic fields $\tilde{B}^{(\text{meas})}_{\text{reduced}}$ and $\tilde{B}'^{(\text{meas})}_{\text{reduced}}$ are shown in Figures 5.4a and 5.4b. The currents in $\tilde{I}_{\text{reduced}}$ (5.10) are those which are scaled to make homogeneous fields during trapping attempts, typically with $B_{z,000} = 100$ mT.

5.1.4 Measurement of a 500 mT homogeneous field

As described in (§5.1.2), the elements (5.3a) of the matrix $\mathbf{\Gamma}(y_0)$ (5.1) may be determined from Taylor expansion coefficients (5.4a). These expansion coefficients may be determined from polynomial fits which are conducted to $B_z^{(n)}(y)$ data, where quasi-continuous (smooth) $B_z^{(n)}(y)$ is evaluated from fits of $B_z^{(n)}(y)$ to the Biot-Savart Law (5.5). It was also mentioned (§5.1.2) that polynomial fits to the seven raw data points $B_z(y)$ from just seven Hall probes gave unreliable high-order coefficients.

TABLE 5.2: Results [97] from the measurements of the 300 mT homogeneous field produced by $\tilde{I}_{\text{reduced}}$ (5.10). The desired field expansion coefficients $\tilde{B}_{\text{reduced}}$ are those desired in (5.10). The measured field expansion coefficients $\tilde{B}^{(\text{meas})}_{\text{reduced}}$ are those determined from the Taylor expansion (5.4a) of the measured magnetic field strengths $B_z(y)$.

$B_{z,0j0}$	Desired: $\tilde{B}_{\text{reduced}}$	Measured: $\tilde{B}^{(\text{meas})}_{\text{reduced}}$
$B_{z,000}$ (mT)	300.00	(302.25 ± 0.07)
$B_{z,010}$ (mT/mm)	0.00	(-0.20 ± 0.08)
$B_{z,020}$ (mT/mm^2)	0.0	(0.0 ± 0.2)
$B_{z,030}$ (mT/mm^3)	(floating)	(-0.8 ± 0.2)

TABLE 5.3: Results [97] from the measurements of the 300 mT homogeneous field produced by $\tilde{I}'_{\text{reduced}}$ (5.11). The desired field expansion coefficients $\tilde{B}'_{\text{reduced}}$ are those desired in (5.11). The measured field expansion coefficients $\tilde{B}'^{(\text{meas})}_{\text{reduced}}$ are those determined from the Taylor expansion (5.4b).

$B_{z,0j0}$	Desired: $\tilde{B}'_{\text{reduced}}$	Measured: $\tilde{B}'^{(\text{meas})}_{\text{reduced}}$
$B_{z,000}$ (mT)	300.00	(300.95 ± 0.007)
$B_{z,010}$ (mT/mm)	0.00	$(-0.04 \pm .06)$
$B_{z,020}$ (mT/mm^2)	(floating)	(-0.7 ± 0.2)
$B_{z,030}$ (mT/mm^3)	(floating)	(-0.5 ± 0.2)

In order to demonstrate the obligation to first fit to the Biot-Savart Law (5.5), a matrix $\mathbf{\Gamma}_{500\text{ mT}}(y_0)$ was determined by performing the polynomial fit to obtain the Taylor expansion coefficients (5.4a) from the Hall probe data points $B_z(y)$ [97], **without** first fitting to the Biot-Savart Law to determine a smooth plot $B_z^{(n)}(y)$ [97]. This matrix $\mathbf{\Gamma}_{500\text{ mT}}(y_0)$ was then used to obtain the currents $\tilde{I}_{\text{reduced, 500 mT}}$ for an homogeneous 500 mT field (where no optimisation was required) [97] which can be defined using

$$\underbrace{\begin{pmatrix} B_{z,000} = 500\text{ mT} \\ B_{z,010} = 0 \\ B_{z,020} = 0 \\ B_{z,030} = 0 \end{pmatrix}}_{\tilde{B}_{\text{reduced, 500 mT}}} = \mathbf{\Gamma}_{500\text{ mT}}(y_{E,0} = 1.45\text{ mm}) \cdot \underbrace{\begin{pmatrix} 9.070\text{ A} \\ 3.012\text{ A} \\ 8.288\text{ A} \\ 0.6419\text{ A} \end{pmatrix}}_{\tilde{I}_{\text{reduced, 500 mT}}} . \tag{5.12}$$

Please note, a quench (§5.2) permanently damaged the prototype shim 2 which was used in this determination of $\mathbf{\Gamma}_{500\text{ mT}}(y_0)$ and the subsequent 500 mT measurement. Therefore, a replacement was built (by Dr Jonathan Pinder) which was calibrated in (§5.1.2) and used to make a 300 mT field (§5.1.3), which is still in use at the time of the submission of this thesis in order to make (typically) 100 mT homogeneous fields while trying to trap electrons. In other words, the magnetic field source which was discussed in (§5.1.2) and (§5.1.3), was built after (as a result of a replacement only of shim 2) the magnetic field source which is discussed in this section (§5.1.4).

The currents $\tilde{I}_{\text{reduced, 500 mT}}$ in (5.12) were set and the Hall probe array (§5.1.1) was used to measure $B_z(y)$ [97], with each data point in the final $B_z(y)$ being stated as the mean of 221 independent measurements. The field expansion coefficients $\tilde{B}^{(\text{meas})}_{\text{reduced, 500 mT}}$ for the measured 500 mT field were determined from a polynomial fit to a Biot-Savart fit (the same method that was used to determine $\tilde{B}'^{(\text{meas})}_{\text{reduced}}$ and $\tilde{B}^{(\text{meas})}_{\text{reduced}}$ in Tables 5.2 and 5.3 for the 300 mT field) [97]. Once again, due to the offsets in two Hall probes, the magnetic field distribution $\tilde{B}^{(\text{meas})}_{\text{reduced, 500 mT}}$ of the measured 500 mT field was defined as the mean of two distributions [97], where one distribution was fit to all seven probes and the other distribution was just fit to the five less unreliable probes [97].

TABLE 5.4: Results [97] from the measurements of the 500 mT homogeneous field produced by $\tilde{I}_{\text{reduced, 500 mT}}$ (5.12). The desired field expansion coefficients $\tilde{B}_{\text{reduced, 500 mT}}$ are those desired in (5.12) (no optimisation was applied and so there are no floating inhomogeneities). The measured field expansion coefficients $\tilde{B}^{(\text{meas})}_{\text{reduced, 500 mT}}$ are those determined from the Taylor expansion (5.4b).

$B_{z,0j0}$	Desired: $\tilde{B}_{\text{reduced, 500 mT}}$	Measured: $\tilde{B}^{(\text{meas})}_{\text{reduced, 500 mT}}$
$B_{z,000}$ (mT)	500.0	(512.5 ± 0.8)
$B_{z,010}$ (mT/mm)	0.0	(-2.4 ± 0.2)
$B_{z,020}$ (mT/mm^2)	0.0	(-3.1 ± 0.6)
$B_{z,030}$ (mT/mm^3)	0.0	(-0.4 ± 0.3)

The final values are included in Table 5.4 and the measured magnetic field data are plotted in Figure 5.4c. By comparing the results $\tilde{B}^{(\text{meas})}_{\text{reduced, 500 mT}}$ for the 500 mT field in Table 5.4, to the results $\tilde{B}^{(\text{meas})}_{\text{reduced}}$ for the 300 mT field produced by $\tilde{I}_{\text{reduced}}$ (5.10) in Table 5.2, it can be seen that the relative inhomogeneities $B_{z,010}$ and $B_{z,020}$ for the 500 mT field are much greater than the corresponding relative inhomogeneities for the 300 mT field [97]. In particular, it is the inhomogeneities relative to $B_{z,000}$ which should be considered and which are also worse for the 500 mT field (the matrix $\mathbf{\Gamma}(y_0)$ without the Biot-Savart Law (5.5)) than for the 300 mT field (the matrix $\mathbf{\Gamma}(y_0)$ with the Biot-Savart Law (5.5)). Furthermore, the relative differences between the desired and measured homogeneous terms $B_{z,000}$ are worse for the 500 mT field.

Therefore, when determining the matrix $\mathbf{\Gamma}(y_0)$ via the determination of the Taylor series coefficients (5.4a) from polynomial fits [97], fits to the Biot-Savart Law (5.5) should first be conducted in order to determine smooth functions $B_z^{(n)}(y)$ for fitting [97]. A fit to the Biot-Savart Law (5.5) is required to determine $b^{(n)}_{z,002}$ (5.3b) in the matrix $\mathbf{\Gamma}'(y_0)$ (5.9) [97], because in order to determine the Taylor expansion (5.4b) in z, $B_z(z)$ cannot first be measured using the Hall probe array (§5.1.1) with the existing setup but may instead first be determined from the three-dimensional model of the Biot-Savart Law (5.5) [97].

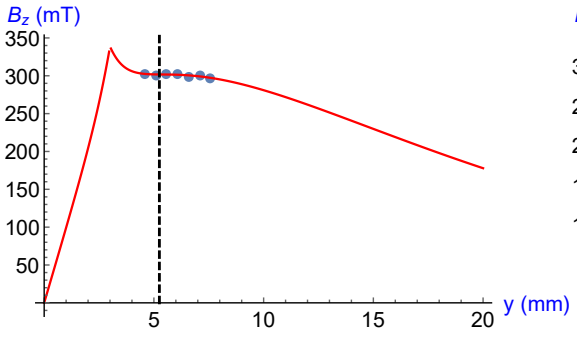

(A) The measured $\tilde{B}^{(\text{meas})}_{\text{reduced}}$ as produced by $\tilde{I}_{\text{reduced}}$ (5.10), for a 300 mT homogeneous field with a desired $B_{z,020} = 0$.

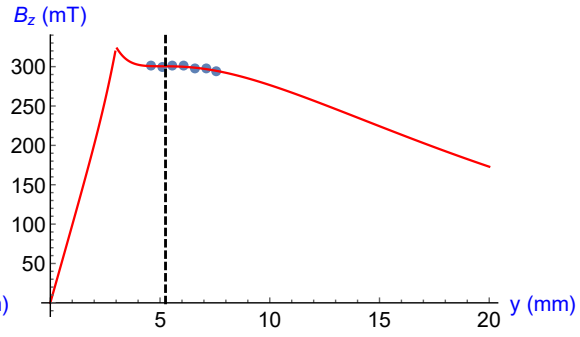

(B) The measured $\tilde{B}'^{(\text{meas})}_{\text{reduced}}$ as produced by $\tilde{I}'_{\text{reduced}}$ (5.11), for a 300 mT homogeneous field with a desired $B_{z,002} = 0$.

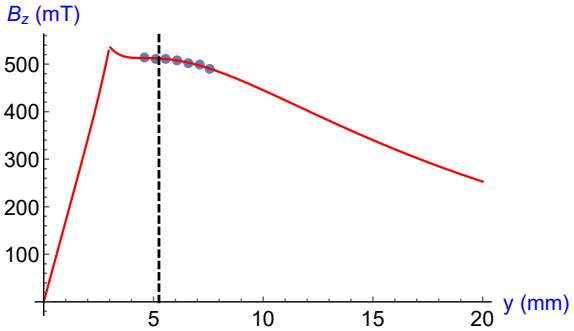

(C) The measured $\tilde{B}^{(\text{meas})}_{\text{reduced, 500 mT}}$ as produced by $\tilde{I}_{\text{reduced, 500 mT}}$ (5.12), for a 500 mT homogeneous field with desired $B_{z,020} = B_{z,030} = 0$.

FIGURE 5.4: Plots of the magnetic field distributions which were produced by the planar magnetic field source. The blue circles show the mean raw data measured with the Hall probe array, the continuous red lines show the fits to the Biot-Savart Law (5.5) and the black vertical dashed lines show the trapping height $y_{B,0} = 5.25$ mm or $y_{E,0} = 1.45$ mm [97].

5.2 Superconductor quenching

5.2.1 An introduction to superconductor quenching

The current carrying coils in the Geonium Chip magnetic field source are constructed from niobium-titanium NbTi wire (§3.3). NbTi may only superconduct if the temperature, magnetic field and current density are all below their critical values T_c, B_c, and J_c respectively, where the combinations of parameters may be described by a three-dimensional *critical surface* [196]. By considering this critical surface [196, p. 16], in a magnetic field of 1 T (§5.1.4) and with a current density of 50 A/mm^2 (Table 5.1), the critical temperature is approximately 9-10 K. If any region of the superconductor enters the resistive state [197], then a *thermal runaway* (also known as a *quench* when in the context of liquid helium cryostats with rapid cryogen boil-off) may occur [197], where ohmic heating from the initial resistive part may cause more superconducting volume to enter the resistive state and so-on [197].

Some ReBCO high temperature superconductor tape is also used to deliver the currents to the NbTi superconducting field source itself [97, 146], which in principle may also quench. However, in practice this has a critical temperature $T_c \sim 90$ K which is much higher than the temperature of the first-stage cold-head at ≈ 60 K [97] which also exhibits high cooling power at 30 W [36] and so it is less likely to quench than the NbTi field source itself. As discussed in (§3.3), air and water cooling systems have been fabricated and installed [32], which help to reduce the thermal load on the first stage cold-head which might otherwise risk a quench of the ReBCO tape.

A quench measured in the Geonium Chip Penning trap is shown below in Figure 5.5. It can be seen that for approximately 40 minutes, the temperatures in all three sensors remained reasonably stable in time and with low noise. Then, after 43.2 minutes had elapsed, the measured temperature rose suddenly at an extremely high rate. The temperature started to decrease after 44.0 minutes had elapsed, approximately 50 s after the quench had begun, due to a combination of active and passive quench protection measures which automatically occurred shortly after the quench had begun. This quench is

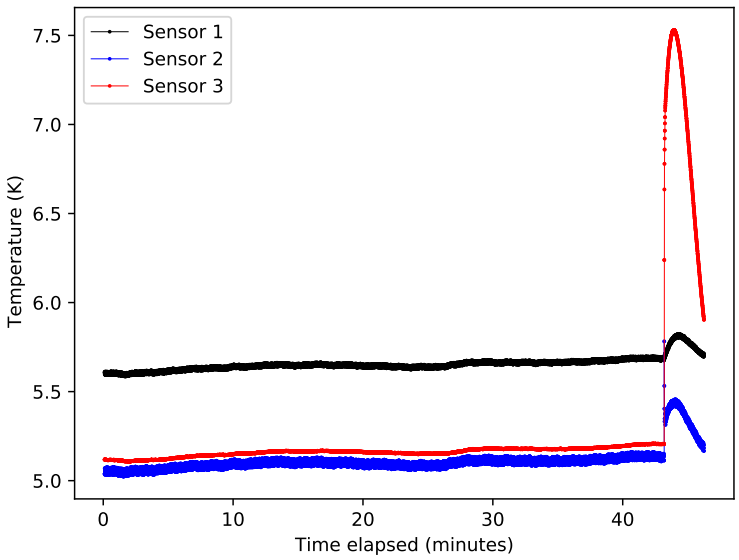

FIGURE 5.5: Measurements of the temperatures at three sensors as functions of time. A quench is visible at 43.2 minutes. Sensor 1 is positioned on the second-stage cold-head and the other two sensors are positioned close to the chamber and the magnetic field source (§3.1).

also depicted in Figure 5.6. These quench protection measures which are also discussed in (§5.2.2) stopped the magnetic field source from undergoing any permanent damage as a result of this quench.

5.2.2 An introduction to quench protection

In order to stop the NbTi magnetic field source from undergoing a quench (§5.2.1), passive and active quench protection measures are in place in the Geonium Chip Penning trap experiment. The coils of the magnetic field source (§3.3) are at a particularly high risk of damage from quenches, because unlike superconducting solenoids which are cooled with liquid helium cryogen [35, 157] with high cooling power, the NbTi coils are encased in epoxy (albeit a thermally conductive epoxy) which only receive < 0.5 W cooling power from the second stage cold-head [36] and so the temperature may rise rapidly. Furthermore, the NbTi wire is only 100 μm in diameter [32] and so i) there is high resistivity and ii) the thermal-mass-per-unit-length is low, both of which also cause a high rate of

increase of temperature.

As discussed in [97], in the event of a quench occurring, passive measures include thick copper braid (installed by Dr Jonathan Pinder) at the inputs and outputs of the coils (visible at the bottom of Figure 3.6b), which have lower resistance than NbTi (when NbTi is in the resistive state) and draw the current. Another form of passive protection is the good thermalisation of the current lines [97, 146], which helps to divert thermal energy (from e.g. the room temperature sections of the current lines) into the cryostat cold-heads.

Another passive measure [97] is the installation of back-to-back reverse (antiparallel) diodes which bridge each coil input to its output, which were installed by Dr Jonathan Pinder. In the event of a coil entering the resistive state, a voltage drop occurs across the coil (and thus also across the diodes), which, prior to setting the currents to zero, makes the diodes conduct and divert driven current away from the coils, which is then dissipated within the power supply. An implementation of such diodes (where current is also to be dissipated within *dump resistors* [198]) is evaluated in [198] and is also discussed in [199]. The diodes for the Geonium Chip Penning trap's magnetic field source are effective to the extent that it is possible to turn off the power supply for the currents (to nearly-instantaneously completely de-energise the coils) and have the magnetic potential energy be safely dumped through the diodes, without causing any permanent damage to the magnetic field source [97]. Although it is generally undesirable to de-energise the coils in this way, it has been the policy of the group to de-energise in this way in the event of a computer crash which would result in the loss of active quench protection (§5.3.2).

At present, the magnetic field source is used in a driven mode whereby each coil with current pair I_n is continuously driven by a different channel of a *Rohde and Schwarz HMP4040* power supply. Active quench protection systems in driven superconductors may halt the current supply to a coil [197]. A typical method to identify a quench is to measure the voltage across the superconductor - if the superconductor enters the resistive state then a voltage appears across the superconductor and if some voltage threshold is

met then the currents are halted [197]. For example, quench detection via measuring voltages has been implemented [199, 200]. However, this method is complicated to implement and so in the Geonium Chip Penning trap active quench protection system (§5.3.2), quenches are identified simply by measuring the temperatures at three locations within the region of the second-stage coldhead ($\approx$ 4 K) (§3.1), as discussed in (§5.3.2) and [97]. This simplified active quench protection system is possible due to i) the passive protection measures and ii) the fact that the coils have low inductances which don't store much potential energy [97].

One limitation of the quench protection in the Geonium Chip Penning trap is that in the event of a power outage to the control computer, there would be an automatic instantaneous unplanned shutting-down of the control computer. This would result in the loss of active quench protection and the experiment would rely on the passive protection measures which are discussed above. If the power outage were to also shut-down the power supply for the magnetic field source currents, then the coils would be de-energised instantaneously and the passive protection measures should protect the magnetic field source as discussed above. However, if the power supply for the magnetic field source currents were to remain powered-on, the currents would be driven indefinitely by the power supply, without there being any active quench protection (§5.3.2). This would carry significant risk because any real quench would initially remain driven (before the passive protection could respond) and this could cause permanent damage. If a human operator were to be supervising the experiment during the power outage, then the currents would be halted immediately (manually, by turning off the channel outputs on the power supply for the magnetic field source currents). The magnetic field source is not left energised overnight and typically the source is not left unsupervised, so the risk of damage due to a power outage is low and a power-outage related issue has not occurred in the last four years.

5.3 A control system for the magnetic field source

5.3.1 An introduction to the control system

Active quench protection [97] was implemented in the form of a *LabVIEW* control program which is used to continuously monitor the temperatures of the experiment. Due to the high importance of the active quench protection, one custom-built desktop computer with reasonably-high performance is reserved solely for the use of providing this active quench protection. The computer was designed with the assistance of Dr Jonathan Pinder and the University of Sussex IT department. The computer features:

1. an *Intel Xeon E-2274G* CPU with integrated graphics, which is server-grade for high reliability. There are 4 cores at 4.0 GHz, in order to minimise computation time.

2. 16 GB of DDR4 memory, which is a reasonably high amount in order to minimise computation time. Also, this memory is error-correcting for high reliability.

3. a 512GB M.2 PCIe NVMe solid state drive, which has fast read and write times in order to minimise delays when i) writing data files and ii) restarting the computer in the event of a crash.

4. a full-height PCIe card with a serial port and a parallel port, so that a GPIB card may be installed for connection to some legacy laboratory apparatus.

5. a *Windows 10 Pro* operating system.

The *LabVIEW* control program was developed over the course of approximately three years, evolving due to mistakes that were made with general procedures and the program itself. One primary auxiliary program has also been written to read in and plot the temperature data.

The main requirement of the *LabVIEW* program is to identify a quench and then to send a command to the power supply which drives the currents, in order to halt the currents [197]. While a current is driven through a resistive (quenched) NbTi coil, the temperature continues to rise due to ohmic heating and so the currents need to stop

being driven as soon as possible. The first working iteration of the *LabVIEW* program for quench protection could only detect a quench and then stop the currents, which is discussed in (§5.3.2). The currents in each of the coils still had to be ramped manually from 0 A to the target currents, which at a rate of 20 mA / 3 s with each coil being ramped sequentially, could take approximately an hour in total for all four coils.

On at least one occasion, human error caused the ramping to be undertaken at too high a rate which induced a quench, which was suspected to result from a too-rapid changing of the magnetic flux. Therefore, the ability to ramp the currents to a new set was also introduced, as discussed in (§5.3.3). The program worked reasonably well, however on one occasion it failed which resulted in permanent damage to shim 2 (§5.1.4) and some vital diagnostic data was not saved. Therefore, the ability to reliably save data was also introduced (§5.3.4). Also, the program may not have been restarted after a previous false quench had occurred (§5.3.2) and so an ability was introduced which meant that the currents would be turned off even if they already had been as a result of a previous quench. Also, rather than just sending the command once to turn off the currents, it was introduced to instead send it twice. Some **OPC?* synchronisation commands were also added, so that the power supply would always be under the control of the *LabVIEW* control program.

5.3.2 Active quench protection

As introduced in (§5.3.1) and [97], the aim of the *LabVIEW* program is to firstly identify a quench and then to secondly halt all four currents from being driven by the power supply. Every 200 ms the temperature is measured at one location far from the magnetic field source (sensor 1) and at two locations close to the magnetic field source (sensors 2 and 3) [97], using a *Lakeshore 218* temperature monitor [97]. After the temperature has been measured simultaneously at each of these three locations, checks are completed for each of the three locations, to make sure that none of the maximum permitted values have been exceeded [97].

Maximum permitted values for the mth sensor are chosen for i) the absolute temperature T_m, ii) the absolute temperature change ΔT_m and iii) the heating rate Q_m [97]. If at least one maximum permitted value is exceeded, the control program assumes that a quench has started and the currents are halted with a 200 ms response time [97]. The quench monitoring is conducted within the *LabVIEW* control program, where ΔT_m and Q_m for the mth sensor after the ith temperature measurement $T_{m,i}$ at time t_i are calculated using the previous temperature measurement $T_{m,i-1}$ at time t_{i-1} using

$$\Delta T_m = T_{m,i} - T_{m,i-1} \tag{5.13}$$

$$Q_m = \frac{\Delta T_m}{t_i - t_{i-1}}. \tag{5.14}$$

A false quench

All of the maximum permitted values (T_m, ΔT_m (5.13) and Q_m (5.14)) may be changed while the program is already running. In order to be most sensitive when detecting quenches, the maximum permitted values should be as close to the typical measured values. However, the magnetic field source is not perfectly thermalised and so the measured temperatures may rise slowly in time (see Figure 5.5), especially as a result of having energised another coil, after which a new thermal equilibrium is reached. Therefore, the maximum permitted absolute temperature is typically increased periodically to stop a quench from being falsely detected, which would otherwise result in the unnecessary de-energising of the coils. When choosing the maximum permitted values, a trade-off must be reached between i) the likelihood of not identifying a *real quench* and ii) the likelihood of falsely identifying random noise as a quench (a *false quench* [199]).

A real quench and a false quench are compared in Figure 5.6. In order to plot the data from both quenches on the same axes and compare the temperature evolution, the times in each datset have been shifted by a constant value in order to have the temperature rises begin at a new time of zero seconds. The false quench occurred approximately 70 minutes after the real quench had occurred and so the measurement setups were identical for both quenches and so the temperature evolution after the quenches is comparable. The real quench (also shown in Figure 5.5) occurred unintentionally, during an energising of the coils where the ramping rate was set at the lower of 600 mA/min or 8 mT/min. The false quench also occurred unintentionally, but as a result of a communication interruption to the temperature monitor device, which temporarily resulted in *LabVIEW* falsely recording a temperature of 0 K at sensor 1 (as can be seen in Figure 5.6a). The change in the temperature at sensor 1 from 0 K to the true value ($\approx$ 5.68 K) at -0.710 s exceeded the maximum permitted values for ΔT_m (5.13) and Q_m (5.14), which resulted in a quench being falsely identified and the following unnecessary cessation of the driving of all the currents. The sudden change in currents induced a sudden change in flux and so it is suspected that this change in flux produced eddy-current heating which resulting in a quench-like temperature evolution.

Sensor 1 was located close to the second-stage cold-head and so it reasonably unaffected by quenching and so it is of no further interest, in comparison to sensors 2 and 3 which were located close to the chamber and the magnetic field source (§3.1). As can be seen in Figure 5.6, in the case of the real quench, the temperatures of sensors 2 and 3 reached higher maximum values than those during the false quench. Furthermore, in the case of the real quench, these temperatures took longer to thermalise to the base temperature of the second-stage cold-head than in the case of the false quench, as a result of there having been a higher thermal energy dissipation during the real quench. This is because in the case of the real quench, the currents were momentarily driven during the computational time delays, whereas in the case of the false quench, the heating only resulted from suspected eddy-current (dissipative) heating.

An example use of the program to identify a quench

In this section an example use of the program is discussed, where some noise on the temperature measurement of sensor 3 was interpreted by the program as a quench (i.e. it was a false quench). This false quench has not been previously discussed in this thesis. This false quench is shown in Figure 5.7. It can be seen in this plot that the false quench was caused by noise on sensor 2 at a time 4144.25 s elapsed which was followed by heating in sensors 2 and 3 at a time 4144.76 s elapsed. This puts an upper limit of 510 ms between a quench starting to occur and the currents being halted.

Figure 5.8 shows a section of the front panel (user interface) of the *LabVIEW* quench protection program, which displays information about how the quench was identified. It can be seen that the program identified the quench from the temperature data points at time 4144,2... s elapsed, which is in agreement with the noise spike plotted in Figure 5.7. In particular, the maximum permitted values of all three parameters for sensor 2 (T_2, ΔT_2 (5.13) or Q_2 (5.14)) were identified as a quench. It is also interesting to note that at a time 4145.0... s elapsed, the suspected eddy-current heating is powerful enough to exceed the maximum permitted value Q_3 of sensor 3 (5.14).

Limitations

This simple procedure for active quench protection has some limitations. Firstly, there is a time delay between a quench truly beginning to occur and the temperature monitor sending the next temperature reading to the control computer. Secondly, there is another time delay between the *LabVIEW* control program identifying the beginning of a quench and the power supply turning off its channels, due to the finite communication time and the finite computation time of the internal processor of the power supply. The currents in all four coils would be continuously driven during these two time delays in which the temperature in resistive (non-superconducting) regions would continue to rise rapidly and risk permanent damage. Thirdly, once the outputs of the power supply have been set to *off*, there is a further time delay while the magnetic potential energy in the coils is dumped through the power supply. Computational time delays and dumping delays could be reduced by implementing a field-programmable-gate-array method [200]. A fourth limitation is that the maximum permitted values have to be changed whenever there is a significant change to the noise fluctuations in the measured temperatures, or due to base temperature changes resulting from different levels of cryostat thermalisation. As a result of the fourth limitation, the quench protection program (and the auxiliary program (§5.3.4)) have the ability to plot the set maximum temperatures on the plots of the temperatures as functions of the time.

5.3.3 Changing the magnetic field distribution

Another function of the quench protection program is to control the magnetic field distribution $\tilde{B}$ or $\tilde{B}'$ by being able to ramp to a new set of currents $\tilde{I}$ or $\tilde{I}'$ ((5.1b) or (5.2b)). Ideally for the ease of programming, a separate and independent *LabVIEW* program would be used to change the currents of the power supply. However, it is vitally important that in the event that a quench is detected, a command is sent to the power supply as soon as possible in order to halt the driving of the currents. Therefore, in order to reasonably guarantee that the currents will be halted as soon as a quench has been identified, the subroutines for the current ramping have been integrated into the quench protection

program, so there is only one *LabVIEW* program competing to communicate with the power supply. Once the final currents have been reached, the program automatically continues to act solely as a quench protection program again. At any time, a new set of currents may be specified and the program will ramp to these, including the ramping down to 1 mA in each channel prior to turning off the power supply.

The control program has the ability to ramp from any set of existing currents to any set of desired currents. Starting with I_0 and working sequentially through I_1, I_2 and I_3, each coil is ramped from its initial current to its desired final current before the next current is ramped. The currents are always changed by the same amount, which at present is set to 5 mA. Eventually the desired current is exceeded and then a final step is made to set the desired current. If the rate of change of the current (and thus of the magnetic flux) is too high, then the coils might quench. Therefore, the program also allows the user to set i) the maximum permitted rate R_I of the increase in current and ii) the maximum rate R_B of the increase in magnetic field strength, where $I_n^{(i)}$ (§3.3) and $B_{z,000}^{(i)}$ (2.21) are I_n and $B_{z,000}$ at a time t_i respectively and where $I_n^{(i-1)}$ and $B_{z,000}^{(i-1)}$ are I_n and $B_{z,000}$ at a time t_{i-1} respectively:

$$R_I = \frac{I_n^{(i)} - I_n^{(i-1)}}{t_i - t_{i-1}} \qquad (5.15) \qquad\qquad R_B = \frac{B_{z,000}^{(i)} - B_{z,000}^{(i-1)}}{t_i - t_{i-1}}. \qquad (5.16)$$

During the ith iteration, the program measures all three temperatures T_m and then calculates what R_I (5.15) and R_B (5.16) would be if the current were to be ramped during the ith iteration. If neither of the maximum set values R_I and R_B would be exceeded, the current is changed. If R_I and/or R_B would be exceeded, then the program does not change the current and the next iteration of the loop begins. The user specifies the magnitude of the change in current and so this works for both increases and decreases in the currents. On the ith iteration, the program calculates $B_{z,000}^{(i)}$ using the first row of the matrix $\mathbf{\Gamma}(y_{E,0} = 1.45\,\text{mm})$ (5.8) and the potential new currents.

The power supply is driven in constant-current mode, where the current is set to a desired value and where the voltage is set arbitrarily high, so that the voltage floats to a reduced value decided by Ohm's Law. The voltage setting is maintained to be just above the constant-current threshold, by also ramping the voltage whenever the current is ramped. The voltages are calculated using effective resistances, which at present are

set to 0.6 Ω for all the coils except for shim 3 at 0.9 Ω. While the current is changing, even while in a superconducting state, the voltage across a superconductor is non zero due to Lenz's Law and also additional voltage is required to drive the currents through the resistive parts of the line which are at room temperature. If a coil were to begin to quench and enter the resistive state, the voltage across the coil would increase, thus limiting the current and reducing the thermal load, which is another passive quench protection control. Furthermore on one occasion, there was a suspected floating-point error, where it was suspected that the command to set the current was misinterpreted by the power supply to be a much higher value. A sudden change in current risks a quench occurring due to the sudden change in flux and so in order to avoid floating-point errors, the program also rounds any calculated current to four decimal places, prior to sending the current value to the power supply.

A section of the front panel (user interface) of the *LabVIEW* control panel is shown in Figure 5.9.

5.3.4 Data storage and an auxiliary program

It is important to record the temperature values as functions of time, so that i) any gradual rises in temperature which are indicative of a potential future quench may be spotted and ii) in the event of a quench it can be determined if the quench was real or false. In the event of a false quench, the maximum permitted values may be adjusted to give higher tolerances, prior to running the program again.

Initially, one office computer was used to control not only the active quench protection for the magnetic field, but also all other programs including those required to load the trap and to try to observe electrons. The *Lakeshore 218* temperature monitor is queried approximately four times per second for three temperature values each time and so in one hour there will be approximately 43200 data points. Reasonably often the computer would crash after a few hours of use, resulting in the coils having to be immediately manually de-energised while there was no active quench protection.

Therefore, the quench protection program was changed so that at any time, the data arrays in *LabVIEW* were smaller, so that the computer would not crash due to suspected memory issues. The user may specify how many data points are plotted in the program (typically 100), before the data is written to a *.txt* file and then the data is removed from the storage arrays and also from the plot of the temperatures as a function of time. The program retains a user-specified number of data points (typically 40), so that the user can identify some temperature gradients. In the event that a quench is detected, the program retains more data points than normal (typically 1000) so that the user may investigate the quench. Using this method, no crashes have been observed due to the temperature monitoring. However, the user cannot easily identify any small but non-zero gradients in the temperatures, which might be indicative of a future quench.

Therefore, an auxiliary program was written to read in all the *.txt* files which have been written by the main quench protection program during a particular use of the quench protection program, to allow the user to identify any gradients in the temperature. Figure 5.10 shows a section of the front panel (user interface) of the auxiliary *LabVIEW* program. The data shown in the plot is that of the false quench introduced in (§5.3.2). This auxiliary program can also be useful in the event of a quench, because the user can quickly view all the temperature data and zoom-in on relevant data, in order to try to determine if the quench was real or false.

One important feature of the auxiliary program is the ability to selectively remove some of (to *thin*) the data, prior to plotting. When each *.txt* file is opened, the user may select which percentage of data points in the *.txt* files are saved into the storage arrays prior to plotting. Typically it is chosen to only plot 20 % of the data when running the auxiliary program within the first twenty minutes of temperature measurements, but this is typically reduced to just 2 % after twenty minutes and eventually to just 1 % after several hours. In this way, there are fewer data stored in the computer memory, which reduces the load on the computer and reduces the risk of a crash. Furthermore, the auxiliary program is run on the same computer as the quench protection program and it has been observed on some instances that when the auxiliary program was run without thinning

the data, the quench protection program showed jitter while the auxiliary program used the majority of the CPU performance. This jitter was a temporary loss of active quench protection (§5.3.2).

5.3.5 Application: checking if the UV light is reaching the chamber

While the UV light is illuminating the chamber, a temperature rise is visible at sensor 3, which is close to the chamber (§3.1). Plots of the temperatures as functions of time are shown in Figure 5.11, during a photocurrent measurement (§4.1). The UV shutter remained closed until 100 s had elapsed, while the temperature at sensor 3 remained constant. This was followed by six pairs of the UV shutter remaining open and closed (ending after 340 s had elapsed), which caused the temperature at sensor 3 to rise and fall respectively. After this, the UV shutter remained open until 430 s had elapsed, with a thermal equilibrium being reached after 380 s had elapsed. After 430 s had elapsed, the shutter was left closed and sensor 3 cooled down to thermal equilibrium.

The UV shutter can be changed by applying a 5.62 V pulse for 60 ms using a serial communication protocol. The same pulse is applied whether opening or closing the shutter and so if a control program is stopped before it has finished running, the UV shutter state may be incorrect. This occurs reasonably often and so temperature checks in this way allow the user to quickly check if the UV shutter state is correct.

5.4 A summary of the magnetic field source implementation

This chapter discusses the progress towards the implementation of the planar magnetic field source for the Geonium Chip Penning trap. In (§5.1), there is a discussion about the calibration of the source and there is some verification of the calibration. The theoretical background of the calibration (the determination of the matrices $\mathbf{\Gamma}(y_0)$ (5.1) and $\mathbf{\Gamma}'(y_0)$ (5.2)) is discussed in (§5.1.1). This is followed by the calibration of the source (§5.1.2) and verification checks of two different homogeneous 300 mT homogeneous fields (§5.1.3), which show a good degree of homogeneity. This is followed by a demonstration of a 500

mT field (§5.1.4) which shows that i) the field source can produce a strong field and that ii) the raw calibration data should first be fit to the Biot-Savart Law in order to improve the validity of the matrices $\mathbf{\Gamma}(y_0)$ (5.1) and $\mathbf{\Gamma}'(y_0)$ (5.2).

In (§5.2) there is an introduction to a superconductor quench (§5.2.1) and there is an introduction to the quench protection of the field source (§5.2.2).

The *LabVIEW* control system for the magnetic field source is discussed in (§5.3), which begins with a description of the control computer (§5.3.1). This is followed by a discussion about how the active quench protection works (§5.3.2), which includes a demonstration of a false quench (§5.3.2), an example use of the program to identify and deal with a false quench (§5.3.2) and some limitations (§5.3.2) of the method. There are also discussions about how the currents are changed (§5.3.3), how data is managed in order to reduce the load on the computer (§5.3.4) and about an application whereby the state of the UV shutter may be determined (§5.3.5).

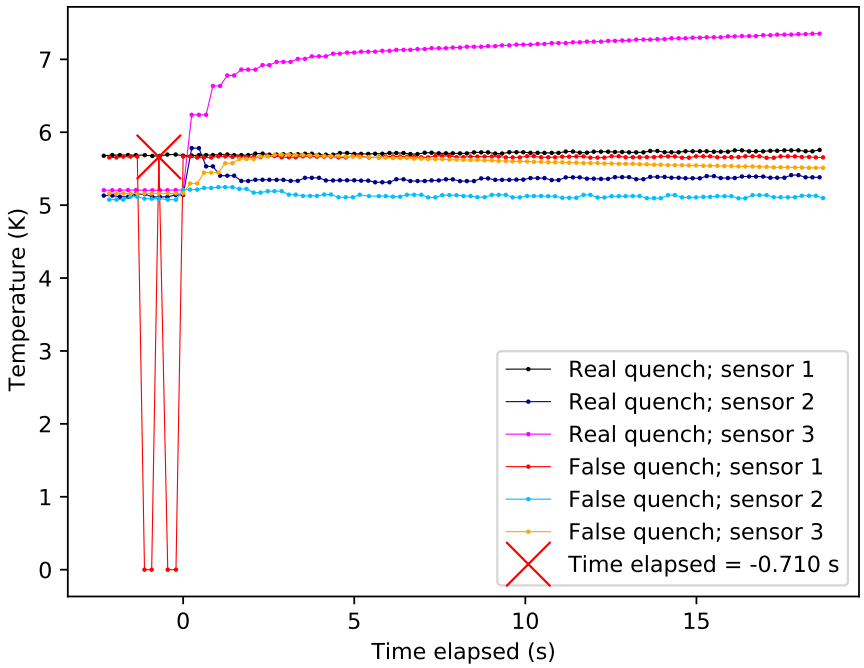

(A) A wider-ranged plot showing the temperatures at all three sensors. The false temperature readings of sensor 1 which caused the false quench are visible.

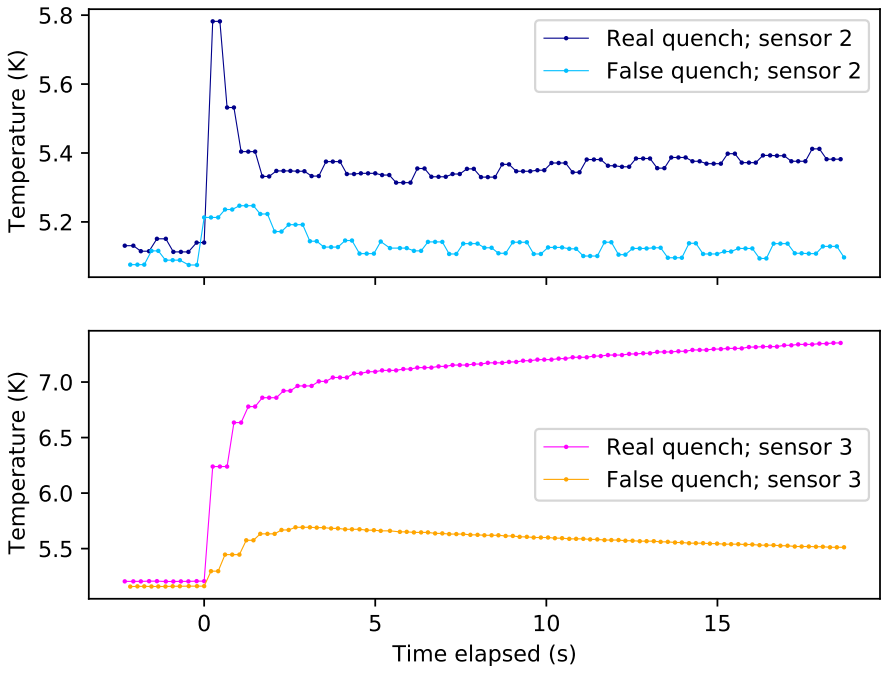

(B) A wider-ranged plot showing the temperatures only of sensors 1 and 2.

FIGURE 5.6: Plots of the temperature evolution at three temperature sensors, during a real quench and a false quench.

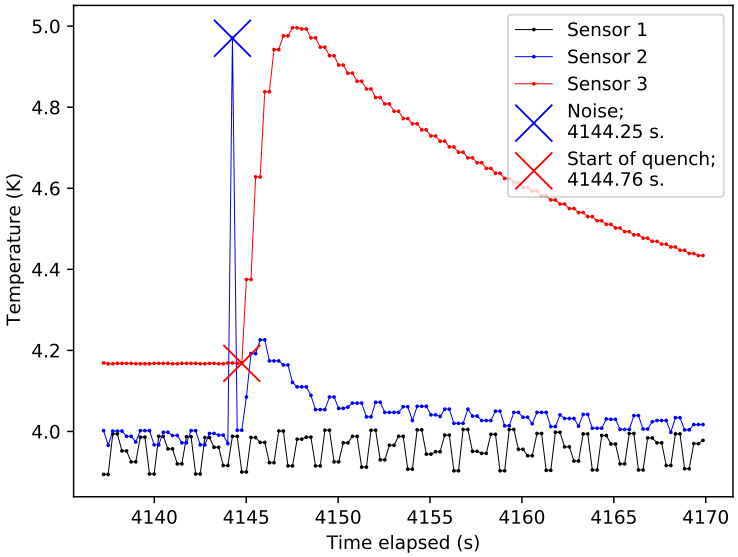

FIGURE 5.7: A plot of the temperatures around the time of the false quench. Some noise after 4144.25 s had elapsed was wrongly interpreted as a quench which lead to (suspected eddy-current) heating which began after 4144.76 s had elapsed.

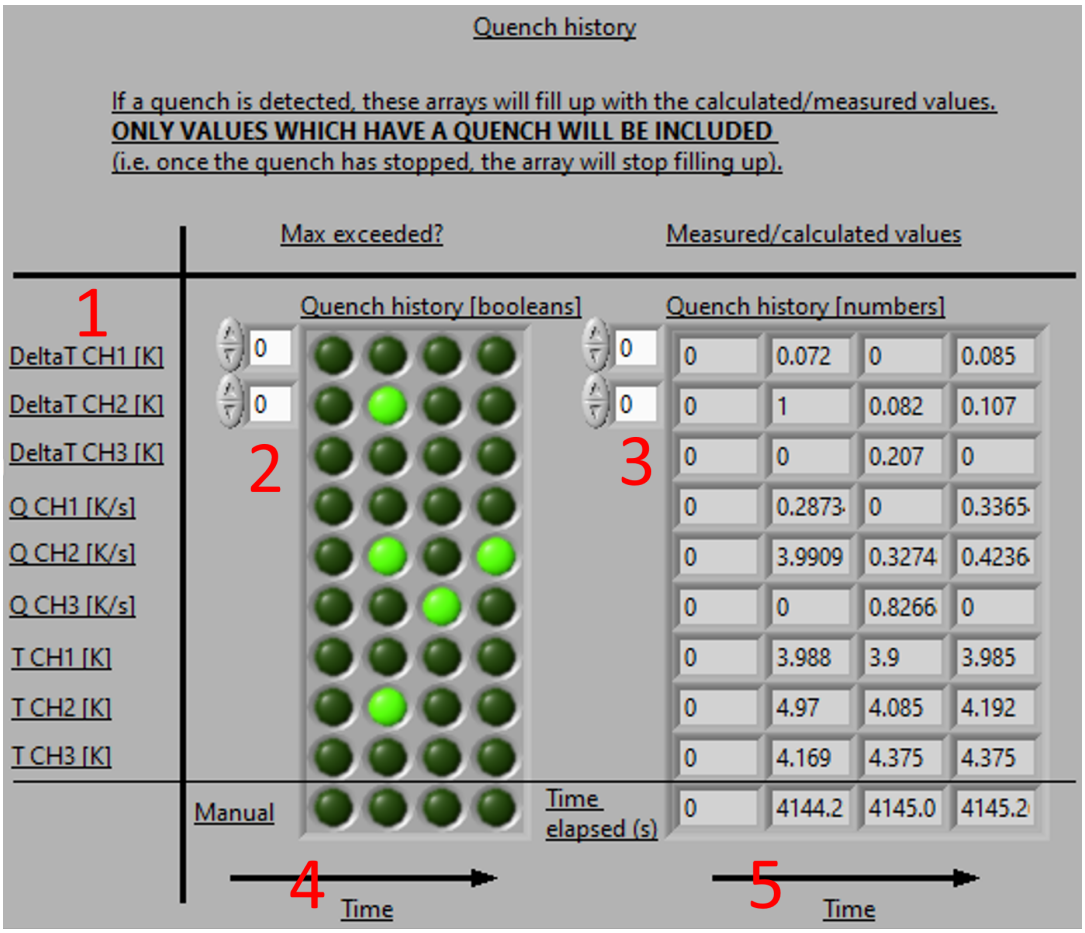

FIGURE 5.8: Some indicators on the front panel (user interface) of the *LabVIEW* quench protection program, after a quench had been detected. Each column corresponds to a different time and each row corresponds to a different parameter (T_m, ΔT_m (5.13) or Q_m (5.14)) (1), where sensor m is written as CHm. The element (i, j) of the boolean array (2) corresponds to the element (i, j) of the numerical array (3) and so the two axes of time (4) and (5) are identical. Each boolean value in (2) is light green if that parameter has exceeded the maximum permitted value, otherwise it is dark green. Each numerical value in (3) is the measured/calculated value. The first columns in both (2) and (3) are not measurements.

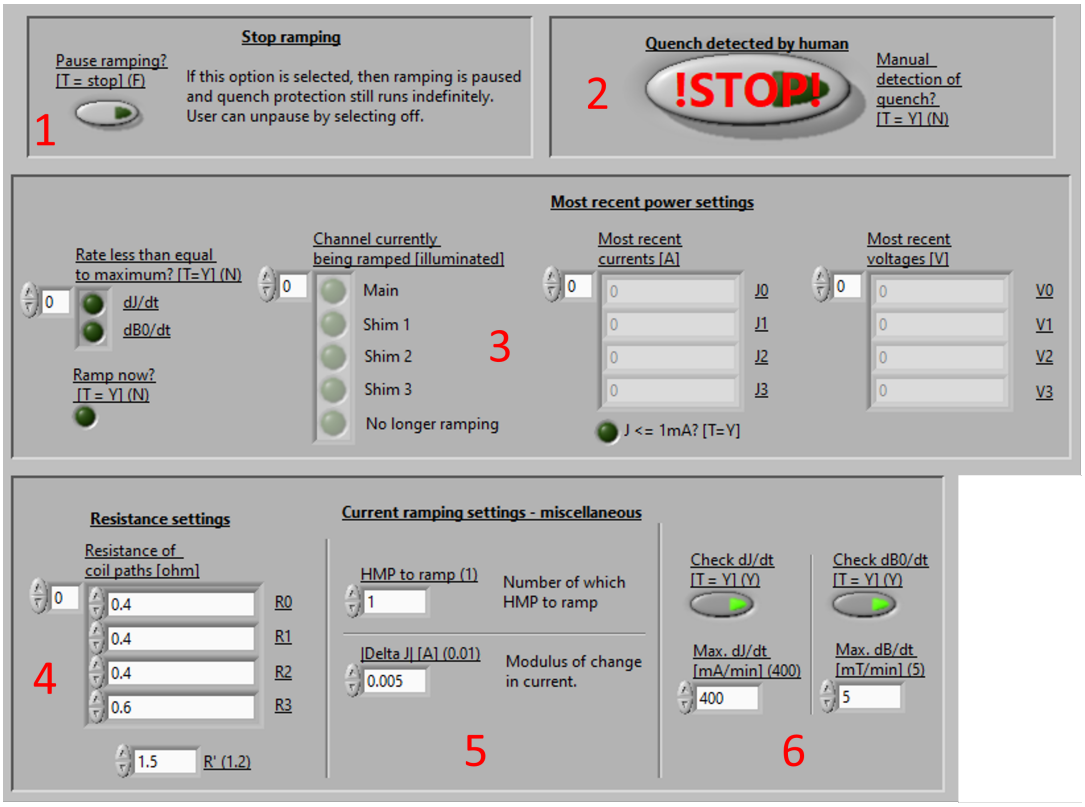

FIGURE 5.9: A section of the front panel (user interface) of the quench protection program, which shows some of the current ramping settings. The controls (1) and (2) allow the user to pause the ramping (while maintaining quench protection) or tell the program that a quench has occurred, respectively. In (3) there are indicators which update with each successive iteration of the program. In particular it may be useful to see the present states of the currents and voltages. The controls in (4), (5) and (6) may be changed at any time. These controls include i) the setting of the effective resistances (4) which set the voltage, ii) the magnitude of the desired change in current in each step (5) and iii) the maximum permitted rates of change R_I (5.15) and R_B (5.16) (6). The controls for the settings of the current values themselves have not been included in this figure.

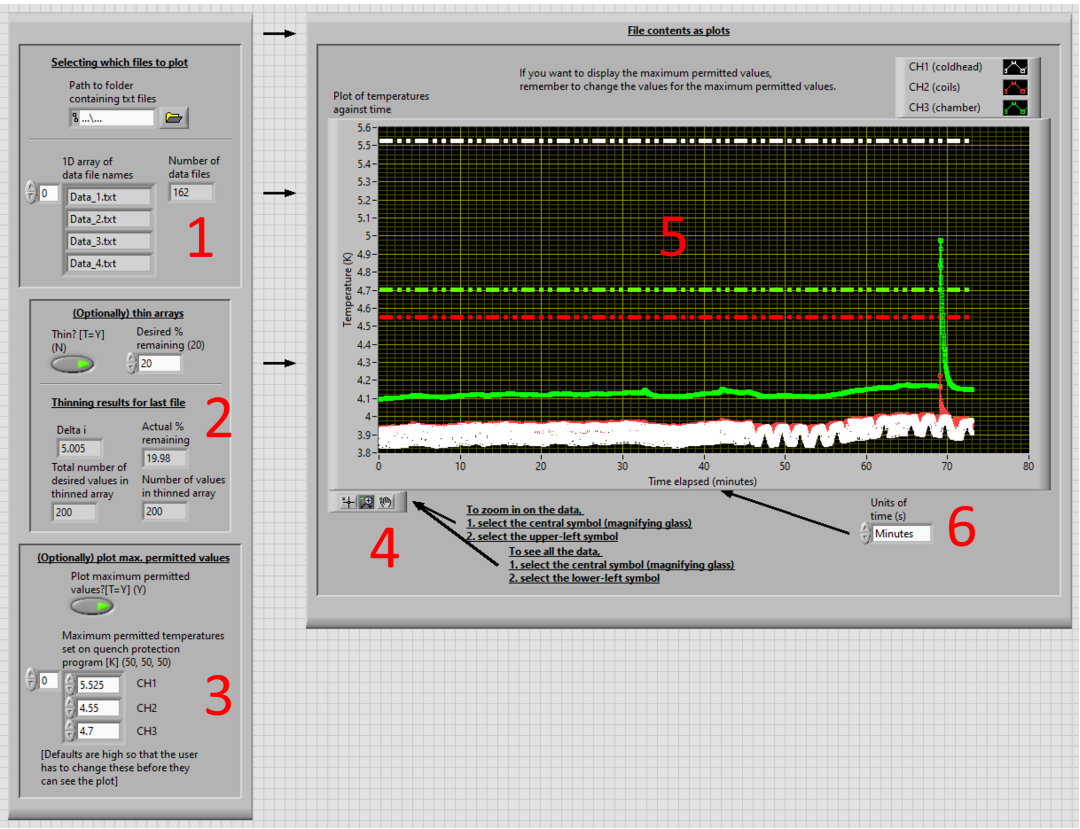

FIGURE 5.10: A section of the front panel (user interface) of the auxiliary *LabVIEW* quench protection program. There are controls to select the data files (1); to (optionally) thin the data (2); to (optionally) display the maximum permitted temperatures T_m (3); to set the time and temperature axis ranges or to pan the data (4) which is plotted in (5) and finally to choose the unit of time (6).

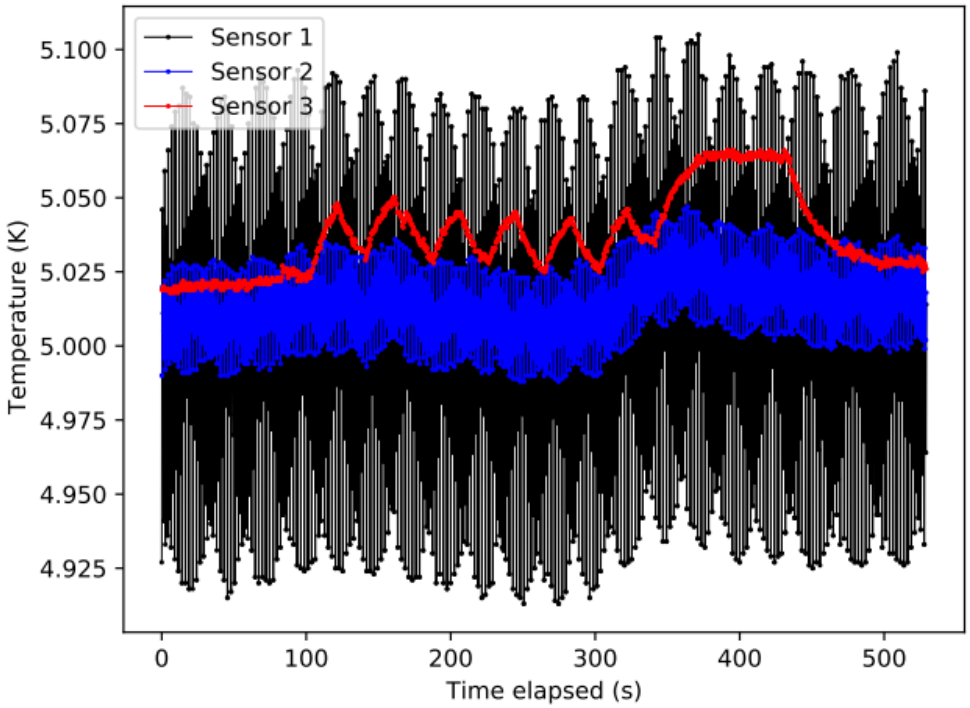

FIGURE 5.11: A plot of the temperatures as a function of time, during a photocurrent measurement (§4.1). Sensor 1 is close to the second-stage cold-head, sensor 2 is close to the coils and sensor 3 is close to the cyrogenic trapping chamber (§3.1), into which the UV light is aimed.

Chapter 6

Towards the loading and detection of trapped electrons

6.1 The loading procedure

6.1.1 An overview of the loading procedure

The majority of the attempts to trap electrons in the Geonium Chip Penning trap tried to trap *primary electrons* [32], which are photoelectrons which are liberated from the UV target (§4). The primary electrons were guided along $\hat{u}_z$ using the magnetic field lines, into an asymmetric (along $\hat{u}_z$) electrostatic trapping potential within the trapping region (around $\vec{r}_0 = (0, y_0, 0)$ (§2.1.1)). The trap was subsequently made quadrupolar (symmetrical along $\hat{u}_z$) in a very short length of time (measured to be ≈50 ns) in order to provide axial confinement. This method to trap primary electrons has previously been successfully implemented [195], however this implementation [195] used a 248 nm (UV) laser with a peak power of 2 MW and 10 ns laser pulses, whereas the UV source in the Geonium Chip Penning trap (§4) has a power of much less than 2 MW (albeit run continuously). The authors report [195] that "up to 10 million electrons per laser pulse cool into the smaller central well" (are *trapped*), whereas simulations performed by Dr José Verdú-Galiana predicted that with a primary photocurrent of approximately 100 pA (measured with the old fibre setup (§4.7.1)) and a trap closing time of ≈ 50 ns, the number of primary electrons trapped per closing of the trap should be approximately twenty.

In principle, the electronic detection system (§3.5) should have been able to detect twenty trapped primary electrons. However, even if primary electrons had been trapped, they were not visible using the electronic detection technique (§2.2). If there were trapped primary electrons which were never detected, then perhaps this could have resulted from, among other reasons, a combination of i) the axial frequencies of any electrons never being brought to the resonance frequency of the detection circuit (§2.2), or ii) the lifetime of the electrons being too short (§6.1.4) - resulting in the electrons not having enough time to interact with the detection coil prior to their loss from the trap, or iii) the axial energies of any trapped clouds of electrons being too widely distributed in frequency due to trap imperfections (§2.1.2) - resulting in the axial signals never exceeding the electronic noise. Therefore, the most recent trapping attempts have used a more conventional technique which instead tries to trap *secondary electrons*.

In order to generate secondary electrons, primary electrons may be released from thermionic [175] or field-emission-point sources [34] and then accelerated to gain high energy before ionising rest gas [175] in the trapping region around $\vec{r}_0 = (0, y_0, 0)$ (§2.1.1). The electrons which are liberated from rest gas are denoted *secondary electrons*. This technique may be called *electron impact ionisation* [201] and is discussed in detail for helium (the most common particle in the trap (§6.1.5)) in [85, pg. 14-17]. However, as previously discussed (§4), rather than using a field emission point which would require a high voltage, or thermionic emission which would require high thermal loads, the electrons are released using the photoelectric effect (§4). In order to accelerate the electrons, the UV target is biased with a voltage (typically between -30 V and -90 V) so that it acts as a photocathode. Therefore, the beam of primary electrons acts as an electron beam ion source (EBIS) [202]. This is similar to the method discussed in [203], which instead used an RF field to accelerate electrons.

The trapping of secondary electrons has some advantages over the trapping of primary electrons. Firstly, many secondary electrons should be continuously liberated (and accumulated) in the trapping region around $\vec{r}_0 = (0, y_0, 0)$ (§2.1.1), which is already within a quadrupole field. This is in comparison to trying to trap approximately 20

primary electrons as discussed above. Secondly, the lifetime of electrons in the cryogenic trapping chamber (§3.4) might be very short and so primary electrons might not be trapped and detected prior to being lost from the trap. The secondary electrons should continuously be liberated within the trapping region and so there is a greater chance of trapping and detecting secondary electrons prior to them being lost.

6.1.2 The resistive wall effect in the Geonium Chip Penning trap

One significant consideration for the lifetime of trapped electrons in the Geonium Chip Penning trap is for the resistive wall effect (resistive wall destabilisation of the magnetron motion) as introduced in (§2.3.2). To summarise (§2.3.2), the resistive wall effect is where the radius of the magnetron motion grows as a result of resistive cooling of the magnetron motion, due to the magnetron energy having negative polarity. In the Geonium Chip Penning trap, the beam of primary electrons is guided along $\hat{u}_z$, with the beam centred around $x \approx 0$ and $y \approx y_0$, which is similar to other planar Penning traps which have successfully trapped electrons (§1.1.2), for example at Mainz [11], Ulm [13] and Harvard [19]. However, whereas the Geonium Chip (§3.2) electrodes lie in the $\hat{u}_z - \hat{u}_x$ plane, in the alternative planar Penning traps for electrons [11, 13, 19], there is an alternative topology where the electrodes instead lie in the $\hat{u}_x - \hat{u}_y$ plane (§1.1.2). In these alternative traps [11, 13, 19], above the circular electrodes (§2.1.1) and in the $\hat{u}_x - \hat{u}_y$ plane, there is vacuum for radii of at least 8.1 mm [11], 5.2 mm [13] and 8.19 mm [18, 19] (including the inter-electrode gaps, but excluding the ground planes which mean that these vacuum radii are underestimated). Therefore, the other traps [11, 13, 19] can permit larger magnetron radii before the electrons are grounded and lost, compared to the Geonium Chip Penning trap. Simulations by Dr José Verdú-Galiana have shown that the distance between y_0 and the release height y translates into the radius of the magnetron motion and so electrons liberated far from y_0 are more at risk of being lost by collisions with the Geonium Chip electrodes.

The electrodes in traps with circular symmetry have effective coupling distances $D_{\text{eff}}^{(y)}$ (2.28) (§2.3.2) which are infinite (due to radial symmetry - see similar arguments in [91])

and so ions trapped in these traps should not undergo resistive wall destabilisation (note that $D_{\text{eff}}^{(y)} = D_{\text{eff}}^{(x)}$ in a trap with circular symmetry). However a complication of the Geonium Chip Penning trap is that $D_{\text{eff}}^{(y)}$ is non-zero for the ring electrode [91] and $D_{\text{eff}}^{(y)}$ may also be non-zero for some y for the correction electrodes [91]. Also as simulated in a similar way by Dr José Verdú-Galiana, $D_{\text{eff}}^{(y)}$ for the endcap electrode is also non-zero. Therefore, the resistive wall effect requires consideration in the Geonium Chip Penning trap and so the $\approx$ 4 K low-pass RC filters [146, Fig. 7.6 and 7.10)] have been changed by Dr Jonathan Pinder and Dr José Verdú-Galiana, in order to avoid the resistive cooling which causes the resistive wall destabilisation. This was done by reducing the resistances and increasing the capacitances of these filters. The series resistances (between the voltage supplies and the electrodes) were decreased from 100 kΩ to 1 kΩ. The capacitances to ground were increased to the significantly high values of 1 μF at the endcap and correction electrodes and also to 11.3 μF at the ring electrode. The ring electrode requires a higher capacitance than the other electrodes due to a much smaller $D_{\text{eff}}^{(y)}$.

Magnetron cooling may be applied in the form of *RF sideband cooling* [103] with a drive frequency ω_d of $\omega_d = \omega_m + \omega_z$ [103], in order to reduce the radius of the magnetron motion [103]. Prior to the changing of the filters as described above, RF sideband cooling was applied through the left correction electrode, but the new high capacitance would have grounded the applied cooling field. Therefore, in order to increase the impedance at ω_d (while keeping the impedance at ω_m low to avoid the resistive wall effect) the new filter for the left correction electrode was tuned by Dr Jonathan Pinder and Dr José Verdú-Galiana. This was achieved with the introduction of a 0.5 μH inductor in series with the existing 1 kΩ resistor of the RC filter. Also, an additional 1.62 kΩ resistor was added in parallel only with the new inductor, in order to reduce the Q-factor to allow for a broader range of useful frequencies ω_d. This filter is shown in Figure 6.1.

6.1.3 Trapping procedures

Many different trapping procedures were attempted during the time permitted for the research for this thesis. Only the most recent procedures for trapping secondary electrons

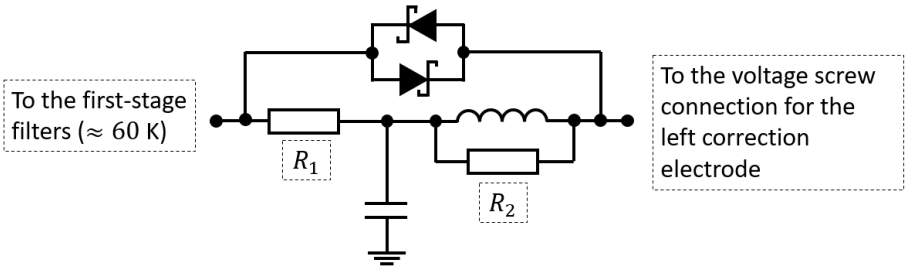

FIGURE 6.1: Circuit schematics for the new second stage (≈ 4 K) (§3.1) filters on the left correction electrode. The capacitor has a capacitance of 1 μF and the inductor has an inductance of 0.5 μH. The resistors have resistances of $R_1 = 1$ kΩ and $R_2 = 1.62$ kΩ. The two back-to-back Schottky diodes may be used to bypass the filter.

are discussed in this section.

Electrostatic potentials and trap depths

The plots in this section (§6.1.3) of the electrostatic potentials have been calculated using *Mathematica* functions provided by Dr José Verdú-Galiana, to compute (3.1) using formulae in [22, App. A].

Simulations (by Dr José Verdú-Galiana) of the electrostatic potential predicted that in order for the axial frequency ω_z to be in resonance with the axial resonator ($\omega_z \approx 2\pi \cdot 25.7979$ MHz), this would require a ring voltage of approximately $V_R = -0.67937$ V. This simulation assumed values for the trap anharmonicities and inhomogeneities (§2.1.2) and also assumed temperatures for the electron eigenmotions. The theoretical optimal tuning ratio (§2.1.2) (3.2) for electric compensation of the electrostatic potential has also previously been estimated (by Dr José Verdú-Galiana) using simulations to be $T_C^{(\mathrm{opt})} = 1.400844$. Also, the endcap tuning ratio (3.3) has previously been optimised (by Dr José Verdú-Galiana) to be $T_E = 5.7$, in order to set a trapping height (2.6) $y_0 = 1.45$ mm. The spatial dimensions of the chamber were chosen to give some degree of mechanical anharmonic optimisation at $y_0 \approx 1$ mm, however this low height risks electron loss due to the resistive wall effect (§6.1.2) and so a trade-off was made at $y_0 = 1.45$ mm. The magnetic field has been optimised (5.10) for $y_0 = 1.45$ mm.

If electrons were to be loaded with the electrostatic potential defined by $V_R = -0.67937$ V, $T_C^{(\mathrm{opt})} = 1.400844$ and $T_E = 5.7$, this would not be a deep axial trap $\phi(z)$ and so it is unlikely that electrons would remain trapped. This electrostatic potential is shown in Figure 6.2, where the photocathode bias voltage is $V_{\mathrm{cath}} = 0$ V. By inspecting Figure 6.2a, the axial trap depth is approximately $\mathrm{e}|-2.16\ \mathrm{V} - -0.87\ \mathrm{V}| = 1.29$ eV, which may confine electrons with axial energy up to 1.29 eV. For comparison, another planar Penning trap for trapping electrons with circular symmetry [13] had an axial well depth of 4.5 eV, which is significantly deeper than that of the Geonium Chip at 1.29 eV. The trap depth of planar Penning traps with circular geometry has previously been discussed [10]. Furthermore, it has been experimentally determined that the shallowest trap for the stable trapping of electrons is ~ 1 eV [85]. The axial frequency was calculated to be $\omega_z = 2\pi \cdot 25.7979$ MHz.

The voltages for the electrodes are provided by *Time Electronics 5018* programmable DC voltage calibrators with high precision and good temporal stability. The maximum magnitude of the voltage output from one calibrator (with either polarity) is 22 V. Therefore, again with a tuning ratio of $T_E = 5.7$, the maximum possible ring voltage for $V_E = -21.95$ V is approximately $V_R = -3.85088$ V. The electrostatic potential with $V_E = -21.95$ V, $T_E = 5.7$, $V_R = -3.85088$ V and $T_C^{(\mathrm{opt})} = 1.400844$ is shown in Figure 6.3. The photocathode bias voltage V_{cath} is 0 V. By inspection from Figure 6.3a, the axial trap depth is approximately $\mathrm{e}|-12.25\ \mathrm{V} - -4.94\ \mathrm{V}| = 7.31$ eV, which is deeper than the depth of 4.5 eV [13]. This means that the Geonium Chip Penning trap should be able to confine secondary electrons with the same axial energies as those [13] secondary electrons which were trapped previously. The axial frequency was calculated to be $\omega_z = 2\pi \cdot 70.4$ MHz.

The photocathode bias voltage distorts the electrostatic potential close to the equilibrium trapping position $\vec{r}_0 = (0, y_0, 0)$ (§2.1.1). The same deep electrostatic potential as produced by the trap electrodes shown in Figure 6.3 is shown in Figure 6.4, but with the additional effect of a photocathode bias voltage $V_{\mathrm{cath}} = -70$ V. The most common rest gas particle is helium (§6.1.5), where the ionisation cross section for obtaining secondary electrons with low kinetic energy peaks at ~ 30 eV [85] and where the ionisation cross

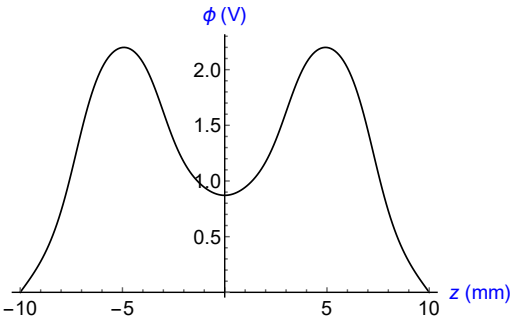

(A) Plotting the electrostatic potential $\phi(z)$ at $x = 0$ mm and $y = 1.45$ mm.

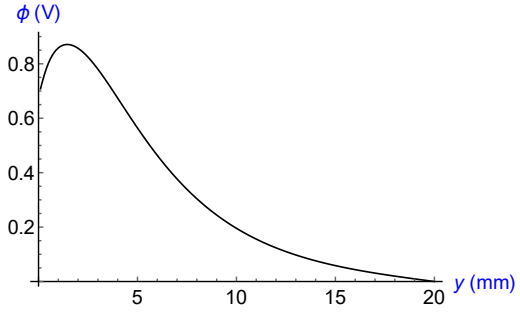

(B) Plotting the electrostatic potential $\phi(y)$ at $z = x = 0$ mm. The trapping height y_0 is approximately 1.45 mm, as expected.

FIGURE 6.2: Plots of the electrostatic potential (3.1) defined by $V_{\text{cath}} = 0$ V, $V_R = -0.67937$ V, $T_C^{(\text{opt})} = 1.400844$ and $T_E = 5.7$. The trap has $y_0 = 1.45$ mm and an axial frequency which should be in resonance with the axial resonator at ≈ 26 MHz. Both potentials (Figures 6.2a and 6.2b) have been multiplied by (-1) for ease of interpretation.

section for producing secondary electrons of any kinetic energy is $\sim$ 120 eV [85]. The loading trap is deep (approximately 7.31 eV deep) and it was decided to bias the photocathode with $V_{\text{cath}} = -70$ V, with a trade-off of trying to keep the energies low but trying to ionise and trap as many rest gas atoms as possible. The trap electrodes have biases defined by $T_E = 5.7$, $V_E = -21.95$ V, $V_R = -3.85088$ V, $T_C^{(\text{opt})} = 1.400844$ and $V_{\text{cath}} = -70$ V. This potential no longer has a trapping height y_0 of 1.45 mm, due to the perturbation of the photocathode. Also, as visible in Figures 6.4a and 6.4b, the axial potential well has a depth of approximately $\text{e}|-12.46\text{ V} - -5.03\text{ V}| = 7.43$ eV. This trap should still be deep enough to confine electrons, however the anharmonicities (§2.1.2) would most likely broaden the axial dip (§2.2) (or for hot electrons spread the energy over a wider frequency bandwidth) and thus make the axial motion unobservable. Furthermore, the anharmonicities would shift the axial frequency ω_z (§2.1.2).

Procedures for trapping

Two broadly similar methods for trapping secondary electrons have been attempted.

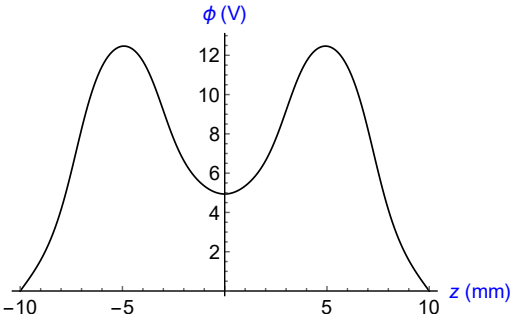

(A) Plotting the electrostatic potential $\phi(z)$ at $x = 0$ mm and $y = 1.45$ mm.

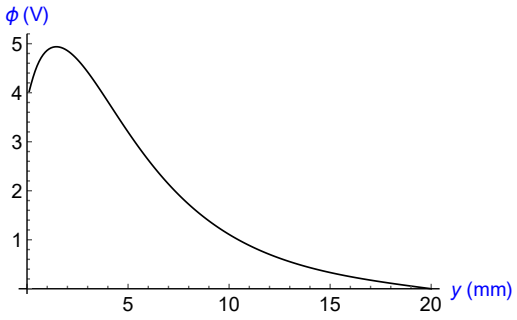

(B) Plotting the electrostatic potential $\phi(y)$ at $z = x = 0$ mm. The trapping height y_0 is approximately 1.45 mm, as expected.

FIGURE 6.3: Plots of a deep electrostatic potential ((3.1) with the photocathode modelled as another electrode) defined by $V_{\text{cath}} = 0$ V, $V_R = -3.85088$ V, $T_C^{(\text{opt})} = 1.400844$, $V_E = -21.95$ V and $T_E = 5.7$. The trap has $y_0 = 1.45$ mm. Both potentials (Figures 6.3a and 6.3b) have been multiplied by (-1) for ease of interpretation.

The first method involved maintaining $T_C^{(\text{opt})} = 1.400844$ (3.2) and $T_E = 5.7$ (3.3) while leaving the UV shutter open (to continuously liberate secondary electrons), while slowly ramping down (decreasing) $|V_R|$. The photocathode is continuously biased with a voltage of high magnitude (typically $V_{\text{cath}} = -70$ V). Typically, the ring voltage is ramped from $V_R = -1$ V to $V_R \approx -0.4$ V (discussed further in (§6.1.3)). The axial frequency ω_z is proportional to the curvature C_{002} of the electrostatic field (2.9c), where $C_{ijk} = V_R \cdot c_{ijk}$ [21] and therefore the axial frequency is proportional to the square-root of the ring voltage V_R. Therefore, while maintaining the tuning ratios $T_C^{(\text{opt})} = 1.400844$ and $T_E = 5.7$ and reducing $|V_R|$, the axial frequency ω_z of trapped electrons should decrease. At some V_R, the axial frequency ω_z of the trapped electrons should start to transit that of the resonance of the axial resonator, thus showing a transiting axial dip (or most likely an axial peak due to the expected axial energy being high). The calculated (by Dr José Verdú-Galiana) time constant (2.30) of the axial cooling is 4.3 ms, which results in part from the high Q-factor of the axial resonator. The most significant disadvantage of this method is that the photocathode bias voltage is always high (non-zero), and so there is always an asymmetric trap (Figure 6.4), which may give a large spread to the axial energies, which

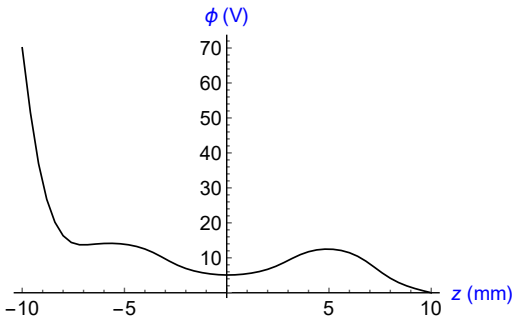

(A) Plotting the electrostatic potential $\phi(z)$ at $x = 0$ mm and $y = 1.45$ mm.

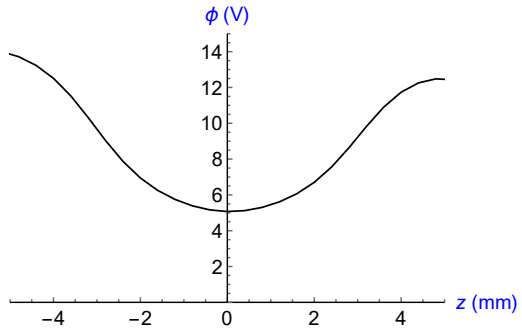

(B) Plotting the electrostatic potential $\phi(z)$ at $x = 0$ mm and $y = 1.45$ mm.

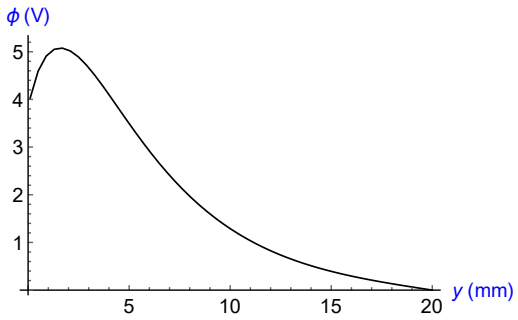

(C) Plotting the electrostatic potential $\phi(y)$ at $z = x = 0$ mm.

FIGURE 6.4: Plots of a deep electrostatic potential ((3.1) with the photocathode modelled as another electrode) defined by $V_{\text{cath}} = -70$ V, $V_R = -3.85088$ V, $T_C^{(\text{opt})} = 1.400844$, $V_E = -21.95$ V and $T_E = 5.7$. By inspection, the trapping height has increased to $y_0 = 1.69$ mm. Figures 6.4a and 6.4b show the same data but with different z ranges. All three potentials (Figures 6.4a, 6.4b and 6.4c) have been multiplied by (-1) for ease of interpretation.

may make the electrons unobservable using the electronic detection technique (§2.2). By finding the derivative of the axial frequency ω_z with respect to the ring voltage V_R (6.1a), an approximation may be derived (6.1b) around V_R [33] ($\omega_z = 2\pi\nu_z$):

$$\left.\frac{\partial}{\partial V_R}\omega_z\right|_{V_R} = \frac{\partial}{\partial V_R}\sqrt{2V_R \cdot c_{002} \cdot \frac{q}{m}} \tag{6.1a}$$

$$\left.\frac{\Delta\omega_z}{\omega_z}\right|_{V_R} \approx \frac{1}{2}\frac{\Delta V_R}{V_R}. \tag{6.1b}$$

The approximation (6.1b) suggests that at an initial ring voltage V_R with an axial frequency $\omega_z = 2\pi \cdot 30$ MHz, a change in the ring voltage $\Delta V_R = +1$ mV should correspond to a change $\Delta\omega_z = -2\pi \cdot 15$ kHz. However, due to the inverse square law (6.1a), this approximation ($\Delta V_R = +1$ mV corresponding to $\Delta\omega_z = -2\pi \cdot 15$ kHz) is particularly inaccurate when far from $\omega_z = 2\pi \cdot 30$ MHz.

The second method involves firstly liberating some secondary electrons with the deepest possible trap as shown in Figure 6.4. Then, the photocathode is grounded as soon as possible in approximately 1.5 s (§6.1.4), which causes the electrostatic potential to change to the deep trap shown in Figure 6.3. Then, the ring voltage is rapidly changed in one step (while maintaining $T_C^{(\mathrm{opt})} = 1.400844$ and $T_E = 5.7$) in order to bring the ring voltage to $V_R = -0.67937$ V (the potential shown in Figure 6.2), which should be in resonance with the axial resonator. This may be followed by the ramping of the ring voltage as described in the first method above (6.1b) and discussed further in (§6.1.3).

The axial frequency ramping procedure

As introduced in (§6.1.3), in order to bring any trapped electrons into resonance with the axial resonator, V_R may be ramped. While doing so, it is important to maintain the tuning ratio $T_C^{(\mathrm{opt})}$ (3.2) in order to minimise the electrical anaharmonicity (§2.1.2). It is also important to maintain the tuning ratio T_E (3.3) in order to maintain the trapping height y_0 (§2.6).

As introduced in (§6.1.2), in order to avoid resistive wall destabilisation, the filters in the second-stage (§3.1) (≈ 4 K) were changed to include large capacitances. These filters massively increased the rise-time of the voltage at every electrode. It took approximately 67.7 s for the voltage at the ring electrode to finish changing and approximately 6 s for each of the other four electrodes. Therefore, the differences in the rise times would have caused the tuning ratios to no longer be maintained while trying to ramp the voltages.

Although the voltages at the electrodes were measured to rise (with time) in a way that would be expected from the charging of a capacitor, it was noticed that while the

voltage changed from the initial voltage until halfway towards the final voltage, the voltage rises were reasonably linear. Therefore, a *LabVIEW* routine was written to maintain the voltage rises in these linear regions. This *LabVIEW* routine works when increasing and decreasing the ring voltage. After some empirical optimisation of the timing with assistance from Dr Jonathan Pinder, this method allowed the ring voltage to be changed from any initial voltage to any final voltage in approximately 3 s, while simultaneously ramping the voltages at the endcap electrodes and correction electrodes while maintaining the tuning ratios.

In order to test this routine, it was inserted into a loop and repeated several times in order to continuously ramp the voltages, to simulate a trapping attempt. The voltages were measured using an oscilloscope at the voltage screw connections (Figure 3.3) for the right correction electrode, the left endcap electrode and the right endcap electrode. The tuning ratios were calculated using (3.3) and (3.2) and are shown in Figure 6.5. There is some discrepancy between the target tuning ratios of $T_C^{(\mathrm{opt})} = 1.400844$ and $T_E = 5.7$, when compared to the experimentally-determined ones, because of the finite input impedances of the oscilloscope. It can be identified in Figure 6.5 that each run of the subroutine took approximately 3.16 s.

6.1.4 Implementation of an EBIS

An introduction to the photocathode

In order to implement an electron beam ion source (EBIS) [30], a photocathode was designed, fabricated and installed by Dr Jonathan Pinder. The photocathode was fabricated from some printed-circuit-board with a $(3\ \mathrm{mm})^2$ gold-plated square surface area and with a dielectric thickness of 1 mm. Some gold leaf was applied to the gold-plated surface for use as a target (§4.2). The rear of the photocathode has no conductive surface and is attached to a DC line, making the board into an electrode that may be biased with a voltage, i.e. the target is a photocathode. A hole was drilled through the wall of the chamber and the DC line was pushed through the hole from inside the chamber by Dr Jonathan Pinder, in order to fix the photocathode to the chamber while hiding the DC line, so that

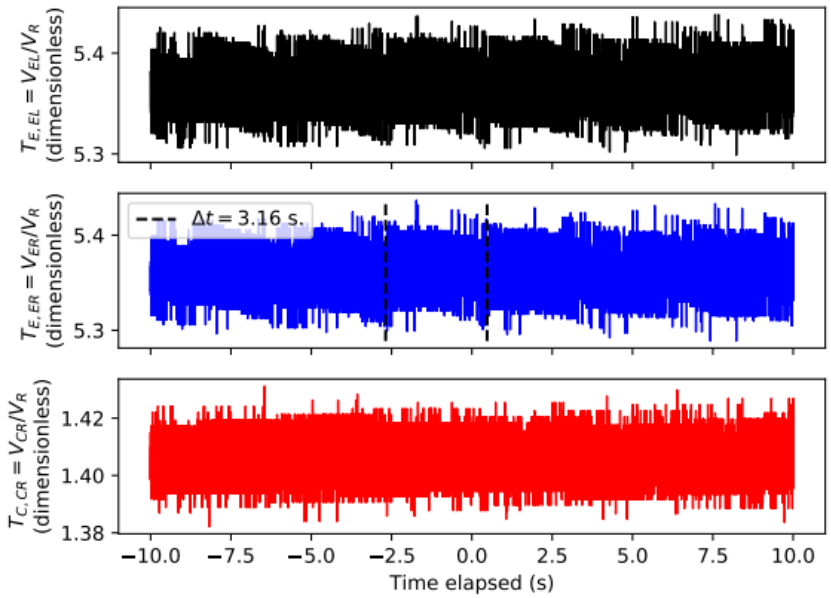

FIGURE 6.5: The measured tuning ratios $T_{E,EL}$, $T_{E,ER}$, and $T_{C,CR}$ for the left endcap electrode, the right endcap electrode and the right correction electrode respectively. The time taken to change all the voltages using one run of the subroutine was approximately 3.16 s.

the electrostatic trapping potential (§3.2) inside the chamber is not affected by the DC line. This setup is a prototype and the cryogenic trapping chamber (§3.4) cannot be hermetically sealed. Due to the superposition of the finite thicknesses, the gold leaf target is approximately 0.5 mm away from the chamber wall.

Numerical simulations conducted by Dr José Verdú-Galiana have shown that if a photoelectron reaches the centre of the trapping region $x = z = 0$ with a height $y' = y_0 + \Delta y$, then the initial magnetron radius is approximately Δy (assuming that $x = 0$). Therefore, ideally the photoelectrons should be liberated from as close to $\{x = 0, y = y_0\}$ as possible, in order to minimise the magnetron radius and thus stop the electrons from rapidly becoming grounded (§6.1.2). The chamber wall (Figure 3.5) is positioned in an $\hat{u}_x - \hat{u}_y$ plane at $z = -10$ mm (§3.4) and the 1 mm thick photocathode was recessed into the chamber wall by 0.5 mm, so the target is centred around $x = 0, z = -9.5$ mm, $y = 2$ mm (where $y \sim y_0 = 1.45$ mm - see Figure 6.3). A photograph of the photocathode is shown in Figure 6.6.

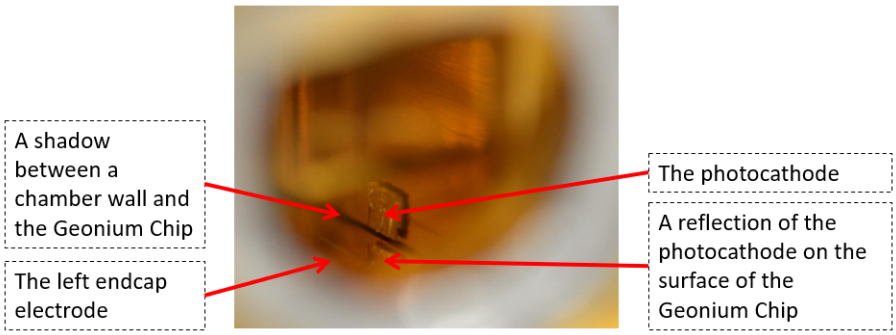

FIGURE 6.6: A photograph of the photocathode, taken from outside the chamber and looking in through the space where the window (§3.4) would have been, had it not been removed. The original photo was taken by Dr Jonathan Pinder.

The rise time of the photocathode

The DC bias line between the voltage supply and the photocathode was connected through two stages of low-pass filters (which were designed and implemented by Dr Jonathan Pinder), which are similar to the filters on the electrode DC voltage bias lines [146]. The filters slow the rate of change of voltage at the photocathode. As discussed in (§6.1.3), the photocathode bias voltage V_{cath} shifts the axial frequency ω_z and broadens the axial signal and so in order to detect trapped electrons, the photocathode needs to be electrically grounded as quickly as possible after having ionised the rest gas to produce secondary electrons (§6.1).

The rise time and the fall time of the voltage at the photocathode were measured to check that the photocathode bias voltage may be grounded sufficiently quickly, in case the lifetimes (§3.4) of trapped electrons are short. The voltage rises/falls were measured for various V_{cath}. The voltages were measured at the output of the final filter for the photocathode, using an oscilloscope. The nominal bias voltage was set to some value on the power supply while its output was off and then a *LabVIEW* program was used to turn the output on, then wait 5 seconds and then turn the output off. The currents were sufficiently high so that the power supply remained in constant voltage mode (with a floating current). The oscilloscope measurements are shown in Figure 6.7. The measured voltages did not reach the target voltages, because the oscilloscope has a finite input

TABLE 6.1: Results of measurements of the voltage rise times Δt_{rise} and fall times Δt_{fall} for different V_{cath}. The final row shows the mean values for Δt_{rise} and Δt_{fall}, along with their standard deviations.

V_{cath} (V)	Δt_{rise} (s)	Δt_{fall} (s)
-50	1.27	1.47
-60	1.39	1.58
-70	1.34	1.55
-80	1.29	1.49
-90	1.29	1.51
$\bar{\Delta t} \pm \sigma$	1.32 ± 0.04	1.52 ± 0.04

impedance.

The rise-time Δt_{rise} between changing from 0 V to V_{cath} and the fall-time Δt_{fall} between changing from V_{cath} to 0 V were both estimated by inspection of the plots in Figure 6.7. The rise/fall times were denoted this way around due to the voltage polarity being negative. The results are shown in Table 6.1. For all photocathode bias voltages, the change in voltage from the desired V_{cath} to ground took no longer than $\Delta t_{\text{fall}} = 1.5$ s. The Geonium Chip Penning trap was not hermetically sealed during the final trapping attempts and so the pressure was likely somewhere between $\sim 10^{-8}$ mBar with an electron lifetime on the order of seconds [11] and $\sim 10^{-11}$ mBar with an electron lifetime on the order of hours [13]. Therefore, although electrons will not be detectable within the first 1.5 s after having tried to ground the photocathode, this rise/fall time should still be shorter than the lifetime of any trapped electrons.

6.1.5 Evidence of ionisation

Introduction

The electron-impact cross-section for an atomic species is a function of the kinetic energy of the incident photoelectrons [204] (§6.1). This relation gives rise to an *ionisation curve*. An ionisation curve may be measured in the Geonium Chip Penning trap, using a technique similar to that used to measure photocurrents (§4). In (§4), primary electrons were

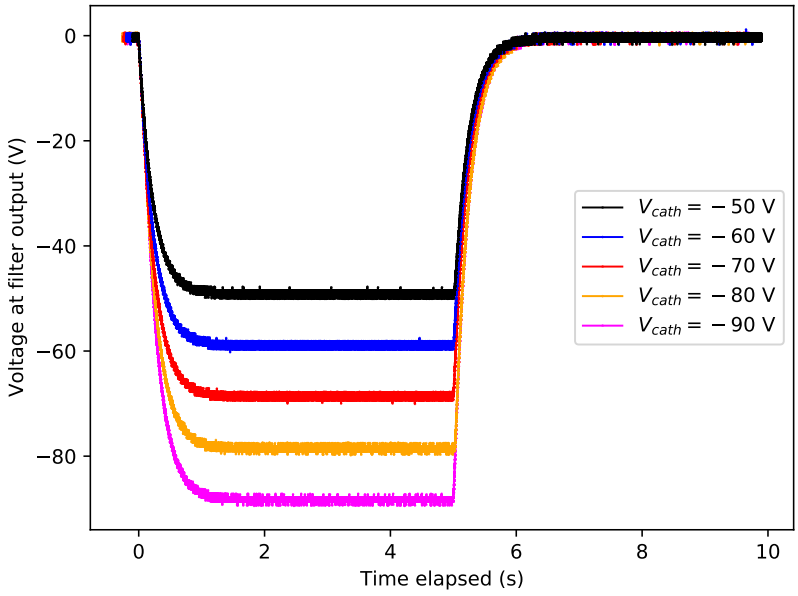

FIGURE 6.7: A plot showing the rise and fall of the voltage at the photocathode, for different desired photocathode bias voltages V_{cath}. The plotted time values have been shifted so that at 0 s time elapsed, all of the measured voltages start to increase in magnitude.

collected and so the collector required a positive bias voltage V_{col}. However, if the collector is instead biased with a negative bias voltage V_{col}, then any ionised rest gas particles (with a net positive charge) should be collected at the collector. The voltage V_{col} is set and so a *recombination current* of electrons should flow from the power supply for V_{col} in order to neutralise the collected ions.

This recombination current may be measured by putting an ammeter in series with the power supply for V_{col} and the collector electrode. If it can be assumed that all positive ions are collected at the collector, then the ionisation cross section is proportional to the photocurrent. The kinetic energy of the photoelectrons at the position of impact would also be similar to $e \cdot V_{\text{col}}$ (they would only be equal if the electrons would reach a 0 V potential at the position of impact, which is not true as can be seen in Figure 6.4). Therefore, a plot of the measured recombination current as a function of the photocathode bias voltage V_{col} should give a similar lineshape to the electron impact ionisation cross-section. This setup is identical to that used in (§4.7), but with a reversed polarity of V_{col}.

Demonstrating the ionisation of helium

An ionisation curve was obtained using the method and setup described in (§6.1.5). In particular, the left endcap electrode was used as the collector, which was biased with -5.000 V (nominal to the power supply). The other four trap electrodes were shorted together outside the cryostat and collectively electrically grounded. There was no magnetic field produced by the magnetic field source (§5). A *LabVIEW* control program was used to control the measurement. The photocathode bias voltage V_{cath} was ramped from 0 V to -320 V in steps of -5 V. The voltages between 0 V and -250 V were supplied by a power supply with a high precision and with a high temporal stability, whereas the voltages between -255 V and -320 V were supplied by a power supply with a lower precision and with a lower temporal stability, hence there being larger error bars for the latter voltage range. At each photocathode bias voltage, the recombination current was determined using the photocurrent determination technique (§4.1), which would be described with $N_{\text{skip}} = 5$, $N_{\text{bunch}} = 20$ and $N_{\text{pairs}} = 5$.

The resulting ionisation curve is shown in Figure 6.8. The peak photocurrent suggests that there is a peak in the ionisation cross-section at approximately $|V_{\text{cath}}| = |-110|$ V, which is in good agreement with a known ionisation cross section for helium [204].

The dependence of the ionisation curve on various trap parameters

In order to investigate the validity of the principle of the ionisation curve measurement using this technique, ionisation curves were obtained with variations of the collector bias voltage and the magnetic field strength.

The setup which was used in (§6.1.5) was also used to investigate the effect of the collector voltage V_{col} on the measured ionisation curve. Three ionisation curves were obtained with different collector bias voltages of -15 V, -10 V and -5 V. The data are plotted in Figure 6.9a. At increasing magnitudes of the collector bias voltage V_{col} the ionisation curves have higher amplitudes, which probably results from the collection of positive ions with increasing energy and/or increasing distance to the location of ionisation from the collector. Also at increasing magnitudes of the collector bias voltage, the ionisation

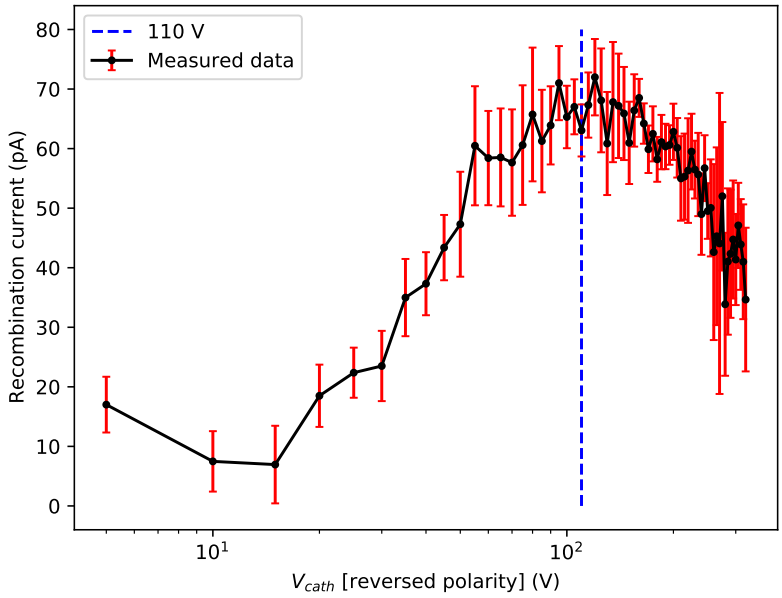

FIGURE 6.8: A plot of the measured recombination current, as a function of the photocathode bias voltage V_{cath} (with reversed polarity). A fiducial marker at 110 V is shown, which is similar to the peak ionisation cross-section for helium [204].

curve shifts downwards in V_{cath} (a decrease in the absolute value - which appears as a shift to the right in the plot), as can be seen by comparing the local minima around $V_{\text{cath}} \approx -20$ V and the peaks. The shift in V_{cath} is a similar value to the shift in the collector bias voltage V_{col} ($\approx$ 5 V each time). Therefore, this shift could result from the effect of the collector bias voltage (the collector was the left endcap electrode which is located between the photocathode and the centre of the trap) reducing the kinetic energy of the photoelectrons which ionise in the centre of the trap and beyond. The local minima around $V_{\text{cath}} = -20$ V have been observed for many different ionisation curve measurements and are suspected to result from the superposition of the electrostatic potentials produced by the photocathode and the left endcap electrode.

The setup which was used in (§6.1.5) was also used to investigate the effect of a magnetic field on the ionisation curve. The ionisation curve data were obtained for V_{cath} between 0 V and -250 V, while i) in the presence of an homogeneous $B_{z,000} = B_0 = 5$ mT (2.21) (2.11a) magnetic field and ii) not in the presence of an externally applied magnetic

field. The 5 mT magnetic field was scaled from the currents $\tilde{I}_{\text{reduced}}$ (5.10) which are typically used to make homogeneous fields during trapping attempts. The data are plotted in Figure 6.9b. The presence of the magnetic field scales the amplitude of the measured ionisation curve, but does not affect the lineshape. For example, in magnetic field strengths of 0 mT and 5 mT, there exist firstly local minima at $V_{\text{cath}} = -15$ V and secondly the peak recombination currents both occur at similar V_{cath}. It is suspected that the magnetic field increases the measured recombination current as a result of it focussing the primary electrons and guiding them towards the centre of the trap.

6.2 A *LabVIEW* control system

The Geonium Chip Penning trap is controlled by *LabVIEW* programs. There are two custom-built high performance computers which have identical hardware that is described in (§5.3.1). One computer is solely reserved for the control of the magnetic field source (§5.3) which includes quench protection with temperature monitoring and the changing of the source currents. The second computer is used to control all other aspects of the experiment (§6.2.1), with two main programs. One program is for the attempted loading of the trap (with electrons) and the second is for the detection of any trapped electrons (§6.2.2). The aim of the programs is to be able to have complete control of the experiment from one chair and while this has nearly been accomplished, due to the need for rapid prototyping of loading procedures, some devices (for example function generators) still require manual input. Computer control is important for some aspects of the trap loading procedure (e.g. for the ramping of the ring voltage (§6.1.3)), because it allows for a level of repeatability with a high degree of precision, which may occur in a time frame that is practically very nearly impossible to match with manual control.

6.2.1 Main control program 1: controlling the trap

The first control program controls the attempted loading of electrons and the searching for electrons. There are two similar versions of the control program, one for each variation of the loading procedure (§6.1.3), but both programs have the following features.

At the start of the first run of the program, all devices are initialised to the desired presets, ready for the immediate attempted loading of electrons. If the program has already been run, only certain devices which require reinitialising are reinitialised. For example, the voltage outputs from the calibrators for the DC electrode biasing are ramped to their starting voltages, but the *Rohde and Schwarz FSV30* spectrum analyser is not reconfigured. Rather than saving presets on the devices themselves, the preset settings are stored within the *LabVIEW* program itself, in order to keep all the information in one location which is stored reliably. During the loading procedure, the control program controls the trap electrode voltages, the voltage of the photocathode, the state of the UV shutter and a function generator for RF sideband cooling [103]. Historically, in previous versions of the program the states of relay switches have also been controlled. The loading procedure also features controls for the ramping of the ring voltage as discussed in (§6.1.3). The loading procedure also features an estimation of the time required for the electron axial signal to transit the axial resonance (§3.5), using (6.1).

6.2.2 Main control program 2: detection

For many years, trapping attempts were conducted while observing the resonance of the axial resonator (§3.5) by-eye. The Geonium Chip Penning trap experiment is yet to successfully trap any electrons and so there are many unknowns which contribute a lot of uncertainty to what the axial signal might look like. Simulations have been conducted by Dr José Verdú-Galiana in order to predict the axial signals with different trap imperfections and motional energies, for example [21, 22]. However, the electrical anaharmonicites (§2.1.2) and magnetic inhomogeneities (§2.1.2) in the real trap are unknown, along with the mean motional energies and their distributions. It is likely that during the first successful trapping attempt, the electrons will be hot and in an imperfect trap and

therefore they will probably exhibit an axial peak rather than an axial dip. Futhermore, due to the resistive wall effect, the magnetron radius should be minimised as soon as possible via magnetron cooling, however this is not possible yet because the axial and magnetron frequencies are unknown.

Therefore, it is not known what the axial signal might look like and so a second control program was written to help identify any electron transits of the axial resonator. The *Rohde and Schwarz FSV30* spectrum analyser has an internal function which conducts a *band power* measurement. Conducted over a user-specified frequency span and centre in a finite time, the band power measurement is an integration of the power, which calculates one value with units of dBm (power). Once every 50 ms, the second control program continuously queries the band power and frequency spectrum and saves both to a *.txt* file along with a time coordinate. The band power is plotted as a function of the time, but only shows the previous N measurements, which is typically set to $N = 200$. A similar technique which used a zero-span measurement demonstrated the trapping of electrons [13].

This technique has some benefits over observing the resonance by-eye. Firstly, if the axial signal has a small amplitude which may be unobservable by-eye, it still may appear somewhat clearly in the band power measurement. Secondly, the band power for the previous 200 times are also plotted, which may be checked if the user has diverted their attention elsewhere. Thirdly, the data is recorded and an auxiliary program was written which plots the measurement data so that trapping attempts may be reviewed. The auxiliary program is a while loop, where for each iteration i) all the band power data as a function of time (until the ith iteration) is plotted and ii) the ith frequency spectrum is also plotted.

6.3 A summary of the attempted loading and observation procedures

This chapter discusses the progress that has been made towards the loading of and the observation of electrons. Trapped electrons have not yet been observed.

This chapter discusses progress which has been made to the loading procedure (§6.1), which includes the attempted mitigation of the resistive wall effect (§6.1.2). An introduction to the trapping procedures (§6.1.3) is also given, which includes some important electrostatic potentials (§6.1.3), some procedures which attempt to trap electrons (§6.1.3) and a description of the procedure which is used to ramp the voltage of the ring electrode while trying to observe electrons (§6.1.3). Also included is an implementation of an EBIS (§6.1.4) which discusses the implementation of a photocathode (§6.1.4) and its rise time (§6.1.4).

There is also evidence of the ionisation (§6.1.5), which includes a demonstration of the ionisation of helium (§6.1.5) and the effect of trap parameters on the measured ionisation curves (§6.1.5).

The chapter also discusses two of the main *LabVIEW* control programs (§6.2), including a program which is used to control the trapping procedure (§6.2.1) and another program which is used to assist with the observation of any trapped electrons (§6.2.2).

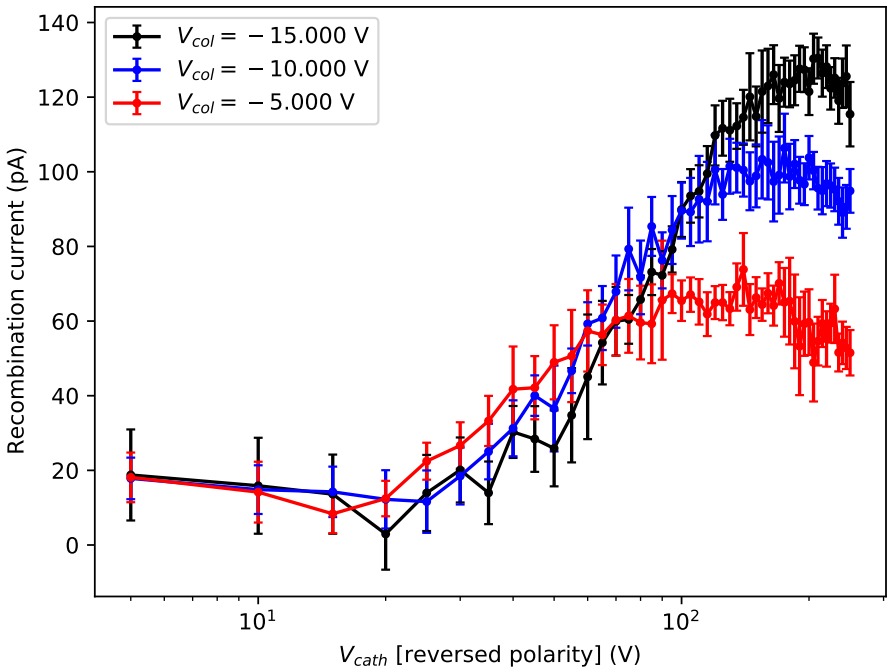

(A) Investigating the effect of the collector bias voltage V_{col} on the measured ionisation curve.

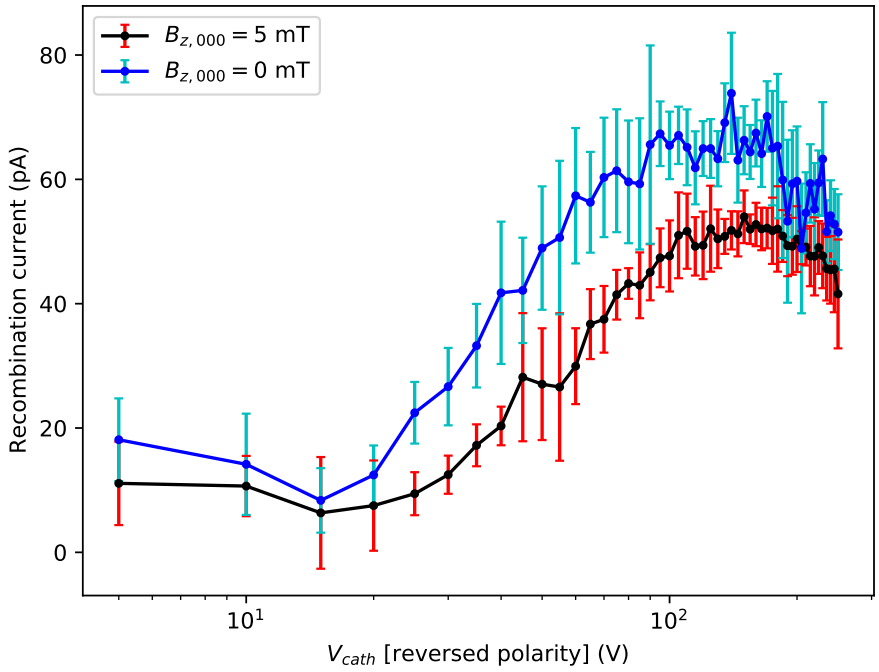

(B) Investigating the effect of a magnetic field on the measured ionisation curve.

FIGURE 6.9: Plots of the measured recombination current, as functions of the photocathode bias voltage V_{cath} (with reversed polarity).

Chapter 7

Summary and outlook

7.1 Summary

The first attempts to trap and observe electrons in the Geonium Chip Penning trap were undertaken prior to the research which is documented in this thesis, by researchers other than the author of this thesis. The main aim of the research of the author of this thesis was to trap and observe electrons and this thesis documents progress which has been made towards this aim. This thesis discusses characterisations of the cryogenic trapping chamber via the photoelectric effect, the calibration and control of the magnetic field source and a new trap loading method which utilises electron impact ionisation.

A comprehensive photoelectric characterisation of the cryogenic trapping chamber has been undertaken. An automated photocurrent determination system has been developed (§4.1), which can estimate the photocurrent despite the presence of electrical noise. A measurement of the photocurrent as a function of the bias voltage of the collector (§4.3.1) helped to verify the electrostatic models which the group uses when trying to load and trap electrons. The relation between the photocurrent and the pressure has been investigated (§4.4.1), which may be used for leak detection (§4.5.3), which is useful because the cryogenic trapping chamber does not feature a conventional pressure gauge. It was observed (§4.4.2) that in a pinched-off chamber which had not been baked-out, that the outgassing of water caused the pressure to rise to that of the saturation vapor pressure of water. This measurement of outgassing lead to a bake-out being undertaken (§4.5), which increased the photocurrent by a factor of (5.49 ± 0.06) (dimensionless). A new

fibre-integrated-flange has been introduced (§4.7.1) which increased the photocurrent by a factor of (21 ± 1) compared to the previous fibres and flange. Several applications of photocurrent measurements have been demonstrated, including for the verification of the alignment of the optical fibre (§4.7.3) and to verify the electrode DC bias connections (§4.7.4), both of which would not be verifiable by other means in the current setup.

A robust implementation of the planar magnetic field source for the Geonium Chip Penning trap has been undertaken. Despite being designed for the Geonium Chip Penning trap, this unique magnetic field source also has applications in other technologies. The first direct (in-situ) calibration of the source (§5.1.2) while at $\approx$ 4 K has been undertaken and the magnetic field has been measured to show a good degree of homogeneity with two different homogeneous 300 mT homogeneous fields (§5.1.3). A strong 500 mT field (§5.1.4) has also been demonstrated. A control system for the magnetic field source has been engineered (§5.3), which provides active quench protection (§5.3.2) and which may also control the currents (and thus the magnetic field distribution) (§5.3.3). An application whereby the state of the UV shutter may be determined has also been demonstrated (§5.3.5).

The change from the loading of primary electrons, to the loading of secondary electrons (via electron impact ionisation which uses an electron beam ion source), has been introduced (§6.1). An attempted mitigation of the resistive wall effect (§6.1.2) has also been discussed, which might otherwise severely reduce the lifetimes of any trapped electrons. Some procedures (§6.1.3) have been implemented to try to trap electrons along with a procedure (§6.1.3) which is used to ramp the voltage of the ring electrode (to ramp the axial frequency) while trying to observe electrons. The implementation of an EBIS (§6.1.4) which uses a photocathode (§6.1.4) has been discussed and experimental evidence to show the ionisation of helium (§6.1.5) has been included. Two main *LabVIEW* control programs (§6.2) have been implemented, which are used to control the trapping procedure (§6.2.1) and to assist with the observation of any trapped electrons (§6.2.2).

7.2 Outlook

Although progress has been made towards the aim of trapping and observing trapped electrons in the Geonium Chip Penning trap, this aim has not yet been met. Therefore, further work should be undertaken in order to improve the trap and achieve this aim. There is no known fundamental issue with the Geonium Chip Penning trap. This outlook contains a thorough investigation into the Geonium Chip Penning trap in its current form, including evaluations of the electric field source (§7.2.1), the magnetic field source (§7.2.2), the stability of the trap (§7.2.3), the detection system (§7.2.4) and the loading procedure (§7.2.5). This outlook concludes with a summary and recommendations about how to improve the trap so that electrons may be trapped and subsequently detected (§7.2.6).

7.2.1 Evaluating the electric field

The electrostatic model

The most important electrostatic potentials $\phi(x, y, z)$ (3.1) in the Geonium Chip Penning trap have been simulated (§6.1.3). For example, the loading trap should be deep enough at 7.31 eV to provide the axial confinement of secondary electrons, because this is deeper than the depth of 4.5 eV which has previously demonstrated [13] the trapping of secondary electrons. The electrostatic models used in these simulations have been verified in the real trap by using photoelectric characterisation techniques (§4.3.1), which suggests that if the desired DC electrode voltages were to successfully reach the electrodes, then the electrostatic potentials in the real trap should be those which have been simulated. Furthermore, another application of the photoelectric effect verified that DC voltages were reaching the trap electrodes (§4.7.4). This verification was limited in that the magnitude of the voltages on the electrodes remained unknown, however the magnitudes of these voltages were likely correct because i) in theory the DC bias lines for the trap electrodes are open circuits and so there shouldn't be any voltage drops across any resistances in the DC bias lines and ii) the voltages at the chip were measured to have the

correct polarities and magnitudes prior to the closing-up of the cryostat. Therefore, it is likely that the electrostatic potentials $\phi(x,y,z)$ (3.1) in the real trap are sufficient for loading and detecting electrons and so further optimisation is not a priority.

The ellipticity

The ellipticity of the trap should also be considered. An elliptical Penning trap has been investigated experimentally for argon and fullerene ions [92], where an elliptical term was introduced into the electrostatic trapping potential of a Penning trap with hyperbolic electrodes by segmenting the ring electrode. Here [92] the authors report difficulties in storing ions with electrode voltages defined by $U_{\text{ellipt}}/U_0 \geq 0.4$ [92, pg. 39] and by evaluating [92, Eqn. 12] with $a_{2,0} \simeq 0.78$ [92, pg. 35], $c_2 \simeq 1.45$ [92, pg. 35] and $U_{\text{ellipt}}/U_0 = 0.4$, it would suggest that there were storage difficulties for $\epsilon \geq 0.905$. The electrostatic potential $\phi(x,y,z)$ (3.1) in the Geonium Chip Penning trap which should make the axial frequency ω_z resonant with the axial resonator (to make the trapped electrons observable (§2.2)), which may be defined by $V_R = -0.67937$ V, $T_C^{(\text{opt})} = 1.400844$, $T_E = 5.7$ and $V_{\text{cath}} = 0$ V (as plotted in Figure 6.2), has an ellipticity $\epsilon \approx (0.0203 - 0.0544)/-0.0747 = 0.456$ (2.2). Also note that these trap voltages give rise to an axial frequency of $\omega_z = 2\pi \cdot 25.7979$ MHz. This ellipticity was calculated using the curvatures C_{200}, C_{020} and C_{002} (2.2) after evaluating the analytic function [22, App. A] for $\phi(x,y,z)$ (3.1), where the Mathematica functions were provided by Dr José Verdú-Galiana. Therefore, the ellipticity of the Geonium Chip Penning trap potentials (e.g. $\epsilon = 0.456$) are unlikely to be high enough (e.g. $\epsilon = 0.905$) to cause difficulties when trying to trap. **However, if the side electrodes (§3.2) were to be implemented, a suitable choice of their voltage bias V_G should allow for the ellipticity ϵ to be set to zero, as is the case with conventional traps with circular symmetry (§2.1.1).**

7.2.2 Evaluating the magnetic field

The typical magnetic field

It has been experimentally determined that the magnetic field source can produce a magnetic field with sufficient magnitude along $\hat{u}_z$ and also sufficient homogeneity (small inhomogeneities (§2.1.2)). For example, two suitable $B_0 = B_{z,000} = 300$ mT homogeneous fields have been set and measured (§5.1.3), along with one $B_0 = B_{z,000} = 500$ mT homogeneous field (§5.1.4). Typically during trapping attempts, the currents in $\tilde{I}_{\text{reduced}}$ (5.10) for a $B_0 = B_{z,000} = 300$ mT field (with a desired $B_{z,020} = 0$) are scaled linearly to make a $B_0 = B_{z,000} = 100$ mT homogeneous field (§5.1.3). This is a linear algebra system ($\tilde{B}_{\text{reduced}} = \mathbf{\Gamma}(y_{E,0} = 1.45\,\text{mm}) \cdot \tilde{I}_{\text{reduced}}$) (5.10). Firstly, this means that the inhomogeneities $B_{z,010}$, $B_{z,020}$ and $B_{z,030}$ (§2.1.2) should also scale linearly and so the inhomogeneities for a $B_0 = B_{z,000} = 100$ mT field should also be one-third those of the $B_0 = B_{z,000} = 300$ mT field, so the $B_0 = B_{z,000} = 100$ mT field should be homogeneous enough to contain secondary electrons. Secondly this also means that the alignment of the $B_0 = B_{z,000} = 100$ mT field should also be in the same direction as the $B_0 = B_{z,000} = 300$ mT field, which should have the same alignment as the trap (electrostatic potential) axis $\hat{u}_z$ and so the magnetic field should still be orientated correctly.

As mentioned above, the currents in $\tilde{I}_{\text{reduced}}$ (5.10) (with a desired $B_{z,020} = 0$) are those which are scaled to make homogeneous fields during trapping attempts, typically with $B_{z,000} = 100$ mT. Figure 5.4a shows the measured $\tilde{B}^{(\text{meas})}_{\text{reduced}}$ as produced by $\tilde{I}_{\text{reduced}}$ (5.10) for a desired 300 mT homogeneous field and this 300 mT field is analysed in Table 5.2. Although no 100 mT field has been measured, the calibration of the magnetic field source is a linear algebra system ($\tilde{B}_{\text{reduced}} = \mathbf{\Gamma}(y_{E,0} = 1.45\,\text{mm}) \cdot \tilde{I}_{\text{reduced}}$) (5.10) and so in order to predict the magnetic field distribution $B_z(x, y, z)$ for a 100 mT field, the model for the 300 mT field has been linearly scaled by a factor of 3. To be more specific, the measured data of the 300 mT field $B_z(y)$ from the Hall probe array (Figure 5.4a) was input into the 3D Biot-Savart model (5.5) (§5.1.2) and using this model, the magnetic field $B_z(x, y, z)$ values for a 300 mT field were multiplied by $1/3$ and are shown in Figures 7.1,

7.2 and 7.3. The Mathematica functions for this model were provided by Dr José Verdú-Galiana. As discussed (§5.1.1), in theory it is only necessary to compensate for the vertical inhomogeneities $B_{z,0j0}$ (2.21) [97], i.e. it is of most concern that $B_z(y)$ is homogeneous around the trapping region $\vec{r}_0 = (0, y_0, 0)$ (§2.1.1), which is verified by considering Figure 7.2b. Also, Figures 7.1b and 7.2a show that close to the trapping position, $B_z(z)$ and $B_z(x)$ are also homogeneous, where it is more important that $B_z(x)$ is homogeneous than $B_z(z)$, because the reduced/modified cyclotron motion orbits in the $\hat{u}_x - \hat{u}_y$ plane (§2.1.1). The gradient $\partial B_z/\partial z$ plotted in Figure 7.1c is relevant during the loading procedure and is discussed in (§7.2.2). Figure 7.3 shows plots of the magnetic field B_z in three spatial dimensions.

In the future, the existing magnetic field source prototype will be further optimised by using trapped electrons as precise magnetic field sensors (§3.3.1). As introduced in (§3.3) the existing source is continuously driven with current [36], but a source running in persistent mode would have maximum stability [36]. **As discussed in [97], the existing source will be replaced with a flux pumped source which runs in persistent mode, which is expected to produce homogeneous fields which are stronger than 1 T.** Progress towards a flux pumped source is discussed in [123, 205]. As discussed in [36], one advantage of having the magnetic field source bolted to the electric field source (the chip) as can be seen in Figure 3.6b, is that both sources should move together (relative to any externally-induced vibration) and so the trap should allow for high precision measurements and possibly improve fundamental measurements (§1.1.3).

The magnetic mirror effect

The effect of a gradient in the magnetic field [92], which is also known as a *magnetic mirror field* [206], has also been considered regarding the loading procedure. This is relevant for considering the change in the kinetic energy of the primary electrons as a result of their travel from the photocathode to the rest gas in the centre of the trap. While in the presence

of a magnetic field gradient, a trapped electron would experience a force $\vec{F}_{\text{mir}}$ [92]

$$\vec{F}_{\text{mir}} = \vec{\nabla}(\vec{\mu} \cdot \vec{B}), \tag{7.1}$$

where $\vec{\mu}$ is the magnetic moment and $\vec{B}$ is the magnetic field vector [92]. Assuming that the magnetic moment $\vec{\mu}$ is aligned parallel/antiparallel with the axis $\hat{u}_z$ of the magnetic field, then this may be simplified to

$$\vec{F}_{\text{mir}} = \pm|\vec{\mu}|\frac{\partial B_z}{\partial z}\hat{u}_z, \tag{7.2}$$

where $\partial B_z/\partial z$ is the gradient of the $\hat{u}_z$ component of the magnetic field (B_z) along z. The direction (governed by $\pm$) is dependant on whether the magnetic moment aligns parallel or antiparallel with the magnetic field axis $\hat{u}_z$. Depending on their initial velocities in the $\hat{u}_x - \hat{u}_y$ plane, some primary electrons undergo cyclotron motions with "clockwise" directions and some with "anticlockwise" directions and therefore some electrons will align parallel with $\hat{u}_z$ and some antiparallel. The change in kinetic energy ΔE_{mir} of a photoelectron due to the magnetic field gradient between the cathode and the rest gas can be found by integrating (7.2)

$$\Delta E_{\text{mir}} = \int \pm|\vec{\mu}|\frac{\partial B_z}{\partial z}\hat{u}_z \cdot d\vec{z}. \tag{7.3}$$

A robust investigation of the magnetic mirror effect would need to consider the position z evolution of the magnitude of the magnetic moment $|\vec{\mu}|(z)$ of the electron during its movement along $\hat{u}_z$, from the photocathode at $z = -9.5$ mm to the rest gas at $z = 0$ mm (§6.1.4). While close to the centre of the trap $\vec{r}_0 = (0, y_0, 0)$ (§2.1.1), the magnetic moment $\vec{\mu}$ of a primary electron is a combination of the magnetic moments for the spin, cyclotron and magnetron motions [87], which may be parallel or antiparallel with $\hat{u}_z$ [87]. However, firstly, when close to the centre of the trap the magnetron magnetic moment $\vec{\mu}$ is negligible compared to that of the cyclotron magnetic moment [121] and secondly when far from the centre of the trap the primary electrons (§6.1) shouldn't undergo any

magnetron motion. Also, when close to the centre of the trap the spin magnetic moment is much smaller than the cyclotron magnetic moment (see the expressions in [121]). Therefore, for simplicity it can be crudely assumed that the magnetic moment is always dominated by the cyclotron magnetic moment $\vec{\mu}_p$, which can be defined as [121]

$$\vec{\mu}_p = -(2n_p + 1)\mu_B, \tag{7.4}$$

where n_p is the reduced cyclotron oscillator number (2.33b) and where μ_B is the Bohr magneton.

In order to simplify the integral (7.3) in order to estimate the change in the kinetic energy ΔE_{mir}, it can be crudely assumed that the gradient is constant for all z and so the integral may be approximated using

$$\Delta E_{\text{mir}} \approx \pm \overbrace{|-(2n_c + 1)\mu_B)|}^{|\vec{\mu}|} \frac{\partial B_z}{\partial z} \Delta z. \tag{7.5}$$

Here, $\Delta z = +9.5$ mm is the change in z from $z = -9.5$ mm at the photocathode to $z = 0$ mm in the centre of the trap where the rest gas is located (§6.1.4) (§3.4). The gradient $\partial B_z/\partial z$ is plotted as a function of z in Figure 7.1c and the mean gradient between $z = -9.5$ mm and $z = 0$ mm is -4.20 mT/mm, with a standard deviation of 2.38 mT/mm. An overestimation of the cyclotron oscillator energy of 1 eV corresponds to $n_p \approx 86000$ in a $B_0 = 100$ mT field ((2.33b) while assuming that $\omega_p \simeq \omega_c$ [37]). Therefore, when $\vec{\mu}$ is parallel with $\hat{u}_z$, $\Delta E_{\text{mir},\uparrow\uparrow} \approx +400$ meV (overestimated) and similarly, if $\vec{\mu}$ is antiparallel with $\hat{u}_z$, $\Delta E_{\text{mir},\uparrow\downarrow} \approx -400$ meV (magnitude overestimated).

The cathode is normally biased with $V_{\text{cath}} = -70$ V (§6.1.3) and so ± 400 meV is negligible - the kinetic energies of all the primary electrons, whether their magnetic moments are parallel or antiparallel with the axis of the magnetic field, should still suffice to ionise rest gas because the ionisation cross section should not change too much (§6.1.5). Nonetheless, a new set of magnetic field source currents was determined (by Dr José Verdú-Galiana) and subsequently driven through the source, where the mean gradient

$\partial B_z/\partial z$ and its standard deviation were both close to zero in order to avoid the magnetic mirror effect, but this still didn't result in the observation of any trapped electrons.

7.2.3 Evaluating the stability of the trap

The stability criterion

As previously discussed (§2.1.1), there is a stability condition $2\omega_z^2 < \omega_c^2$ [23]. While also considering the dependence of the free cyclotron frequency ω_c (2.11a) on the magnetic field strength $B_0 = B_{z,000}$, this stability criterion suggests that an electron in a $B_{z,000} = 100$ mT magnetic field (typical) would remain trapped so long as the axial frequency is lower than $2\pi \cdot 6.42 \times 10^{18}$ Hz. This maximum axial frequency is ten orders of magnitude greater than the highest known expected axial frequency of $\omega_z = 2\pi \cdot 70.4$ MHz (Figure 6.3) to exist in the Geonium Chip Penning trap. It should also be mentioned that experimental observations of electrons trapped in a Penning trap with hyperbolic electrodes showed that the trap became unstable with a ring voltage of half that suggested by the criterion $2\omega_z^2 < \omega_c^2$ [207] and so it could be expected that the trap would become unstable for axial frequencies lower than $2\pi \cdot 6.42 \times 10^{18}$ Hz. As discussed (§6.1.3), the axial frequency ω_z is proportional to the square-root of the ring voltage V_R and so by using (6.1b) with $\Delta V_R = \frac{1}{2} V_R$ it can be calculated that $\Delta\omega_z = \frac{1}{4}\omega_z$. Therefore, with a $B_{z,000} = 100$ mT magnetic field (typical), the Geonium Chip Penning trap might become unstable for axial frequencies of greater than $\frac{3}{4} \cdot (2\pi \cdot 6.42 \times 10^{18})$ Hz which is still ten orders of magnitude greater than $\omega_z = 2\pi \cdot 70.4$ MHz which is used in the Geonium Chip Penning trap at present.

Static resonance

Another set of trap instabilities result from static (non-time-varying) trap imperfections (electrostatic anharmonicities (§2.1.2) and magnetostatic inhomogeneities (§2.1.2)) when the trap eigenfrequencies are integer ratios of one another [207, 208]. Furthermore, the instabilities may result from a misalignment between the axes of the magnetic field and the electrostatic field [207], which might be the case if the Hall probe array (§5.1.1) was

misaligned with the $\hat{u}_x$, $\hat{u}_y$ or $\hat{u}_z$ axes during the calibration of the magnetic field source (§5.1.2), however visually the Hall probe array appeared to be well aligned. Also, the instabilities may result from the resulting Coulomb potential from a cloud of trapped electrons [207], however due to a lack of observation of trapped electrons this Coulomb potential is unlikely to cause instabilities, but the primary and secondary electrons might cause space-charge/plasma instabilities (§7.2.3). These instabilities have been observed experimentally for trapped electrons in a Penning trap [207], which resulted in electrons being lost from the trap [207].

The static resonance instabilities may occur when integer multiples of the particle motional frequencies (§2.1.1) sum to zero [207]

$$n_z^{(\text{ins})}\omega_z + n_p^{(\text{ins})}\omega_p + n_m^{(\text{ins})}\omega_m = 0 \tag{7.6}$$

where $n_z^{(\text{ins})}$, $n_p^{(\text{ins})}$ and $n_m^{(\text{ins})}$ are integers [207] (note, these integers are **not** the quantum numbers (2.33) of the motional quantum harmonic oscillators). A phenomenological explanation of this *static resonance* [208] effect is that the static imperfections cause static perturbations to the motion of the trapped particle [208] and these perturbations add constructively at certain spatial positions as a result of the synchronisation of motional time periods [208]. Another phenomenological interpretation [207] considers these instabilities from static perturbations in a Penning trap to be analogous to instabilities from time-varying perturbations in a Paul trap.

These frequencies will have some amount of broadening due to the existence of trap imperfections (§2.1.2) and so to reduce the chance of an instability existing (7.6), it is best to have the motional frequencies as far apart from one another as possible. For example, using the electrostatic potential defined by $V_R = -0.67937$ V, $T_C^{(\text{opt})} = 1.400844$, $T_E = 5.7$ and $V_{\text{cath}} = 0$ V (which should make the electrons observable) and while also in the presence of a $B_0 = B_{z,000} = 100$ mT homogeneous magnetic field, the motional frequencies (§2.1.1) are $\omega_z = 2\pi \cdot 25.7979$ MHz, $\omega_p = 2\pi \cdot 2.799$ GHz and $\omega_m = 2\pi \cdot 105.78$ kHz. These motional frequencies are very far apart and so the likelihood of developing a static

resonance instability is low. The reduced cyclotron frequency ω_p is much greater than the axial frequency because of the high strength of the magnetic field ($\omega_p \approx \omega_c(B_0)$ (2.11a) [37]). When these instabilities were observed experimentally for trapped electrons in a Penning trap [207], the magnetic field strengths were at most 4.37 mT, which is much less than the $B_0 = B_{z,000} = 100$ mT field in typical use in the Geonium Chip Penning trap.

Resistive-wall destabilisation and space-charge/plasma effects

The theory of the resistive-wall destabilisation effect has been introduced in (§2.3.2) and the improvements made to the experiment have been discussed in (§6.1.2). The resistive cooling time constants $\tau^{(i)}(Z(\omega_m), D^{(i)}_{\text{eff}})$ (2.30) of the magnetron motion from the improved low-pass filters of each of the five DC trap electrodes (§3.2) have been calculated by Dr José Verdú-Galiana for one such deep trap (with $V_R = -10.85$ V which corresponds to $\omega_m = 2\pi \cdot 1.69$ MHz and $\omega_z \approx 2\pi \cdot 103$) MHz to be on the order of days. Also, the photocathode bias line has low-pass filters (§6.1.4) which would also induce resistive cooling, however the effective coupling distance should be high because i) the electrons are trapped spatially-far (≈ 10 mm) from the photocathode (§6.1.4) and ii) the magnetron motion only has $\hat{u}_x$ and $\hat{u}_y$ components while the photocathode is in the $\hat{u}_x - \hat{u}_y$ plane. Therefore, it is unlikely that the resistive-wall destabilisation effect is causing a trap instability.

Although the aforementioned discussion would suggest that the resistive wall effect has been avoided, another solution would be to increase the maximum permitted magnetron radius (2.15) **by raising the equilibrium trapping position** $\vec{r}_0 = (0, y_0, 0)$ **(§2.1.1).** However, this would require a new set of magnetic field currents (§5.1.1) because the calibration matrix $\mathbf{\Gamma}(y_0)$ (5.1a) or $\mathbf{\Gamma}'(y_0)$ (5.2a) is only valid for one trapping height y_0 (§2.1.1). This would also require a new set of trapping voltages V_R, V_C and V_E (3.1), where simulations have shown that the trapping height is strongly dependent on the tuning ratio T_E (3.3).

In the current setup, the cryogenic trapping chamber (§3.4) is gold plated internally.

Despite the inside of the chamber having a matt finish, any illumination of the chamber through the window illuminates a significant amount of the chamber as a result of reflections. Therefore, primary electrons will be continuously liberated from all the chamber walls and the surface of the chip (§3.2). Although electrons shouldn't build up on the visible chip substrate (alumina) between the electrode gaps (§3.2), there might be a space-charge effect [110] which might distort the electrostatic trapping potential (3.1). However, the magnetic field should cause photoelectrons liberated from the chip surface and the walls (other than from the wall opposite to the photocathode which is perpendicular to the magnetic field axis $\hat{u}_z$) to be rapidly grounded via a cyclotron motion (§2.1.1). Photoelectrons which are liberated from the wall opposite to the photocathode (§6.1.4) are not accelerated by the photocathode and so they should not have enough kinetic energy to enter the centre of the trap. However, if the trapping volume is nonetheless flooded with electric charge, then this might cause instability, or perhaps undesirable plasma effects (§2.3.2). Unlike the Geonium Chip Penning trap, other planar Penning traps [11, 13, 16, 18] introduce their beams of primary electrons through apertures and so their beams are well focussed and therefore secondary electrons are not produced in other locations within their trapping regions. **Therefore, in order to avoid undesired primary and secondary electrons being in places other than the centre of the trap, it is recommended that the photocathode should be moved outside the cryogenic trapping chamber (§3.4). This should be done in such a way that i) no UV light would enter the chamber (to stop photoelectrons from being liberated from anywhere other than the cathode) and that ii) primary electrons would enter the chamber through an aperture (e.g. [13]) so that all primary electrons would enter the trap at the trapping height y_0 (to avoid large magnetron radii (§6.1.2)).**

The expected lifetime

The lifetime of the electrons is strongly dependent on the pressure (§3.4). The pressure in the Geonium Chip Penning trap experiment typically reads $\sim 10^{-8}$ mBar at the flange which is at room temperature (§3.1), while the cryogenic trapping chamber (§3.4) is at

≈ 4 K. Therefore, even if the cryogenic trapping chamber is not hermetically sealed prior to its installation in the experiment, a cryovacuum should be reached with pressures of $< 10^{-8}$ mBar. Pressures of $\sim 10^{-8}$ mBar and $\sim 10^{-11}$ mBar gave rise to measured lifetimes (time constants from exponential fits) of (22 ± 2) seconds [11] and 3.5 hours [13] respectively for trapped electrons in planar Penning traps. This should give trapped electrons a lifetime of between seconds and hours in the Geonium Chip Penning trap, which should be long enough to detect them.

7.2.4 Evaluating the detection system

It is plausible that electrons have been trapped and not subsequently detected. The theory (§2.2) and the experimental realisation (§3.5) of the bolometric electronic detection method have been introduced, where any trapped electrons will only be visible if their axial frequencies are resonant with the niobium axial resonator (detection coil). It is likely that initially multiple electrons (a cloud) will be loaded into the trap. The high charge-to-mass-ratio of the electron suggests that motion-based gates using trapped electrons should be quick [28], which suggests that electrons in the cloud should undergo Coulomb interactions with each other rapidly and therefore each of the eigenmotions should rapidly reach thermal equilibrium across the cloud (§2.3.1), so there should only be one (albeit perhaps broad-in-frequency) axial signal. The trap has not yet been experimentally optimised and so the initial trap imperfections, that is the electric anharmonicities (§2.1.2) and the magnetic inhomogeneities (§2.1.2), would most likely shift the axial frequency ω_z of a trapped electron (§2.1.2) and also broaden the axial dip (§2.2) for one trapped electron. Therefore, it is likely that the trap imperfections would spread the combined energy of the cloud over a wider axial frequency bandwidth, however it is likely that the electrons are loaded with relatively high energies (on the order of 1 eV) and so their axial signal should still be visible against the noise. An automated band power measurement has been implemented (§6.2.2) in order to help identify any electron transits which occur across the axial resonator, similar to the use of a zero-span measurement which demonstrated the trapping of electrons [13].

Improvement: widening the detection window

The main disadvantage of the use of one detection coil is that there is a narrow finite detection window [32] - electrons will only be visible if their axial signal is in resonance with the detection coil [32]. At present, the centre frequency of the coil is $\omega_z \approx 2\pi \cdot 25.7979$ MHz (corresponding to a ring voltage of approximately $V_R = -0.67937$ V).

The full-width-half-maximum Γ_{FWHM} of the niobium coil is approximately 100 kHz (e.g. see Figure 3.11b). Therefore, the useful detection window of approximately 150 kHz is between $\approx \omega_z = 2\pi \cdot 25.723$ MHz and $\approx \omega_z = 2\pi \cdot 25.883$ MHz. As discussed (§6.1.3), the electrostatic potential which corresponds to an axial frequency of $\omega_z \approx 2\pi \cdot 25.7979$ MHz (Figure 6.2) may be too shallow with an axial depth of only 1.29 eV. Alternatively, electrons may instead be loaded in the deepest possible trap (not a fundamental limit) which corresponds to $V_R = -3.85088$ V (Figure 6.3) with an axial depth of 7.31 eV (§6.1.3), which is deeper than the depth of 4.5 eV which has successfully trapped electrons in another planar Penning trap with circular electrode geometry [13]. However, the axial frequency corresponding to $V_R = -3.85088$ V is $\omega_z = 2\pi \cdot 70.4$ MHz, which is far from the detection window of the niobium axial resonator.

As discussed (§6.1.3), there are two alternative but broadly similar procedures for trapping electrons. The first procedure involves continuously liberating secondary electrons, while slowly ramping down (decreasing) $|V_R|$ from $\approx |-1|$ V to to $\approx |-0.4|$ V in order to decrease ω_z (§6.1.3). The limitation of this method is that the photocathode is continuously biased with a voltage of high magnitude (typically $V_{\text{cath}} = -70$ V) and so the electrostatic potential is asymmetric (there is a high degree of anharmonicity (§2.1.2)) which might make the electrons unobservable. The second procedure involves initially loading the electrons in the deep trap (with $V_R = -3.85088$ V), before rapidly grounding the photocathode (to reduce the anharmonicity and make the electrons easier to observe) and then immediately bringing any trapped electrons into resonance with the coil at $V_R = -0.67937$ V. The limitation of this method is that trapped electrons might be lost either as a result of the resulting excitation from a rapid change in the electrostatic potential, or as a result of their collision with rest gas if the pressure is too high (§7.2.3).

Both procedures typically end in further ramping of the ring voltage in order to try to bring any trapped electrons into resonance with the axial resonator (§6.1.3). There is still uncertainty about the energies (and thus about the axial frequencies) of the trapped electrons and there is also uncertainty about the lifetime of any trapped electrons. Therefore, it would be helpful if the detection window were not to be so narrow. **A second axial resonator in series with the existing niobium one, with a resonance frequency of $\omega_0 = 2\pi \cdot 70.4$ MHz, should allow for the detection of electrons in the deep loading potential ($V_R = -3.85088$ V).** Experimental investigations have begun with the implementation of a second axial resonator, but no trapping attempts have been made yet.

Eventually, the spatially-large axial resonator (§3.5) between the left-correction electrode and ground (Figure 3.8) will be replaced with a spatially-small and low-capacitance surface-mount resistor between both correction electrodes [32, 33]. This will be a "broadband, universal and compact detection system" [32], where the detection will be broadband and universal because the parasitic capacitance of the detection circuit is low [32] and so the high frequency impedance of the detection circuit does not decay to zero until very high frequencies are reached. In particular, two low measurements of the total parasitic capacitance (contributed by a resistor and the chip mutual capacitance) have been undertaken, measuring (0.17 ± 0.0002) pF and (0.13 ± 0.0003) pF (for nominal resistances of 24.8 kΩ and 50.0 kΩ respectively) [32, 33]. Also, the mutual capacitance between the correction electrodes has been measured to be very low at 85 fF [33]. This means that a wide range of axial frequencies should be measurable with the same inter-correction-electrode resistor, where $\omega_z = \omega_z(q/m, C_{002})$ (2.9c) ($C_{ijk} = V_R \cdot c_{ijk}$ [21]), so a wide range of ion species with different charge-to-mass ratios can be detected [33]. A broadband detection circuit would be useful in mass spectrometry [32, 33] (§1.1.3). A simulation of a dip (§2.2) in the impedance of the resistor due to a trapped electron (which used measured values of the parasitic capacitance) suggests that this new detection circuit should allow for the observation of a trapped electron [32]. **Instead of amplifying the induced voltage ($V_{\text{ind}}(t)$ (§2.3.2)) between the axial resonator (tank circuit) and ground using the existing preamplifier (§3.5), the voltage across the resistor will be measured using**

a cryogenic differential amplifier [32, 33].

Improvement: destructive detection using a multichannel plate

Rather than use the non-destructive bolometric electronic detection technique (§2.2) (§3.5), instead the trapped electrons could be intentionally ejected from the trap and subsequently collected using a multichannel plate detector (detected destructively). This would not allow for the detection of single microwave photons (because the Continuous Stern-Gerlach Effect requires a measurement of the axial frequency) nor for the undertaking of some fundamental physics experiments (§1.2), however if electrons were to be detected then it would suggest that there is an issue with the existing detection system (§2.2) (§3.5). One particular benefit of using a multichannel plate is that the detection would be independent of the axial frequency ω_z - and the axial frequencies are currently unknown (§7.2.4). A multichannel plate has previously been used to detect electrons in a planar Penning trap [11] and also to detect electrons in a Paul trap [28], where both of these measurements used room-temperature traps. However, the magnetic field source is constructed using loops of NbTi wire (§3.3) which require a temperature of less than 9-10 K otherwise the source would be in the resistive state (§5.2.1) and the required currents would not be sustainable. Multichannel plate detectors might not work at a temperature of $\approx$ 10 K [209] and so perhaps the use of a multichannel plate detector might not be possible.

7.2.5 Evaluating the loading procedure

Ionisation

Assuming that the ideal gas law still holds, the number of secondary electrons produced is also directly proportional to the pressure of the rest gas, because the pressure is directly proportional to the number of neutral atoms. During trapping attempts, the photocathode is typically biased with $V_{\text{cath}} = -70$ V (§6.1.3). The ionisation curve (Figure 6.8) shows that the difference between the recombination current (of collected positively charged ions) at $V_{\text{cath}} = -70$ V and the dark current at $V_{\text{cath}} = 0$ V is approximately

$(60 - 20 = 40)$ pA. Charge must be conserved and so this suggests that approximately 40 pA$/(1.60 \times 10^{-19})$ C $\approx$ 250 million secondary electrons are produced in the cryogenic trapping chamber (§3.4) per second. Assuming that only electrons ionised in a trapping volume of (1 mm)^3 centred around $\vec{r}_0 = (0, y_0, 0)$ (§2.1.1) may be trapped and that electrons are ionised everywhere in the trapping chamber with even density, out of the total trapping chamber volume of (20 mm)^3, this would suggest that there are approximately 30000 secondary electrons produced every second which may be trapped. The primary electrons will most likely be guided/focussed towards the centre of the trap as a result of the magnetic field lines and so 30,000 trappable electrons is an underestimate. Therefore, it is unlikely that the pressure is much too low (and it is also unlikely that the pressure is much too high (§7.2.3)).

In order to increase the likelihood of detecting the first electrons, it would be helpful for the cloud of trapped electrons to contain as much energy as possible (§7.2.4) and so it would be helpful to load many electrons into the trap (unless the resulting Coulomb potential becomes an issue (§7.2.3). One planar Penning trap [18] was loaded using a beam of primary electrons from a field-emission-point of 8 nA (and initially 20-25 nA), which is much greater than has been measured in the Geonium Chip Penning trap (§4.7.1) with a peak collected photocurrent of (549 ± 12) pA. Only secondary electrons which are liberated close to the centre of the trap $\vec{r}_0 = (0, y_0, 0)$ (§2.1.1) are likely to be trapped (if the magnetron radius is too large then the electron will probably be lost (§6.1.4)) and so it is also significant that a focussed 8 nA beam has a much higher density of primary electrons at the trapping region than in the Geonium Chip Penning trap, where the photocathode has a surface area of (3 mm)^2 (§6.1.4). **Therefore, it would also be beneficial to try to improve the magnitude of the photocurrent (possibly by choosing a different cathode material [182]) and also to focus the beam of primary electrons (possibly by using focus electrodes [210] or an inhomogeneous magnetic field to apply Herrmann's theory [210]) towards the centre of the trap $\vec{r}_0 = (0, y_0, 0)$ (§2.1.1).**

7.2.6 Summary and recommended improvements

The main principles of the Geonium Chip Penning trap have been evaluated, in order to recommend some improvements to the trap so that electrons may be trapped and subsequently detected.

Firstly, the electric field source has been evaluated (§7.2.1). The electrostatic potentials while the trap is loaded should suffice (§7.2.1) and the ellipticity ϵ (§7.2.1) should not be an issue. However (§7.2.1), the ellipticity could eventually be eradicated ($\epsilon = 0$) if side electrodes were to be implemented into the Geonium Chip. The magnetic field source has also been evaluated (§7.2.2). The alignment and homogoneity of the typical 100 mT trapping field should suffice for trapping electrons (§7.2.2). However (§7.2.2), the magnetic field source could eventually be replaced with a similar flux pumped source which runs in persistent mode, in order to make a stronger field and improve the stability. The magnetic mirror effect has also been considered for the primary electrons as they travel from the photocathode to the rest gas (§7.2.2), however this should only have a negligible effect on the ionisation cross section and so this shouldn't be an issue.

The stability of the trap has also been evaluated (§7.2.3). The stability criterion is met (§7.2.3) because the magnetic field strength is strong at $B_{z,000} = 100$ mT. Static resonances (§7.2.3) are unlikely because the motional frequencies are far apart, again partly due to the strong $B_{z,000} = 100$ mT magnetic field. The resistive-wall effect (§7.2.3) should have been mitigated, however it may be further mitigated by trapping at a higher height y_0 above the surface of the Geonium Chip. The lifetime of trapped electrons should be long enough (§7.2.3), between seconds and hours for the typically expected pressures of $\leq 10^{-8}$ mBar.

It is plausible that electrons are being trapped but not subsequently detected, so the detection system has also been evaluated (§7.2.4). One solution might be to widen the detection window (§7.2.4), by introducing a second axial resonator in series with the existing one, which is currently being investigated. A better way to widen the detection window (§7.2.4) would be to use a differential amplifier to amplify the voltage induced

in a low-capacitance resistor between the correction electrodes, for a broadband detection circuit (an extremely wide detection window). Alternatively, a destructive detection technique using a multichannel plate (§7.2.4) could be implemented, which should be effective because it is independent of the axial frequency, however it might not be possible to implement a multichannel plate at a temperature of ≈ 4 K.

Potential issues have also been highlighted during the evaluation of the loading procedure (§7.2.5). An evaluation of the ionisation (§7.2.5) suggests that although enough (250 million) secondary electrons should be generated every second in the chamber such that they should be detectable, they might not be generated with a low enough energy or close enough to the centre of the trap, in order to remain trapped. Therefore, (§7.2.5) it is recommended that the magnitude of the photocurrent should be increased and the beam of primary electrons should be focussed towards the centre of the trap. It is also quite possible that space-charge or plasma effects might make the trap unstable (§7.2.3). Therefore, it is also recommended that (§7.2.3) the photocathode should be moved outside the chamber in such a way that i) no UV light would enter the chamber and that ii) primary electrons would enter the chamber through an aperture so that all primary electrons would enter the trap at the trapping height y_0.

To conclude, it is recommended that in order to increase the likelihood of trapping and detecting electrons in the Geonium Chip Penning trap (in decreasing order of significance) that:

- the loading procedure should be improved. The photocathode should be moved outside the chamber in such a way that (§7.2.3) i) no UV light would enter the chamber and that ii) primary electrons would enter the chamber through an aperture so that all primary electrons would enter the trap at the trapping height y_0. The magnitude of the photocurrent should be increased and the beam of primary electrons should be focussed towards the centre of the trap (§7.2.5).

- the detection system should be improved. A broadband detection circuit with a differential amplifier should be implemented, in order to significantly widen the detection window (§7.2.4). Alternatively, a destructive detection technique using

a multichannel plate (§7.2.4) could be implemented as a possible temporary solution, but this would not allow for single microwave photon detection, nor for some fundamental physics measurements.

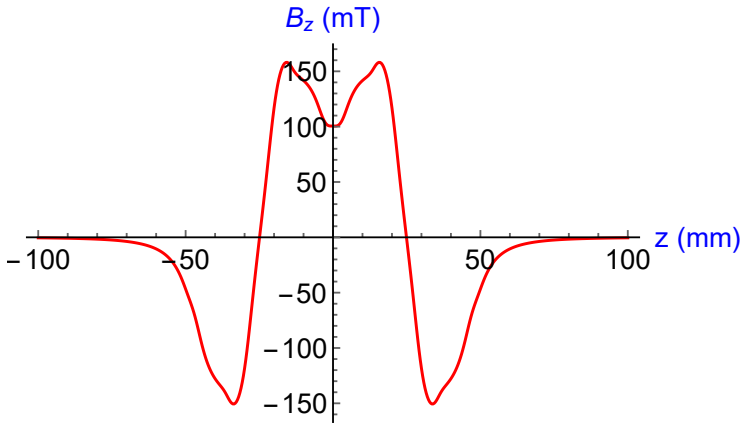

(A) Plotting the magnetic field strength B_z as a function of z, in the planes $y = y_0$ and $x = 0$, for a large range of z.

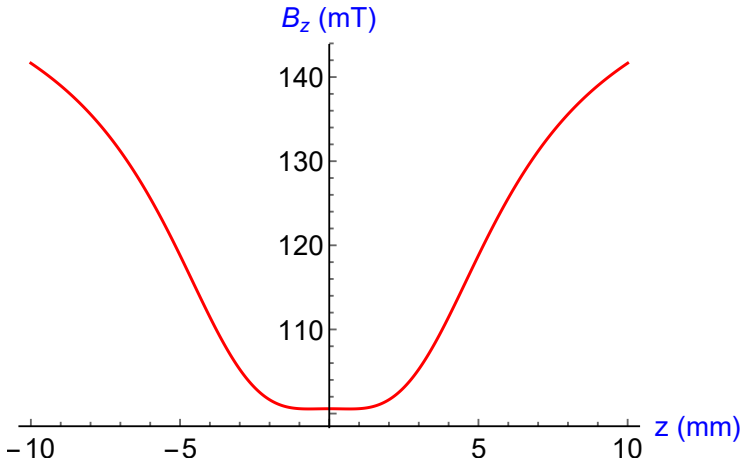

(B) Plotting the magnetic field strength B_z as a function of z, in the planes $y = y_0$ and $x = 0$, for a small range of z.

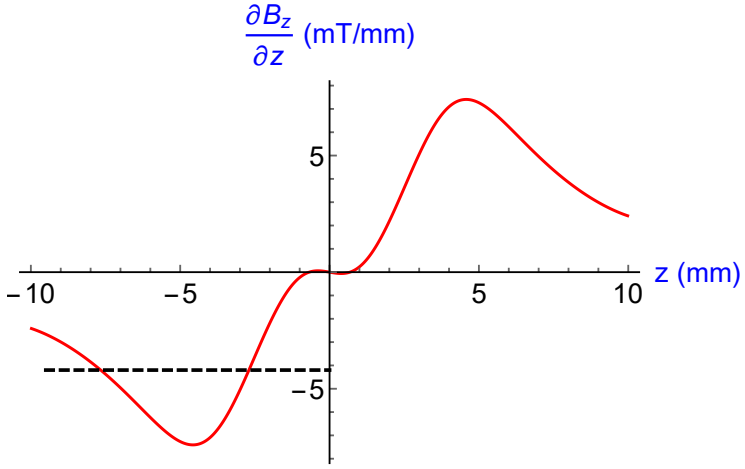

(C) Plotting the gradient $\partial B_z/\partial z$ of the magnetic field strength B_z as a function of z, in the planes $y = y_0$ and $x = 0$. The gradient was estimated numerically using the data shown in Figure 7.1b, by calculating $(\Delta B_z/\Delta z)|_z$. The black horizontal dashed line shows the mean gradient over $-9.5 \leq z\,(\text{mm}) \leq 0$.

FIGURE 7.1: Plots of the predicted $B_0 = B_{z,000} = 100$ mT field.

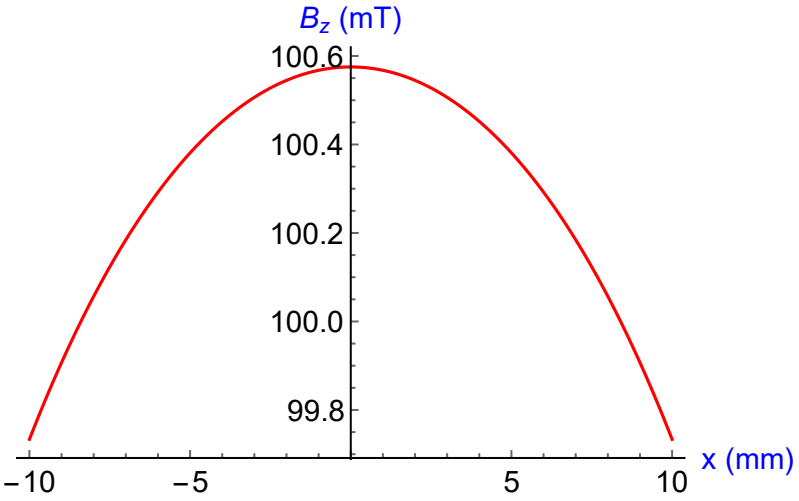

(A) Plotting the magnetic field strength B_z as a function of x, in the planes $y = y_0$ and $z = 0$. As can be seen in Figure 3.6b, the smallest pair of concentric coils (the main coils) have a length of approximately 71 mm along $\hat{u}_x$ (centred around $z = 0$) [36] before they curve by 90° and head along $\pm\hat{u}_z$. Therefore, it is to be expected that the field $B_z(x)$ should not exhibit much inhomogeneity, which agrees with this plot.

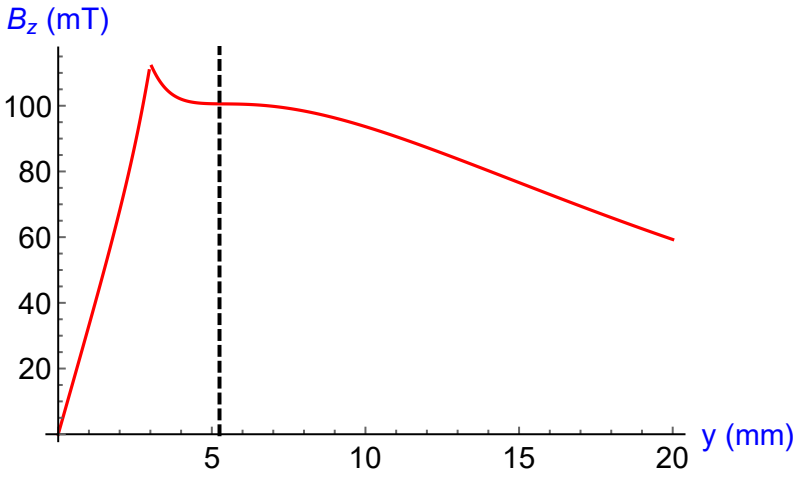

(B) Plotting the magnetic field strength B_z as a function of y, in the planes $z = 0$ and $x = 0$. The black vertical dashed line shows the trapping height $y_{B,0} = 5.25$ mm or $y_{E,0} = 1.45$ mm (§5.1.1). The degree of inhomogeneity around $y = y_0$ is low as expected, because the source was calibrated (§5.1.1) to make an homogeneous field $B_z(y)$ (5.10) around $y = y_0$.

FIGURE 7.2: Plots of the predicted $B_0 = B_{z,000} = 100$ mT field.

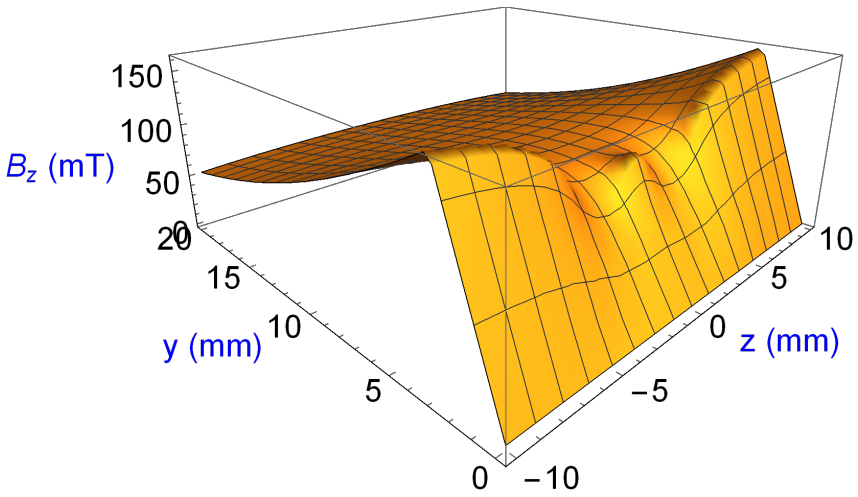

(A) Plotting the magnetic field strength B_z as a function of z and y, in the plane $x = 0$. Cross-sections are shown in Figures 7.1b and 7.2b.

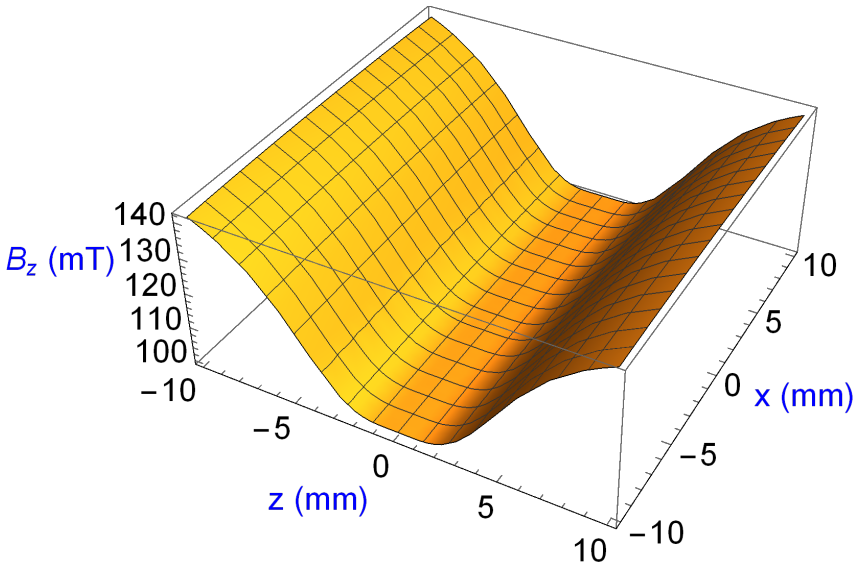

(B) Plotting the magnetic field strength B_z as a function of z and x, in the plane $y = y_0$. Cross-sections are shown in Figures 7.1b and 7.2a.

FIGURE 7.3: Plots of the predicted $B_0 = B_{z,000} = 100$ mT field.

Bibliography

1. Knoop, M., Madsen, N. & Thompson, R. C. *Physics with Trapped Charged Particles* eng. https://doi.org/10.1142/9781783264063_0001 (2013).

2. Dehmelt, H. Radiofrequency Spectroscopy of Stored Ions I: Storage. *Advances in Atomic and Molecular Physics* **3,** 53–72. ISSN: 0065-2199. https://doi.org/10.1016/S0065-2199(08)60170-0 (1968).

3. Dehmelt, H. Radiofrequency Spectroscopy of Stored Ions II: Spectroscopy. *Advances in Atomic and Molecular Physics* **5,** 109–154. ISSN: 0065-2199. https://doi.org/10.1016/S0065-2199(08)60156-6 (1969).

4. Penning, F. Die glimmentladung bei niedrigem druck zwischen koaxialen zylindern in einem axialen magnetfeld. *Physica* **3,** 873–894. ISSN: 0031-8914. https://doi.org/10.1016/S0031-8914(36)80313-9 (1936).

5. Dehmelt, H. G & Walls, F. L. "Bolometric" Technique for the rf Spectroscopy of Stored Ions. eng. *Physical review letters* **21,** 127–131. ISSN: 0031-9007. https://doi.org/10.1103/PhysRevLett.21.127 (1968).

6. Dehmelt, H. Continuous Stern–Gerlach Effect: Principle and Idealized Apparatus. eng. *Proceedings of the National Academy of Sciences - PNAS* **83,** 2291–2294. ISSN: 0027-8424. https://doi.org/10.1073/pnas.83.8.2291 (1986).

7. Wineland, D, Ekstrom, P & Dehmelt, H. Monoelectron Oscillator. eng. *Physical review letters* **31,** 1279–1282. ISSN: 0031-9007. https://doi.org/10.1103/PhysRevLett.31.1279 (1973).

8. Van Dyck, R. S, Schwinberg, P. B & Dehmelt, H. G. Precise Measurements of Axial, Magnetron, Cyclotron, and Spin-Cyclotron-Beat Frequencies on an Isolated 1-meV

Electron. eng. *Physical review letters* **38,** 310–314. ISSN: 0031-9007. https://doi.org/10.1103/PhysRevLett.38.310 (1977).

9. Dehmelt, H. Experiments with an isolated subatomic particle at rest. *Rev. Mod. Phys.* **62,** 525–530. https://doi.org/10.1103/RevModPhys.62.525 (3 1990).

10. Stahl, S. *et al.* A planar Penning trap. eng. *The European Physical Journal D - Atomic, Molecular, Optical and Plasma Physics* **32,** 139–146. ISSN: 1434-6060. https://doi.org/10.1140/epjd/e2004-00179-x (2005).

11. Galve, F., Fernández, P. & Werth, G. Operation of a planar Penning trap. eng. *The European Physical Journal D - Atomic, Molecular, Optical and Plasma Physics* **40,** 201–204. ISSN: 1434-6060. https://doi.org/10.1140/epjd/e2006-00152-9 (2006).

12. Galve, F. & Werth, G. Motional frequencies in a planar Penning trap. eng. *Hyperfine interactions* **174,** 41–46. ISSN: 0304-3843. https://doi.org/10.1007/s10751-007-9576-6 (2007).

13. Bushev, P. *et al.* Electrons in a cryogenic planar Penning trap and experimental challenges for quantum processing. eng. *The European Physical Journal D* **50,** 97–102. ISSN: 1434-6060. https://doi.org/10.1140/epjd/e2008-00186-y (2008).

14. Bushev, P *et al.* Erratum to: Electrons in a cryogenic planar Penning trap and experimental challenges for quantum processing: Eur. Phys. J. D 50, 97–102 (2008). eng. *The European physical journal. D, Atomic, molecular, and optical physics* **57,** 301–301. ISSN: 1434-6060. https://doi.org/10.1140/epjd/e2010-00021-0 (2010).

15. Bushev, P *et al.* Trapped electron coupled to superconducting devices. eng. *The European physical journal. D, Atomic, molecular, and optical physics* **63,** 9–16. ISSN: 1434-6060. https://doi.org/10.1140/epjd/e2011-10517-6 (2011).

16. Goldman, J & Gabrielse, G. Optimized planar Penning traps for quantum-information studies. eng. *Physical review. A, Atomic, molecular, and optical physics* **81.** ISSN: 1050-2947. https://doi.org/10.1103/PhysRevA.81.052335 (2010).

17. Goldman, J & Gabrielse, G. Optimized planar Penning traps for quantum information studies. *Hyperfine interactions.* **199,** 279–289. ISSN: 0304-3843. https://doi.org/10.1007/s10751-011-0323-7 (2011-7).

18. Goldman, J. D. *Planar Penning Traps with Anharmonicity Compensation for Single-Electron Qubits* eng. Doctoral thesis (Harvard University (USA), 2011).

19. Wessels, M. A. *Progress Toward a Single-Electron Qubit in an Optimized Planar Penning Trap* eng. 2019.

20. Gabrielse, G. & Mackintosh, F. Cylindrical Penning traps with orthogonalized anharmonicity compensation. *International Journal of Mass Spectrometry and Ion Processes* **57,** 1–17. ISSN: 0168-1176. https://doi.org/10.1016/0168-1176(84)85061-2 (1984).

21. Verdú, J. Theory of the coplanar-waveguide Penning trap. *New Journal of Physics* **13,** 113029. https://doi.org/10.1088/1367-2630/13/11/113029 (2011).

22. Pinder, J & Verdú, J. A planar Penning trap with tunable dimensionality of the trapping potential. eng. *International journal of mass spectrometry* **356,** 49–59. ISSN: 1387-3806. https://doi.org/10.1016/j.ijms.2013.10.003 (2013).

23. Hellwig, M, Bautista-Salvador, A, Singer, K, Werth, G & Schmidt-Kaler, F. Fabrication of a planar micro Penning trap and numerical investigations of versatile ion positioning protocols. eng. *New journal of physics* **12,** 065019–. ISSN: 1367-2630. https://doi.org/10.1088/1367-2630/12/6/065019 (2010).

24. Jain, S., Alonso, J., Grau, M. & Home, J. P. Scalable Arrays of Micro-Penning Traps for Quantum Computing and Simulation. *Phys. Rev. X* **10,** 031027. https://doi.org/10.1103/PhysRevX.10.031027 (3 2020).

25. Castrejón-Pita, J. R & Thompson, R. C. Proposal for a planar Penning ion trap. eng. *Physical review. A, Atomic, molecular, and optical physics* **72.** ISSN: 1050-2947. https://doi.org/10.1103/PhysRevA.72.013405 (2005).

26. CASTREJÓN-PITA, J. R *et al.* Novel designs for Penning ion traps. eng. *Journal of modern optics* **54,** 1581–1594. ISSN: 0950-0340. https://doi.org/10.1080/09500340600736793 (2007).

27. Crick, D. R, Donnellan, S, Ananthamurthy, S, Thompson, R. C & Segal, D. M. Fast shuttling of ions in a scalable Penning trap array. eng. *Review of scientific instruments* **81,** 013111–013111–5. ISSN: 0034-6748. https://doi.org/10.1063/1.3276699 (2010).

28. Matthiesen, C., Yu, Q., Guo, J., Alonso, A. M. & Häffner, H. Trapping Electrons in a Room-Temperature Microwave Paul Trap. *Phys. Rev. X* **11,** 011019. https://doi.org/10.1103/PhysRevX.11.011019 (1 2021).

29. Tseng, C. H. & Gabrielse, G. Portable trap carries particles 5000 kilometers. eng. *Hyperfine interactions* **76,** 381–386. ISSN: 0304-3834. https://doi.org/10.1007/BF02316739 (1993).

30. Alonso, J. *et al.* A miniature electron-beam ion source for in-trap creation of highly charged ions. eng. *Review of scientific instruments* **77,** 3–. ISSN: 0034-6748. https://doi.org/10.1063/1.2162857 (2006).

31. Marrs, R. E., Beiersdorfer, P. & Schneider, D. The Electron-Beam Ion Trap. eng. *Physics today* **47,** 27–34. ISSN: 0031-9228. https://doi.org/10.1063/1.881419 (1994).

32. Uribe Jiménez, A. J. *High frequency properties of the Geonium Chip Penning Trap and development of a broadband ion detection system* eng. Doctoral thesis (University of Sussex (UK), 2021).

33. Uribe, A. J. *et al.* High frequency properties of a planar ion trap fabricated on a chip. eng. *Review of scientific instruments* **93,** 083202–083202. ISSN: 0034-6748. https://doi.org/10.1063/5.0091745 (2022).

34. Häffner, H *et al.* High-accuracy measurement of the magnetic moment anomaly of the electron bound in hydrogenlike carbon. eng. *Physical review letters* **85,** 5308–5311. ISSN: 0031-9007. https://doi.org/10.1103/PhysRevLett.85.5308 (2000).

35. Hanneke, D, Fogwell Hoogerheide, S & Gabrielse, G. Cavity control of a single-electron quantum cyclotron: Measuring the electron magnetic moment. eng. *Physical review. A, Atomic, molecular, and optical physics* **83.** ISSN: 1050-2947. https://doi.org/10.1103/PhysRevA.83.052122 (2011).

36. Pinder, J. *The Geonium Chip: engineering a scalable planar Penning trap* eng. Doctoral thesis (University of Sussex (UK), 2017).

37. Cridland, A., Lacy, J. H., Pinder, J. & Verdú, J. Single Microwave Photon Detection with a Trapped Electron. *Photonics* **3.** ISSN: 2304-6732. https://doi.org/10.3390/photonics3040059 (2016).

38. Thompson, R. C. Ion Coulomb crystals. eng. *Contemporary physics* **56,** 63–79. ISSN: 0010-7514. https://doi.org/10.1080/00107514.2014.989715 (2015).

39. Verdú, J *et al.* Electronic g factor of hydrogenlike oxygen 16O7. eng. *Physical review letters* **92,** 093002–093002. ISSN: 0031-9007. https://doi.org/10.1103/PhysRevLett.92.093002 (2004).

40. Sturm, S., Werth, G. & Blaum, K. Electron g-factor determinations in Penning traps. eng. *Annalen der Physik* **525,** 620–635. ISSN: 00033804. https://doi.org/10.1002/andp.201300052 (2013).

41. Fan, X & Gabrielse, G. Circumventing Detector Backaction on a Quantum Cyclotron. eng. *Physical review letters* **126,** 070402–070402. ISSN: 0031-9007. https://doi.org/10.1103/PhysRevLett.126.070402 (2021).

42. Hanneke, D, Fogwell, S & Gabrielse, G. New measurement of the electron magnetic moment and the fine structure constant. eng. *Physical review letters* **100,** 120801–120801. ISSN: 0031-9007. https://doi.org/10.1103/PhysRevLett.100.120801 (2008).

43. Gabrielse, G, Hanneke, D, Odom, B, Kinoshita, T & Nio, M. New Determination of the Fine Structure Constant from the Electron g Value and QED. eng. *Physical review letters* **97.** ISSN: 0031-9007. https://doi.org/10.1103/PHYSREVLETT.97.030802 (2006).

44. Gabrielse, G, Hanneke, D, Kinoshita, T, Nio, M & Odom, B. Erratum: New Determination of the Fine Structure Constant from the ElectrongValue and QED [Phys. Rev. Lett.97, 030802 (2006)]. eng. *Physical review letters* **99.** ISSN: 0031-9007. https://doi.org/10.1103/PhysRevLett.99.039902 (2007).

45. Sturm, S *et al.* g-factor measurement of hydrogenlike28Si13+as a challenge to QED calculations. eng. *Physical review. A, Atomic, molecular, and optical physics* **87.** ISSN: 1050-2947. https://doi.org/10.1103/PhysRevA.87.030501 (2013).

46. Sturm, S. *et al.* g Factor of Hydrogenlike $^{28}Si^{13+}$. *Phys. Rev. Lett.* **107,** 023002. https://doi.org/10.1103/PhysRevLett.107.023002 (2 2011).

47. Werth, G. The g-factor of the bound electron as a test of quantum electrodynamics. eng. *Physica scripta* **89,** 98004. ISSN: 0031-8949. https://doi.org/10.1088/0031-8949/89/9/098004 (2014).

48. Van Dyck Jr, R., Schwinberg, P. & Dehmelt, H. New high-precision comparison of electron and positron g factors. eng. *Physical review letters* **59,** 26–29. ISSN: 1079-7114. https://doi.org/10.1103/PhysRevLett.59.26 (1987).

49. Mooser, A *et al.* Direct high-precision measurement of the magnetic moment of the proton. eng. *Nature (London)* **509,** 596–599. ISSN: 0028-0836. https://doi.org/10.1038/nature13388 (2014).

50. Nagahama, H *et al.* Sixfold improved single particle measurement of the magnetic moment of the antiproton. eng. *Nature communications* **8,** 14084–14084. ISSN: 2041-1723. https://doi.org/10.1038/ncomms14084 (2017).

51. Malmberg, J. H & deGrassie, J. S. Properties of Nonneutral Plasma. eng. *Physical review letters* **35,** 577–580. ISSN: 0031-9007. https://doi.org/10.1103/PhysRevLett.35.577 (1975).

52. Tietje, I. C. Low-energy antimatter experiments at the antiproton decelerator at CERN: Testing CPT invariance and the WEP. eng. *Journal of physics. Conference series* **1071,** 12021. ISSN: 1742-6588. https://doi.org/10.1088/1742-6596/1071/1/012021 (2018).

53. Hori, M & Walz, J. Physics at CERN's Antiproton Decelerator. eng. *Progress in particle and nuclear physics* **72,** 206–253. ISSN: 0146-6410. https://doi.org/10.1016/j.ppnp.2013.02.004 (2013).

54. Baker, C. J. *et al.* Laser cooling of antihydrogen atoms. eng. *Nature (London)* **592,** 35–42. ISSN: 1476-4687. https://doi.org/10.1038/s41586-021-03289-6 (2021).

55. Bertsche, W. A. Prospects for comparison of matter and antimatter gravitation with ALPHA-g. eng. *Philosophical transactions of the Royal Society of London. Series A: Mathematical, physical, and engineering sciences* **376,** 20170265–20170265. ISSN: 1364-503X. https://doi.org/10.1098/rsta.2017.0265 (2018).

56. Pérez, P *et al.* The GBAR antimatter gravity experiment. eng. *Hyperfine interactions* **233,** 21–27. ISSN: 0304-3843. https://doi.org/10.1007/s10751-015-1154-8 (2015).

57. Banerjee, D *et al. Towards a test of the weak equivalence principle of gravity using antihydrogen at CERN* in *2016 Conference on Precision Electromagnetic Measurements (CPEM 2016)* (IEEE, 2016-7). ISBN: 1-4673-9135-2. https://doi.org/10.1109/CPEM.2016.7540781.

58. Amsler, C. *et al.* Pulsed production of antihydrogen. eng. *Communications physics* **4,** 1–11. ISSN: 2399-3650. https://doi.org/10.1038/s42005-020-00494-z (2021).

59. Tardiff, E *et al.* Two-symmetry Penning-Ioffe trap for antihydrogen cooling and spectroscopy. eng. *Nuclear instruments and methods in physics research. Section A, Accelerators, spectrometers, detectors and associated equipment* **977,** 164279–. ISSN: 0168-9002. https://doi.org/10.1016/j.nima.2020.164279 (2020).

60. Dilling, J., Blaum, K., Brodeur, M. & Eliseev, S. Penning-Trap Mass Measurements in Atomic and Nuclear Physics. eng. *Annual review of nuclear and particle science* **68,** 45–74. ISSN: 0163-8998. https://doi.org/10.1146/annurev-nucl-102711-094939 (2018).

61. Heiße, F *et al.* High-Precision Measurement of the Proton's Atomic Mass. eng. *Physical review letters* **119,** 033001–033001. ISSN: 0031-9007. https://doi.org/10.1103/PhysRevLett.119.033001 (2017).

62. Brown, L. S. & Gabrielse, G. Precision spectroscopy of a charged particle in an imperfect Penning trap. eng. *Physical review. A, General physics* **25,** 2423–2425. ISSN: 0556-2791. https://doi.org/10.1103/PhysRevA.25.2423 (1982).

63. Sturm, S *et al.* High-precision measurement of the atomic mass of the electron. eng. *Nature (London)* **506,** 467–470. ISSN: 0028-0836. https://doi.org/10.1038/nature13026 (2014).

64. Ulmer, S *et al.* High-precision comparison of the antiproton-to-proton charge-to-mass ratio. eng. *Nature (London)* **524,** 196–199. ISSN: 0028-0836. https://doi.org/10.1038/nature14861 (2015).

65. Eliseev, S., Novikov, Y. N. & Blaum, K. Penning-trap mass spectrometry and neutrino physics. eng. *Annalen der Physik* **525,** 707–719. ISSN: 0003-3804. https://doi.org/10.1002/andp.201300056 (2013).

66. Heck, M. *et al.* An online FT-ICR Penning-trap mass spectrometer for the DPS2-F section of the KATRIN experiment. *Nuclear Instruments and Methods in Physics Research Section A: Accelerators, Spectrometers, Detectors and Associated Equipment* **757,** 54–61. ISSN: 0168-9002. https://doi.org/10.1016/j.nima.2014.03.057 (2014).

67. Aker, M. *et al.* Analysis methods for the first KATRIN neutrino-mass measurement. *Phys. Rev. D* **104,** 012005. https://doi.org/10.1103/PhysRevD.104.012005 (1 2021).

68. Schneider, A. *et al.* A Novel Penning-Trap Design for the High-Precision Measurement of the 3 He 2 + Nuclear Magnetic Moment. eng. *Annalen der Physik* **531,** 1800485–. ISSN: 0003-3804. https://doi.org/10.1002/andp.201800485 (2019).

69. Carney, D., Häffner, H., Moore, D. C. & Taylor, J. M. Trapped Electrons and Ions as Particle Detectors. eng. *Physical review letters* **127,** 061804–061804. ISSN: 1079-7114. https://doi.org/10.1103/PhysRevLett.127.061804 (2021).

70. DiVincenzo, D. P. The Physical Implementation of Quantum Computation. eng. *Fortschritte der Physik* **48,** 771–783. ISSN: 0015-8208. https://doi.org/10.1002/1521-3978(200009)48:9/11<771::AID-PROP771>3.0.CO;2-E (2000).

71. Ciaramicoli, G, Marzoli, I & Tombesi, P. Realization of a quantum algorithm using a trapped electron. eng. *Physical review. A, Atomic, molecular, and optical physics* **63.** ISSN: 1050-2947. https://doi.org/10.1103/PhysRevA.63.052307 (2001).

72. Deutsch, D. Quantum Theory, the Church-Turing Principle and the Universal Quantum Computer. eng. *Proceedings of the Royal Society of London. Series A, Mathematical and physical sciences* **400,** 97–117. ISSN: 1364-5021. https://doi.org/10.1098/rspa.1985.0070 (1985).

73. Ciaramicoli, G, Marzoli, I & Tombesi, P. Scalable quantum processor with trapped electrons. eng. *Physical review letters* **91,** 017901–017901. ISSN: 0031-9007. https://doi.org/10.1103/PhysRevLett.91.017901 (2003).

74. Ciaramicoli, G, Marzoli, I & Tombesi, P. Trapped electrons in vacuum for a scalable quantum processor. eng. *Physical review. A, Atomic, molecular, and optical physics* **70.** ISSN: 1050-2947. https://doi.org/10.1103/PhysRevA.70.032301 (2004).

75. Marzoli, I *et al.* Experimental and theoretical challenges for the trapped electron quantum computer. eng. *Journal of physics. B, Atomic, molecular, and optical physics* **42,** 154010–. ISSN: 0953-4075. https://doi.org/10.1088/0953-4075/42/15/154010 (2009).

76. Porras, D & Cirac, J. I. Effective quantum spin systems with trapped ions. eng. *Physical review letters* **92,** 207901–207901. ISSN: 0031-9007. https://doi.org/10.1103/PhysRevLett.92.207901 (2004).

77. Wang, C.-C. J., Keith, A. C. & Freericks, J. K. Phonon-mediated quantum spin simulator employing a planar ionic crystal in a Penning trap. eng. *Physical review. A, Atomic, molecular, and optical physics* **87.** ISSN: 1050-2947. https://doi.org/10.1103/PhysRevA.87.013422 (2013).

78. McAneny, M, Yoshimura, B & Freericks, J. K. Effect of defects on phonons and the effective spin-spin interactions of an ultracold Penning-trap quantum simulator. eng. *Physical review. A, Atomic, molecular, and optical physics* **88.** ISSN: 1050-2947. https://doi.org/10.1103/PhysRevA.88.043434 (2013).

79. Khan, A, Yoshimura, B & Freericks, J. K. Theoretical basis for quantum simulation with a planar ionic crystal in a Penning trap using a triangular rotating wall. eng. *Physical review. A, Atomic, molecular, and optical physics* **92.** ISSN: 1050-2947. https://doi.org/10.1103/PhysRevA.92.043405 (2015).

80. Ball, H *et al.* Site-resolved imaging of beryllium ion crystals in a high-optical-access Penning trap with inbore optomechanics. eng. *Review of scientific instruments* **90,** 053103–053103. ISSN: 0034-6748. https://doi.org/10.1063/1.5049506 (2019).

81. Jordan, E. *et al.* Near Ground-State Cooling of Two-Dimensional Trapped-Ion Crystals with More than 100 Ions. eng. *Physical review letters* **122,** 053603–053603. ISSN: 0031-9007. https://doi.org/10.1103/PhysRevLett.122.053603 (2019).

82. Lamata, L, Porras, D, Cirac, J. I, Goldman, J & Gabrielse, G. Towards electron-electron entanglement in Penning traps. eng. *Physical review. A, Atomic, molecular, and optical physics* **81.** ISSN: 1050-2947. https://doi.org/10.1103/PhysRevA.81.022301 (2010).

83. Cerrillo, J. & Rodríguez, D. Motional quantum metrology in a Penning trap. eng. *Europhysics letters* **134.** ISSN: 0295-5075. https://doi.org/10.1209/0295-5075/134/38001 (2021).

84. Wolf, F. *et al.* Motional Fock states for quantum-enhanced amplitude and phase measurements with trapped ions. eng. *Nature communications* **10,** 2929–2929. ISSN: 2041-1723. https://doi.org/10.1038/s41467-019-10576-4 (2019).

85. Kotler, S., Simmonds, R. W., Leibfried, D. & Wineland, D. J. Hybrid quantum systems with trapped charged particles. *Phys. Rev. A* **95,** 022327. https://doi.org/10.1103/PhysRevA.95.022327 (2 2017).

86. Peng, P., Matthiesen, C. & Häffner, H. Spin readout of trapped electron qubits. *Phys. Rev. A* **95,** 012312. https://doi.org/10.1103/PhysRevA.95.012312 (1 2017).

87. Brown, L. S. & Gabrielse, G. Geonium theory: Physics of a single electron or ion in a Penning trap. eng. *Reviews of modern physics* **58,** 233–311. ISSN: 0034-6861. https://doi.org/10.1103/RevModPhys.58.233 (1986).

88. Kretzschmar, M. Theory of the elliptical Penning trap. *International Journal of Mass Spectrometry* **275,** 21–33. ISSN: 1387-3806. https://doi.org/10.1016/j.ijms.2008.05.009 (2008).

89. Kretzschmar, M. Particle motion in a Penning trap. eng. *European journal of physics* **12,** 240–246. ISSN: 0143-0807. https://doi.org/10.1088/0143-0807/12/5/010 (1991).

90. Kretzschmar, M. Single particle motion in a Penning trap: description in the classical canonical formalism. eng. *Physica scripta* **46,** 544–554. ISSN: 1402-4896. https://doi.org/10.1088/0031-8949/46/6/011 (1992).

91. Al-Rjoub, A & Verdú, J. Electronic detection of a single particle in a coplanar-waveguide Penning trap. eng. *Applied physics. B, Lasers and optics* **107,** 955–964. ISSN: 0946-2171. https://doi.org/10.1007/s00340-012-5069-7 (2012).

92. Breitenfeldt, M. *et al.* The elliptical Penning trap: Experimental investigations and simulations. *International Journal of Mass Spectrometry* **275,** 34–44. ISSN: 1387-3806. https://doi.org/10.1016/j.ijms.2008.05.008 (2008).

93. Ketter, J., Eronen, T., Höcker, M., Streubel, S. & Blaum, K. First-order perturbative calculation of the frequency-shifts caused by static cylindrically-symmetric electric and magnetic imperfections of a Penning trap. eng. *International journal of mass spectrometry* **358,** 1–16. ISSN: 1387-3806. https://doi.org/10.1016/j.ijms.2013.10.005 (2014).

94. Blaum, K. High-accuracy mass spectrometry with stored ions. *Physics Reports* **425,** 1–78. ISSN: 0370-1573. https://doi.org/10.1016/j.physrep.2005.10.011 (2006).

95. DJEKIC, S *et al.* Temperature measurement of a single ion in a Penning trap. eng. *The European physical journal. D, Atomic, molecular, and optical physics* **31,** 451–457. ISSN: 1434-6060. https://doi.org/10.1140/epjd/e2004-00168-1 (2004).

96. Gabrielse, G. Relaxation calculation of the electrostatic properties of compensated Penning traps with hyperbolic electrodes. eng. *Physical review. A, General physics* **27,** 2277–2290. ISSN: 0556-2791. https://doi.org/10.1103/PhysRevA.27.2277 (1983).

97. Pinder, J. *et al.* Planar, strong magnetic field source for a chip ion trap. *Review of Scientific Instruments* **91,** 103201. ISSN: 0034-6748. https://doi.org/10.1063/5.0024735 (2020).

98. Gabrielse, G. The true cyclotron frequency for particles and ions in a Penning trap. eng. *International journal of mass spectrometry* **279,** 107–112. ISSN: 1387-3806. https://doi.org/10.1016/j.ijms.2008.10.015 (2009).

99. Wineland, D. J & Dehmelt, H. G. Principles of the stored ion calorimeter. eng. *Journal of applied physics* **46,** 919–930. ISSN: 0021-8979. https://doi.org/10.1063/1.321602 (1975).

100. Feng, X, Charlton, M, Holzscheiter, M, Lewis, R. A & Yamazaki, Y. Tank circuit model applied to particles in a Penning trap. eng. *Journal of applied physics* **79,** 8–13. ISSN: 0021-8979. https://doi.org/10.1063/1.360947 (1996).

101. JOHNSON, J. B. Thermal Agitation of Electricity in Conductors. eng. *Nature (London)* **119,** 50–51. ISSN: 0028-0836 (1927).

102. Crimin, F. *Quantum theory of the Penning trap: an exploration of the low temperature regime* eng. Doctoral thesis (University of Sussex (UK), 2018).

103. Itano, W. M., Bergquist, J. C., Bollinger, J. J. & Wineland, D. J. Cooling methods in ion traps. eng. *Physica scripta* **1995,** 106–120. ISSN: 1402-4896. https://doi.org/10.1088/0031-8949/1995/T59/013 (1995).

104. Wineland, D & Dehmelt, H. Line shifts and widths of axial, cyclotron and G-2 resonances in tailored, stored electron (ion) cloud. *International Journal of Mass Spectrometry and Ion Physics* **19,** 251. ISSN: 00207381. https://doi.org/10.1016/0020-7381(76)80009-5 (1976-02).

105. Gabrielse, G. Detection, damping, and translating the center of the axial oscillation of a charged particle in a penning trap with hyperbolic electrodes. English. *Physical Review A* **29,** 462–469. https://doi.org/10.1103/PhysRevA.29.462 (1984).

106. Ebrahimi, M. S. *et al.* Resistive cooling of highly charged ions in a Penning trap to a fluidlike state. *Phys. Rev. A* **98,** 023423. https://doi.org/10.1103/PhysRevA.98.023423 (2 2018).

107. Vogel, M. *et al.* Resistive and sympathetic cooling of highly-charged-ion clouds in a Penning trap. *Phys. Rev. A* **90,** 043412. https://doi.org/10.1103/PhysRevA.90.043412 (4 2014).

108. White, W. D, Malmberg, J. H & Driscoll, C. F. Resistive-Wall Destabilization of Diocotron Waves. eng. *Physical review letters* **49,** 1822–1826. ISSN: 0031-9007. https://doi.org/10.1103/PhysRevLett.49.1822 (1982).

109. Chao, E. H., Davidson, R. C., Paul, S. F. & Morrison, K. A. Effects of background gas pressure on the dynamics of a nonneutral electron plasma confined in a Malmberg–Penning trap. eng. *Physics of plasmas* **7,** 831–838. ISSN: 1070-664X. https://doi.org/10.1063/1.873879 (2000).

110. Bettega, G *et al.* Experimental and numerical analysis of the electron injection in a Malmberg-Penning trap. eng. *Physics of plasmas* **14,** 42104–. ISSN: 1070-664X. https://doi.org/10.1063/1.2721072 (2007).

111. Romé, M & Lepreti, F. Turbulence and coherent structures in non-neutral plasmas. eng. *European physical journal plus* **126,** 1–17. ISSN: 2190-5444. https://doi.org/10.1140/epjp/i2011-11038-4 (2011).

112. Dyavappa, B. M., Datar, D., Prakash & Ananthamurthy, S. Dependence of the confinement time of an electron plasma on the magnetic field in a quadrupole Penning trap. eng. *EPJ techniques and instrumentation* **4,** 1–13. ISSN: 2195-7045. https://doi.org/10.1140/epjti/s40485-017-0039-4 (2017).

113. Fajans, J, Gilson, E & Backhaus, E. Y. Bifurcations in elliptical, asymmetric non-neutral plasmas. eng. *Physics of plasmas* **7,** 3929–3933. ISSN: 1070-664X. https://doi.org/10.1063/1.1290480 (2000).

114. Backhaus, E. Y., Fajans, J & Wurtele, J. S. Stability of highly asymmetric non-neutral plasmas. eng. *Physics of plasmas* **6,** 19–30. ISSN: 1070-664X. https://doi.org/10.1063/1.873299 (1999).

115. Fajans, J, Backhaus, E. Y. & McCarthy, J. E. Equilibrium of highly asymmetric non-neutral plasmas. eng. *Physics of plasmas* **6,** 12–18. ISSN: 1070-664X. https://doi.org/10.1063/1.873253 (1999).

116. Hollmann, E. M, Anderegg, F & Driscoll, C. F. Confinement and manipulation of non-neutral plasmas using rotating wall electric fields. eng. *Physics of plasmas* **7,** 2776–2789. ISSN: 1070-664X. https://doi.org/10.1063/1.874128 (2000).

117. Huang, X.-P, Anderegg, F, Hollmann, E. M, Driscoll, C. F & O'Neil, T. M. Steady-State Confinement of Non-neutral Plasmas by Rotating Electric Fields. eng. *Physical review letters* **78,** 875–878. ISSN: 0031-9007. https://doi.org/10.1103/PhysRevLett.78.875 (1997).

118. Anderegg, F, Hollmann, E. M & Driscoll, C. F. Rotating Field Confinement of Pure Electron Plasmas Using Trivelpiece-Gould Modes. eng. *Physical review letters* **81,** 4875–4878. ISSN: 0031-9007. https://doi.org/10.1103/PhysRevLett.81.4875 (1998).

119. Dehmelt, H. Continuous Stern-Gerlach effect: Noise and the measurement process. *Proceedings of the National Academy of Sciences of the United States of America.* **83,** 3074–3077. ISSN: 0027-8424. https://doi.org/10.1073/pnas.83.10.3074 (1986-05-01).

120. Peil, S & Gabrielse, G. Observing the Quantum Limit of an Electron Cyclotron: QND Measurements of Quantum Jumps between Fock States. eng. *Physical review letters* **83,** 1287–1290. ISSN: 0031-9007. https://doi.org/10.1103/PhysRevLett.83.1287 (1999).

121. Peil, S. E. *Quantum jumps between Fock states of an ultracold electron cyclotron oscillator* eng. 1999.

122. Gabrielse, G & Dehmelt, H. Observation of inhibited spontaneous emission. eng. *Physical review letters* **55,** 67–70. ISSN: 0031-9007. https://doi.org/10.1103/PhysRevLett.55.67 (1985).

123. Lacy, J. H. *Development of a planar magnetic field source for the Geonium Chip Penning Trap* eng. Doctoral thesis (University of Sussex (UK), 2019).

124. Cridland Mathad, A. *et al.* Coherent coupling of a trapped electron to a distant superconducting microwave cavity. eng. *Applied physics letters* **117.** ISSN: 0003-6951. https://doi.org/10.1063/5.0023002 (2020).

125. Stahl, S *et al.* Phase-sensitive measurement of trapped particle motions. eng. *Journal of physics. B, Atomic, molecular, and optical physics* **38,** 297–304. ISSN: 0953-4075. https://doi.org/10.1088/0953-4075/38/3/013 (2005).

126. Inomata, K. *et al.* Single microwave-photon detector using an artificial Λ-type three-level system. eng. *Nature communications* **7,** 12303–12303. ISSN: 2041-1723. https://doi.org/10.1038/ncomms12303 (2016).

127. Lescanne, R. *et al.* Irreversible Qubit-Photon Coupling for the Detection of Itinerant Microwave Photons. *Phys. Rev. X* **10,** 021038. https://doi.org/10.1103/PhysRevX.10.021038 (2 2020).

128. Khan, W. *et al.* Efficient and continuous microwave photoconversion in hybrid cavity-semiconductor nanowire double quantum dot diodes. eng. *Nature communications* **12,** 5130–5130. ISSN: 2041-1723. https://doi.org/10.1038/s41467-021-25446-1 (2021).

129. Romero, G, García-Ripoll, J. J. & Solano, E. Microwave photon detector in circuit QED. eng. *Physical review letters* **102,** 173602–173602. ISSN: 0031-9007. https://doi.org/10.1103/PhysRevLett.102.173602 (2009).

130. Peropadre, B. *et al.* Approaching perfect microwave photodetection in circuit QED. eng. *Physical review. A, Atomic, molecular, and optical physics* **84.** ISSN: 1050-2947. https://doi.org/10.1103/PhysRevA.84.063834 (2011).

131. Grimsmo, A. L. *et al.* Quantum Metamaterial for Broadband Detection of Single Microwave Photons. eng. *Physical review applied* **15.** ISSN: 2331-7019. https://doi.org/10.1103/PhysRevApplied.15.034074 (2021).

132. Guarcello, C. *et al.* Josephson-Based Scheme for the Detection of Microwave Photons. eng. *Physical review applied* **16.** ISSN: 2331-7019. https://doi.org/10.1103/PhysRevApplied.16.054015 (2021).

133. Golubev, D. S., Il'ichev, E. V. & Kuzmin, L. S. Single-Photon Detection with a Josephson Junction Coupled to a Resonator. eng. *Physical review applied* **16.** ISSN: 2331-7019. https://doi.org/10.1103/PhysRevApplied.16.014025 (2021).

134. Koshino, K., Inomata, K., Lin, Z., Nakamura, Y. & Yamamoto, T. Theory of microwave single-photon detection using an impedance-matched λ system. eng. *Physical review. A, Atomic, molecular, and optical physics* **91.** ISSN: 1050-2947. https://doi.org/10.1103/PhysRevA.91.043805 (2015).

135. Inomata, K., Yamamoto, T., Billangeon, P.-M., Nakamura, Y. & Tsai, J. S. Large dispersive shift of cavity resonance induced by a superconducting flux qubit in the straddling regime. *Phys. Rev. B* **86,** 140508. https://doi.org/10.1103/PhysRevB.86.140508 (14 2012).

136. Macklin, C. *et al.* A near-quantum-limited Josephson traveling-wave parametric amplifier. eng. *Science (American Association for the Advancement of Science)* **350,** 307–310. ISSN: 0036-8075. https://doi.org/10.1126/science.aaa8525 (2015).

137. Sathyamoorthy, S. R., Stace, T. M. & Johansson, G. Detecting itinerant single microwave photons. eng. *Comptes rendus. Physique* **17,** 756–765. ISSN: 1631-0705. https://doi.org/10.1016/j.crhy.2016.07.010 (2016).

138. Johnson, B. R *et al.* Quantum non-demolition detection of single microwave photons in a circuit. eng. *Nature physics* **6,** 663–667. ISSN: 1745-2473. https://doi.org/10.1038/nphys1710 (2010).

139. Kono, S, Koshino, K, Tabuchi, Y, Noguchi, A & Nakamura, Y. Quantum non-demolition detection of an itinerant microwave photon. eng. *Nature physics* **14,** 546–549. ISSN: 1745-2473. https://doi.org/10.1038/s41567-018-0066-3 (2018).

140. Suri, B. *et al.* Nonlinear microwave photon occupancy of a driven resonator strongly coupled to a transmon qubit. eng. *Physical review. A, Atomic, molecular, and optical physics* **92,** Art. no. 063801–. ISSN: 1050-2947. https://doi.org/10.1103/PhysRevA.92.063801 (2015).

141. Albertinale, E. *et al.* Detecting spins by their fluorescence with a microwave photon counter. eng. *Nature (London)* **600,** 434–438. ISSN: 0028-0836. https://doi.org/10.1038/s41586-021-04076-z (2021).

142. Jones, M. L., Wilkes, G. J. & Varcoe, B. T. H. Single microwave photon detection in the micromaser. eng. *Journal of physics. B, Atomic, molecular, and optical physics* **42,** 145501–145501 (4). ISSN: 0953-4075. https://doi.org/10.1088/0953-4075/42/14/145501 (2009).

143. Thorne, K. S., Drever, R. W. P., Caves, C. M., Zimmermann, M. & Sandberg, V. D. Quantum Nondemolition Measurements of Harmonic Oscillators. eng. *Physical review letters* **40,** 667–671. ISSN: 0031-9007. https://doi.org/10.1103/PhysRevLett.40.667 (1978).

144. Hermanspahn, N *et al.* Observation of the continuous stern-gerlach effect on an electron bound in an atomic Ion. eng. *Physical review letters* **84,** 427–430. ISSN: 0031-9007. https://doi.org/10.1103/PhysRevLett.84.427 (2000).

145. Lacy, J. H. *et al.* Superconducting Flux Pump for a Planar Magnetic Field Source. eng. *IEEE transactions on applied superconductivity* **30,** 1–12. ISSN: 1051-8223. https://doi.org/10.1109/TASC.2020.3004768 (2020).

146. Cridland, A. L. *Development of a planar penning trap for quantum applications with electrons* eng. Doctoral thesis (University of Sussex (UK), 2018).

147. Verdú, J *pat.* WO 2013/041615 A2 (International) (2013).

148. Verdú, J *pat.* US 8,362,423 B1 (US) (2013).

149. Wen, C. Coplanar Waveguide: A Surface Strip Transmission Line Suitable for Nonreciprocal Gyromagnetic Device Applications. eng. *IEEE transactions on microwave theory and techniques* **17,** 1087–1090. ISSN: 0018-9480. https://doi.org/10.1109/TMTT.1969.1127105 (1969).

150. Verdú, J *et al.* Calculation of electrostatic fields using quasi-Green's functions: application to the hybrid Penning trap. eng. *New journal of physics* **10,** 103009–. ISSN: 1367-2630. https://doi.org/10.1088/1367-2630/10/10/103009 (2008).

151. Le Gressus, C *et al.* Charging phenomena on insulating materials: Mechanisms and applications: Charging phenomena in insulating materials. eng. *Scanning* **12,** 203–210. ISSN: 0161-0457. https://doi.org/10.1002/sca.4950120406 (1990).

152. *PW Circuits Ltd* http://pwcircuits.co.uk/.

153. Stehling, M. K., Turner, R & Mansfield, P. Echo-Planar Imaging: Magnetic Resonance Imaging in a Fraction of a Second. eng. *Science (American Association for the Advancement of Science)* **254,** 43–50. ISSN: 0036-8075. https://doi.org/10.1126/science.1925560 (1991).

154. Vandersypen, L. M. K & Chuang, I. L. NMR techniques for quantum control and computation. eng. *Reviews of modern physics* **76,** 1037–1069. ISSN: 0034-6861. https://doi.org/10.1103/RevModPhys.76.1037 (2005).

155. Marshall, A. G. & Chen, T. 40 years of Fourier transform ion cyclotron resonance mass spectrometry. eng. *International journal of mass spectrometry* **377,** 410–420. ISSN: 1387-3806. https://doi.org/10.1016/j.ijms.2014.06.034 (2015).

156. Blaum, K *et al.* g-factor experiments on simple systems in Penning traps. eng. *Journal of physics. B, Atomic, molecular, and optical physics* **42,** 154021–. ISSN: 0953-4075. https://doi.org/10.1088/0953-4075/42/15/154021 (2009).

157. Van Dyck, R. S, Farnham, D. L, Zafonte, S. L & Schwinberg, P. B. Ultrastable superconducting magnet system for a penning trap mass spectrometer. eng. *Review of scientific instruments* **70,** 1665–1671. ISSN: 0034-6748. https://doi.org/10.1063/1.1149649 (1999).

158. GABRIELSE, G & TAN, J. Self-shielding superconducting solenoid systems. eng. *Journal of applied physics* **63,** 5143–5148. ISSN: 0021-8979. https://doi.org/10.1063/1.340416 (1988).

159. Gabrielse, G *et al.* A superconducting solenoid system which cancels fluctuations in the ambient magnetic field. eng. *Journal of magnetic resonance (1969)* **91,** 564–572. ISSN: 0022-2364. https://doi.org/10.1016/0022-2364(91)90382-4 (1991).

160. Repp, J *et al.* PENTATRAP: a novel cryogenic multi-Penning-trap experiment for high-precision mass measurements on highly charged ions. eng. *Applied physics. B, Lasers and optics* **107,** 983–996. ISSN: 0946-2171. https://doi.org/10.1007/s00340-011-4823-6 (2012).

161. Sturm, S. *et al.* High-Precision Measurements of the Bound Electron's Magnetic Moment. eng. *Atoms* **5,** 4–. ISSN: 2218-2004. https://doi.org/10.3390/atoms5010004 (2017).

162. Bason, M. G. *et al.* Non-invasive current density imaging of lithium-ion batteries. *Journal of power sources* **533.** ISSN: 0378-7753. https://doi.org/10.1016/j.jpowsour.2022.231312 (2022).

163. Verdú, J. L. *et al.* Determination of the g-Factor of Single Hydrogen-Like Ions by Mode Coupling in a Penning Trap. eng. *Physica scripta* **2004,** 68–. ISSN: 1402-4896. https://doi.org/10.1238/Physica.Topical.112a00068 (2004).

164. Cornell, E., Weisskoff, R., Boyce, K. & Pritchard, D. Mode coupling in a Penning trap: pi pulses and a classical avoided crossing. eng. *Physical review. A, Atomic, molecular, and optical physics* **41,** 312–315. ISSN: 1050-2947. https://doi.org/10.1103/PhysRevA.41.312 (1990).

165. GABRIELSE, G *et al.* Thousandfold improvement on the measured antiproton mass. eng. *Physical review letters* **65,** 1317–1320. ISSN: 0031-9007. https://doi.org/10.1103/PhysRevLett.65.1317 (1990).

166. Haefer, R. A. Cryogenic vacuum techniques. eng. *Journal of physics. E, Scientific instruments* **14,** 273–288. ISSN: 0022-3735. https://doi.org/10.1088/0022-3735/14/3/002 (1981).

167. GABRIELSE, G, DEHMELT, H & KELLS, W. Observation of a relativistic, bistable hysteresis in the cyclotron motion of a single electron. eng. *Physical review letters* **54,** 537–539. ISSN: 0031-9007. https://doi.org/10.1103/PhysRevLett.54.537 (1985).

168. Ulmer, S *et al.* A cryogenic detection system at 28.9MHZ for the non-destructive observation of a single proton at low particle energy. eng. *Nuclear instruments and methods in physics research. Section A, Accelerators, spectrometers, detectors and associated equipment* **705,** 55–60. ISSN: 0168-9002. https://doi.org/10.1016/j.nima.2012.12.071 (2013).

169. Pozar, D. M. *Microwave engineering* Fourth edition. eng. ISBN: 9781118213636 (John Wiley and Sons, Inc., Hoboken, New Jersey, 2012).

170. Alsberg, D. Transistor metrology. eng. *Transactions of the I.R.E. Professional Group on Electron Devices* **ED-1,** 12–17. ISSN: 0197-6370. https://doi.org/10.1109/T-ED.1954.14018 (1954).

171. Ibarra-Medel, E, Velázquez, M, Ventura, S, Ferrusca, D & Gómez-Rivera, V. 4 Kelvin Cryogenic Characterization of Commercial pHEMT Transistors at 9 kHz to 8.5 GHz Range. eng. *Journal of low temperature physics* **184,** 418–423. ISSN: 0022-2291. https://doi.org/10.1007/s10909-015-1461-0 (2016).

172. Keysight Technologies. *Time Domain Analysis Using a Network Analyzer. Application Note.* Online. Literature number: 5989-5723EN. USA.

173. Ulmer, S *et al.* The quality factor of a superconducting rf resonator in a magnetic field. eng. *Review of scientific instruments* **80,** 123302–123302–8. ISSN: 0034-6748. https://doi.org/10.1063/1.3271537 (2009).

174. Richardson, O. *Thermionic phenomena and the laws which govern them* Nobel lecture. 1929. https://www.nobelprize.org/uploads/2018/06/richardson-lecture.pdf.

175. Hoogerheide, S. *et al.* Experiments with Highly-Ionized Atoms in Unitary Penning Traps. eng. *Atoms* **3,** 367–391. ISSN: 2218-2004. https://doi.org/10.3390/atoms3030367 (2015).

176. Paul, S. F *et al.* Off-axis electron injection into a cooler Penning trap. eng. *Hyperfine interactions* **240,** 1–9. ISSN: 0304-3843. https://doi.org/10.1007/s10751-019-1587-6 (2019).

177. Einstein, A. Über einen die Erzeugung und Verwandlung des Lichtes betreffenden heuristischen Gesichtspunkt (On a heuristic point of view concerning the production and transformation of light). ger. *Annalen der Physik* **322,** 132–148. ISSN: 0003-3804. https://doi.org/10.1002/andp.19053220607 (1905).

178. Wass, P. J., Hollington, D., Sumner, T. J., Yang, F. & Pfeil, M. Effective decrease of photoelectric emission threshold from gold plated surfaces. eng. *Review of scientific instruments* **90,** 064501–064501. ISSN: 0034-6748. https://doi.org/10.1063/1.5088135 (2019).

179. Kawano, H. Erratum to "Effective work functions for ionic and electronic emissions from mono- and polycrystalline surfaces" [Prog. Surf. Sci. 83 (2008) 1–165]. eng. *Progress in surface science* **83,** 215–215. ISSN: 0079-6816. https://doi.org/10.1016/j.progsurf.2008.04.001 (2008).

180. Dowell, D. H. & Schmerge, J. F. Quantum efficiency and thermal emittance of metal photocathodes. eng. *Physical review special topics. PRST-AB. Accelerators and beams* **12,** 074201–. ISSN: 1098-4402. https://doi.org/10.1103/PhysRevSTAB.12.074201 (2009).

181. Dowell, D. H. & Schmerge, J. F. Erratum: Quantum efficiency and thermal emittance of metal photocathodes [Phys. Rev. ST Accel. Beams 12 , 074201 (2009)]. eng. *Physical review special topics. PRST-AB. Accelerators and beams* **12,** 119901–. ISSN: 1098-4402. https://doi.org/10.1103/PhysRevSTAB.12.119901 (2009).

182. Le Pimpec, F, Milne, C. J, Hauri, C. P & Ardana-Lamas, F. Quantum efficiency of technical metal photocathodes under laser irradiation of various wavelengths. eng. *Applied physics. A, Materials science & processing* **112,** 647–661. ISSN: 0947-8396. https://doi.org/10.1007/s00339-013-7600-z (2013).

183. Andrew, D *et al.* A GaAs-Cs-O transmission photocathode. eng. *Journal of physics. D, Applied physics* **3,** 320–326. ISSN: 0022-3727. https://doi.org/10.1088/0022-3727/3/3/310 (1970).

184. Earle, G. D., Copp, B. L., Klenzing, J. H. & Bishop, R. L. A novel empirical study of the photoelectric effect in thin gold films. eng. *American journal of physics* **71,** 766–769. ISSN: 0002-9505. https://doi.org/10.1119/1.1574040 (2003).

185. Balalykin, N. I. *et al.* Electron gun with a transmission photocathode for the Joint Institute for Nuclear Research photoinjector. eng. *Physics Uspekhi* **60,** 1051–1058. ISSN: 1063-7869. https://doi.org/10.3367/UFNe.2017.03.038145 (2017).

186. Jousten, K. & Nakhosteen, C. B. *Handbook of Vacuum Technology* eng. ISBN: 9783527413386 (John Wiley and Sons, Incorporated, Berlin, 2016).

187. Drobyshev, A., Aldiyarov, A., Zhumagaliuly, D., Kurnosov, V. & Tokmoldin, N. Thermally stimulated transformations in cryovacuum water ices. *Low Temperature Physics* **33,** 355–361. https://doi.org/10.1063/1.2720084 (2007).

188. Bharadia, S. *Towards Laser Spectroscopy of Highly Charged Ions: Dynamics of 40Ca+ Ions in a Penning Trap* eng. Doctoral thesis (Imperial College (London, UK), 2011).

189. Preston-Thomas, H. The International Temperature Scale of 1990 (ITS-90). *Metrologia* **27,** 3–10. https://doi.org/10.1088/0026-1394/27/1/002 (1990).

190. Preston-Thomas, H. The International Temperature Scale of 1990 (ITS-90). *Metrologia* **27,** 107–107. https://doi.org/10.1088/0026-1394/27/2/010 (1990).

191. Linford, L. B. Recent Developments in the Study of the External Photoelectric Effect. eng. *Reviews of modern physics* **5,** 34–61. ISSN: 0034-6861. https://doi.org/10.1103/RevModPhys.5.34 (1933).

192. Winch, R. P. Photoelectric Properties of Thin Unbacked Gold Films. eng. *Physical review* **38,** 321–324. ISSN: 0031-899X. https://doi.org/10.1103/PhysRev.38.321 (1931).

193. Mamun, M., Hernandez-Flores, M., Morales, E., Hernandez-Garcia, C. & Poelker, M. Temperature dependence of alkali-antimonide photocathodes: Evaluation at cryogenic temperatures. eng. *Physical review. Accelerators and beams* **20,** 103403–. ISSN: 2469-9888. https://doi.org/10.1103/PhysRevAccelBeams.20.103403 (2017).

194. Wolgast, R. C. Design of the Cryopumping Vacuum System for ESCAR. eng. *IEEE transactions on nuclear science* **22,** 1496–1499. ISSN: 0018-9499. https://doi.org/10.1109/TNS.1975.4327918 (1975).

195. Levitt, B *et al.* Single-component plasma of photoelectrons. eng. *Physics letters. B* **656,** 25–29. ISSN: 0370-2693. https://doi.org/10.1016/j.physletb.2007.08.092 (2007).

196. Dresner, L. *Stability of superconductors* eng. ISBN: 9780306450303 (Plenum Press, New York, 1995).

197. Ekin, J. W. *Experimental Techniques for Low-Temperature Measurements. Cryostat Design, Material Properties and Superconductor Critical-Current Testing* eng. ISBN: 9780198570547 (Oxford University Press, Oxford, 2006).

198. Bian, W.-L. *et al.* Design of an asymmetric superconducting magnet for a Penning trapSupported by National Natural Science Foundation of China (11302225). eng. *Chinese physics C* **39.** ISSN: 1674-1137. https://doi.org/10.1088/1674-1137/39/5/057004 (2015).

199. Coull, L, Hagedorn, D, Remondino, V & Rodriguez-Mateos, F. LHC magnet quench protection system. eng. *IEEE transactions on magnetics* **30,** 1742–1745. ISSN: 0018-9464. https://doi.org/10.1109/20.305593 (1994).

200. Amole, C *et al.* The ALPHA antihydrogen trapping apparatus. eng. *Nuclear instruments and methods in physics research. Section A, Accelerators, spectrometers, detectors and associated equipment* **735,** 319–340. ISSN: 0168-9002. https://doi.org/10.1016/j.nima.2013.09.043 (2014).

201. Ren, X *et al.* Electron-impact ionization of helium: A comprehensive experiment benchmarks theory. eng. *Physical review. A, Atomic, molecular, and optical physics* **83.** ISSN: 1050-2947. https://doi.org/10.1103/PhysRevA.83.052711 (2011).

202. Donets, E. D. Historical review of electron beam ion sources (invited). eng. *Review of Scientific Instruments* **69,** 614–619. ISSN: 0034-6748. https://doi.org/10.1063/1.1148642 (1998).

203. Gamez, G., Zhu, L., Schmitz, T. A. & Zenobi, R. Photoelectron Emission as an Alternative Electron Impact Ionization Source for Ion Trap Mass Spectrometry. eng. *Analytical chemistry (Washington)* **80,** 6791–6795. ISSN: 0003-2700. https://doi.org/10.1021/ac8007187 (2008).

204. Kim, Y. & Rudd, M. Binary-encounter-dipole model for electron-impact ionization. eng. *Physical review. A, Atomic, molecular, and optical physics* **50,** 3954–3967. ISSN: 1050-2947. https://doi.org/10.1103/PhysRevA.50.3954 (1994).

205. Lacy, J. H. *et al.* Flux Pumping of Multiple Double-Loop Superconducting Structures for a Planar Magnetic Field Source. *IEEE Transactions on Applied Superconductivity* **32,** 1–11. https://doi.org/10.1109/TASC.2022.3178359 (2022).

206. Higaki, H, Ito, K, Saiki, W, Omori, Y & Okamoto, H. Properties of non-neutral electron plasmas confined with a magnetic mirror field. eng. *Physical review. E, Statistical, nonlinear, and soft matter physics* **75,** 066401–066401. ISSN: 1539-3755. https://doi.org/10.1103/PhysRevE.75.066401 (2007).

207. Paasche, P *et al.* Instabilities of an electron cloud in a Penning trap. eng. *The European physical journal. D, Atomic, molecular, and optical physics* **22,** 183–188. ISSN: 1434-6060. https://doi.org/10.1140/epjd/e2002-00239-3 (2003).

208. Schweikhard, L., Ziegler, J., Bopp, H. & Lützenkirchen, K. The trapping condition and a new instability of the ion motion in the ion cyclotron resonance trap. eng. *International journal of mass spectrometry and ion processes* **141,** 77–90. ISSN: 0168-1176. https://doi.org/10.1016/0168-1176(94)04092-L (1995).

209. Roth, P. & Fraser, G. Microchannel plate resistance at cryogenic temperatures. eng. *Nuclear instruments & methods in physics research. Section A, Accelerators, spectrometers, detectors and associated equipment* **439,** 134–137. ISSN: 0168-9002. https://doi.org/10.1016/S0168-9002(99)00792-5 (2000).

210. The Heidelberg compact electron beam ion traps. eng. *Review of scientific instruments* **89,** 063109–063109. ISSN: 0034-6748. https://doi.org/10.1063/1.5026961 (2018).